
Narrow line kinematics in a spectroscopic survey of X-ray selected AGN in the XMM-XXL North

Marie-Luise Menzel



München 2016

Narrow line kinematics in a spectroscopic survey of X-ray selected AGN in the XMM-XXL North

Marie-Luise Menzel

Dissertation
an der Fakultät für Physik
der Ludwig-Maximilians-Universität
München

vorgelegt von
Marie-Luise Menzel
aus Cottbus, Deutschland

München, den 9. September 2016

Erstgutachter: Prof. Kirpal Nandra

Zweitgutachter: Prof. Barbara Ecolano

Tag der mündlichen Prüfung: 18. Oktober 2016

Contents

Abstract	1
1. Introduction	5
1.1. Mass accretion in AGN	7
1.1.1. From Galactic scale to black hole scale	7
1.1.2. Accretion luminosity and rate	7
1.1.3. Accretion models	8
1.2. Components and multi-wavelength view of AGN and host galaxy	10
1.2.1. Unification model	11
1.2.2. AGN emission	11
1.2.3. Host galaxy emission	15
1.3. AGN selection	17
1.4. Evolution of AGN and host galaxies	18
1.4.1. AGN evolution	18
1.4.2. AGN-galaxy-coevolution and feedback processes	20
1.5. Motivation of this Thesis	24
1.6. Outline of the Thesis	26
2. Datasets and Analysis Methods	27
2.1. Introduction	27
2.2. Introduction of imaging data sets	29
2.2.1. <i>XMM-XXL</i> survey and X-ray source catalogue	29
2.2.2. Optical source catalogue of <i>SDSS</i>	29
2.2.3. Infrared source catalogue of <i>WISE</i>	30
2.2.4. Cross-matching of data sets	30
2.3. Introduction of spectroscopic data set	33
2.3.1. BOSS spectroscopic survey	33
2.3.2. Spectroscopic target selection	33
2.4. Spectroscopic AGN Sample: Redshift Determination and Classification	38
2.4.1. BOSS pipeline products	38
2.4.2. Redshift determination	39
2.4.3. Spectroscopic Classification	42
2.4.4. Final classified sample	47
2.5. Spectroscopic AGN Sample: Class Properties	48
2.5.1. X-ray and Optical properties	48
2.5.2. BLAGN1	49
2.5.3. NLAGN2 and NLAGN2cand	50
2.5.4. eAGN-ALG and eAGN-SFG	50

2.6. Summary: Understanding the AGN population in the XMM-XXL north . . .	54
3. Study of optical emission line, optical colour, mid-IR colour and X-ray AGN selection techniques	55
3.1. Motivation	55
3.2. Introduction	56
3.3. Outline	57
3.4. Optical: emission lines diagnostics	58
3.4.1. Spectroscopic properties of optical emission line selected AGN	58
3.5. Optical: XDQSO targeting algorithm	60
3.5.1. X-ray detection fraction	60
3.5.2. Morphological and spectroscopic properties of XDQSO-selected AGN	61
3.6. Infrared: <i>WISE</i> colour selection	64
3.6.1. X-ray detection fraction	64
3.6.2. Infrared and spectroscopic properties of <i>WISE</i> selected AGN	65
3.7. Summary: Uniqueness of X-ray AGN selection	70
3.7.1. Optical emission line diagnostics	70
3.7.2. Photometric AGN selection methods	71
3.8. Conclusion	74
4. Kinematic properties of narrow line regions in X-ray selected AGN	75
4.1. Motivation	75
4.2. Introduction	76
4.2.1. Feedback models	76
4.2.2. Outflows types: AGN and star formation excitation	76
4.2.3. Observation of outflows	77
4.3. Outline	78
4.4. Emission line fit of [OII] and [OIII]	79
4.4.1. Fitting Algorithm	79
4.4.2. Characterization of asymmetric [OIII] emission line profiles	81
4.5. Presentation of AGN and ELG dataset	84
4.5.1. X-ray catalogue	84
4.5.2. ELG catalogue	84
4.5.3. Redshift, magnitude and S/N ratio distributions	85
4.6. Incidence of [OIII] outflows in star forming galaxies and AGN	87
4.6.1. Significant [OII] and [OIII] emission lines	87
4.6.2. [OIII] outflow incidence	87
4.7. Comparison of [OIII] emission line profiles in ELG and AGN	89
4.7.1. $F_{\text{OII-to-OIII}}$ -ratio	89
4.7.2. Match of star forming galaxies and AGN in star formation rate	91
4.7.3. Average [OIII] profiles in host galaxies of high and low star formation rate	93
4.8. Correlation of [OIII] outflows with AGN accretion properties	99
4.8.1. AGN subsample with significant ionized [OIII] outflows/inflows	99
4.8.2. [OIII] outflows in the entire AGN population	108

4.8.3. The average outflow momentum rate and kinetic power of AGN outflows	114
4.9. Discussion	118
4.10. Summary: Relevance of ionized outflows for AGN feedback	124
5. Forecast for <i>eROSITA</i> AGN population, summary and prospects for the future	125
5.1. Forecast for the AGN population of <i>eROSITA</i>	125
5.1.1. <i>eROSITA</i> instrument	125
5.1.2. Follow-up programmes of <i>eROSITA</i> sources	127
5.1.3. <i>SPIDERS</i> - Spectroscopic follow-up of <i>eROSITA</i> sources	129
5.1.4. Spectroscopic completeness for <i>SPIDERS</i>	130
5.1.5. Comparison of AGN selections for <i>eROSITA</i> depths	133
5.2. Summary of the Thesis	135
5.3. Future prospects	138
5.3.1. X-ray selected AGN populations	138
5.3.2. Impact of outflows on AGN feedback	139
A. AGN Catalogue in the XMM-XXL	141
B. Spectral stacks of star formation calibrated AGN and ELG	143
C. Spectral stacks of hard X-ray and optical/UV continuum luminosity binned AGN sample	147

List of Figures

1.1. Schematic view of AGN	10
1.2. Schematic spectral energy distribution of AGN	12
1.3. Schematic Grotrian diagram of OIII	13
1.4. AGN and galaxy SEDs of AGN and Galaxies	16
1.5. Bolometric AGN luminosity function for different redshifts	19
1.6. Break luminosity and luminosity density of of best double power-law fit to the quasar bolometric luminosity function	19
1.7. Comparison of star-formation history with the massive black hole accretion history	20
1.8. $M_{\text{BH}} - \sigma_*$ relation for galaxies with dynamical black hole mass measurements	21
2.1. Histogram of the soft X-ray flux for point-like X-ray sources in the northern XMM-XXL area	31
2.2. Distribution and histogram of r -band magnitude for X-ray counterparts . .	31
2.3. Distribution and histogram of $W2$ -band magnitude for X-ray counterparts .	32
2.4. Spectroscopic target selection in the XMM-XXL north field	34
2.5. XMM-XXL north field with sky coordinates of <i>XMM-Newton</i> sources and associated <i>BOSS</i> observed targets	35
2.6. Distribution of <i>BOSS</i> pipeline redshifts and the S/N ratio	41
2.7. Average FWHM distribution of emission lines	42
2.8. Classification flow-chart for <i>BOSS</i> spectra	43
2.9. BPT-NII and Blue-OII optical emission line diagrams	46
2.10. Distribution of optical and X-ray flux and luminosity	48
2.11. Luminosity and visual redshift distribution of BLAGN1	49
2.12. Median spectral stack of BLAGN1	51
2.13. Luminosity and visual redshift distribution of NLAGN2 and elusive AGN .	52
2.14. Median spectral stack of NLAGN2 and elusive AGN	53
3.1. Cumulative number density and X-ray detection fraction of XDQSO selected AGN	61
3.2. Median spectral stack of XDQSO selected AGN	63
3.3. Cumulative number density and X-ray detection fraction of infrared selected AGN	65
3.4. <i>WISE</i> colour diagram with infrared AGN selections, class regions and as a function of redshift	66
3.5. Median spectral stack of infrared selected AGN	68
3.6. Venn diagram of X-ray, optical and infrared AGN selections	72

4.1. Example spectra for OIII fitting algorithms	81
4.2. Schematic diagram of asymmetric emission line with characteristic parameters	82
4.3. Hard X-ray luminosity and redshift distribution of complete AGN sample .	85
4.4. Redshift and r_{model} magnitude distribution of ELG and X-ray selected AGN	86
4.5. S/N ratio in OII and OIII emission line region	86
4.6. Distribution of F_{OII}/F_{OIII} ratio for ELG and AGN	90
4.7. Distribution and histogram of OII star formation luminosity or star formation rate as function of redshift	92
4.8. Distribution and histogram for upper limits of OII star formation luminosity and star formation rate as function of redshift	92
4.9. Spectral stack of ELG, BLAGN1 and NLAGN2 in star formation rate bins .	94
4.10. Normalized spectral stack of OIII for ELG, BLAGN1 and NLAGN2 in star formation rate bins	95
4.11. W_{80} of spectral stacks of ELG, BLAGN1, NLAGN2 in different OII star formation luminosity bins	96
4.12. Normalized spectral stacks of ELG, BLAGN1, NLAGN2 for OII star formation luminosity upper limits	97
4.13. Distribution of OIII emission line parameters for BLAGN1 and NLAGN2 .	100
4.14. Distribution of the offset velocity and velocity dispersion of AGN	101
4.15. Selected <i>BOSS</i> spectra with extreme outflow/inflow characteristics.	102
4.16. Correlation of hard X-ray luminosity and optical/UV continuum luminosity	104
4.17. Spearman Rank correlation of flux and luminosities of OIII components with optical/UV continuum flux or luminosity and hard X-ray flux or luminosity	106
4.18. Spearman Rank correlation of velocity-related OIII parameters with optical/UV continuum flux or luminosity and hard X-ray flux or luminosity . .	107
4.19. Histogram of hard X-ray luminosity and optical/UV continuum luminosity for AGN subsets	108
4.20. Spectral stacks of BLAGN1 in hard X-ray and continuum luminosity bins .	109
4.21. Distribution of OIII parameters from stacked AGN binned in optical/UV continuum and hard X-ray luminosity	110
4.22. Spectral stack of AGN in hard X-ray luminosity bins	111
4.23. Spectral stack of AGN in comparable hard X-ray luminosity bins	111
4.24. Kinetic power of ionized outflow and contribution to bolometric luminosity .	116
4.25. Momentum rate of ionized outflow and ratio with AGN momentum rate . .	117
4.26. Model of conical and dispersing outflows	122
5.1. Schematic diagram of <i>eROSITA</i> telescope structure.	126
5.2. <i>eROSITA</i> sky coverage of selected wide area surveys.	128
5.3. Spectroscopic completeness in the XMM-XXL north	132
5.4. Comparison of <i>SPIDERS</i> soft X-ray and redshift distribution in comparison to other surveys.	133
5.5. Cumulative number density and X-ray detection fraction of XDQSO and infrared selected AGN at <i>eROSITA</i> depths	134
5.6. Venn diagram of X-ray, optical and infrared AGN selections at <i>eROSITA</i> depths	134

B.1. Spectral stacks of OIII region for BLAGN1 and NLAGN2 from Sec. 4.7.3 . 144

B.2. Spectral stacks of OIII region for ELG from Sec. 4.7.3 145

C.1. Spectral stacks of OIII region for BLAGN1 from Sec. 4.8.2 binned in hard
X-ray and optical/UV continuum luminosity 148

C.2. Spectral stacks of OIII region for NLAGN2 and eAGN-SFG from Sec. 4.8.2
binned in hard X-ray luminosity 149

C.3. Spectral stacks of OIII region for BLAGN1&NLAGN2 and complete sample
from Sec. 4.8.2 binned in hard X-ray luminosity 150

List of Tables

2.1.	<i>BOSS</i> plate information of the <i>XMM-SDSS</i> targets in the XMM-XXL north	36
2.2.	Final redshifts and redshift confidence of <i>BOSS</i> spectra after the visual inspection	40
3.1.	XDQSO properties of X-ray selected AGN with spectroscopic information .	62
3.2.	<i>WISE</i> properties of X-ray selected AGN with spectroscopic information . .	67
4.1.	ELG and AGN sources with significant line features	87
4.2.	Fraction of ionized OIII outflows/inflows in BLAGN1 and NLAGN2.	88
4.3.	Redshift dependence of OII-OIII-flux-ratio	90
4.4.	Emission line parameters of OII and OIII for spectral stacks in different star forming luminosity bins	98
4.5.	Median and Spearman rank correlation of OIII line parameters with hard X-ray flux and optical/UV continuum flux	105
4.6.	OIII emission line parameter in bins of hard X-ray luminosity and optical/UV continuum luminosity.	113
5.1.	<i>eROSITA</i> flux limits	127
5.2.	Number densities for X-ray sources in the XMM-XXL north at different flux depths	131
A.1.	Information about catalogue columns of X-ray selected AGN in the northern XMM-XXL field	142

Abstract

This thesis addresses the interaction of supermassive black holes (SMBH) with their host galaxies through feedback processes during 'active' phases (Active Galactic Nuclei, AGN). Current numerical and analytical models of galaxy formation postulate that AGN driven feedback is the key ingredient to regulate the galaxy growth. We study the origin and impact of feedback processes by focussing on the kinematic properties of the ionized gas in the AGN host galaxies, as traced by optical narrow emission lines of [OIII]. These emission lines are sensitive to large scale ionized outflows, and can be assessed for a large AGN population with both obscured or unobscured nuclear regions. The properties of these outflows can give further insights into the processes which shape the multi-phase intergalactic medium and the nature of central obscuration mechanisms in AGN. Furthermore, they allow to probe the unification model of AGN by comparing their properties in optically obscured and unobscured AGN.

We approached these inquiries about feedback and obscuration processes a) by gathering an unbiased dataset of AGN based on X-ray selection, in order to probe the entire AGN population with as little biases as possible, and b) by analyzing optical spectroscopic data, to reveal the detailed properties of the ionized gas signatures of feedback processes. Previous works on the subject have been performed either on individual sources, or comparably small surveys.

We chose the XMM-XXL north region which serves as a pilot study for the *eROSITA* follow-up programme *SPIDERS* in *SDSS-IV* and provides a suitable dataset due to the X-ray selection and optical spectroscopic follow-up. As part of our work, we presented and publicly released one of the largest contiguous catalogues of X-ray selected and spectroscopically observed AGN to date. A parent sample of 8445 point-like X-ray sources is detected by the *XMM-Newton* satellite above a limiting flux of $F_{0.5-10\text{keV}} > 1 \cdot 10^{-15} \text{ erg cm}^{-2} \text{ s}^{-1}$ in a $\sim 18 \text{ deg}^2$ equatorial area. The sample was matched to optical (*SDSS*) and infrared (*WISE*) counterparts, and we followed up 3042 sources brighter than $r = 22.5$ mag with the *BOSS* spectrograph from *SDSS*. The spectra yielded a reliable redshift measurement for 2578 AGN in the redshift range $z = 0.02 - 5.0$, with 0.5-2 keV luminosities ranging from $\sim 10^{39} - 10^{46} \text{ erg s}^{-1}$. We performed a classification of the AGN based on common optical emission line properties.

In the first part of this thesis, we present an extensive comparison of optical, infrared and X-ray AGN selection criteria, and analyze their impact on the selected populations. X-rays directly trace high-energetic processes in the neighborhood of the SMBH and are only weakly disturbed by star-formation processes or effects of obscuration. Therefore, they probe a wide variety of AGN classes and assess an unique population of AGN, which is likely to be missed otherwise.

In the second part of this thesis, we study the narrow emission line kinematics in X-ray selected AGN. The [OIII] emission line ($\lambda = 5008 \text{ \AA}$, accessible by *SDSS/BOSS* for

$0 < z < 1$) allows the detection of ionized gas clouds which are affected by the gravitational potential of the galaxies, and additionally shows signatures of outflows/inflows generated by AGN or star formation activity. We developed a dedicated line fitting algorithm to decompose the contribution of both mechanisms to the profile of the [OIII] emission. A highly redshift complete AGN sample (with $F_{2-10\text{keV}} > 2.5 \cdot 10^{-14} \text{ erg s}^{-1}$ and $0 < z < 0.8$) comprises 35 per cent of AGN with signatures of ionized [OIII] outflows/inflows. This is probably a lower limit of the true incidence of outflows/inflows, due to the limited SN ratio of the faintest sources in the sample. Out of those AGN with outflow/inflow signatures, 75 per cent are blueshifted with respect to the systemic velocity of the galaxy and can be interpreted as outflows.

Our analysis required a careful estimate of the star formation contribution to the emission lines and we demonstrate that the ionized outflow/inflow signatures in the [OIII] emission lines of our X-ray selected AGN sample cannot be assigned to solely star formation. Moreover, we find strong correlations of line luminosity and widths with AGN accretion power indicators such as hard X-ray luminosity and optical/UV continuum luminosity. This is a strong evidence that the narrow line region is influenced by AGN-powered outflows, which are part of the feedback process.

Furthermore, we observe that the [OIII] emission line signatures of ionized outflows are independent of the nuclear obscuration, which disagrees with the standard ‘obscuration by orientation’ picture of AGN and might be due to a complex structure of the central torus. Finally, based on the complete dataset of X-ray selected AGN, we determine the average kinetic power and momentum rate of ionized [OIII] outflows in AGN. Despite large model uncertainties, we estimate that the kinetic power is a constant fraction of ≈ 0.01 per cent of the bolometric luminosity, and in any case never exceeds 0.2 per cent. The momentum boost of the [OIII] outflow is a constant fraction of ≈ 0.1 reaching a maximal fraction 1. Based on current models studying the impact of feedback on the scaling relation between black hole and host galaxy growth, we concluded that ionized [OIII] outflows do not provide sufficient kinetic energy or momentum boost to have a major effect on feedback processes in AGN host galaxies.

Kurzdarstellung

Die vorliegende Dissertation thematisiert die Interaktion zwischen Supermassiven Schwarzen Löchern und ihren umgebenden Galaxien. Diese Interaktion geschieht insbesondere während der aktiven Phasen (Aktive Galaktische Kerne, englisch: Active Galactic Nuclei, AGN) durch sogenannte 'Feedbackprozesse' (Rückkopplungsprozesse). Für die aktuellen numerischen und analytischen Modelle zur Galaxienbildung ist das AGN-getriebene Feedback ein Hauptbestandteil des Galaxienwachstums. Wir analysieren den Ursprung und den Einfluss von Feedbackprozessen im Hinblick auf die kinematischen Eigenschaften ionisierter Gaswolken in den Galaxien von AGN. Diese Gaswolken befinden sich u.a. in einer Region, die schmale Emissionlinien aussendet - die sogenannte 'narrow line region' (NLR) - und können in einer großen AGN-Population mit überdeckten oder unüberdeckten Kernen beobachtet werden. Die Emissionslinien dieser Region werden von ausgedehnten und ionisierten Ausflüssen beeinflusst. Die Eigenschaften dieser Ausflüsse liefern weitere Einblicke in die Mechanismen zur Beeinflussung intergalaktischer Materie und der Überdeckung von Galaxienkernen.

Wir untersuchen die vorgestellten Fragestellungen über Feedbackprozesse und Überdeckungsmechanismen mit einem unvoreingenommenen Datensatz Röntgen-selektierter AGN um die vollständige AGN-Population zu repräsentieren. Desweiteren analysieren wir optische Spektroskopiedaten um die detaillierten Eigenschaften von ionisierten Gaswolken, welche Feedbackprozessen unterliegen, aufzuzeigen. Vorhergehende Arbeiten zu diesem Thema wurden an individuellen Objekten oder Datensätzen mit nur wenigen Objekten durchgeführt.

In der vorliegenden Arbeit untersuchen wir die XMM-XXL Nord Region, welche sehr gute Datenvoraussetzungen für die Durchführung der geplanten Studien hat und veröffentlichten damit den bisher größten zusammenhängenden Katalog Röntgen-selektierter AGN mit optischer spektroskopischer Nachverfolgung. Der Datensatz befindet sich in einem 18 deg^2 großen äquatorialen Feld in der XMM-XXL North Region und umfasst 8445 punktförmige Objekte. Die AGNs wurden vom *XMM-Newton* Satelliten beobachtet und anschließend mit den entsprechenden optischen (*SDSS*) und infraroten (*WISE*) Partnerdaten zusammengebracht. Für 3042 dieser Objekte mit einer Helligkeit von $r < 22.5$ wurde eine optische spektroskopische Nachverfolgung mit dem *BOSS* Spektrographen durchgeführt. Für 2587 dieser Spektren konnten verlässliche Rotverschiebungen im Bereich $z = 0.02 - 5.0$ festgestellt werden. Die Leuchtstärke dieser Objekte im Wellenlängenbereich $0.5 - 2 \text{ keV}$ umfasst $10^{39} - 10^{46} \text{ erg s}^{-1}$. Die AGN wurden basierend auf den Eigenschaften ihrer optischen Spektren in optische Klassen eingeteilt. Der erhobene Datensatz dient als Pilotstudie für das *eROSITA*-Nachverfolgungsprogramm *SPIDERS* in Rahmen von *SDSS-IV*.

Im ersten Teil der Dissertation präsentieren wir einen ausführlichen Vergleich verschiedener Optik-, Infrarot- und Röntgen-Selektionskriterien von AGN. Desweiteren untersuchen wir deren Einfluss auf die Eigenschaften der beobachteten AGN-Populationen. Dabei stellt die

Röntgenstrahlung die direkte hoch-energetische Strahlung dar, die im nahen Umfeld des Supermassiven Schwarzen Lochs emittiert wird. Desweiteren wird diese Strahlung von Sternbildungsprozessen oder Überdeckungen des Kerns nur schwach beeinflusst. Aus diesem Grund ermöglicht Röntgenstrahlung einen besonderen Zugang zu einer großen Vielfalt von AGN-Klassen und insbesondere zu AGN, die durch andere Selektionskriterien nicht entdeckt worden wären.

Im zweiten Teil der Dissertation untersuchen wir die kinematischen Eigenschaften der 'narrow line region' in Röntgen-selektierten AGN. Die [OIII]-Emissionslinie ($\lambda = 5008 \text{ \AA}$) – beobachtbar mit *BOSS* innerhalb von $0 < z < 1$ – kann ionisierte Gaswolken nachweisen, die vom Gravitationspotential der Galaxie beeinflusst sind. Desweiteren gibt die Form dieser Emissionslinie Hinweise über die Präsenz von Ausflüssen/Zuflüssen, die durch AGN oder Sternbildungsaktivität produziert worden sind. Wir entwickelten einen dedizierten Emissionslinien-Algorithmus, der ein Zerlegen in die Galaxie- und die Ausflussdominierten Komponenten ermöglicht. Unser Datensatz enthält eine Untergruppe von AGN, die im Rahmen einer bestimmten Rotverschiebungs- und Flussgrenze eine komplette Bestimmung der Rotverschiebung aufweisen ($F_{2-10 \text{ keV}} > 2.5 \cdot 10^{-14} \text{ erg s}^{-1}$ und $0 < z < 0.8$). In diesem vollständigen Datensatz enthalten 35 Prozent der AGNs Hinweise auf ionisierte [OIII]-Ausflüsse/Zuflüsse. Dieser Anteil kann als unteres Limit des wahren Anteils gesehen werden, da das Signal-Rausch-Verhältnis der lichtschwächsten Objekte begrenzt ist. Bezogen auf die Ausflüsse/Zuflüsse zeigen 75 Prozent der AGN eine Blauverschiebung, die auf einen Ausfluss hindeutet.

Unsere Analyse bedarf einer sorgfältigen Abschätzung des Sternbildungsanteils an den beobachteten Ausflüssen/Zuflüssen. Wir zeigen auf, dass die Eigenschaften der Emissionslinien unseres Röntgen-selektierten Datensatzes nicht ausschließlich auf die Sternbildung zurückzuführen sind. Wir beobachten im Gegenteil eine starke Korrelation zwischen der Leuchtkraft sowie der Breite der Emissionslinien mit den charakteristischen Parametern der Akkretionsleistung des schwarzen Lochs wie z.B. Röntgen-Leuchtkraft oder Leuchtkraft des optischen/UV Kontinuums. Dies ist ein besonders starker Beweis, dass interstellares Gas von AGN-betriebenen Ausflüssen als Teil des Feedback-Prozesses beeinflusst wird.

Weiterhin beobachten wir, dass die [OIII]-Emissionslinien-Eigenschaften von ionisierten Ausflüssen unabhängig von der Überdeckung des Kerns sind. Trotzdem treten Ausflüsse in AGN mit unüberdeckten Kernen häufiger auf. Das weist darauf hin, dass die Überdeckung des AGN-Kerns durch einen evolutionären Prozess hervorgerufen wird und Ausflüsse die überdeckende Gas- und Staubschicht um den Kern wegtragen können.

Zum Abschluss bestimmen wir die mittlere kinetische Leistung und Impulsrate ionisierter Ausflüsse in AGN unter Verwendung des (Rotverschiebungs-)vollständigen Datensatzes. Trotz großer Ungenauigkeiten des Modells stellen wir fest, dass die kinetische Leistung einen konstanten Anteil von 0.01 Prozent der bolometrischen Leuchtkraft umfasst und dabei als Maximalwert 0.2 Prozent erreicht. Die Impulsrate der [OIII] Ausflüsse liegt bei 10 Prozent der gesamten AGN-Impulsrate und hat ein oberes Limit von 100 Prozent. Basierend auf den aktuellen theoretischen Modellen zum Einfluss von Feedback-Prozessen auf die Wachstumsbeziehung zwischen Schwarzen Löchern und ihren umgebenden Galaxien haben [OIII] Ausflüsse weder genügend kinetische Energie noch eine ausreichende Impulsrate um einen bedeutenden Einfluss auf Feedback-Prozesse in den umgebenden Galaxien zu nehmen.

1. Introduction

A large body of evidences suggests, that nearly all local spheroids host a super-massive black hole (SMBH) with masses in the order of $10^6 - 10^{10} M_{\odot}$ (see e.g. Merloni & Heinz 2013 for a recent review). This evidence is based on e.g. gas and stellar dynamics (Ford et al., 1994; Magorrian et al., 1998; Ghez et al., 2002; Schödel et al., 2002), reverberation mapping (Krolik, 2001; Peterson et al., 2004; Shen et al., 2015) and gravitationally shifted broad Fe $K\alpha$ lines (Tanaka et al., 1995; Nandra et al., 1997; Reynolds & Begelman, 1997). From studies of e.g. Soltan (1982) and Marconi et al. (2004), we know that the black hole growth occurs predominantly through accretion processes from material of the host galaxy or the extra-galactic environment. For the group of heavily accreting ‘active galactic nuclei’ (AGN), the energy released during the accretion process strongly impacts the surrounding region of the AGN and causes characteristics imprints in the observed multi-wavelength properties (see e.g. Netzer 1990; Peterson 1997; Risaliti & Elvis 2004; Osterbrock & Ferland 2006).

From various observations of AGN and ambient host galaxies, we know that key properties of the black hole and galaxy are closely correlated. This includes e.g. the black hole mass and properties of the stellar bulge, such as mass, luminosity, velocity dispersion and gravitational potential (Magorrian et al., 1998; Gebhardt et al., 2000; Ferrarese & Merritt, 2000; Gültekin et al., 2009), but also black hole mass accretion and star formation history (e.g. Merloni & Bongiorno 2013, Madau & Dickinson 2014).

It is highly intriguing that the connection of AGN and host galaxy properties consists over such a large scale difference. Theoretical models explain this coevolution with feedback processes, where the AGN injects energy in the surrounding gas (see reviews of Fabian 2012; Alexander & Hickox 2012). This is supposed to result in gas depletion inside star forming regions, which leads to the decrease of black hole fuel. Among various processes, which are discussed to cause the feedback, we focus on radiative ionized outflows which are reaching the extended narrow line region of AGN and can be traced by [OIII]. The goal of this thesis is to understanding how ionized [OIII] outflows interact with the AGN environment and how strong they contribute to the total feedback process. Furthermore, we use the properties of the [OIII] outflows in optically obscured and unobscured AGN to test the unification model of AGN by Antonucci (1993) and Urry & Padovani (1995).

The topic of feedback has been matter of extensive study since many years and is very closely linked to the properties of the observed AGN populations. Since AGN differ in their black hole and host galaxy properties, the selection criteria of AGN will always probe only a subsample of the entire AGN population. Thus, before solving the questions of galaxy and AGN co-evolution, it is necessary to revise the concepts of the AGN engine and

the associated emission in the spectral energy distribution. Only in this way, we can assess whether our census of AGN is complete or not and whether our finding can be generalized.

In the Introduction of this thesis, we will firstly present in Sec. 1.1 the concept of accretion, which is the fundamental process of the black hole growth. In Sec. 1.2, we will describe the physical components of AGN and host galaxies, introduce the 'unification model' and explain the spectral energy distribution. This leads to the introduction of common AGN selection criteria in Sec. 1.3. In a next step, we are going to introduce the concepts of AGN and host galaxy co-evolution, accompanied by a description of the properties of feedback in Sec. 1.4. Finally, the motivation and outline of the thesis will be presented in Sec. 1.5 and Sec. 1.6.

1.1. Mass accretion in AGN

Since the discovery of the first 'quasi-stellar object' and the introduction of models about SMBH (Salpeter 1964; Zel'dovich & Novikov 1964; Lynden-Bell & Rees 1971), the improvement in multi-wavelength imaging and spectroscopy has revealed insight into the nature of AGN. In our understanding, AGN are the sites of powerful emission processes, are supposed to interact with their host galaxies, and even allow for studies of cosmological questions. The mass accretion represents a fundamental process of this powerful engine.

In this section, we are going to give an overview of the physical processes behind the mass accretion in AGN. This includes the explanation of the path of fueling gas, which has to overcome large angular momentum barriers and stellar winds from the star formation processes in order to reach the AGN at $\ll 0.1$ pc. Furthermore, we will describe the physical concepts behind the accretion disk's emission, which represents the most important energy source for the environment of the AGN.

1.1.1. From Galactic scale to black hole scale

Part of the gas' angular momentum is assumed to be reduced by large-scale gravitational torques caused by e.g. galaxy bars, galaxy interactions or major mergers (Alexander & Hickox, 2012). This allows for the gas to approach the black hole down to 10 – 100 pc. The gas accretion on the 1 – 10 pc scale falls in the regime where the black hole's gravitational influence overcomes the galaxy's one. The radius r_{infl} where the black holes gravitational pull starts to dominate is determined by the black hole mass M_{BH} and the velocity dispersion of gas and/or stars in the galaxy spheroid σ_{spheroid} :

$$r_{\text{infl}} < \frac{G M_{\text{BH}}}{\sigma_{\text{spheroid}}^2}. \quad (1.1)$$

Assuming a black hole mass of $10^8 M_{\odot}$ and a velocity dispersion of $\sigma = 200 \text{ km s}^{-1}$, we obtain a radius of $r_{\text{infl}} \approx 10$ pc. At this distance, gas and matter face an attracting gravitational force of the black hole and a repelling force due to stellar winds from star formation. These processes cause a deposition of gas and matter in this region, the so-called 'torus', which is suggested to be the outer gas reservoir for the black hole accretion disk and at the same time place of star formation.

1.1.2. Accretion luminosity and rate

The accretion onto black holes, results in the radiative output which can be understood as dissipation of gravitational potential energy as matter falls towards the black hole; assuming that the angular momentum can be transferred. The process may be counterbalanced by the radiation pressure of the photons which is directed outwards:

$$F_{\text{rad}} = F_{\text{grav}} \quad (1.2)$$

$$\frac{\sigma_T}{c} \frac{L}{4\pi r^2} = \frac{-G M_{\rho} m_p}{r^2}. \quad (1.3)$$

Based on this equation, we can derive the Eddington luminosity L_{Edd} which represents the maximal radiation luminosity balancing the matter-infall:

$$L_{\text{Edd}} = \frac{4\pi G M_{\text{BH}} m_p c}{\sigma_T} \approx 1.3 \cdot 10^{38} \frac{M_{\text{BH}}}{M_{\odot}} \text{ erg s}^{-1} \quad (1.4)$$

with the proton mass m_p and the Thomson cross-section σ_T . The Eddington ratio λ is supposed to be strongly related to the black hole growth rate. This rate is subject to the efficiency of converting the mass-energy of accreting material into radiation. The Eddington ratio is calculated as follows:

$$\lambda = \frac{L_{\text{bol}}}{L_{\text{Edd}}}. \quad (1.5)$$

If we assume that the luminosity of AGN is dominated by the energy release during the accretion process, then the luminosity L_{acc} correlates with accretion rate $dm/dt = \dot{M}$ as below:

$$L_{\text{acc}} = \frac{G M_{\text{BH}} \dot{M}}{r} = \frac{\dot{M} c^2 R_s}{2r} = \epsilon \dot{M} c^2. \quad (1.6)$$

R_s is the Schwarzschild radius, which stands for the event horizon of the Schwarzschild-metric for a non-spinning black hole. The parameter ϵ indicates the accretion efficiency and is defined as $\epsilon = L_{\text{acc}}/(\dot{M} c^2) = R_s/(2r)$ (for non-spinning black holes) and is typically in the range of $\epsilon \approx 0.05 - 0.2$ (Marconi et al., 2004). We can now derive the maximum accretion rate based on the Eddington luminosity as follows:

$$L_{\text{acc}} = L_{\text{Edd}} \quad (1.7)$$

$$\dot{M}_{\text{Edd}} = \frac{4\pi G M_{\text{BH}} m_p}{\epsilon c \sigma_T} = \frac{L_{\text{Edd}}}{\epsilon c^2}. \quad (1.8)$$

1.1.3. Accretion models

The gas in AGN is supposed to be collapsed into a disk-like structure in order to radiate away the energy. The release of the angular momentum can be explained by different models. We refer to the standard alpha-disk model around sub-Eddington black holes, introduced by Shakura & Sunyaev (1973).

In this model, the angular momentum of the gas is lost by the viscosity in optically thick (high opacity) but geometrically thin ($h/r \ll 1$, height h and radius r) disks. The gas falls on tight spirals down into the black hole, comparable to Keplerian geodesic orbits. The accretion disk has to conserve the total momentum which is granted by momentum 'transport' from the inner regions to the outer regions of the disk. In this model, the momentum conservation is enabled by turbulences of the gaseous material in the disk causing increased viscosity and leading into viscous heating of the disk. The viscosity ν corresponds to:

$$\nu = \alpha c_s h \quad (1.9)$$

with the sound speed c_s and the disk height h . The viscosity parameter α ranges between 0 for no accretion and 1 for maximal accretion.

We assume that the accretion energy is dissipated within a small region of the disk. According to the Stefan-Boltzmann-Law for black body spectra, the temperature of the disk annuli at radius r is subject to following correlations:

$$L_{\text{SB}} = L_{\text{acc}} \quad (1.10)$$

$$4\pi r^2 \sigma_{\text{SB}} T^4 = \frac{G M_{\text{BH}} \dot{M}}{r} \quad (1.11)$$

$$T \propto \left(\frac{G M_{\text{BH}} \dot{M}}{r^3} \right)^{1/4} \quad (1.12)$$

with the Stefan-Boltzmann constant σ_{SB} . The accretion disk structure can be calculated by combining the equation of hydrostatic equilibrium with the angular momentum conservation and the assumption of a thin disk. Applying the α -description in order to account for the visous dissipation of energy, one obtains a disk temperature of:

$$T(r) = \left[\frac{3 G M_{\text{BH}} \dot{M}}{8\pi \sigma_{\text{SB}} r^3} \left(1 - \frac{r}{R_{\text{in}}} \right) \right]^{1/4} \quad (1.13)$$

for the individual annuli of the disk at radius r . The emergent spectrum of the accretion disk consists of the sum of Planck functions emitted from the black bodies of each individual disk annulus.

From equation (1.13), we can determine the typical emission wavelength range of the accretion disk. By assuming a $10^8 M_{\odot}$ black hole with an efficiency of $\epsilon = 0.1$, we derive a temperature of $\sim 6 \cdot 10^5$ K. This corresponds to an energy of ≈ 50 eV which is observable in the EUV (extreme ultraviolet) wavelength range.

1.2. Components and multi-wavelength view of AGN and host galaxy

The physical processes in AGN, such as accretion disk emission and reprocessed emission, as well as the emission of the host galaxy strongly shape the observed overall spectral energy distribution (SED). In this section, we are going to introduce the main physical components of AGN and host galaxies going along with an explanation of the associated emission characteristics. This is the basis for the definition of AGN selection criteria, which will be presented in the following section 1.3.

In Fig. 1.1, we show a simple model of AGN (Beckmann & Shrader, 2012) according to today's understanding and give a short overview about the involved components. The AGN is supposed to be surrounded by an accretion disk, which comprises gas of high angular momentum and emits in optical/EUV. Above the black hole and the accretion disk resides a hot 'corona'. This electron plasma is mainly responsible for the X-ray emission observed in AGN. The entire accretion disk is surrounded by a dusty torus, which is assumed to be created due to a complex interaction of in-falling gas and star formation processes. The dust in the torus reprocesses the continuum of the accretion disk and emits in infrared. In the opening cone of the torus settle gas clouds at different distances from black hole: the so-called broad line region is located at around 0.1 pc whereas the narrow line region is supposed to be located at 100 – 1000 pc. The host galaxy is not displayed in the graphic because it typically extends up to kiloparsec scale. We will not present radio emitting jets in this section, because it is outside the scope of this work.

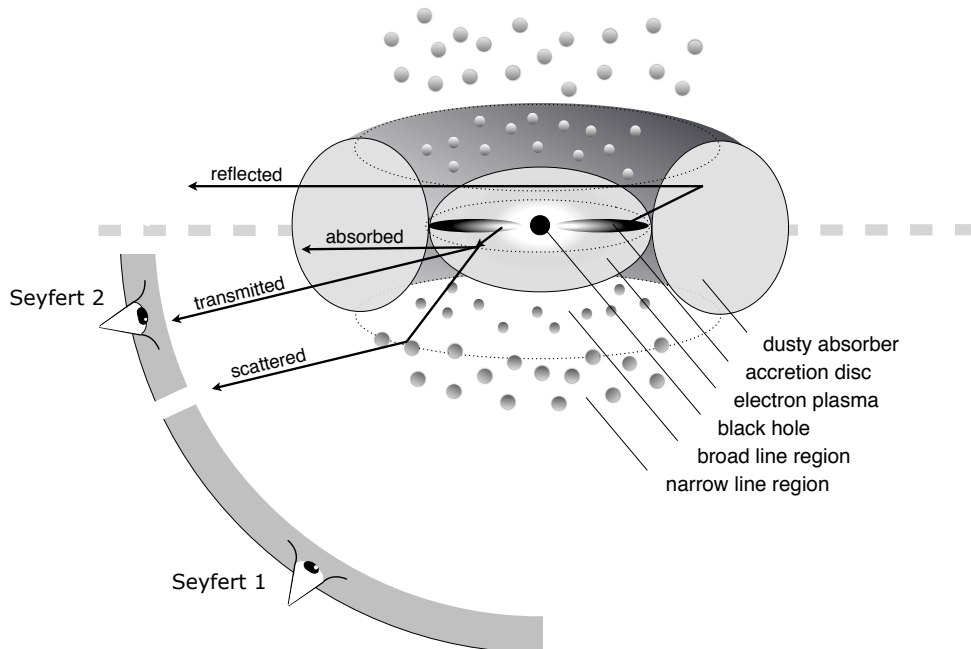


Figure 1.1.: Schematic view of AGN. The graphic is adapted from Beckmann & Shrader (2012).

1.2.1. Unification model

In the “unification by orientation” scheme of Antonucci (1993) and Urry & Padovani (1995), it is assumed that galaxies host SMBH in their center. Furthermore, the torus is co-aligned with the accretion disk and partly obscures the emission from the accretion disk. This leads to the fact that the appearance of the central AGN region depends on the inclination of the AGN towards the line of sight of the observer.

In the case of a direct line of sight into the center of the AGN (see „Seyfert 1” in Fig. 1.2), the observer sees the emission from the accretion disc and the high velocity clouds close to the black hole (Broad Line Region). These objects are typically classified as optical Seyfert-1 AGN (or broad line QSO), and their spectra show the optical/EUV continuum from the accretion disk and characteristic broad emission lines.

If the inclination of the AGN is such that the obscuring torus is in front of the AGN (see „Seyfert 2” in Fig. 1.2), the accretion disk continuum and the BLR clouds close to the black hole may not be visible anymore. This leads to a dominating contribution of the host galaxy spectrum in the optical/UV part of the SED in comparison to Seyfert-1. Furthermore, the characteristic broad permitted emission lines from the AGN center are missing and only narrow forbidden lines from far-away clouds in low density environments (Narrow Line Region, NLR) are visible in the spectrum. The group of these objects form the optical class of Seyfert-2 AGN (or Type 2 AGN).

1.2.2. AGN emission

We now introduce the main components of AGN and the resulting characteristic SED features. In the following, we will refer to the schematic SED of AGN as shown in Fig. 1.2.

Accretion disk: ‚blue bump’

We assume that the standard alpha-disk model from Shakura & Sunyaev (1973) describes the accretion disk of AGN. As explained in detail in Sec. 1.1.3, we derive that the majority of the disk emission is emitted in optical/EUV. In Fig. 1.2, this emission is highlighted in blue and will be referred to as ‚big blue bump’ (observed in SDSS spectra e.g. by Vanden Berk et al. 2001; Davis et al. 2007; Xie et al. 2016). This bump represents the sum of all temperature-dependent black bodies of the disk’s annuli. The lower and higher wavelength parts of the distribution can be approximated with power laws ($300 - 1200 \text{ \AA}$ with $\alpha = -1.76$ and $1200 - 5000 \text{ \AA}$ with $\alpha = -0.44$, where $f_\nu \propto \nu^\alpha$, Vanden Berk et al. 2001). Typically, the luminosity at 5100 \AA is used as a surrogate for the disk luminosity. This continuum region is free of emission lines, but close enough to the $H\beta$ emission, which allows to estimate e.g. the black hole mass.

Broad and narrow line region: optical/UV emission and absorption lines

The broad line region (BLR) and narrow line region (NLR) of AGN are considered to be gas clouds ionized by the optical/UV continuum of the accretion disk. In Fig. 1.2, they

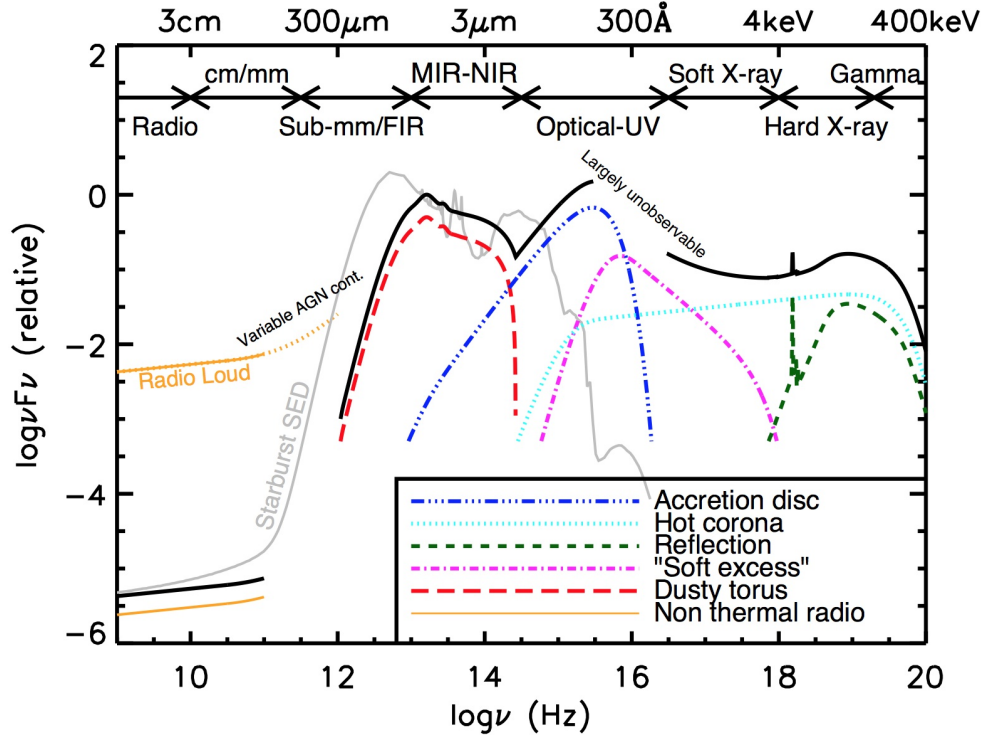


Figure 1.2.: Schematic SED of AGN. Graphic Courtesy: PhD Thesis Harrison (2016).

are displayed as circles above and below the accretion disk. These regions have different properties regarding their location in respect to the central black hole, their gravitational potential and their electron densities. However, a large fraction of atoms in the BLR and NLR have atomic transitions in the optical/UV wavelength range. This makes them interesting probes for the physical properties, such as kinematics, electron density, electron temperature and metallicity, of these regions (e.g. Whittle 1985; Netzer 1990; Whittle 1994; Peterson 1997; Osterbrock & Ferland 2006; Fabian 2012).

Permitted and Forbidden Lines

We can assume that the excitation and de-excitation of ionized atoms in BLR and NLR happens through radiation or collisions (Pradhan & Nahar, 2011). The radiative transitions can be split into 'permitted' and 'forbidden' according to their agreement with the common selection rules for electron transitions in the atomic shells. In high density environments, the relatively slow radiative 'forbidden' transition is negligible, whereas in low-density environments, the time between two collisions is longer than the decay time via forbidden transitions. As an example, we present the Grotrian diagram of [OIII] in Fig. 1.3. It indicates the permitted and forbidden transitions which are visible e.g. in optical spectra of AGN.

Broad emission line region (BLR)

Gas clouds in close proximity of the black hole (< 0.1 pc) are excited by the optical/UV continuum of the accretion disk and their kinematics is strongly affected by the gravitational potential of the black hole. Because of the electron density of $n_e \approx 10^{10} \text{ cm}^{-3}$,

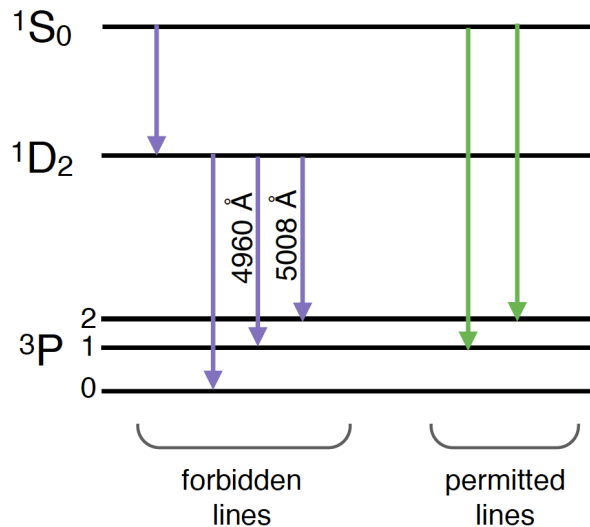


Figure 1.3.: Schematic Grotrian diagram of [OIII] with forbidden transitions and permitted transitions.

they emit dominantly permitted atomic transitions: The most prominent of these lines are the hydrogen Balmer series $H\alpha$ ($\lambda 6563$), $H\beta$ ($\lambda 4861$), $H\gamma$ ($\lambda 4340$) and hydrogen Lyman line $Ly\alpha$ ($\lambda 1216$). In addition, one also observes emission lines from the ions $Mg\ II$ ($\lambda 2798$), $[CIII]$ ($\lambda 1909$), CIV ($\lambda 1549$). If the BLR is in approximate virial equilibrium, and if the distance to the central black hole is determined by photoionization equilibrium, then we should expect that the FWHM of the emission lines scales with the black hole mass M_{BH} and the monochromatic UV-Luminosity $L_{5100\text{\AA}}$:

$$FWHM \propto M_{BH}^{1/2} \cdot L_{5100\text{\AA}}^{1/4} \quad (1.14)$$

(see, e.g. Kaspi et al. (2000), Bentz et al. (2009), Peterson et al. (2004) and references therein). Works on AGN observe the characteristically doppler-broadened emission lines in the order of $FWHM \approx 500 - \text{few } 1000 \text{ km s}^{-1}$ (e.g. reviews by Netzer 1990; Risaliti & Elvis 2004).

Narrow emission line region (NLR)

The gas clouds of the NLR are probes of the largest spatial scale ($\approx 100 - 1000 \text{ pc}$) where ionizing radiation from nuclei dominates other energy sources. We benefit from the fact that they can be spatially resolved in optical and thus give insights in the fueling and feedback mechanisms of AGN (see review papers of Fabian 2012 and Alexander & Hickox 2012). The NLR is kinematically separate from the gravitational potential of the black hole and instead dominated by the kinematics of the stellar bulge. In addition, this region has a much lower electron density ($n_e \approx 10^2 - 10^6 \text{ cm}^{-3}$) than BLR, which makes it likely for the observation of forbidden transitions, e.g. $[SII]$ ($\lambda 6716$), $[NII]$ ($\lambda 6548$), $[OIII]$ ($\lambda 5007$), $[OII]$ ($\lambda 3727$) and $[NeV]$ ($\lambda 3426$). The variability of narrow lines is less expected due to the long light-travel time across the extended NLR which averages out short-term variability (Peterson, 1997).

For a large group of AGN, one also observes different kinds absorption lines. Among

others, these might be due to Ly α gas clouds on the line of sight between the AGN hosting galaxy and the observer (e.g. in Ly α forest systems, Lynds 1971; Gunn & Peterson 1965; Woo et al. 2013) or absorbing gas flows outward from the AGN nucleus (e.g. broad absorption line quasars, Lynds 1967; Allen et al. 2011).

Corona: X-ray emission

Close to the accretion disk of AGN resides the - in analogy to the sun - corona, which consists of hot electron plasma. The origin of the hot corona is studied by various theoretical simulations, e.g. in works by Balbus & Hawley (1998) and Schnittman et al. (2013), who demonstrated that the magnetohydrodynamic turbulence in the disk could lead to dissipation causing the corona, which is less dense than the disk.

In the corona, energetic photons from the accretion disk are reprocessed by inverse Compton scattering on free electrons (e.g. Fabian et al. 1989; Zdziarski et al. 1994). The up-scattered radiation ranges in X-ray and can be approximated as a power law in the SED with the photon index $\Gamma = 1.5 - 2.5$, where $F(E) \propto E^{-\Gamma}$ (Nandra & Pounds, 1994; Reeves & Turner, 2000; Piconcelli et al., 2005). The ‘cut-off’ of the power law in the SED is related to the maximal thermal energy of the electrons and gives insights into the coronal temperature (e.g. Fabian et al. 2015). We indicate this emission with a pale blue line in Fig. 1.2.

X-rays also reveal further high-energetic processes happening in the central region of the AGN. If the primary X-ray emission of the AGN is reflected on very dense matter in the nuclear region ($N_H > 10^{24} \text{ cm}^{-2}$), it causes a Compton hump at $\approx 20 - 30 \text{ keV}$ and a fluorescence line Fe-K at 6.4 keV in the X-ray spectrum (Reynolds et al., 1999; Fabian & Ross, 2010). Furthermore, one also observes warm ionized absorbers causing absorption in the soft X-ray band. The soft excess at $E \approx 0.2 - 1 \text{ keV}$ might originate from either warm emitting gas clouds or is part of the big blue bump extension (Done et al., 2007). Both the reflection spectrum (green line) and the soft excess (pink line) are displayed in Fig. 1.2. The obscuration of X-rays by neutral gas on the line of sight decreases for more energetic X-rays and therefore, the hard X-ray band ($2 - 10 \text{ keV}$) is typically less effected by obscuration and represent a good measure for unobscured X-ray emission.

In agreement with the thermal comptonization nature of X-ray, studies show a connection of the X-ray variability with the optical/UV continuum (Clavel et al., 1992; Uttley et al., 2000; Shemmer et al., 2001); excluding short time variations in the order of hours (Nandra et al., 1998).

Torus: ‘red bump’

The torus of AGN consists of gas and dust, and is supposed to be located well within the region dominated by the gravitational potential of the black hole. Parts of optical/UV/X-ray emission from the central source in radio-quiet AGN are absorbed by dust particles of the torus (as well as the host galaxy), and reprocessed as infrared radiation causing the characteristic ‘red bump’ (e.g. Rees et al. 1969, Lawrence et al. 1991). This SED feature

is indicated with a red line in Fig. 1.2.

The historical assumption, that the torus is a homogenous dusty and torus-like structure (as used in the unification model by Antonucci 1993 and Urry & Padovani 1995) has been reformulated since, e.g. based on extensive infrared and infrared interferometry observations. Tristram et al. (2014) find that the infrared emitting material is distributed in form of a disk perpendicular to ionization cone and elongated along the poles. The elongated component causes the majority of obscuration and collimates the nuclear radiation. The inner radius of the torus is probably linked to the luminosity-dependent dust sublimation radius r_{subl} and reaching out to 10 to 100 r_{subl} (Granato & Danese, 1994; Radomski et al., 2003; Kishimoto et al., 2011). X-ray and infrared reverberation mapping of passing torus clouds lead to the conclusion that the torus structure is clumpy (Krolik & Begelman, 1986; Markowitz et al., 2014). Due to the clumpiness, the surfaces of the clouds can have different temperatures depending on the orientation towards the central source (Elitzur & Shlosman, 2006; Nenkova et al., 2008; Feltre et al., 2012). In addition, the clumpy torus structure is considered to be dynamic and changing, suggesting that the material is flowing toward or away from the central sources. Models about the origin of the torus study scenarios of inflows from galactic scale (Hopkins et al., 2012), the impact of nuclear star formation (Schartmann et al., 2009) or also outwards flowing material from the nuclei Elitzur & Shlosman (2006).

The integrated infrared emission in AGN spans over a wavelength range of 2 – 200 μm . As displayed by a red line in Fig. 1.2, the shape of the SED is formed by a minimum at 1 – 2 μm , which is caused by the typical sublimation temperature of dust (Sanders et al., 1989), and the 'red bump' at $\approx 10 - 30 \mu\text{m}$ corresponding to the temperature-dependent thermal emission of the dust. Typical solid state spectral features are coming from silicates (10 – 20 μm), the stretch of the C-H molecule (3.4 μm) and ice absorption (see review of Mason 2015). First radiative transfer modeling of the red bump were carried out by Pier & Krolik (1992, 1993) by assuming a torus with cylindrical geometry and homogenous smooth dust; today's modeling use physically motivated geometry and dust distribution (e.g. Schartmann et al. 2005).

1.2.3. Host galaxy emission

The emission of the host galaxy around AGN can have a strong impact on the observed SED shapes. As discussed by Merloni & Heinz (2013), AGN of high luminosity without central obscuration typically outshine the host galaxy features in the SED due to the strong accretion disk continuum; but in case of low luminosity AGN or obscured AGN, the 'contrast' between AGN and host galaxy emission strongly decreases.

The constituents of galaxies such as stars, gas and dust strongly define characteristic SEDs. As shown in Fig. 1.4, galaxies hosting young stellar generations are very bright and emit the maximum of the radiation in optical/UV. Their spectra are very rich in emission lines of excited atoms. Older stellar populations are less hot and emit mostly in near-infrared; their optical spectra are dominated by absorption lines. The modeling of galaxy templates

(see libraries by e.g. Coleman et al. 1980; Fioc & Rocca-Volmerange 1997; Devriendt et al. 1999; Polletta et al. 2007) is based on a complex interplay of stellar populations characteristics, the history of star formation activity, chemical evolution and dust attenuation (e.g. see works by Silva et al. 1998; Bruzual & Charlot 2003).

Works on the host galaxies of AGN (among others Kauffmann et al. 2003 and Bongiorno et al. 2012) study characteristic line features or perform complicated SED decompositions to derive stellar population characteristics, stellar masses and star formation rate. They find that AGN host galaxies span a large range of stellar masses and star formation rates, and are found to be mainly massive, red galaxies.

The dust which is associated with star formation or starburst activity can contribute or dominate parts of the 'red bump' of the AGN's SED, see Sec. . Furthermore, organic molecules (polycyclic aromatic hydrocarbons) re-emit the optical-UV continuum and are characteristic features in the wavelength range of $5 - 12\mu\text{m}$. They have been used to evaluate the star formation in AGN (e.g. Schweitzer et al. 2006; Shi et al. 2007; Woo et al. 2012).

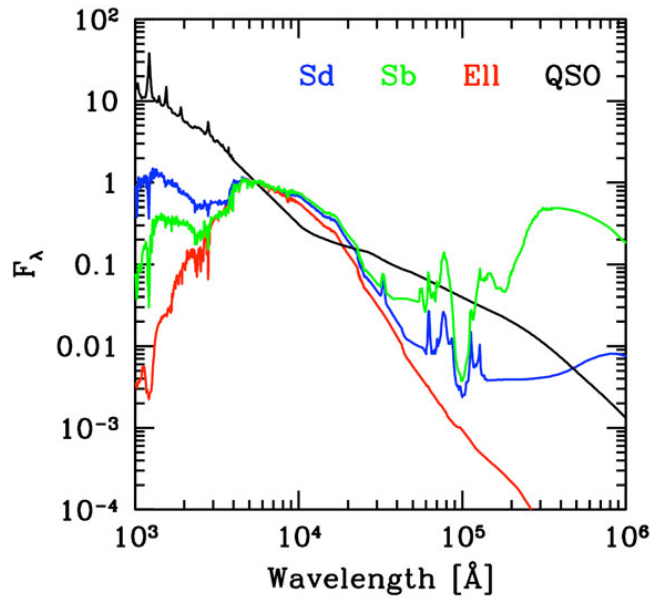


Figure 1.4.: SED of 'young' spiral galaxies (Sd, blue; Sb, green), 'old' ellipticals (Ell, red) and QSO (black). The SED templates are taken from Polletta et al. (2007) and do not include emission lines.

1.3. AGN selection

As described in the last sections, the accretion processes in SMBHs are highly complex and initiate emissions within a large wavelength range from the surrounding components. Furthermore, the presence of dust and gas, and the influence of host galaxy emission shape the SED in a different way for each individual AGN. However, the observed SED of AGN-hosting galaxies include features, which allow to define dedicated selection criteria for AGN populations. These selection criteria can be split into two groups: photometric/color selection criteria and spectroscopic criteria. One has to note that these selections can only pick up a limited part of the entire AGN population and it is strongly required to perform complementary selection methods.

Routinely, AGN are identified by a) X-ray emission caused by the inverse Compton scattering of the disk emission (Brandt & Hasinger, 2005; Brandt & Alexander, 2015), b) mid-infrared emission, which has been re-processed by dust (Lacy et al., 2007; Stern et al., 2005, 2012) and c) optical continuum emission, which is directly released by the accretion disk (Bovy et al., 2011). Further selections concentrate on radio emission which is caused by jets (Donley et al., 2005; Del Moro et al., 2013). Each selection has its benefits and disadvantages, for example, X-rays are known to be less sensitive to absorption by gas and contribution from star formation. However, they are biased against strongly obscured (Compton-thick) AGN, which are likely to be selected in infrared. This is comparable to the optical selection of QSO, which fails in case of host galaxy dominated AGN. The combination of multiple selection methods enables to obtain more complete AGN populations for dedicated areas, as shown in works of Martínez-Sansigre et al. (2005).

Another group of AGN selection criteria benefits from the optical narrow emission lines (Baldwin et al., 1981; Ho et al., 1997; Kauffmann et al., 2003; Kewley et al., 2006; Lamareille, 2010), which are sensitive to the different ionizing radiation from the AGN and stars. In addition, broad emission lines ($\text{FWHM} > 1000 \text{ km s}^{-1}$) are unique spectral features which identify optical unobscured AGN, where the observer has a direct view on the fast moving clouds close to the black hole.

Variability can be an additional parameter to select AGN. Short time-scale variations in the range of hours to Myr are less likely to happen in star formation and can be associated to nuclear processes (Ulrich et al., 1997; Hickox et al., 2014).

1.4. Evolution of AGN and host galaxies

It is of interest, if the luminosity of the disk radiation, emitted during active accretion phases, has an effect on the properties of the surrounding galaxy. Observations find, that despite the large scale difference, there might be a linking mechanism between the evolution of the central SMBH and the ambient host galaxy. In order to study this so called co-evolution, we have to assess the evolutionary properties of AGN and their host galaxies. Thanks to large available galaxy and AGN surveys with precise redshift estimates, one can now study black hole and galaxy properties during the history of the Universe. The research on the processes causing the co-evolution is still young and turns out to be highly complex. Current studies suggest that feedback processes, which are driven by the energy release of the AGN, have a major impact on the interstellar matter and gas in the host galaxy.

In this section, we firstly introduce the AGN luminosity function to evaluate the evolution of AGN density and luminosity. We then explain indications for the co-evolution of AGN and galaxies, and present the concept of feedback.

1.4.1. AGN evolution

As a characteristic tracer of AGN evolution, we introduce the luminosity function $\phi(L)$. This corresponds to the space density of sources of different intrinsic luminosities. The number of sources per unit volume of luminosity between L and $L + dL$ is calculated as $dN = \phi(L)dL$.

The shape of this function can be approximated by a broken double power law. At different redshifts, this shape gives interesting insights into the evolution of AGN activity: the break luminosity represents the 'typical' black hole luminosity and the integrated luminosity can trace the epoch of rapid build-up of SMBH mass density (Merloni & Heinz, 2013).

In Fig. 1.5, we display a bolometric luminosity function based on optical and X-ray data from Aversa et al. (2015); and in Fig. 1.6, we show the characteristics properties of the double power law parameters as a function of redshift (Hopkins et al., 2007). Fig. 1.6 indicates, that there is a strong AGN density increase with redshift up until $z \approx 2$, followed by a decrease for higher redshifts. Furthermore, the luminous sources are more dominant at higher redshifts, whereas in the current Universe, low luminosity AGN become more dominant. The latter effect is also observed in the stellar masses of AGN host galaxies and is referred to as 'cosmic down-sizing' (firstly mentioned by Cowie et al. 1996). The down-sizing is opposed to the hierarchical cold dark matter universe (White & Rees, 1978), where most massive objects were formed last. Instead, there must be a quasar quenching process which may be due to galaxy-internal feedback or galaxy merging processes.

Merloni & Heinz (2008) studied the black hole growth and solve a continuity equation for the black hole mass function by using the luminosity function as tracer of the AGN growth rate distribution and applying locally defined boundary conditions. Their results support the concept of anti-hierarchical evolution, which means that most massive black

holes grew earlier and faster than less massive ones. For redshifts larger than $z \approx 2$, this trend may be reversed.

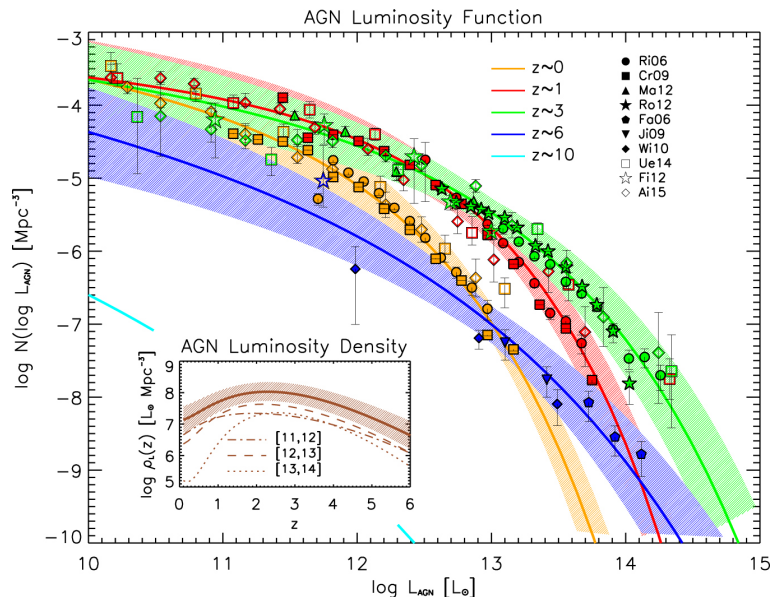


Figure 1.5.: Bolometric AGN luminosity function for different redshifts. The solid lines illustrate the analytic rendition of the luminosity functions and the hatched areas represent the associated uncertainty. The inset shows the AGN luminosity density as a function of redshift, for the overall luminosity range probed by the data (solid line with hatched area), and for AGN bolometric luminosity. The graphic is taken from Aversa et al. (2015).

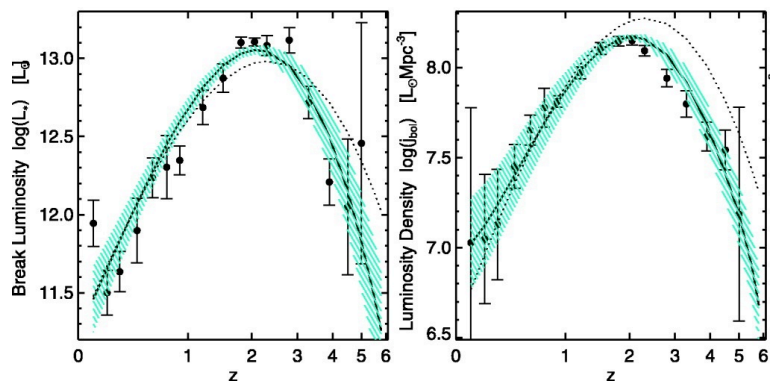


Figure 1.6.: Break luminosity and luminosity density of best double power-law fit of the quasar bolometric luminosity function as a function of redshift. Symbols show the best-fit values to data at each redshift, dotted lines the best-fit 'Pure Luminosity Evolution' model (allowing for the brightness and spectral evolution in the galaxy population), and solid lines the best-fit full model (with cyan shaded range showing the 1σ uncertainty). The graphic is taken from Hopkins et al. (2007).

1.4.2. AGN-galaxy-coevolution and feedback processes

Studying the big picture of black hole and galaxy growth reveals manifold indications for a correlated mechanism. As one example, we refer to the total black hole mass accretion rate, whose maximum at $z \approx 2$ coincides with the maximum of the star formation history, as shown by Madau & Dickinson (2014) in Fig. 1.7. The comparable growth correlation also results in observed scaling relations of black holes and galaxy properties, e.g. black hole mass and galaxy bulge velocity (see works by Gebhardt et al. (2000), Ferrarese & Merritt (2000) and Gültekin et al. (2009)). We present the so-called the $M_{BH} - \sigma_*$ -correlation in Fig. 1.8.

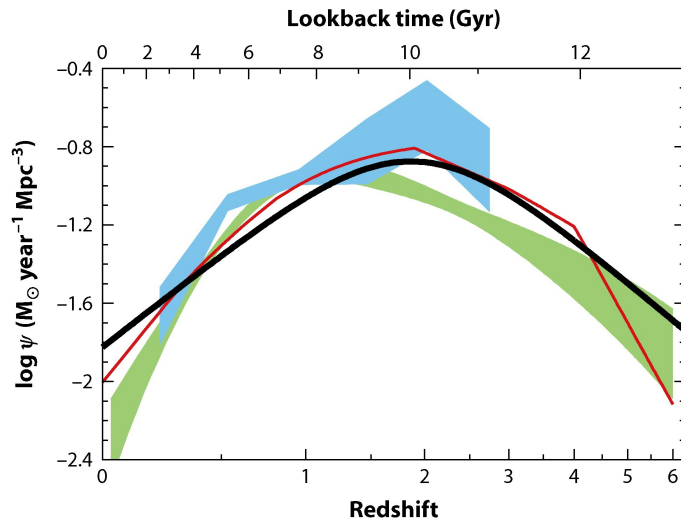


Figure 1.7.: Comparison of the best-fit star-formation history (thick solid curve) with the massive black hole accretion history from X-ray [red curve (Shankar et al., 2009); light green shading (Aird et al., 2010)] and infrared [light blue shading (Delvecchio et al., 2014)] data. The shading indicates the $\pm 1\sigma$ uncertainty range on the total bolometric luminosity density. The radiative efficiency has been set to $\epsilon = 0.1$. The comoving rates of black hole accretion have been scaled up by a factor of 3300 to facilitate visual comparison to the star-formation history. The graphic is taken from Madau & Dickinson (2014).

A mechanism explaining the co-evolution of AGN and galaxies is assumed to be feedback. The general idea of feedback includes some form of energy release from the accreting black hole which either terminates the star formation in large regions of the bulge or blows away the gas supply in the nuclear scale (Di Matteo et al., 2005; Hopkins et al., 2009). The energy release for the AGN is supposed to happen in different outflow modes, often referred to as the ‘radiative mode’ and the ‘kinetic mode’ (see reviews by Fabian 2012; Alexander & Hickox 2012; Kormendy & Ho 2013). Churazov et al. (2005) proposes that the radiative mode shapes the overall galaxy and black hole at early times, and the kinetic mode has since maintained that situation where needed.

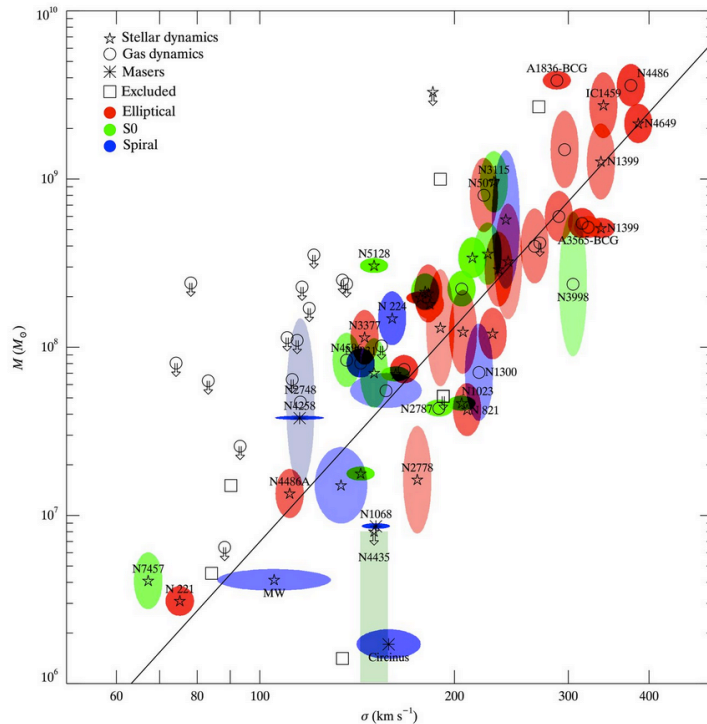


Figure 1.8.: $M_{\text{BH}} - \sigma_*$ relation for galaxies with dynamical black hole mass measurements. The symbols indicate the method of BH mass measurement: stellar dynamical (pentagrams), gas dynamical (circles), masers (asterisks). Arrows indicate 3σ confidence upper limits to black hole mass. The color of the error ellipse indicates the Hubble type of the host galaxy: elliptical (red), S0 (green) and spiral (blue). The saturation of the colors in the error ellipses or boxes is inversely proportional to the area of the ellipse or box. Squares are galaxies not included in the fit. This is shown as solid line for the best fit relation to the full sample: $M_{\text{BH}} = 10^{8.12} M_{\odot} (\sigma_*/200 \text{ km s}^{-1})^{4.24}$ (adopted from Gültekin et al. 2009).

Radiative Mode

The radiative mode is caused by the emitted AGN continuum from the accretion disk. The radiation pressure on electrons itself is not sufficient to explain the observed scaling relationships between AGN and host galaxy. However, stronger interactions of the radiative mode might be due to line-driven winds generated close to the quasar and pushing the gas out while flowing through the galaxy. Furthermore, the radiation pressure acts on dust grains, which is typically charged in the energetic environment of the AGN and embedded in the interstellar partly-ionized gas (Laor & Draine, 1993; Scoville & Norman, 1995).

The radiative mode is observed as wide-angle outflow and mostly active in younger AGN, which are assumed to host cold molecular gas and have more obscured nuclei. Numerous multi-wavelength observations prove, that this mode impacts a large variety of interstellar gas/matter of the galaxy both in the proximity of the AGN (e.g. BLR) but also on larger extents (e.g. NLR). These outflows carry ionized, neutral and molecular phases,

which are observed in a large range of wavelengths (e.g. Rupke et al. 2005, Feruglio et al. 2010, Rupke & Veilleux 2013). This fact makes it very challenging to study general properties, such as mass distribution, velocity structure and energetics of these radiative outflows.

Generally, the AGN radiation originating from the accretion disk has a bipolar pattern (e.g. Crenshaw et al. 2010, Fischer et al. 2011), which is supposed to be shaped by a toroidal obscuring structure. Inside the cones, gas is going to be swept up along the outflow axis. According to the unified AGN model (see Sec. 1.2.1), the observation of conical outflows under a different viewing angle has an impact on the measured emission line properties, such as velocity shift and FWHM. Studying the radiative outflow features of a large sample of optically obscured and unobscured AGN will thus provide a test of this AGN model and give an interesting insight into the nature of the outflow.

Radiative outflows manifest themselves observationally as blueshifted absorption and emission lines. IFU observations of single objects (for local Seyfert 1) show evidences of outflowing gas inside the torus (Young et al., 2007) as well as on scales of 10 – 100 pc (Storchi-Bergmann et al., 2010; Schnorr Müller et al., 2011). X-ray spectroscopic observations by Pounds et al. (2003); Reeves et al. (2003); Gofford et al. (2011), probing the highly ionized phase closest to the black hole, determine outflow velocities of 0.1 – 0.3 c .

While observing broad CIV emission (especially in distant quasars), one finds that the blueshift is anti-correlated to the X-ray luminosity (Richards et al., 2011). Similar results are obtained for broad absorption lines AGN (BAL), where the nuclear continuum is viewed through the outflow (Gallagher et al., 2006; Gibson et al., 2009). This leads to the explanation that, for AGN with absorbers close to the black-hole, the central gas is less ionized and more easily driven by the UV continuum from the quasar. This is an agreement with the model of radiative outflow.

Kinetic Mode

A second outflow mode is the kinetic mode, which involves narrow-angle relativistic jets driven by the AGN’s accretion flow. It is more likely to be observed than radiative outflows, because the surrounding gas is highly ionized and mostly optically thin. The kinetic mode typically operates when the galaxy has a hot halo or is at the centre of a group of galaxies and the accreting black hole has powerful jets. At the present epoch it tends to occur at a lower Eddington fraction and in more massive galaxies (see review paper of Fabian 2012)

Kinetic outflows are known to reach kiloparsec scale and thus influence gas on the scales of the host galaxy and parent dark matter haloes. The origin of jets are still matter of debate and models of e.g. low accretion rates, fueling from hot atmospheres, BH spin have been discussed in the literature. Decelerated jets are supposed to create inflating buoyant bubbles of relativistic plasma in the intracluster or intragroup medium on either side of the nucleus (e.g. Churazov et al. 2000; Bîrzan et al. 2008; Cavagnolo et al. 2010). In this context, SMBH are feeding back energy into the surroundings at a rate balancing the loss of energy through cooling (Rafferty et al., 2008). Observations in X-ray or radio (Boehringer et al. 1993 in the Perseus Cluster, Forman et al. 2007 in M87, Croston et al.

2009 in Centaurus A) show, that the mechanical power in the relativistic kinetic outflows vastly exceeds (~ 1000 times) the radiative output of the AGN.

1.5. Motivation of this Thesis

Following the explanations of Sec. 1.4, feedback mechanisms are a key process to explain the co-evolution of AGN and the host galaxy. As part of this thesis, we study in detail the properties and excitation origin of radiative [OIII] outflows reaching the NLR in AGN, and evaluate their contribution to the feedback processes in AGN. Furthermore, the properties of these outflows in optically obscured and unobscured AGN allow to test the unification model.

However, in order to e.g. correctly estimate the contribution to the feedback process and the characteristics of the central torus, we have to be aware of the limitations of the applied AGN selection criteria, as presented in Sec. 1.3. In Chapter 2 of this thesis, we are going to show the large benefits of X-ray selection and describe the detailed analysis of the selected AGN population. In a next step, we will compare the X-ray selection to other common AGN selection criteria, such as optical and infrared in Chapter 3.

Once, we have understood the impact of the selection, we search for probes of the feedback processes as presented in 1.4 between AGN and their host galaxies conducted by outflows. We study the origin and impact of feedback processes by focussing on the narrow line region kinematic properties of AGN. This region allows us to study ionized phases of large outflows, which are probably strongly involved in the feedback process. The narrow line region is observable for AGN of different nuclear obscuration and current optical spectrographs can assess the characteristic emission line for a very large sample of AGN. To this end, we study in Chapter 4 the ionized gas phase of radiative outflows traced by [OIII]. Our analysis goes along with a careful estimate of the star formation contribution to the observed [OIII] outflows. Furthermore, we study the correlation of this feedback process with AGN properties. This includes a comparison of [OIII] profile properties for optically obscured and optically unobscured AGN in order to test the unification model and study the geometry of the outflows. The final goal of this work is to use a complete dataset of X-ray selected AGN to derive the kinetic energy efficiencies and average momentum of ionized outflows observed in AGN and asses their possible impact on their host galaxies.

We approach the inquiries about selection criteria and feedback processes by a) a dataset, which probes the largest possible AGN population, and b) with spectroscopic data, to reveal the detailed physical properties of the ongoing processes. Therefore, we choose the XMM-XXL north region which provides a suitable dataset for this work, because it is covered by photometric multi-wavelength data of *XMM-Newton*, *SDSS* and *WISE*, and is part of a specific *BOSS* spectrograph programme of optical spectroscopic follow-up for X-ray selected AGN. We perform a complete data reduction of the X-ray and spectroscopic data, including redshift determination, emission line fitting and class definition, and perform the matches to optical and infrared catalogues.

Due to the area of $\approx 18 \text{ deg}^2$, this survey is one of the largest spectroscopic samples of X-ray selected AGN sources allowing to investigate AGN properties including selection methods, host galaxy contamination, demographics (optically obscured vs. unobscured AGN) and emission line properties. The mechanism of feedback between AGN and galaxies has al-

ready been studied in individual sources or small X-ray selected surveys (e.g. Harrison 2016 and Ueda et al. (2015)). Compared to these works, our spectroscopic sample is eight times larger, has been homogeneously selected in X-ray and includes a large subsample with very high redshift completeness.

1.6. Outline of the Thesis

The thesis is organized as follows: Chapter 2 gives a short overview of existing spectroscopic surveys of X-ray selected AGN and presents the XMM-XXL North field, which is in the main focus of our work. There, we introduce the multi-wavelength data sets from *XMM-Newton*, *SDSS*, *BOSS* and *WISE* along with the cross-matching process. In a dedicated section, we concentrate on the spectroscopic target selection for the observation of X-ray selected AGN with the *BOSS* spectrograph. The follow-up spectra are then subject to a visual redshift determination and we perform a dedicated classification based on optical emission line properties. Finally, we describe and analyze the characteristic class properties of X-ray selected AGN.

In Chapter 3, we focus on the impact of AGN selection criteria. We firstly introduce optical emission line selections in order to classify broad line and narrow line emitters. In a next step, we present the optical AGN selection algorithm which has been trained on the QSO dataset of *SDSS*, and we show an infrared AGN selection with *WISE* band photometry. Including our X-ray selected AGN sample, we compare the AGN success for each selection and derive the X-ray detection rate for optical and infrared selections. Furthermore, we study the impact of each selection on the attributes of the AGN populations by analyzing e.g. AGN and host galaxy features in the optical spectra.

Chapter 4 is dedicated to the kinematic properties of the narrow line emission region in the sample of X-ray selected AGN with spectroscopic follow-up. This region is sensitive to feedback processes and traces large-scale ionized outflows in the profile of the [OIII] emission. We perform extensive studies about the excitation process of these outflows by comparing the [OIII] line properties to a sample of star forming galaxies and by correlating the line properties with characteristic accretion-related parameters of AGN. Furthermore, we make studies about the incidence and [OIII] emission line shapes of outflows for both obscured and unobscured AGN. Finally, we derive average ionized outflows properties, such as kinetic power and outflow rate, for a redshift-complete AGN sample.

In Chapter 5, we provide a forecast for the AGN population soon to be assessed by *eROSITA* and *SPIDERS*. We summarize the results of our work and present future prospects.

In this work, we use the J2000 standard epoch and adopt a cosmology with $H_0 = 70 \text{ km s}^{-1} \text{ Mpc}^{-1}$, $\Omega_M = 0.27$, and $\Omega_\Lambda = 0.73$. The optical magnitudes from *SDSS* are given in the AB system and infrared magnitudes from *WISE* are given in the Vega system.

Part of the content of this theses is published in a refereed journal (Menzel et al., 2016).

2. Datasets and Analysis Methods

2.1. Introduction

X-rays represent an AGN selection method which is relatively unaffected by obscuration or host contribution. When combined with optical spectroscopy, this enables the study of AGN physical properties and evolution of a relatively unbiased sample. Here we describe the construction of such a sample based on SDSS spectroscopy of an X-ray selected sample of AGN detected by *XMM-Newton*. The resulting sample can be used for a wide range of investigations, such as AGN accretion properties and host galaxy properties as well as outflow and inflow processes.

In this Chapter, we present such a sample in the XMM-XXL north field, which is an extension of the former XMM-LSS survey (Pierre et al., 2004; Chiappetti et al., 2013; Clerc et al., 2014) and was conceived to study the large scale structure in the Universe by mapping a well-defined statistical sample of galaxy clusters. The *XMM-Newton* X-ray survey in this area covers $\sim 25 \text{ deg}^2$ to a depth of $F_{0.5-2\text{keV}} \sim 1 \cdot 10^{-15} \text{ erg cm}^{-2} \text{ s}^{-1}$, and provides access to large subsamples of AGN when selected by luminosity, morphology or obscuration. Furthermore, many multi-wavelength datasets in optical (e.g. *CFHTLS*, *SDSS*), infrared (e.g. *UKIDSS*, *WISE*, *VIDEO*), UV (e.g. *GALEX*) and radio (e.g. *VLA*) bands are available in this field.

This sample is one of the largest spectroscopic surveys of X-ray selected AGN in a homogenous and contiguous area followed-up by the *BOSS* spectrograph of the Baryonic Oscillation Spectroscopic Survey using the 2.5 meter Sloan Telescope. This dataset allows for a more detailed analysis of properties of X-ray selected AGN, enables a comparison of selection methods for AGN based on different wavelengths, and provides a forecast for the AGN population in the *eROSITA* survey and its follow-up programme SPIDERS (Merloni et al. 2012; Predehl et al. 2014, Dwelly et al. 2016, in prep., Clerc et al. 2016, subm.).

Several recent works (Hickox et al., 2009; Yan et al., 2011; Donley et al., 2012; Mendez et al., 2013) have combined and compared multiple AGN selection methods, such as X-ray, UV, optical, and infrared. These studies have been performed in areas benefiting from synergies of deep X-ray coverage, multi-wavelength observations and spectroscopic follow-up, e.g. the COSMOS, AEGIS and CDFS field (Alexander et al. 2003; Davis et al. 2007; Luo et al. 2010; Brusa et al. 2010; Civano et al. 2012). However, most area surveys are limited to few deg^2 or less. Larger area surveys, such as Boötes (Hickox et al. 2009, 9.3 deg^2), achieve better statistics for rare objects, e.g. luminous AGN, and improve clustering studies, but demonstrate that they are difficult to carry out, mainly due to the small field of view of X-ray imaging telescopes.

In this Chapter, we introduce the imaging datasets of *XMM-Newton*, *SDSS* and *WISE* in the XMM-XXL field, as well as the results of the crossmatching process. This is followed by a detailed description of the target selection of the *BOSS* spectroscopic survey. In a next step, we present the processing of optical spectra in the *BOSS* pipeline and discuss the determination of spectroscopic redshifts by visual inspection. We perform a classification of the dataset based on spectral properties, such as line widths of AGN-induced and star formation-induced emission lines, and discuss their redshift, luminosity and spectral shape properties.

2.2. Introduction of imaging data sets

2.2.1. XMM-XXL survey and X-ray source catalogue

The *XMM-Newton* XXL survey (XMM-XXL, PI Pierre) is a medium-depth (10 ks per pointing) X-ray survey that covers a total area of 50 deg^2 split into two fields equal in size. In this work, we focus on the equatorial sub-region of the XMM-XXL (XMM-XXL north), which overlaps with the *SDSS*-DR8 imaging survey (Aihara et al., 2011). The XMM-XXL north observations were distributed around the area of the original 11 deg^2 XMM-LSS survey (Clerc et al., 2014) and therefore build upon and extend that sample.

The X-ray data used in this work are primarily from the XMM-XXL and XMM-LSS surveys. We also include however, any additional *XMM-Newton* pointings that are contiguous to the area covered by those programmes, such as the *XMM-Newton* observations of the *Subaru/XMM-Newton* Deep Survey (SXDS; Ueda 2008). The data reduction, source detection and sensitivity map construction for the X-ray catalogue follow the methods described by Georgakakis & Nandra (2011). Specific details on the reduction of the *XMM-Newton* observations in the XMM-XXL north field and X-ray spectroscopic properties are presented in Liu et al. (2016). In brief, the X-ray data reduction is carried out using the XMM Science Analysis System (SAS) version 12. Our survey comprises the XMM-XXL data observed prior to 2012 January 23. At that date the XMM-XXL programme was partially complete, which results in the inhomogeneous X-ray coverage shown in Fig. 2.5. In the following, we always refer to this coverage as ‘XMM-XXL north’ area.

The catalogue contains in total 8445 sources including 8016 sources with detections in the soft band ($F_{0.5-2\text{keV}}$), 4802 sources with detections in the hard band ($F_{2-10\text{keV}}$) and 8309 sources with detections in the full band ($F_{0.5-10\text{keV}}$). Within these three bands, ~ 47 per cent, ~ 50 per cent and ~ 45 per cent of the sources have an optical counterpart in the r-band ($r < 22.5 \text{ mag}$), respectively. For the total area of our survey with spectroscopic follow-up (18 deg^2), the observations reach a flux limit of $F_{0.5-10\text{keV}} > 7.50 \times 10^{-15} \text{ erg cm}^{-2} \text{ s}^{-1}$ for 10 per cent of the area and a flux limit of $F_{0.5-10\text{keV}} > 1.27 \times 10^{-14} \text{ erg cm}^{-2} \text{ s}^{-1}$ for 50 per cent of the area.

2.2.2. Optical source catalogue of SDSS

The XMM-XXL north area is covered by the optical imaging of the third programme of the *Sloan* Digital Sky Survey (*SDSS-III*, Eisenstein et al. 2011). This is an optical survey extending over $\sim 14,555 \text{ deg}^2$ at the ground based 2.5-meter telescope at the Apache Point Observatory, New Mexico (Gunn et al., 2006). The five broad bands (average wavelength indicated) u [3551 Å], g [4686 Å], r [6165 Å], i [7481 Å], z [8931 Å] (Fukugita et al., 1996) have the following (AB) magnitude limits: 22.0 mag, 22.2 mag, 22.2 mag, 21.3 mag and 20.5 mag (corresponding to 95 per cent completeness for point sources). We retrieved the *SDSS* imaging data from the DR8 (Aihara et al., 2011) and obtained 538 508 sources in the XMM-XXL north. In this work, we use the flux measurements from *SDSS*: `psfmag` (for point-like sources, `type = 6`) and `modelmag` (for extended objects, `type = 3`). Both magnitudes are not corrected for extinction. Furthermore, we do not apply any cuts to correct for e.g. blending and moving objects.

2.2.3. Infrared source catalogue of *WISE*

The Wide-field Infrared Survey Explorer (*WISE*) observed the entire sky using a four channel imager (mean wavelength indicated): *W1* [3.4 μm], *W2* [4.6 μm], *W3* [12 μm] and *W4* [22 μm] (Wright et al., 2010). For the infrared AGN selection criteria in Section 3.6, we used the *mpro* magnitudes for both point-like and extended objects from the allWISE data release (Wright et al., 2010; Mainzer et al., 2011). We excluded diffraction spikes, persistent sources, halos, optical ghosts and blended sources (*cc_flag* = 0 in the *W1* and *W2* band, *NB* \leq 2) following Stern et al. (2012). In the XMM-XXL north, we obtain in total 334 697 infrared sources which yielded 321 352 sources after cleaning for photometric failures.

2.2.4. Cross-matching of data sets

The X-ray sources from the XMM-XXL north survey have been separately cross-matched to the *SDSS* catalogue and to the allWISE catalogue. This allows an independent comparison of AGN selection criteria with the full multi-wavelength data set. The cross-matching was performed using the Likelihood-Ratio method as presented by Sutherland & Saunders (1992) and implemented by Georgakakis & Nandra (2011). The method takes into account the expected magnitude distribution of the true optical counterparts, the probability distribution function of the positional uncertainties in both catalogues and the background density of optical galaxies at a certain magnitude. The optical counterparts are searched within a 4 arcsec radius around the X-ray position. We apply a lower Likelihood Ratio limit for the matched catalogues, which allows for an estimation of the spurious identification rate. Any cuts for e.g. photometric errors or flux have been applied after the matching process. Fig. 2.1 shows the soft band X-ray flux histogram for the point-like X-ray sources, their associated counterparts and the followed-up spectra (as described in Section 2.3.2).

5294 X-ray sources have an optical counterpart in the *SDSS* DR8 (Aihara et al., 2011) inside a maximal search radius of 4 arcsec. Out of those, 4075 sources with a Likelihood Ratio $\text{LR}_{\text{XMM},\text{SDSS}} > 1.5$ are selected as targets for the spectroscopic follow-up with *BOSS*. The spurious identification rate for these objects is estimated to be about 7 per cent. Fig. 2.2 shows the r_{model} magnitude distribution of both optically extended and point-like *XMM-SDSS* cross-matched sources. The distribution has its maximum at $r_{\text{model}} \sim 22$ mag. The plot also shows the 3042 sources which have been targeted by *BOSS* in our observation programme.

5414 X-ray sources have an infrared counterpart in the *WISE* imaging database within an maximal matching distance of 5 arcsec. We apply a Likelihood Ratio threshold of $\text{LR}_{\text{XMM},\text{WISE}} > 0.5$, corresponding to a spurious identification rate 5 per cent, and retrieve 4844 sources, including 4811 with good *WISE* photometry. In Fig. 2.3, we show the *W2*-band distribution and the histogram of all *XMM-WISE* cross-matched objects. The distribution has its maximum at $W2 \sim 16$ mag. In addition, we indicate the 2474 sources, which have spectroscopic *BOSS* follow-up, too.

The angular distance between the optical and infrared counterpart of X-ray sources gives

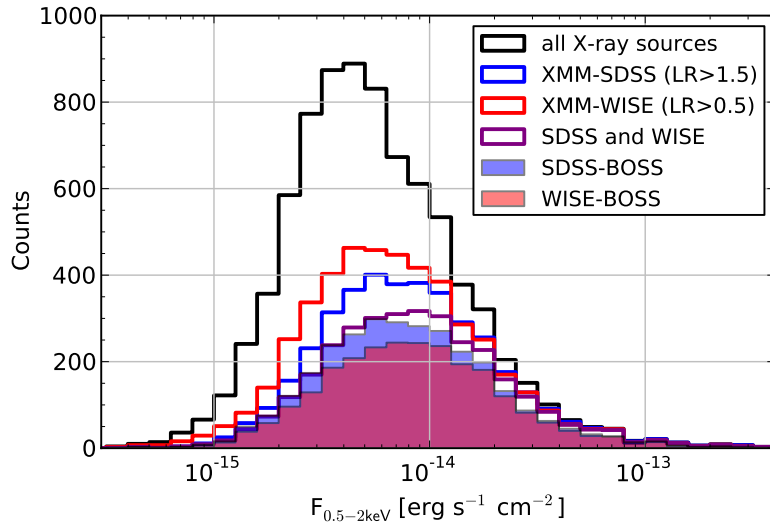


Figure 2.1.: Histogram of the soft X-ray flux $F_{0.5-2\text{keV}}$ for point-like X-ray sources in the northern XMM-XXL area: The plot shows all X-ray sources, the cross-matched sources to *SDSS* with Likelihood-Ratio $\text{LR}_{\text{XMM},\text{SDSS}} > 1.5$, the cross-matched sources to *WISE* with $\text{LR}_{\text{XMM},\text{WISE}} > 0.5$, all *BOSS* spectra and the spectra with *WISE* counterparts.

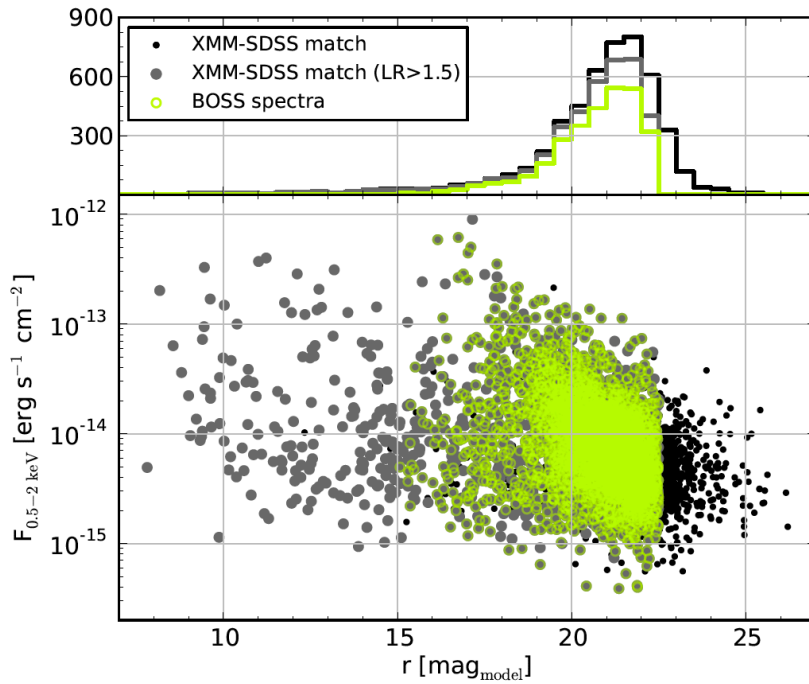


Figure 2.2.: Distribution and histogram of r -band magnitude (*SDSS*: `modelmag`, AB) for X-ray source counterparts in the northern XMM-XXL area: The plot shows all cross-matched *XMM-SDSS* sources (black), the cross-matched sources above the Likelihood-Ratio of $\text{LR}_{\text{XMM},\text{SDSS}} > 1.5$ (grey) and the sources with *BOSS* spectra (green).

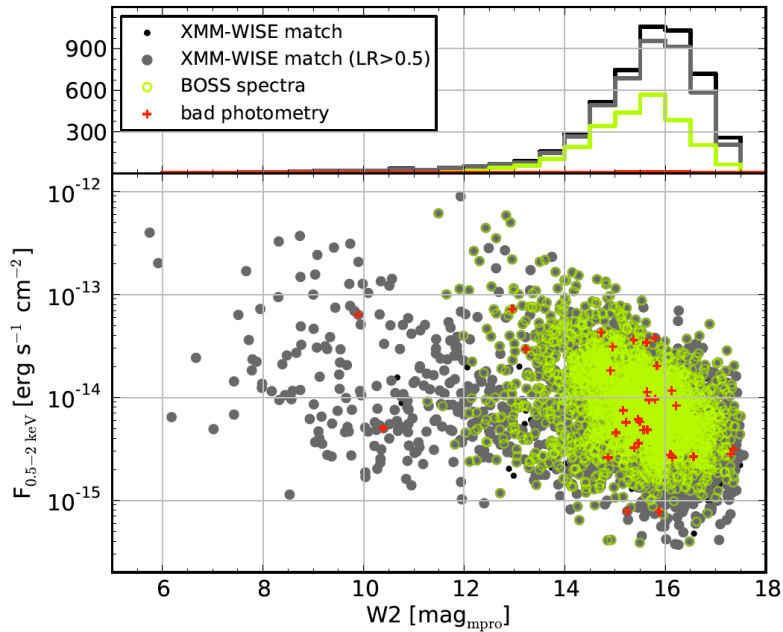


Figure 2.3.: Distribution and histogram of $W2$ -band magnitude ($WISE: m_{\text{pro}}$, Vega) for X-ray source counterparts in the northern XMM-XXL area: The plot shows all cross-matched $XMM-WISE$ sources (black), the cross-matched sources above the Likelihood-Ratio of $LR_{XMM,WISE} > 0.5$ (grey) and the sources with $BOSS$ spectra (green). The red markers are sources with bad $WISE$ photometry and are excluded from the dataset.

the probability to be the counterpart of the same source. We assume an upper bound distance of 1 arcsec, which corresponds to the radius of a $BOSS$ fibre and is a very conservative limit for non-blended $WISE$ sources. Out of the 3305 X-ray sources with both $SDSS$ and $WISE$ cross-matches, 13 per cent have counterparts which are separated by more than 1 arcsec. Such a fraction decreases to 4 per cent for distances larger than 2 arcsec. This number is consistent with expectations, given the predicted numbers of spurious associations we estimate from the Likelihood-Ratio thresholds for the IR and optical matches to the X-ray sources (see above).

2.3. Introduction of spectroscopic data set

2.3.1. BOSS spectroscopic survey

We performed optical spectroscopic follow-up of the *XMM-SDSS* matched sources with the *BOSS* spectrograph of *SDSS* (Smee et al., 2013). *BOSS* is a multiple fibre spectrograph using a standard plate of 7 deg^2 which can host 1000 optical fibres of 2 arcseconds diameter and is typically exposed for 4500 s. The covered wavelength range spans $\lambda = 360 - 1040 \text{ nm}$ with an average resolution of $R = 2000$ and a redshift accuracy of 65 km s^{-1} . The *BOSS* spectroscopic targets are limited in their *r*-band magnitude range. We apply a magnitude cut of $15.0 < r < 22.5 \text{ mag}$. The bright limit is necessary to avoid cross-talk effects in the optical spectrograph, while the faint one is introduced to ensure realistic chances of successfully obtaining a spectrum for strong emission line objects in a typical *BOSS* exposure.

The fibre allocation of one plate is split into fibres for the dedicated science programme and fibres which are assigned to standard calibration stars and sky calibration targets ($n_{\text{star}} \approx 20$ and $n_{\text{calib}} \approx 80$) as well as repeated observations of other *BOSS* programmes. The fibre tiling procedure of the *BOSS* plates starts with the determination of the largest possible subset of targets which do not collide with each other. In a second step, the remaining fibres are optimally distributed to minimize fibre collisions (Blanton et al., 2003). We can conclude that deselection from the initial target list was only due to random fibre collisions.

2.3.2. Spectroscopic target selection

The spectroscopic follow-up of the 4075 matched *XMM-SDSS* AGN comes from three different programmes, including two dedicated *BOSS* ancillary programmes (published as a part of DR12, Alam et al. 2015) and former *BOSS* DR10 observations (Ahn et al., 2012) in the same region. In the following, we explain the target selection and refer to technical details of the *BOSS* observations. In Fig. 2.4, we show a chart of the selection process and Fig. 2.5 presents the full area in the XMM-XXL north as well as the footprint of the individual ancillary plates. Tab. 2.1 lists the plate centre coordinates of the dedicated ancillary programmes.

First BOSS Ancillary Programme

The first group of spectra has been retrieved from the *BOSS* ancillary programme by PI P. Green and A. Merloni. It was devised to test target selection algorithms and strategies for both the *SPIDERS* and *TDSS* survey components of the *SDSS-IV*. *TDSS* (Time Domain Spectroscopic Survey, Morganson et al. 2015) is a follow-up programme of time variable objects (e.g. from PAN-STARRS1), with either single as well as multi-epoch spectroscopy. The dedicated *BOSS* targeting plate covered 7 deg^2 including both the XMM-LSS as well as *Pan-STARRS* Medium Deep Field MD01. In the area, we selected 1159 point-like X-ray sources at a flux limit of $F_{0.5-2 \text{ keV}} > 6 \cdot 10^{-15} \text{ erg cm}^{-2} \text{ s}^{-1}$ and 11 point-like X-ray sources at a flux limit of $F_{2-10 \text{ keV}} > 6 \cdot 10^{-14} \text{ erg cm}^{-2} \text{ s}^{-1}$. These flux limits were chosen to correspond to the planned *eROSITA* limits in the deep exposed ecliptic pole regions. Applying an *r*-band cut of $17.0 \text{ mag} < r_{\text{psf}} < 22.5 \text{ mag}$ and Likelihood-Ratio of $\text{LR}_{\text{XMM,SDSS}} > 1.5$,

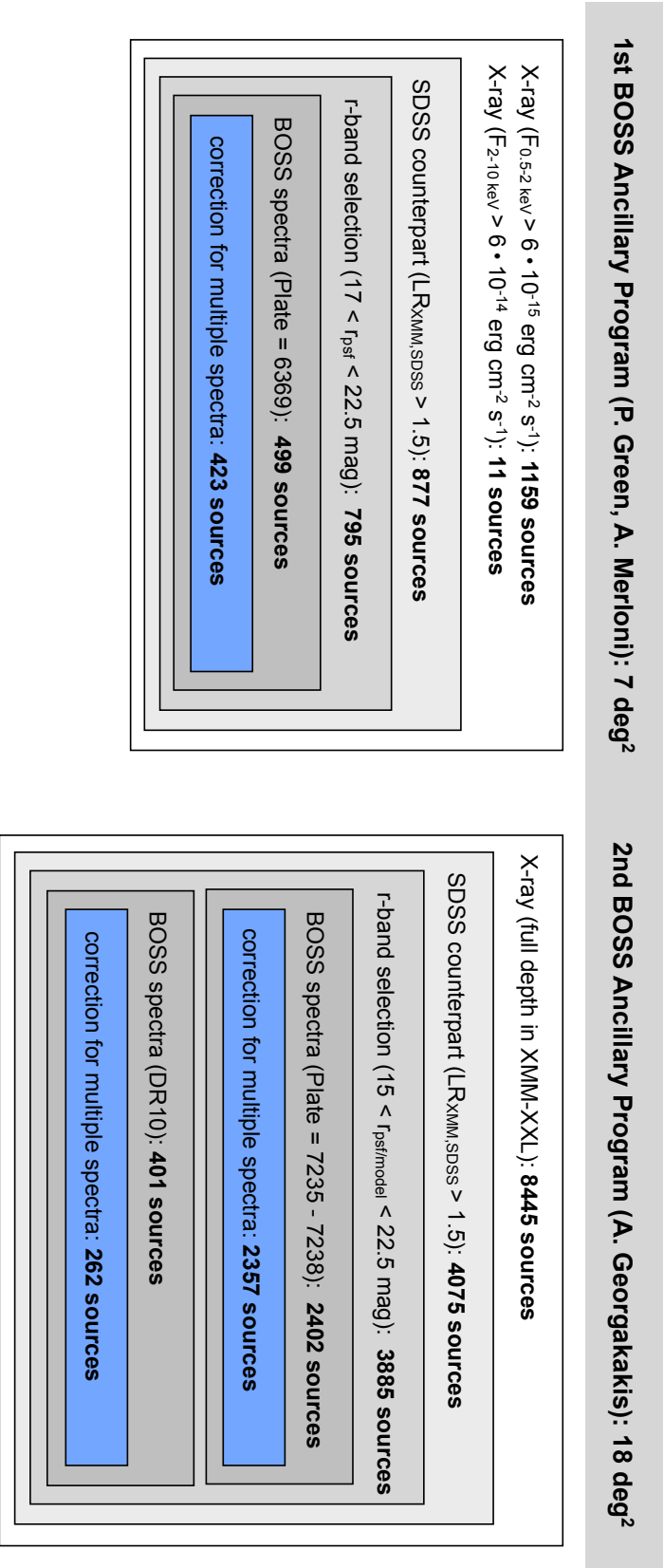


Figure 2.4.: Spectroscopic target selection in the XMM-XXL north field: The targets for the follow-up of AGN come from three different groups, including two dedicated *BOSS* ancillary programmes and former *BOSS* DR10 observations (Ahn et al., 2012) in the same region. We indicate the number of point-like X-ray sources, the matched *SDSS* counterparts, the applied *r*-band cut, the *BOSS* observed spectra, and the correction for multiple spectra for each programme.

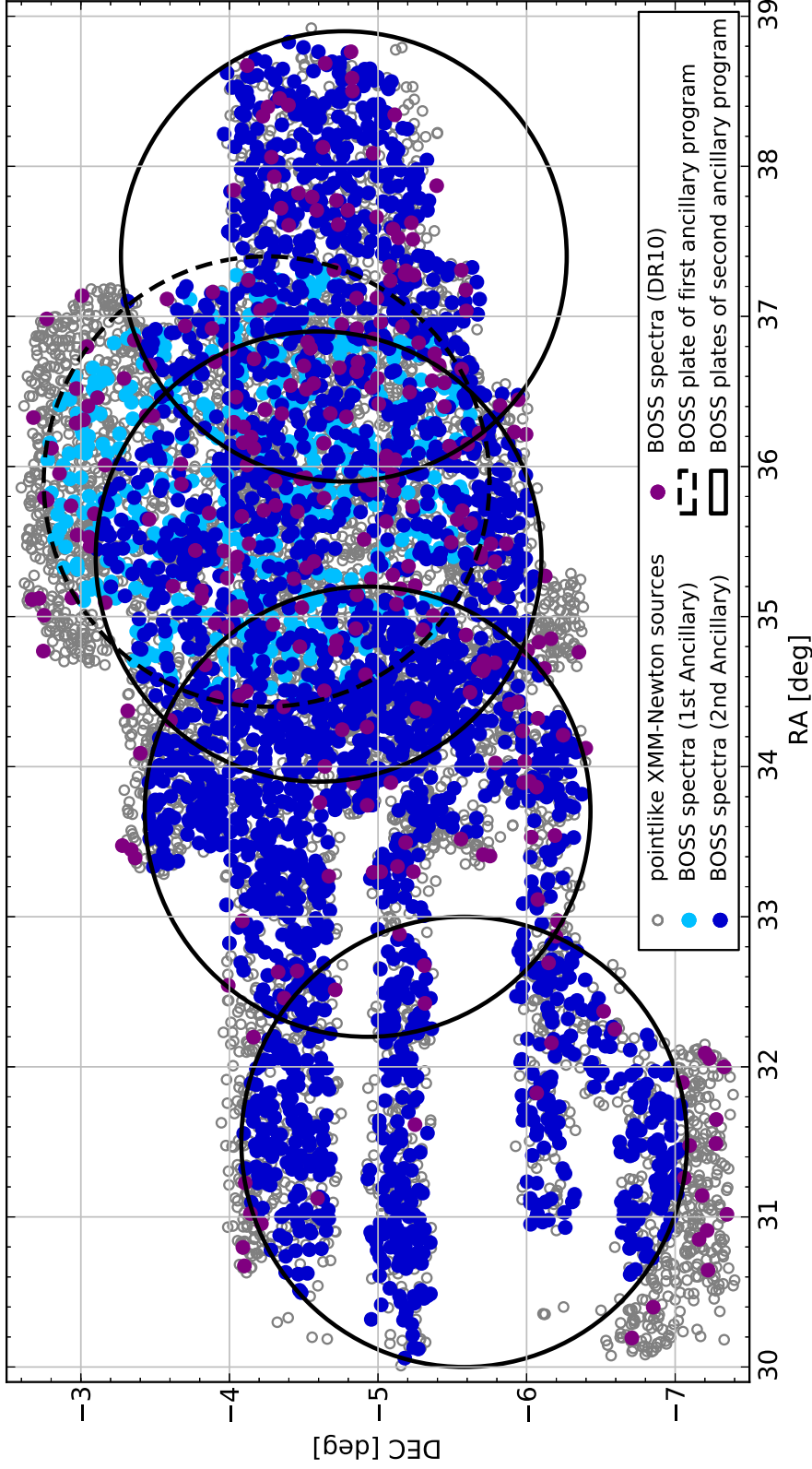


Figure 2.5.: XMM-XXL north area with sky coordinates of *XMM-Newton* sources and associated *BOSS* observed targets: We extracted 8445 point-like X-ray sources (grey) over a $\sim 18 \text{ deg}^2$ area of the XMM-XXL north. By the time of our reduction (January 2012), the pointing of *XMM-Newton* in the XMM-XXL north area was not yet completed. The spectroscopic follow-up of the *XMM-Newton* sources with *BOSS* has been performed during two ancillary programmes (first programme: dashed line circle / light blue markers, second programme: solid black line circle / dark blue markers) and completed by former targets from *BOSS-DR10* (purple markers).

there were 795 *BOSS* targets, out of which 499 sources have been observed. In Fig. 2.5, we show the position of the *BOSS* spectra and the ancillary plate in the northern XMM-XXL area. This first SDSS Ancillary Project is named ‘TDSS/SPIDERS/eBOSS Pilot Survey’, the *BOSS* targeting primary programme is called ‘TDSS/SPIDERS/BOSS Pilot Survey’ and the Ancillary Bit Numbers are 23, 24 and 25. The *BOSS* spectrograph observed the dedicated plate 6369 in October 2012 without the use of washers.

Second BOSS Ancillary Programme

The second group of spectra comes from the larger ancillary programme comprising four *BOSS* plates led by A. Georgakakis. This programme was fully dedicated to the follow-up of point-like X-ray sources covering nearly the entire XMM-XXL north area. Due to the larger amount of available fibres, we selected all 8445 extracted X-ray point-like sources in the 18 deg² XMM-XXL north reaching to a flux of $F_{0.5-10\text{keV}} \approx 1 \cdot 10^{-15}$ erg cm⁻² s⁻¹ and we applied $15.0 < r_{\text{psf}/\text{model}} < 22.5$ mag (see Fig. 2.2) for optically unresolved sources (TYPE = 6: psf-magnitude) and optically resolved sources (TYPE = 3: model-magnitude). Within the 18 deg², our dataset contains 3885 *XMM-SDSS* matched sources within the corresponding *r*-band threshold and with $\text{LR}_{\text{XMM,SDSS}} > 1.5$. The footprint of the four plates (see Fig. 2.5) comprises 3461 *XMM-SDSS* matched sources, out of which 2357 have been followed-up by *BOSS*. This second SDSS Ancillary Project is named ‘Follow-up spectroscopy of wide-area XMM fields’. The observations of the plates 7235, 7236, 7237, 7238 took place in November 2013 and January 2014 without the use of washers, resulting in 2357 spectra. The *BOSS* targeting programme is called ‘Wide-Area XMM fields’ and the Ancillary Bit Numbers are 32 and 33.

Table 2.1.: *BOSS* Plate information of the *XMM-SDSS* targets of the first and second ancillary program in the XMM-XXL north area: We list plate number and plate centre coordinates.

Plate Number	Observation MJD	RA [deg] Plate Centre	Dec [deg] Plate Centre
6369	56217	35.9000	-4.2500
7235	56603	37.3965	-4.7678
7236	56605	35.4477	-4.5985
7237	56662	33.7033	-4.9263
7238	56660	31.5008	-5.5752

DR10 Spectra

Some of the X-ray sources from the second ancillary programme in the same field had already been independently targeted as part of the *BOSS* large-scale structure survey programme as LRG (luminous red galaxies) or candidates for high-redshift QSOs. Thus, in order to increase the spectroscopic completeness of our sample within $15.0 < r_{\text{psf}/\text{model}} < 22.5$ mag, we included this third group of 401 public available spectra from 14 different plates within *BOSS-DR10* (Ahn et al., 2012). The added sources with *BOSS* spectroscopy from the DR10 are located both outside and inside the ancillary plates footprint as indi-

cated in Fig. 2.5. There are 30 spectra from the plate 6369 of the *TDSS* targets which did not meet the flux threshold from the first ancillary programme, but are within the flux criteria of the second ancillary programme.

Summarizing, we selected 8445 X-ray sources and matched 3885 *SDSS* counterparts by applying the r-band criteria $15.0 < r_{\text{psf/model}} < 22.5$ mag and Likelihood Ratio $\text{LR}_{\text{XMM,SDSS}} > 1.5$. From the *BOSS* observations, we obtained 3302 spectra. This number reduces to 3042 unique objects after correction for 260 objects with multiple spectra (257 double observations, 3 triple observations) by prioritizing the spectra with the higher signal-to-noise ratio (S/N ratio). 2474 of the *BOSS* spectra have a *WISE* counterpart.

2.4. Spectroscopic AGN Sample: Redshift Determination and Classification

In this section, we present the processing of optical spectra in the *BOSS* pipeline and discuss the determination of spectroscopic redshifts by visual inspection, as well as objective classification of our X-ray sources based on their spectroscopic properties.

2.4.1. BOSS pipeline products

The *BOSS* pipeline processes the observational raw data in two steps. In the first pass, the `spec2d` pipeline converts the two-dimensional CCD data into one-dimensional spectra, introduces calibrations in wavelength and flux, and combines the red and blue spectral halves. In the second pass, the `spec1d` pipeline automatically analyzes the features of the one-dimensional-spectra and assigns a redshift and a classification with a χ^2 -minimization method (Stoughton et al., 2002; Bolton et al., 2012). The relevant information about redshift and emission line features of the spectra are stored in the pipeline products `spZall` file and `spZline` file (DR12, v5_7_0, Bolton et al. 2012).

For the determination of the redshift, the pipeline fits templates of galaxies ($-0.01 < z < 1.0$) and quasars ($0.0033 < z < 7.0$) with a linear combination of four principal components. The stars have dedicated standard templates. After the fitting process, the *BOSS* pipeline assigns a quality flag (`ZWARNING`) to each redshift `Z_BOSS`. The optimal flag is `ZWARNING = 0`, which is assigned to 80 per cent of our spectra. Redshift identifications with `ZWARNING > 0` may be caused by two best fitting templates with similar χ^2 , outlying points from best-fit model or a minimal χ^2 at the redshift edge.

The line features of every spectrum are provided by the `spZline` data model of the *BOSS* pipeline. We employ these data without any additional line fitting procedure. The line fit is performed for 31 emission lines with a single gaussian on top of the continuum subtracted spectrum. The redshift is re-fit nonlinearly after the initial guess of the main redshift analysis and fixed for all lines beside $\text{Ly}\alpha$. Blueshifts of individual lines are not accounted for. The line widths are calculated as a strength-weighted average of dedicated emission line groups, independent of the broad or narrow line character:

- (i) Balmer lines: $\text{H}\alpha$, $\text{H}\beta$, $\text{H}\delta$, $\text{H}\gamma$, $\text{H}\epsilon$
- (ii) Lyman lines: $\text{Ly}\alpha$
- (iii) Nitrogen line: NV
- (iv) other lines: $[\text{ArIII}]$, $[\text{SII}]$, $[\text{NII}]$, $[\text{OI}]$, $[\text{SIII}]$, HeI , HeII , $[\text{OIII}]$, $[\text{NeIII}]$, $[\text{OII}]$, MgII , CIII , CIV .

The fluxes of $[\text{OIII}]$ 5007 and $[\text{OIII}]$ 4959 as well as $[\text{NII}]$ 6583 and $[\text{NII}]$ 6548 are imposed with a ratio of 3:1. The average width of group (iv) lines is less representative of the true width. It includes both narrow and broad lines, and therefore underestimates the individual broad lines widths and overestimates the individual narrow lines widths.

In our work, we focus on 9 emission lines of interest (λ in vacuum wavelength): CIV (1549.48 Å), CIII (1908.73 Å), MgII (2800.32 Å), the unresolved $[\text{OII}]$ -doublet (3727.09 Å)

and (3729.88 Å), H β (4862.68 Å), [OIII] (5008.24 Å), H α (6564.61 Å), and NII (6585.27 Å). There are three emission line parameters from `spZLine`, which are important for the classification:

- (i) the emission line flux A_{gauss} (`LINEAREA`) and the error ΔA_{gauss} (`LINEAREA_ERR`),
- (ii) the Full-Width-Half-Maximum FWHM derived from $\text{FWHM} = \sigma \cdot (2\sqrt{2 \ln 2})$, where σ is the gaussian width in km s^{-1} (`LINESIGMA`), and
- (iii) the equivalent width EW (`LINEEW`).

We impose a significance threshold of $A_{\text{gauss}}/\Delta A_{\text{gauss}} > 3$ for all emission lines.

2.4.2. Redshift determination

The initial redshifts for the *BOSS*-observed AGN are taken from the `spZall` file of the *BOSS* pipeline. Typically, all QSO observed by *BOSS* are candidates for baryonic oscillations studies and therefore pass a visual inspection (Pâris et al., 2012, 2014). We expect the sources of our pilot study to be different from the majority of the standard *BOSS*-LRG and -QSO targets which are selected based on optical criteria. They will include e.g. narrow emission line AGNs, host galaxy dominated AGNs and AGNs with less steep powerlaws. For this reason, we started a visual screening of our data set.

In order to determine the causes for redshift failures of the *BOSS* pipeline, we first checked all spectra of the first ancillary programme (Plate Number: 6369). Assuming this dataset to be a good representative for all our targets, we applied this knowledge to the second ancillary programme and only inspected the subset of spectra most likely to be problematic. In total, we inspected ~ 1200 spectra. The remaining spectra were part of the visual inspection process of the *BOSS* QSO group and are published in Paris et al. (2015, in prep.). We evaluate the redshift provided by the pipeline `Z_BOSS` by visual inspection and assign both a new redshift `Z` and confidence parameter `Z_CONF`. These parameters, published in Menzel et al. (2016), are explained in the following:

- (i) `Z_BOSS`: the redshift provided by the *BOSS* pipeline before visual inspection;
- (ii) `Z`: the adapted redshift after visual inspection;
- (iii) `ZERR`: the error of `Z`;
- (iv) `Z_CONF`: the redshift confidence after visual inspection:
 - 3 - reliable pipeline redshift,
 - 2 - not robust pipeline redshift,
 - 1 - bad spectrum,
 - 30 - reliable visual redshift and pipeline failure,
 - 20 - not robust visual redshift and pipeline failure,
- (v) `STAR/BLLAC`: star or BL Lac flag.

The spectra, whose visual inspection redshift coincide with the *BOSS* pipeline redshifts, keep their initial redshifts $Z = Z_{\text{BOSS}}$. For the spectra with wrong *BOSS* pipeline redshifts, we rerun the *BOSS* pipeline (`spreduce1d.pro`) in a small redshift range suggested by the visual inspection and assign a new redshift $Z \neq Z_{\text{BOSS}}$. The redshift confidence parameter `Z_CONF` contains information about the reliability of the visual redshift assignment. There are flags for ‘reliable’ and ‘not robust’ redshifts. Furthermore, we assign a flag for ‘bad spectra’ where no redshift can be obtained by visual inspection. For a subsample of spectra,

the pipeline fails to determine a correct redshift as suggested by the visual inspection. In this case, we assign the flags ‘reliable visual redshift and pipeline failure’ or ‘not robust visual redshift and pipeline failure’. During the visual inspection, we mark all stars with the **STAR** parameter. Their precise redshift determination is not included in our visual evaluation, because stars are not in the focus of this study. In Table 2.2, we give an overview about the redshifts obtained from the *BOSS* pipeline after visual inspection.

Table 2.2.: Final redshifts and redshift confidence of *BOSS* spectra after the visual inspection: The data set is divided in reliable redshifts, not robust redshifts, bad redshifts and star. We indicate the redshift confidence and the coincidence of the redshift of the *BOSS* pipeline and the visual inspection.

a.) reliable redshift		2578 spectra
Z_CONF = 3:	Z_BOSS = Z	2525
Z_CONF = 3:	Z_BOSS \neq Z	45
Z_CONF = 30:	good visual redshift, but pipeline failure	8
b.) not robust redshift		122 spectra
Z_CONF = 2:	Z_BOSS = Z	82
Z_CONF = 2:	Z_BOSS \neq Z	29
Z_CONF = 20:	not robust visual redshift and pipeline failure	11
c.) bad redshift		255 spectra
Z_CONF = 1:	Z_BOSS \neq Z	255
d.) stars, BL Lac		87 spectra
STAR/BLLAC = star:		85
STAR/BLLAC = BL Lac:		2

In the following, we want to highlight the critical spectral characteristics which lead to a redshift failure by the *BOSS* pipeline. These characteristics are:

- (i) low redshift quality: ZWARNING > 0 (583 spectra with 293 failures),
- (ii) large redshift error: ZERR_BOSS > 0.01 (56 spectra with 45 failures),
- (iii) low S/N ratio: SN_MEDIAN_ALL < 1.6 (837 spectra with 272 failures),
- (iv) very high redshifts: Z_BOSS > 4 (49 spectra with 39 failures),
- (v) very low redshifts: Z_BOSS < 0.05 (131 spectra with 37 failures).

The items (ii) to (v) are often associated with ZWARNING > 0. The redshifts failures at high redshifts (iv) are often caused by emission line confusion of Ly α , MgII, CIV, CIII] and H α . We have to point out that problematic sources can also be caused by external influences, such as:

- (vi) blending of a neighbour object (1 out of 423 spectra from plate 6369)
- (vii) instrumental fibre problems (4 out of 423 spectra from plate 6369).

These features are not correlated with the S/N ratio or the redshift quality flag. The influence of neighbour objects can be reduced by cross-checking with the optical images. There are some fibres with instrumental problems resulting in spectra which are missing correct spectroscopic information in parts of the observed wavelength range. These spectra provide redshift information for the objects, but classification is not possible. For our catalogue, we will exclude these objects.

As shown in Fig. 2.6, the group of spectra with correct and robust *BOSS* redshifts is defined by $Z_{\text{WARNING}} = 0$, $\text{SN_MEDIAN_ALL} > 1.6$, and $0.05 < Z_{\text{BOSS}} < 4$, and we obtained an extremely high reliability of 99 per cent for the *BOSS* pipeline results. Therefore, within this parameter space, we did not perform any visual inspection for the spectra of the secondary ancillary programme, nor for all added spectra from the DR10.

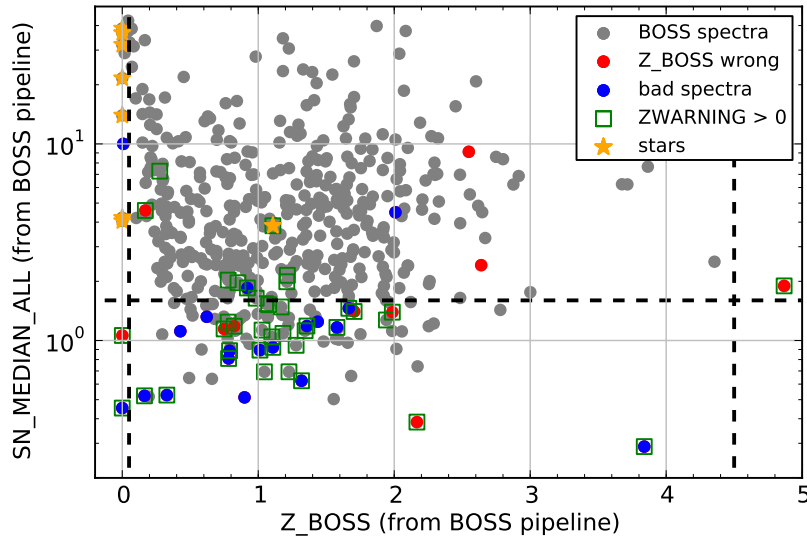


Figure 2.6.: Distribution of BOSS pipeline redshifts and the S/N ratio of the BOSS plate 6369 (first ancillary program, $n_{6369} = 480$) in the XMM-XXL north area: The colors in the plot indicate the results of a complete visual inspection. There are spectra with good BOSS pipeline redshifts, spectra with wrong BOSS pipeline redshifts, bad spectra (e.g. low S/N ratio, broken), stars and spectra with $Z_{\text{WARNING}} > 0$. The dashed line mark the region of $\text{SN_MEDIAN_ALL} > 1.6$ and $0.05 < Z_{\text{BOSS}} < 4$, whose spectra have an extremely high redshift confidence.

After the visual inspection, 2525 sources have a reliable initial redshift assigned by *BOSS* pipeline, which corresponds to 83 per cent of redshift success. Additional 53 sources get a different reliable redshift, out of which 8 have only visual redshifts because they cannot not be correctly fitted by the pipeline ($Z_{\text{CONF}} = 30$). For the classification of the spectra in the following sections, we only use the 2570 BOSS spectra with $Z_{\text{CONF}} = 3$, because they have the complete data products from the *BOSS* pipeline.

2.4.3. Spectroscopic Classification

In this section, we present the classification rules for our X-ray selected sources based on spectroscopic properties. We first introduce the bimodal FWHM distribution of AGN emission lines to separate the population of broad line and narrow line emitters. In a second step, we determine the ionization source of the narrow line emitters with the help of optical emission line diagnostic diagrams. The flow chart in Fig. 2.8 visualizes the steps of the classification process.

Line width bimodality of broad and narrow line emitters

Our large sample of uniformly selected X-ray AGN allows for a systematic analysis of the FWHM of emission lines originating in the different regions of the AGNs. For the classification process, we evaluate the properties of potentially broad lines $H\beta$, MgII, CIII] and CIV. As described in 2.4.1, the widths for $H\beta$ and MgII correspond to the strength-weighted averaged of their groups (i) and (iv).

In Fig. 2.7, we show the FWHM-distribution of all significantly detected $H\beta$ and MgII emission lines. Both distributions show a clear bimodal shape, which suggests the presence of two physically distinct populations. In detail, the minima of the distributions are at $\text{FWHM}_{(H\beta)} = 985 \text{ km s}^{-1}$ and $\text{FWHM}_{\text{MgII}} = 957 \text{ km s}^{-1}$. The high-FWHM sources are associated with broad line region (BLR) emission and the low-FWHM sources are associated with narrow line region (NLR) emission, as introduced in Section 1.2.2. In the following, we will use the FWHM threshold of $\text{FWHM} = 1000 \text{ km s}^{-1}$ to separate BLR and NLR emitters.

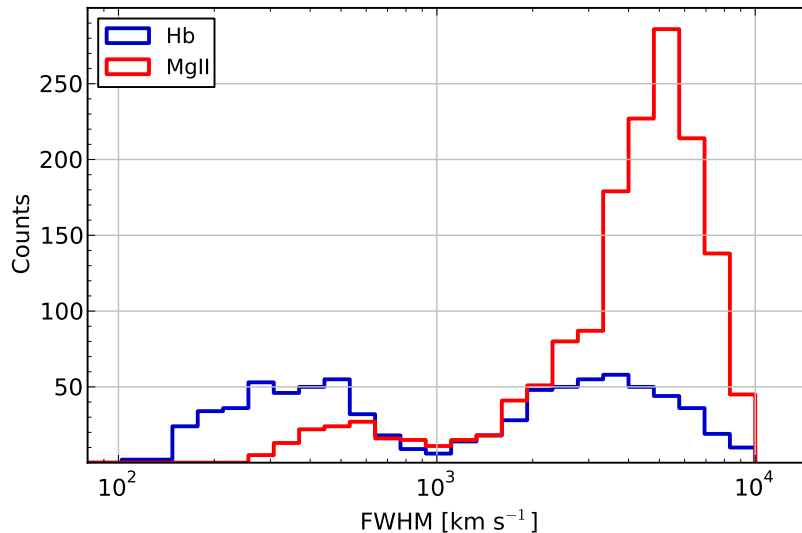


Figure 2.7.: Average FWHM distribution of emission lines: We show the distribution of all significant $H\beta$ and MgII emission lines. The bimodal FWHM distribution implies the presence of two species: narrow line emitters ($\text{FWHM} < 1000 \text{ km s}^{-1}$) and broad line emitters ($\text{FWHM} \geq 1000 \text{ km s}^{-1}$).

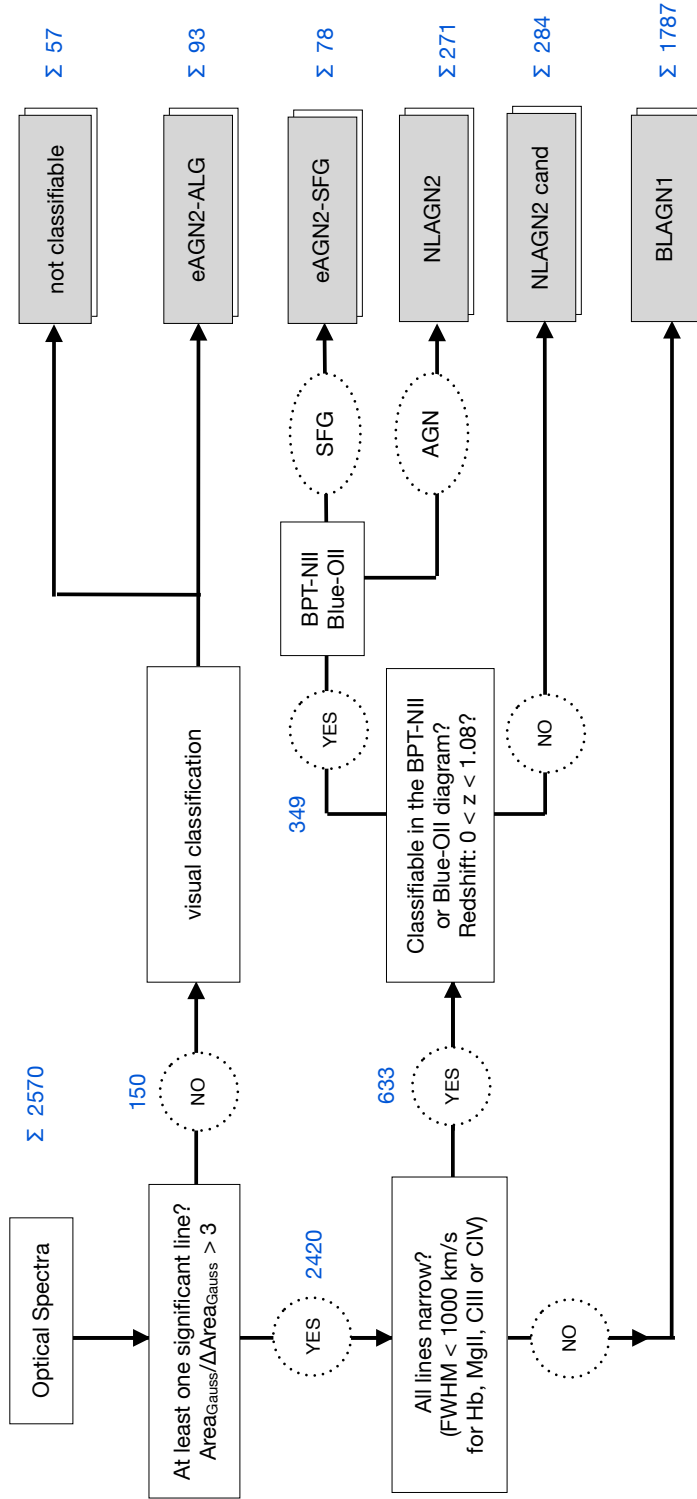


Figure 2.8.: Classification flow-chart of *BOSS* observed sources in the XMM-XXL north area: We use the emission line information provided by *spZline* from the *BOSS* pipeline. For the classification, we refer to common optical AGN selection criteria and assign the classes: BLAGN1, NLGN2/NLGN2cand, eAGN(-ALG/-SFG) or not classifiable spectra.

For our classification, we analyze the FWHM of the H β , MgII, CIII] and CIV lines in sequence. The first significant emission line, which has a FWHM larger than 1000 km s⁻¹ defines an object to be a BLR emitter. For $z > 1.14$, H β is redshifted out of the *BOSS* wavelength range. In this case, the width of MgII, CIII] or CIV are solely used for the classification. We find that at these redshifts, no more NLR emitters with significant emission lines are present in the sample. Therefore, the averaged FWHM for the group (iv) lines is not underestimated by strong narrow emission line contribution.

In the following sections, we will refer to the BLR emitters as ‘unobscured’ (referring to type 1 AGN) from the optical point of view and call them ‘Broad Line AGN [of type] 1’: **BLAGN1**. Their optical spectra show the blue/UV continuum from the accretion disc and the characteristic H β , MgII, CIV and CIII] broad emission lines from the high velocity clouds close to the black hole. The NLR emitters with $\text{FWHM}_{(\text{H}\beta)} < 1000 \text{ km s}^{-1}$ can have different ionization sources, which will be discussed in the following section.

Ionization source diagnostics of narrow line emitters

The ionizing radiation that excites the NLR ($\text{FWHM} < 1000 \text{ km s}^{-1}$) of X-ray detected AGN candidates can originate from different regions in the galaxy: the accretion disc in the nuclear region (AGN), star formation in the host galaxy (SFG) or both. The narrow line emitters powered by an AGN typically have an orientation which prevents a direct look into the accretion disc (Antonucci, 1993; Urry & Padovani, 1995). The BLR clouds close to the black hole are obscured and only narrow lines from distant clouds in low density environments are visible in the spectrum. The excitation of narrow emission lines by star formation typically happens through photo-ionizing radiation from e.g. in OB stars.

As is customary, we derive the dominating source of ionization for our sample of narrow line emitters between $0 < z < 1.08$ by comparing the emission line ratios [OIII]/H β vs. [NII]/H α (BPT-NII-diagram, Meléndez et al. (2014)) or [OIII]/H β vs. [OII]/H β (Blue-OII-diagram, Lamareille (2010)), as presented in the following. AGN have a stronger ionization continuum than SFG and typically reside in the top right corner of the diagrams, whereas SFG reside in the bottom left corner.

BPT-NII-diagram

For spectra with significant H β , [OIII], H α , and [NII], we follow the BPT-NII selection criteria (Baldwin et al., 1981; Kauffmann et al., 2003; Kewley et al., 2006; Meléndez et al., 2014) with the ratios [OIII]/H β vs. [NII]/H α . These ratios are less sensitive to reddening because of the small wavelength separation of the relevant emission lines. In addition, we use EW which removes the direct reddening dependence. The BPT-NII-diagram only classifies objects at a redshift of $0 < z < 0.54$, because H α and [NII] are shifted out of the *BOSS* wavelength range for higher redshifts.

According to Meléndez et al. (2014), the demarcation of star-forming galaxies and AGN-dominated sources, including the effect of dust, is described by:

$$\log \left(\frac{\text{EW}([\text{OIII}])}{\text{EW}(\text{H}\beta)} \right) = \frac{0.13}{\log \left(\frac{\text{EW}([\text{NII}])}{\text{EW}(\text{H}\alpha)} \right) + 0.31} + 1.24 \quad (2.1)$$

and shown as solid line in Fig. 2.9. This demarcation line is based on photoionization modeling for AGN and SFG galaxies. The authors derive a two-zone model including matter-bounded and radiation-bounded components which allows for a theoretical prediction for the BPT-NII diagram. In Fig. 2.9, we also add the demarcation line of Kauffmann et al. (2003), which separates between SFG and AGN as well as the demarcation line of Kewley et al. (2006), which separates AGN-SFG composite objects and pure AGN. For our classification, we only adopt the demarcation of Meléndez et al. (2014).

Blue-OII-diagram

The [OII]/H β emission line ratio diagram identifies objects with significant [OII]-doublet (EW of $\lambda = 3726.032, 3728.815 \text{ \AA}$) at higher redshifts ($0 < z < 1.08$) (Lamareille et al., 2004; Lamareille, 2010). For the sake of simplicity, we refer to the [OII] doublet by the name of ‘[OII]’. The emission lines H β and [OII] have a very large separation in wavelength space and the reddening influences the emission lines as well as the underlying continuum differently. Therefore, even the EW is effected by reddening. For the separation of AGN and SFG, we choose the demarcation line of Lamareille (2010):

$$\log \left(\frac{\text{EW}([\text{OIII}])}{\text{EW}(\text{H}\beta)} \right) = \frac{0.11}{\log \left(\frac{\text{EW}([\text{OII}])}{\text{EW}(\text{H}\beta)} \right) - 0.92} + 0.85, \quad (2.2)$$

shown as the solid line in Fig. 2.9. This equation is the most recent demarcation line derived from the *SDSS* DR7 release and allows to separate between regions of SFG, Seyfert 2/LINERS. This classification is designed to yield highly pure SFG samples, with a correct classification of 99.7 per cent of all SFG and a contamination from AGN/LINERS of 16 per cent. In this work, we only apply the Blue-OII diagnostics for objects which cannot be placed in the BPT-NII-diagram.

Narrow Line Emitters

In total, our dataset contains 633 narrow line emitters out of which 349 sources can be classified by the diagnostic lines diagrams. There are 271 ‘AGN’ (BPT-NII-diagram: 244, Blue-OII-diagram: 27) which form the group of optically ‘obscured’ AGN (referring to type 2 AGN) and, in this work, are named ‘Narrow Line AGN [of type] 2: **NLAGN2**. Furthermore, there are 78 ‘SFG’ (BPT-NII-diagram: 40, Blue-OII-diagram: 38) which will be referred to as ‘elusive’ AGN with star-formation: **eAGN-SFG**. They do not show any AGN-driven emission lines in their optical spectra, but their X-ray luminosities are characteristic of an active accretion process in the centre.

The ionization origin of the remaining 284 narrow line emitters cannot be reliably determined, because the required narrow emission lines are below the significance limit or the redshift of the objects is too high ($z > 1.08$). The low significance of the lines is caused by very strong host galaxy continuum contribution or very low S/N ratio spectra. We classify this group as NLAGN2 candidates: **NLAGN2cand** and refer to their specific properties in Section 2.5.3.

Our dataset also comprises objects whose spectra do not have any significant emission lines at all. Similarly, to the eAGN-SFG, they indeed have characteristic X-ray luminosities for AGN, but only show the features of passive galaxies in their optical spectra. We classify

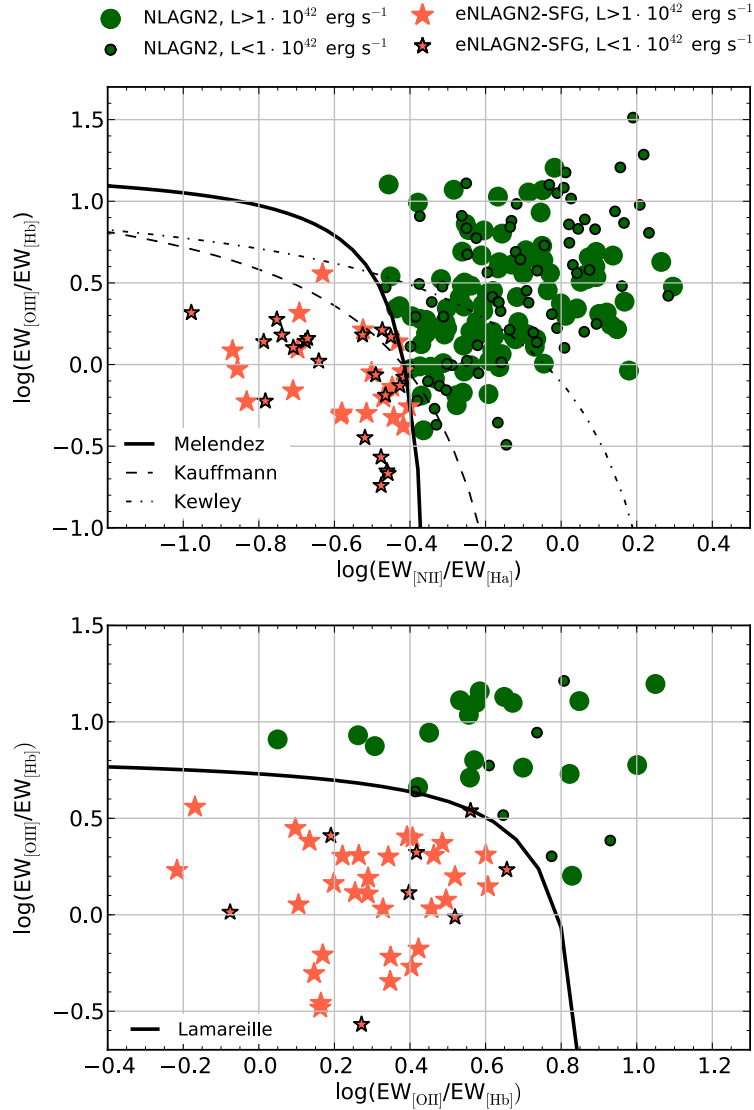


Figure 2.9.: Top Panel: BPT-NII-diagram of NLAGN2 and eAGN-SFG: The size of the marker indicates the luminosity below or above the threshold of $L_{0.5-2\text{keV}} \sim 1 \cdot 10^{42} \text{ erg s}^{-1}$. This luminosity threshold is the upper limit of X-ray emission caused by star formation in SFG. This diagram applies for sources in the redshift range $0 < z < 0.54$. Bottom Panel: Blue-OII-diagram of NLAGN2 and eAGN-SFG: The demarcation curve corresponds to Lamareille (2010). The size of the marker indicates the luminosity below or above the threshold of $L_{0.5-2\text{keV}} \sim 1 \cdot 10^{42} \text{ erg s}^{-1}$. This luminosity threshold is the upper limit of X-ray emission caused by star formation in SFG. This diagram applies for sources in the redshift range $0 < z < 1.08$, and we only project objects which cannot be placed in the BPT-NII-diagram.

them as ‘elusive’ absorption line galaxies: **eAGN-ALG**. For their selection, we apply a significance threshold of $A_{\text{gauss}}/\Delta A_{\text{gauss}} = 3$ to every emission line in the spectrum. Below this significance threshold, there is a large group of sources which are not eAGN-ALG. These are sources whose spectra mainly suffer from very low S/N ratio and do not show any stellar continuum or absorption lines at all. It is possible to derive a secure redshift by visual inspection, but our classification method is not able to automatically separate this group of objects. Therefore, we apply an additional conservative visual inspection to all of these objects. After the inspection, we sort them into two groups: 93 ‘eAGN-ALG’ and 57 ‘not classifiable’ spectra: **NOC**.

2.4.4. Final classified sample

Summarizing our final sample with 2570 spectra of optical counterparts to X-ray sources ($Z_{\text{CONF}} = 3$) with emission line information, we classified:

- (i) 1787 BLAGN1 (70 per cent),
- (ii) 271 NLAGN2 (11 per cent),
- (iii) 284 NLAGN2cand (11 per cent),
- (iv) 78 eAGN-SFG (3 per cent),
- (v) 93 eAGN-ALG (4 per cent) and
- (vi) 57 not classifiable spectra (2 per cent).

The percentages relate to the AGN selection only. We point out that our data set includes also 85 X-ray detected stars and 2 X-ray detected BL Lac.

We publicly release a catalogue of all X-ray selected AGN, including their X-ray, optical, infrared, redshift and classification properties in Menzel et al. (2016).

2.5. Spectroscopic AGN Sample: Class Properties

In this section, we describe in more detail the redshift, X-ray imaging and optical spectra properties of each class. We complement the analysis with spectral stacks, which are performed using the idl script `run_composite` written by Min-Su Shin (January 2009) and adapted by us. In this process, the contributing spectra are normalized to a chosen wavelength and corrected for Galactic extinction as well as the *BOSS* spectroscopic resolution.

2.5.1. X-ray and Optical properties

The optical classification of the X-ray selected AGN candidates from the previous section is also confirmed by their X-ray properties. The top panel of Fig. 2.10 presents the distribution of our classified *BOSS* spectra in the plane of the optical r_{psf} luminosity L_{opt} to hard X-ray luminosity L_x . The sources follow the distributions of Fiore et al. (2003). The BLAGN1 sequence is steep and shows a broad correlation between L_x and L_{opt} , both being tracers of accretion power. The NLAGN2/NLAGN2cand and eAGN-ALG/eAGN-SFG reside at lower optical luminosity ranges and have a flatter distribution. This is caused by the dominating host galaxy continuum in the optical bands, which only weakly correlates with X-ray luminosities.

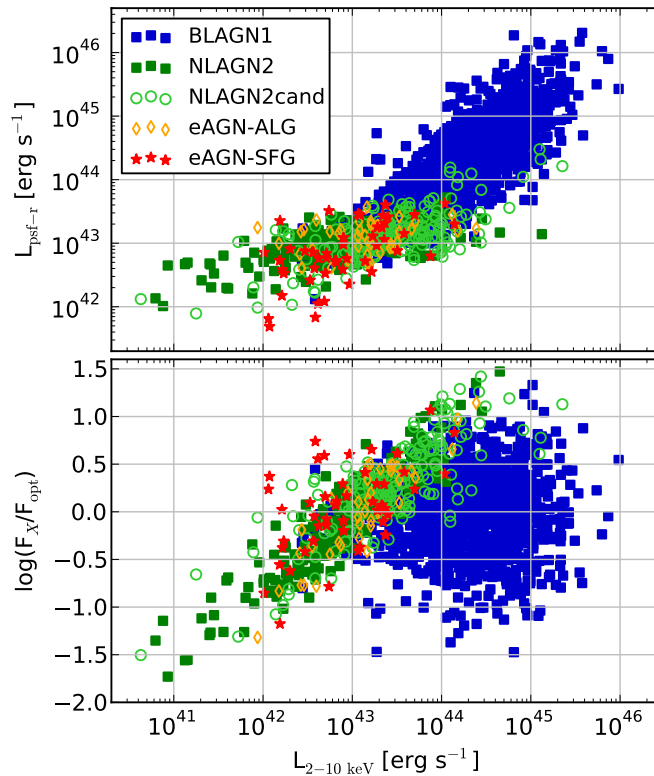


Figure 2.10.: Top Panel: Optical luminosity (r_{psf} -band) and hard X-ray luminosity (2 – 10 keV). Bottom Panel: X-ray to optical flux ratio and hard X-ray luminosity distribution of *BOSS* observed and classified AGN.

The bottom panel of Fig. 2.10 shows the X-ray to optical flux ratio which is calculated as follows:

$$\log\left(\frac{F_{2-10\text{keV}}}{F_{opt}}\right) = \log F_{2-10\text{keV}} - \left(-5.37 - \frac{r_{\text{psf}}}{2.5}\right). \quad (2.3)$$

The populations of BLAGN1 and NLAGN2/eAGN have different locations in this diagram. For $L_{0.5-2\text{keV}} \sim 10^{42} - 10^{44} \text{ erg s}^{-1}$, the NLAGN2/eAGN reside systematically at higher X-ray to optical flux ratio, which is another clear indication for their optical nuclear obscuration.

2.5.2. BLAGN1

The BLAGN1 span a large redshift range of $0.06 < z < 5.01$ and a luminosity range of $4.4 \cdot 10^{41} < L_{0.5-2\text{keV}} < 3.7 \cdot 10^{45} \text{ erg s}^{-1}$ (see Fig. 2.13). The upper redshift limit is strongly related to the faint *SDSS* *r*-band magnitude limit for the *BOSS* targets. This limit hampers the observation of objects at $z > 4.5$. At higher redshift, the Ly α absorption from the intergalactic medium strongly suppresses the spectroscopic features in the observed *r*-band. Our sample contains one exception at $z = 5.01$, which is caused by a Ly β -line in the *r*-band ($r_{\text{psf}} = 20.92 \text{ mag}$).

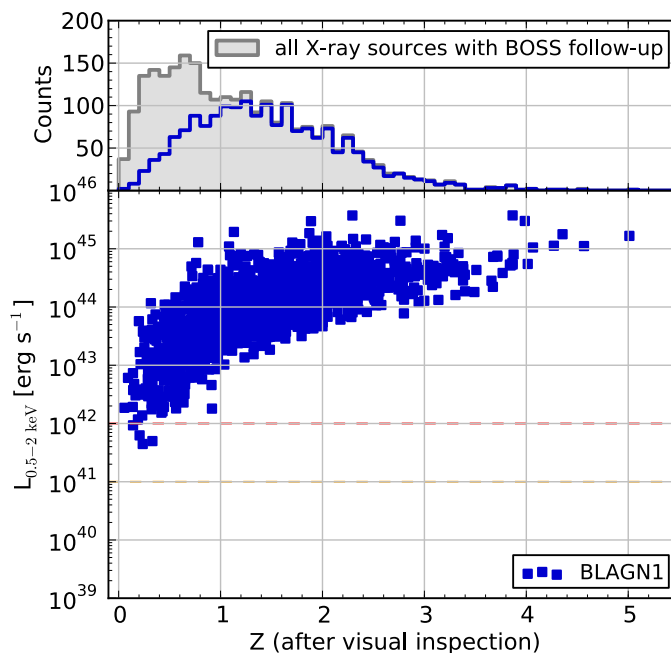


Figure 2.11.: Luminosity and visual redshift distribution of BLAGN1. In the histogram, we indicate the redshift distribution of all X-ray selected spectra (grey).

In the two top panels of Fig. 2.14, we show the spectral stack of all BLAGN1 in the redshift ranges of $0 < z < 1$ and $1 < z < 2$, respectively. For comparison, we overplot the *SDSS* DR4 QSO template (Vanden Berk et al., 2001). The BLAGN1 show clear broad line features for the emission lines MgII, H β and H α . At low redshifts, the spectral stack of the BLAGN1 tends to be redder and flatter than the *SDSS* QSO template. This is caused by the contribution of the host galaxy, indicated by the prominent Ca-doublet absorption and

the continuum at $\lambda > 4000 \text{ \AA}$. At higher redshifts, the stack approaches the QSO template because the host contribution is outshone by the more luminous nuclear emission. The stack is still redder than the template, because our BLAGN1 have different optical colours than the QSO selection criteria and include mildly extinguished objects (see Section 3.5).

2.5.3. NLAGN2 and NLAGN2cand

The NLAGN2 are detected at a relatively low redshift range of $0.04 < z < 0.91$ and a luminosity range of $1.9 \cdot 10^{40} < L_{0.5-2\text{keV}} < 1.9 \cdot 10^{44} \text{ erg s}^{-1}$ (see Fig. 2.13). The upper redshift limit of NLAGN2 is hampered by the optical line diagnostic diagrams. Within the redshift range of $0.5 < z < 0.9$, the NLAGN2 magnitude distribution reaches $r_{\text{model}} = 22.5 \text{ mag}$ and the dominating host contribution becomes too faint for detection in SDSS images. Additionally, the fraction of obscured AGN is known to decrease at higher luminosities (Ueda et al., 2003; Hasinger, 2008; Merloni et al., 2014). Thus, the high redshift and high luminosity objects in our sample tend to be more dominated by BLAGN1.

In the central panel of Fig. 2.14, we show the spectral stack of all NLAGN2. We chose the redshift range of $0 < z < 1$ which corresponds to the upper redshift bound of the optical emission line diagrams. The stack displays the narrow AGN emission lines occurring for [OII], $H\beta$, [OIII], $H\alpha$ and NII. Furthermore, there are strong host galaxy features, such as a clear Ca-doublet with the 4000 \AA -break and the stellar continuum in the red part of the spectrum.

We now introduce the group of NLAGN2cands for narrow line objects whose emission origin cannot be determined by the BPT-NII/Blue-OII diagrams. We find that these sources either have spectra with strong host contribution, low S/N ratio or they are narrow line emitters at $z > 1.08$. They span a redshift range of $0.04 < z < 2.66$ and luminosity range of $2.4 \cdot 10^{40} < L_{0.5-2\text{keV}} < 1.2 \cdot 10^{45} \text{ erg s}^{-1}$ (see Fig. 2.13). Their spectral stack ($0 < z < 1$) in Fig. 2.14 reveals the continuum features of pure NLAGN2 but also the slightly broadened lines of BLAGN1. Furthermore, the optical *SDSS* morphology of 94 per cent of NLAGN2cand is extended and their optical colours differ from QSO (see Section 3.5). Overall, it suggests that the majority of the sources are NLAGN2, which is reflected in their naming. Deeper exposed optical spectra or infrared spectra are needed to properly classify these objects. The three outstanding NLAGN2cand at $2.42 < z < 2.66$ have low S/N ratio spectra and show broad emission line features below the required significance threshold. They are probably faint misclassified BLAGN1.

2.5.4. eAGN-ALG and eAGN-SFG

The group of elusive AGN consists of sources whose spectra are consistent with either absorption line galaxies (ALG) or star-forming galaxies (SFG). The eAGN-ALG reside within a redshift range of $0.14 < z < 0.96$ and a luminosity range of $1.4 \cdot 10^{41} < L_{0.5-2\text{keV}} < 2.0 \cdot 10^{44} \text{ erg s}^{-1}$ (see Fig. 2.13). Their median soft X-ray luminosity is $L_{0.5-2\text{keV}} = 3.43 \cdot 10^{42} \text{ erg s}^{-1}$. The eAGN-SFG span a redshift range of $0.02 < z < 1.01$ and a luminosity range of $2.1 \cdot 10^{39} < L_{0.5-2\text{keV}} < 9.1 \cdot 10^{43} \text{ erg s}^{-1}$. Their median soft X-ray luminosity is at $L_{0.5-2\text{keV}} = 2.89 \cdot 10^{41} \text{ erg s}^{-1}$ (see Fig. 2.13). The counterparts of the eAGN have the same distribution in *r*-band, S/N ratio, Likelihood ratio, separation distance and number

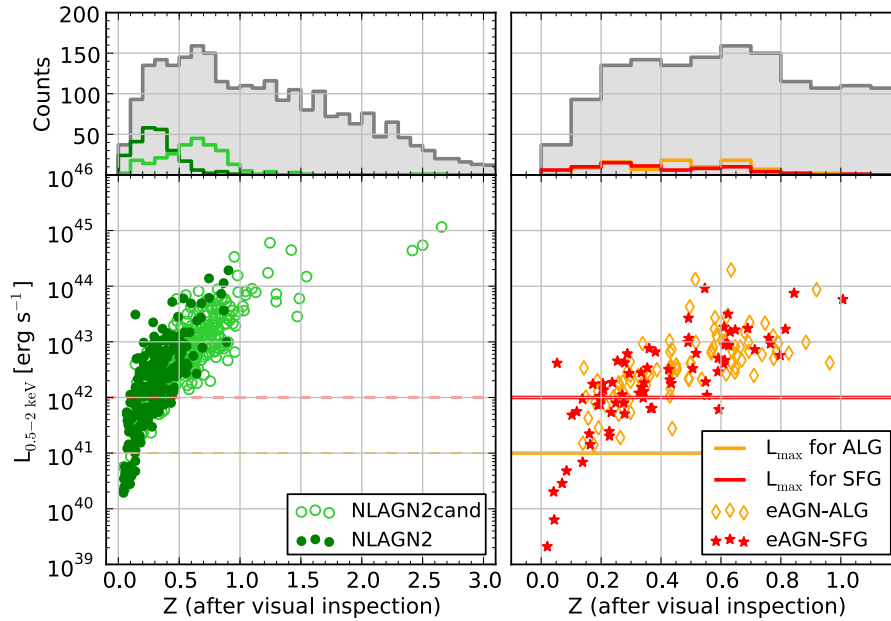


Figure 2.13.: Luminosity and visual redshift distribution of classified *BOSS* spectra. Left panel: NLAGN2 and NLAGN2cand. Right Panel: eAGN-SFG and eAGN-ALG. The luminosity thresholds indicate the upper limit of star forming galaxies (red) (Nandra et al., 2002; Ranalli et al., 2003; Grimm et al., 2003) and absorption line galaxies (yellow) without AGN (Gilfanov, 2004). In the histogram, we indicate the redshift distribution of all X-ray selected spectra (grey).

of counterparts as the entire population. Therefore, they should have the same probability distribution of counterpart association as the other objects and are not results of wrong associations.

The spectral stack of eAGN-ALG in the bottom panel of Fig. 2.14 only shows absorption line features and is very similar to the typical *SDSS* DR4 early type galaxy templates (Yip et al., 2004). On the other hand, the eAGN-SFG reveal the stellar emission lines, e.g. [OII] and [OIII], and resemble the *SDSS* DR4 template for late type galaxies (Yip et al., 2004).

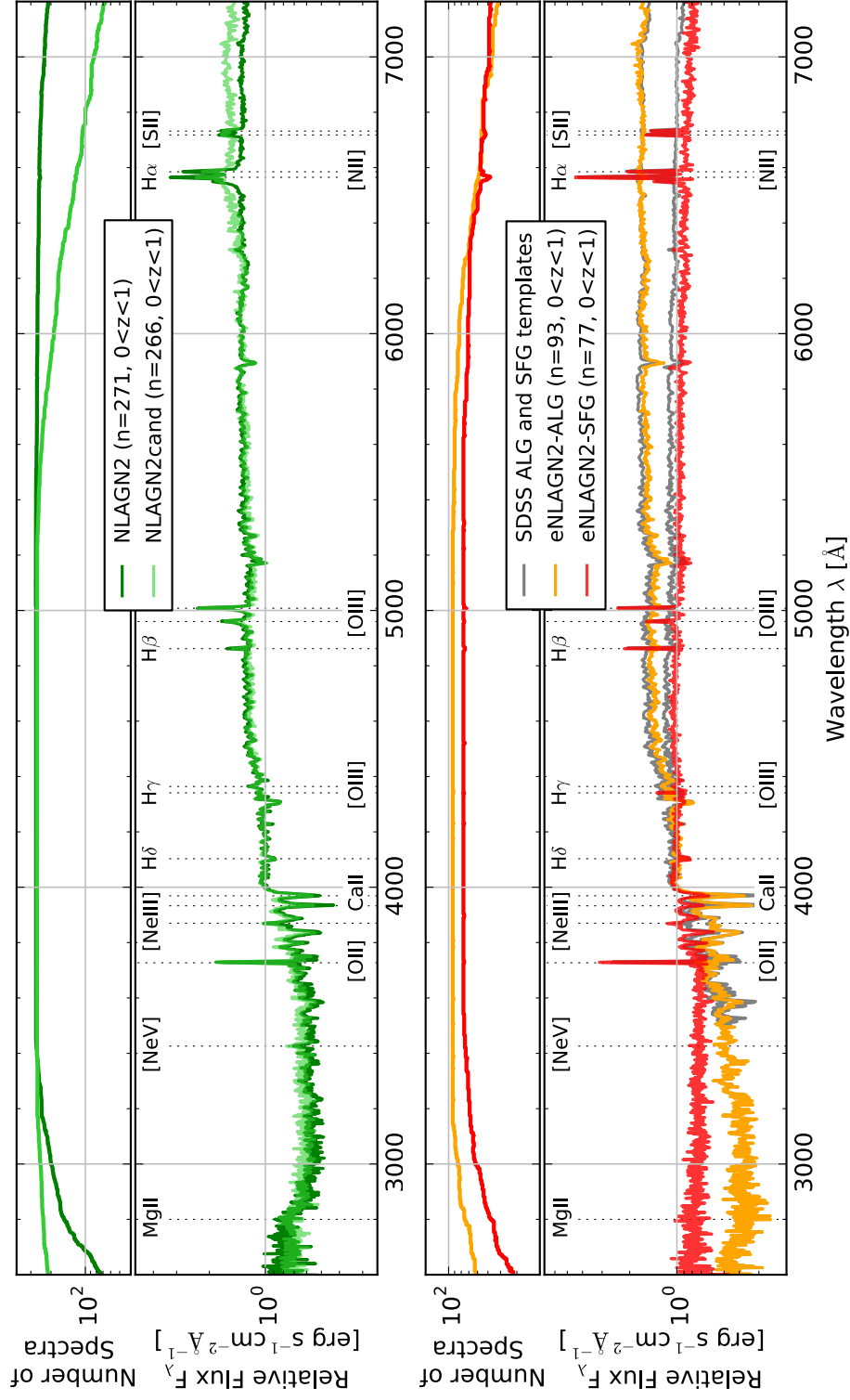


Figure 2.14: Top Panel: Median spectral stack and number of contributing spectra for NLAGN2 and NLAGN2cand in the redshift range of $0.0 < z < 1.0$ (normalized at 4200 \AA). Bottom Panel: Median spectral stack and number of contributing spectra for eAGN-SFG, eAGN-ALG and the *SDSS* template of a passive and active galaxy (Yip et al., 2004) in the redshift range of $0.0 < z < 1.0$ (normalized at 4200 \AA).

2.6. Summary: Understanding the AGN population in the XMM-XXL north

The identification and classification of X-ray sources has been already performed in many subfields of the XMM-XXL north region. Tajer et al. (2007) and Polletta et al. (2007) used a sample of 136 X-ray point like sources at a flux of $F_{2-10\text{keV}} > 1 \cdot 10^{-14} \text{ erg cm}^{-2} \text{ s}^{-1}$ in a 1 deg^2 area and obtained a reliable photometric redshift and classification for 107 sources with optical and infrared photometry. Garcet et al. (2007) used 612 point-like X-ray sources at a limiting flux of $F_{2-10\text{keV}} > 8 \cdot 10^{-15} \text{ erg cm}^{-2} \text{ s}^{-1}$ in an area of 3 deg^2 and associated 99 objects followed up by optical spectroscopy (*2dF*, *VIMOS*, *SALT*) with secure redshift and classification ($R < 22 \text{ mag}$). In the same field, Stalin et al. (2010) selected 829 objects at $F_{0.5-2\text{keV}} > 1 \cdot 10^{-15} \text{ erg cm}^{-2} \text{ s}^{-1}$ and obtained a secure identification for 487 sources with optical spectroscopy at *AAT* ($g' < 22 \text{ mag}$). Compared to all these programmes, our campaign stands out for the sheer number of spectra available from the same instrument, under stable, uniform observing conditions, and for the use of a well tested, well understood and robust data analysis pipeline.

This chapter addresses the construction and spectroscopic properties of the XMM-XXL north survey, which will be subject of the study of feedback processes impacting the narrow emission line region of AGN. We presented the underlying X-ray, optical and infrared imaging datasets of the XMM-XXL north survey. Furthermore, we introduced the target selection for the spectroscopic follow-up with *BOSS*. We obtained 3042 unique *BOSS* spectra and reached a spectroscopic completeness of 32 per cent for all X-ray selected point sources at $F_{0.5-10\text{keV}} > 1 \cdot 10^{-15} \text{ erg cm}^{-2} \text{ s}^{-1}$ and 78 per cent for all optical cross-matched sources with $17 < r < 22.5 \text{ mag}$. In order to increase the number of reliable spectra, we performed a visual inspection for the spectra with critical redshift estimates of the *BOSS* pipeline. We find that 85 per cent of the X-ray selected and *BOSS* observed targets have a reliable redshift identification after the visual inspection. Our classification of X-ray selected and optically followed-up spectra is based on the optical emission line features of the sources. The algorithm presented in this work classifies 2513 AGN and 87 stars. The majority of X-ray sources (70 per cent) are BLAGN1, within a redshift range of $0 < z < 5$ and luminosity range of $4 \cdot 10^{41} < L_{0.5-2\text{keV}} < 4 \cdot 10^{45} \text{ erg s}^{-1}$. The NLAGN2 (22 per cent) reside at $0 < z < 1$ and have luminosities of $1 \cdot 10^{40} < L_{0.5-2\text{keV}} < 2 \cdot 10^{44} \text{ erg s}^{-1}$. The elusive AGN (7 per cent) form an interesting group of objects, because despite the missing AGN features in the optical spectrum they have X-ray luminosities of $2 \cdot 10^{39} < L_{0.5-2\text{keV}} < 2 \cdot 10^{44} \text{ erg s}^{-1}$. For 2 per cent of all spectra with reliable redshift, the emission line information are not sufficient for a classification (e.g. due to large flux errors).

3. Study of optical emission line, optical colour, mid-IR colour and X-ray AGN selection techniques

3.1. Motivation

In order to study the properties of SMBH and their host galaxies, one should approach them by a preferably unbiased data set of AGN. The main limiting factor in AGN selection is the diversity of their spectral energy distributions (SED). As explained in Sec. 1.2, this depends on the presence of dust and gas clouds along the line-of-sight, the contrast between accretion-luminosity and stellar emission from the host galaxy, and the detailed physics of the accretion process itself. Many methods have been developed to account for these factors using different wavelength bands and both photometric as well as spectroscopic selection criteria, but they are always, by construction, subject to selection effects.

In this work, we decided to select our AGN dataset in X-ray, because this wavelength is expected to penetrate matter as well as gas, and is less affected by star formation processes. It therefore identifies accreting black holes which are either obscured, or heavily contaminated by stellar emission processes at optical and NIR wavelengths. Indeed, our classification work presented in the previous Chapter 2 clearly demonstrates that among X-ray selected AGN, we find a variety of objects with a quite diverse set of optical properties. But, we want to evaluate how X-ray selection of AGN compares with spectroscopic optical, photometric optical and mid-infrared colour selection and what characteristic properties the selected AGN have. Thus, we analyze in this Chapter the optical spectroscopic, optical and infrared colour properties of our sample of X-ray selected AGN in the XMM-XXL north.

3.2. Introduction

The accretion processes in SMBHs are highly complex and emit at different wavelengths. The presence of dust and gas, and the influence of stellar emission shape the SED in many different ways for each AGN. We now present characteristic features of the AGN SED and introduce selection criteria which are focussed on these properties.

In the optical/UV spectra of AGN, there is the characteristic ‘blue bump’ which is supposed to originate from a thermally radiating accretion disc. This feature allows AGN to be selected via their blue colours, and has been extensively used (see Boyle et al. 2000; Richards et al. 2009; Ross et al. 2012 and references therein). This selection has its limitations because the galaxy dilution as well as the optical obscuration suppress the blue bump. It is therefore only applied to optically point-like sources.

X-rays directly trace highly energetic processes occurring in the neighbourhood of the supermassive black hole (Brandt & Hasinger, 2005; Brandt & Alexander, 2015). Thus, X-ray selection is highly efficient and provides a clean separation from the host galaxies which typically emit at lower fluxes. However, the most heavily obscured, Compton-thick AGN are opaque even to X-rays.

In this case, infrared AGN selection methods, tracing the reprocessed nuclear emission, benefit from the clearly distinct SED shapes of AGN and galaxy components in this wavelength range. Therefore, infrared is able to detect heavily obscured AGN (Lacy et al., 2007; Stern et al., 2005, 2012; Assef et al., 2013; Messias et al., 2014), but is subject to severe host galaxy contamination (dust-obscured star formation).

A very well-known AGN selection criterion is the optical narrow emission line diagnostic (Baldwin et al., 1981; Ho et al., 1997; Kauffmann et al., 2003; Kewley et al., 2006; Lamareille, 2010). It uses the fact that ionizing radiation from the AGN is harder than that of stars, which has an effect on the measured emission line ratios. However, this method is claimed to suffer from (i) contamination from the host galaxy which can potentially swamp AGN signatures and (ii) the fact that the method selects a large fraction of Low Ionization Narrow Emission Region galaxies (LINERS) whose nature is still debated (e.g. Yan & Blanton 2012). Broad emission lines ($\text{FWHM} > 1000 \text{ km s}^{-1}$) are unique spectral features which identify optical unobscured AGN, where the observer has a direct view on the fast moving clouds close to the black hole. Purely broad line selected samples of AGN have been used for example in the VVDS and zCOSMOS surveys (e.g. Gavignaud et al. 2006; Trump et al. 2009). Unfortunately, these methods require cost-intensive observation and are typically limited to small areas.

Variability can be an additional parameter to select AGN. Short time-scale variations in the range of hours to Myr are less likely to happen in star formation and can be associated to nuclear processes (Ulrich et al., 1997; Hickox et al., 2014). These variabilities might be invoked by disk instabilities (Pereyra et al., 2006) or changes in the amount of accreting material Hopkins & Beacom (2006).

3.3. Outline

We firstly introduce the optical emission line selection of AGN, by referring to the broad emission line selection and the optical line diagnostics for narrow emission lines. We then present an optical selection method of AGN by referring to the XDQSO targeting algorithm, which has been used for baryonic oscillations studies with quasars in *BOSS*. In a next step, we apply this selection to the XMM-XXL north field to study the population of XDQSO-selected AGN, and determine the fraction of AGN with successful X-ray detections. Furthermore, we discuss the spectral properties of the XDQSO-selected AGN. The same procedure is repeated for the infrared selection of AGN. We hereby refer to *WISE* color criteria.

Finally, we compare optical, infrared and X-ray selection AGN criteria applied to the sources in the XMM-XXL north field and discuss similarities and differences of the selected AGN populations.

3.4. Optical: emission lines diagnostics

A large variety of AGN selections benefits from the optical emission lines in AGN. They include firstly the selection of Seyfert1/BLAGN1 based on broad emission lines, and secondly the selection of Seyfert2/NLAGN2 based on narrow line properties. A common selection of broad line emitters is performed by applying thresholds in the order of $> 1000 \text{ km s}^{-1}$ for the FWHM of e.g. $\text{H}\beta$, MgII , $[\text{CIII}]$, CIV (e.g. Hao et al. 2005). The star formation or AGN origin of narrow emission lines can be determined by common narrow line selection methods, such as presented by Baldwin et al. (1981); Kauffmann et al. (2003); Kewley et al. (2006); Lamareille et al. (2004); Lamareille (2010); Yan et al. (2011); Meléndez et al. (2014).

3.4.1. Spectroscopic properties of optical emission line selected AGN

In the following, we analyze the spectroscopic properties of 2513 X-ray selected AGN with reliable *BOSS* follow-up. According to the principles of the classification algorithm in 2.4.3, the bimodal distribution of the emission line FWHM allows for a separation into narrow line region (NLR) emitters and broad line region (BLR) emitters at a FWHM-threshold of $\text{FWHM} \sim 1000 \text{ km s}^{-1}$ for $\text{H}\beta$, MgII , $[\text{CIII}]$ and CIV . The major group (70 per cent) of X-ray selected objects in the XMM-XXL north with spectroscopy are the BLR emitters: BLAGN1. The group of NLR emitters includes objects whose emission originates either from AGN, the star forming region or both. We use the BPT-NII (Baldwin et al., 1981; Kauffmann et al., 2003; Kewley et al., 2006; Meléndez et al., 2014) and Blue-OII diagram (Lamareille et al., 2004; Lamareille, 2010) to determine the underlying excitation mechanism. Out of the X-ray sample with reliable spectroscopy, 11 per cent are excited by a central AGN and belong to the group of NLAGN2. Our data set comprises a group of equal size of NLAGN2 candidates (11 per cent) which do not have enough significant emission lines or lie at a redshift of $z > 1.08$ and cannot be projected in the BPT-NII and Blue-OII diagram. Their spectral stack as well as optical colours and morphology indicate that the majority of the sources are NLAGN2. Deeper exposed optical spectra or infrared spectra are needed to properly classify these objects.

We find, that 3 per cent of the reliable spectroscopy sample are classified as star forming galaxies (SFG) by the BPT-NII the Blue-OII diagram. Another 4 per cent comprises absorption line galaxies (ALG). In order to determine whether these objects really host an AGN we study their soft X-ray luminosities, see Fig. 2.14. We can assume that ALG have a maximal stellar mass of $\sim 1 \cdot 10^{12} M_{\odot}$, based on the massive *BOSS* LRG sample of Maraston et al. (2013). According to Gilfanov (2004), this corresponds to an X-ray luminosity of $L_{0.5-2\text{keV}} \leq 10^{41} \text{ erg s}^{-1}$ caused by low mass X-ray binaries in the galaxy. The soft X-ray luminosity of all 78 eAGN-ALG in our sample is above $10^{41} \text{ erg s}^{-1}$. Therefore, they can be considered as hosts of AGN and are not dominated by luminous massive X-ray binaries.

Focussing on the SFG population, their overall X-ray emission - apart from the nuclear AGN - consists of the collective emission from stellar remnants in a galaxy. The upper limit on the X-ray luminosity can be associated with the maximum of the total Star Formation Rate (Nandra et al., 2002; Ranalli et al., 2003; Grimm et al., 2003). Typically,

the value of $L_{0.5-2\text{keV}} \sim 10^{42} \text{ erg s}^{-1}$ is considered as a threshold above which only AGN should be mainly responsible for the observed emission. Our sample of eAGN-SFG consists of 49 objects above this luminosity limit and 29 objects below this luminosity limit, corresponding to a ratio of 0.59 ± 0.40 . Comparing the number fraction to securely classified NLAGN2 in the same redshift and luminosity range, we obtain 0.72 ± 0.18 . The consistency of both ratios might be an indication that the majority of our eAGN-SFG with $L_{0.5-2\text{keV}} < 10^{42} \text{ erg s}^{-1}$ in our sample really host a comparably weak AGN.

Summarizing, we find that the optical emission lines selections are fundamental to select BLAGN1 and NLAGN2. Anyhow, they are not able to perform selections in case of missing emission lines and low SN of the spectra. Due to the star formation or central obscuration, they also miss elusive AGN.

3.5. Optical: XDQSO targeting algorithm

For the optical selection of AGN, we refer to the XDQSO algorithm (Bovy et al., 2011), which is a probabilistic selection technique developed for the efficient QSO selection on the basis of broad band optical imaging and point-like morphology. It has been employed as a target selection method for the measurement of baryon acoustic features with quasars within the *eBOSS* programme (Myers et al., 2015). The selection is limited to optically point-like objects (`TYPE` = 6), with a dereddened *i*-band magnitude of $17.75 < i < 22.45$ mag and at least one primary detection with $u_{\text{psf}} < 22.5$ mag, $g_{\text{psf}} < 22.5$ mag, $r_{\text{psf}} < 22.5$ mag, $i_{\text{psf}} < 22.0$ mag or $z_{\text{psf}} < 21.5$ mag. We only choose sources with a good *BOSS* quasar targeting flag (`GOOD` = 0, Bovy et al. 2011) excluding the photometric blending, moving sources and interpolation effects. The algorithm uses the density estimation in flux space and assigns probabilities $P(\text{QSO}, z)$ of any *SDSS* point source to be a QSO in dedicated redshift ranges. In this work, we refer to the quasar probability $P_{\text{sum}}(\text{QSO})$ as the sum of the low-redshift ($z < 2.2$), mid-redshift ($2.2 \leq z \leq 3.5$) and high-redshift ($z > 3.5$) probabilities. As a threshold for the AGN selection, we define the arbitrary probability of $P_{\text{sum}}(\text{QSO}) > 0.5$. The algorithm has been trained using a star sample from *SDSS* Stripe 82 and a quasar sample from the *SDSS* DR7 Quasar catalogue.

3.5.1. X-ray detection fraction

In the 18 deg^2 coverage area of *XMM-Newton* in the XMM-XXL north, the XDQSO catalogue contains 49 172 sources with assigned $P(\text{QSO}, z)$ and `GOOD` = 0. There are 1617 XDQSO sources which can be associated to the *XMM-SDSS* catalogue ($\text{LR}_{\text{XMM}, \text{SDSS}} > 1.5$). Considering a QSO probability of $P_{\text{sum}}(\text{QSO}) > 0.5$, the entire XMM-XXL north comprises 2408 XDQSO sources out of which 1159 are also X-ray selected.

In Fig. 3.1, we show the detection fraction of X-ray selected XDQSO sources. We define the number density $N_{\text{XDQSO}, \text{X}}$ of X-ray selected XDQSO sources and the number density N_{XDQSO} of all XDQSO selected sources in the XMM-XXL. The ratio R of the cumulative number densities (hereby X-ray detection fraction) is:

$$R = \frac{N_{\text{XDQSO}, \text{X}}^{\text{cum}}(r, F_X, P_{\text{sum}}(\text{QSO}))}{N_{\text{XDQSO}}^{\text{cum}}(r, P_{\text{sum}}(\text{QSO}))}.$$

and depends on the optical magnitude r , the X-ray flux F_X and the QSO probability $P_{\text{sum}}(\text{QSO})$, as shown in Fig. 3.1. We chose the *r*-band magnitude to account for the magnitude threshold of the *BOSS* observed sources. The individual QSO probabilities of the XDQSO sources are normalized and the sum of individual probabilities corresponds to the expected number of true QSO. For the group of 2408 XDQSO sources with $P_{\text{sum}}(\text{QSO}) > 0.5$ in the XMM-XXL, we derive an averaged reliability of 86 per cent. The fractions in Fig. 3.1 are not corrected for such estimated reliability.

Assuming $P_{\text{sum}}(\text{QSO}) > 0.5$ and $F_{0.5-10\text{keV}} > 1 \cdot 10^{-15} \text{ erg cm}^{-2} \text{ s}^{-1}$, ~ 48 per cent of all XDQSO selected sources will be picked up in X-ray at faint optical magnitudes ($r \leq 22.5$ mag) and up to ~ 72 per cent at bright *r* magnitudes ($r \leq 18.5$ mag).

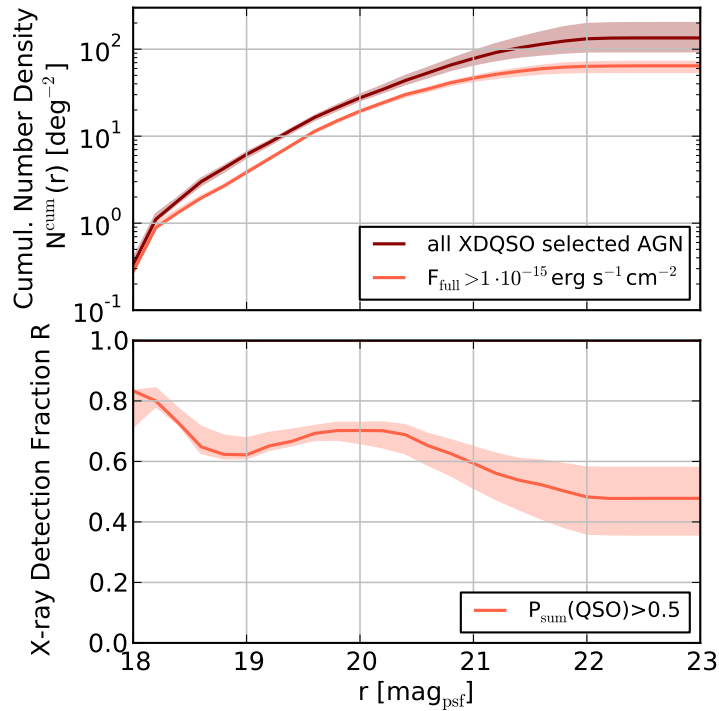


Figure 3.1.: Top Panel: Cumulative number density of all XDQSO selected AGN and of XDQSO AGN with X-ray counterparts in the XMM-XXL north field. We apply the optical selection threshold of $P_{\text{sum}}(\text{QSO}) > 0.5$ (central line) and $P_{\text{sum}}(\text{QSO}) > 0.8$ (lower border) as well as > 0.2 (upper border). Bottom Panel: X-ray detection fraction of XDQSO selected AGN. We divide the number of X-ray detected AGN with $P_{\text{sum}}(\text{QSO}) > 0.5$ over all XDQSO sources with $P_{\text{sum}}(\text{QSO}) > 0.5$ in the XMM-XXL north.

3.5.2. Morphological and spectroscopic properties of XDQSO-selected AGN

In the following section, we analyze the XDQSO properties of the X-ray sources with *BOSS* follow-up: 1203 XDQSO sources have reliable *BOSS* spectra, out of which 902 have $P_{\text{sum}}(\text{QSO}) > 0.5$. As shown in Table 3.1, these objects only comprise optically point-like objects and are dominated by BLAGN1. Only few are classified as NLAGN2cand, NLAGN2 and eAGN. There are 196 point-like BLAGN1 which are not XDQSO selected due to their photometric properties ($\text{GOOD} > 0$). 27 of them are too faint or bright for the initial magnitude thresholds of the XDQSO selection ($17.75 < i_{\text{dered}} < 22.45$ mag). By construction, the selection misses all optically extended objects.

In Fig. 3.2, we perform spectral stacks of X-ray selected XDQSO sources with different QSO probabilities and soft X-ray luminosities. We chose the redshift range of $0 < z < 2$ which covers a representative sample of the entire population. The stack includes the four following groups of X-ray and XDQSO selected targets:

- a) $P_{\text{sum}}(\text{QSO}) > 0.5$, $L_{0.5-2\text{keV}} > 1 \cdot 10^{44}$ erg s $^{-1}$ ($n = 381$),
- b) $P_{\text{sum}}(\text{QSO}) > 0.5$, $L_{0.5-2\text{keV}} < 1 \cdot 10^{44}$ erg s $^{-1}$ ($n = 310$),

Table 3.1.: XDQSO properties (Bovy et al., 2011) of X-ray selected AGN with spectroscopic information: We split the data set of X-ray selected AGN with reliable *BOSS* follow-up into the different classes and optical morphology. We indicate number of XDQSO detection for each population.

spectroscopic classification	optical morphology	$P_{\text{sum}}(\text{QSO})$		
		no	> 0	> 0.5
BLAGN1 (n=1353)	point-like	196	1157	889
BLAGN1 (n=434)	extended	434	-	-
NLAGN2 (n=7)	point-like	1	6	1
NLAGN2 (n=266)	extended	266	-	-
NLAGN2cand (n=32)	point-like	16	16	3
NLAGN2cand (n=252)	extended	252	-	-
eAGN (n=5)	point-like	0	5	0
eAGN (n=166)	extended	166	-	-
not classified (n=57)	pl/ex	38	19	9
total	-	1369	1203	902

c) $P_{\text{sum}}(\text{QSO}) < 0.5$, $L_{0.5-2\text{keV}} > 1 \cdot 10^{44} \text{ erg s}^{-1}$ ($n = 70$),

d) $P_{\text{sum}}(\text{QSO}) < 0.5$, $L_{0.5-2\text{keV}} < 1 \cdot 10^{44} \text{ erg s}^{-1}$ ($n = 134$).

The groups of high optical QSO probability spectra from a) and b) show clear broad line features. The low QSO probability spectra from c) and d) have a less steep power law and a more prominent galaxy contamination at redder wavelengths. Apparently, a more dominant host galaxy continuum affects the optical colour properties of the AGN which leads to a lower QSO probability. The X-ray luminosity for the same QSO probability range has only a very weak impact on the red part of the spectrum, because the host contribution mostly affects $P_{\text{sum}}(\text{QSO})$.

Summarizing, in the XMM-XXL, 48 per cent of the XDQSO selected AGN ($P_{\text{sum}}(\text{QSO}) > 0.5$) are also X-ray selected and 13 per cent of all X-ray sources have XDQSO counterparts. In order to perform a full comparison of both AGN selections, we are missing a representative spectroscopic sample for only XDQSO selected objects without X-ray detection. But we confirm that the XDQSO targeting algorithm selects optically point-like BLAGN1 showing an unobscured and blue optical spectrum with only weak host galaxy contribution.

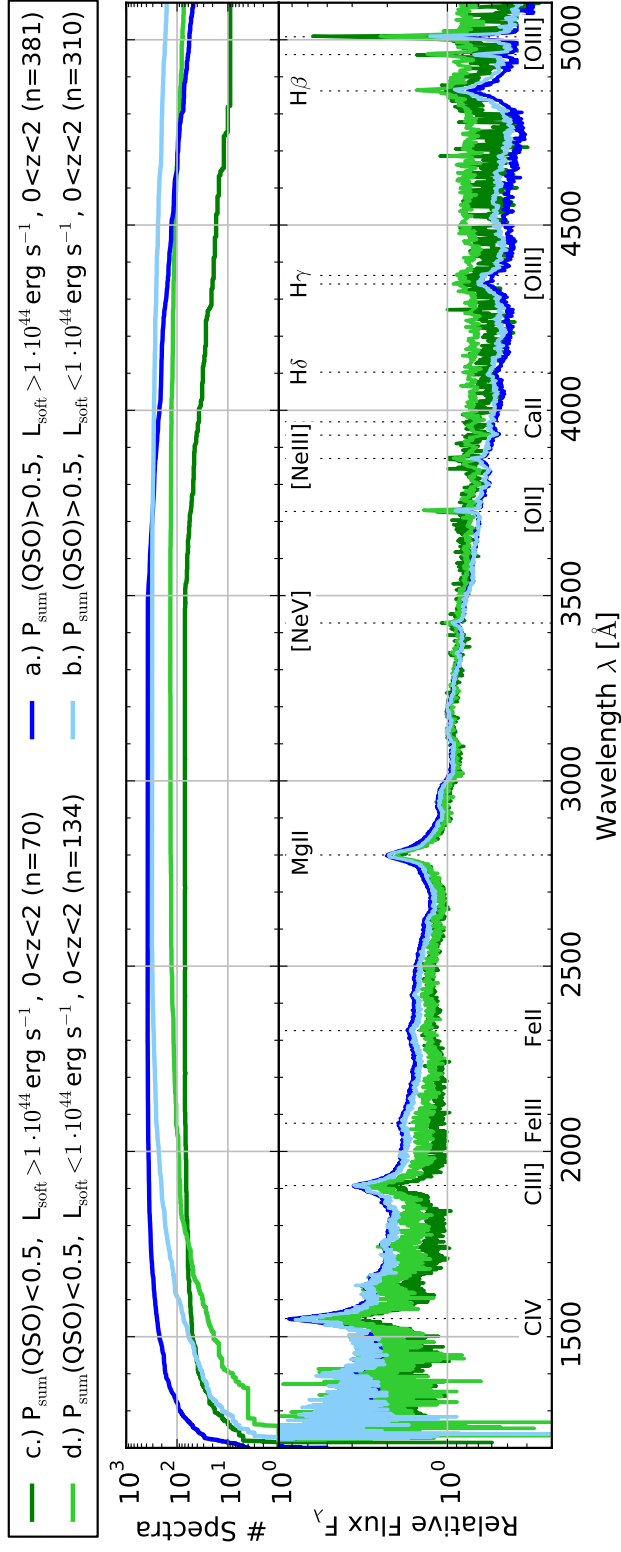


Figure 3.2.: Median spectral stack and number of contributing spectra for optically point-like objects with (a) high soft X-ray luminosity and $P(\text{QSO}) > 0.5$, (b) low soft X-ray luminosity and $P(\text{QSO}) > 0.5$, (c) high soft X-ray luminosity and $P(\text{QSO}) < 0.5$, (d) low soft X-ray luminosity and $P(\text{QSO}) < 0.5$. The spectra have a redshift of $0.0 < z < 2.0$ and are normalized to $\lambda = 3200 \text{ \AA}$.

3.6. Infrared: *WISE* colour selection

The mid-infrared AGN selection benefits from the different spectral energy distributions (SED) of AGN and galaxies in the *WISE* colour range: AGN show a steep power law-shaped spectrum and galaxies have a black body spectrum (see Section 1.2). This translates into a well-defined IR colour difference between the two classes, provided the nuclear AGN emission is the dominant component at these wavelengths. First, we evaluate the colour cut of Stern et al. (2012) using the two most sensitive *WISE* bands *W1* [$3.4\ \mu\text{m}$] and *W2* [$4.6\ \mu\text{m}$]:

$$W1 - W2 > 0.8 \text{ for } W2 \leq 15.05 \text{ mag} \quad (3.1)$$

The *W2* magnitude limit corresponds to $w2snr \geq 10$. This threshold is established from a well studied AGN-sample in COSMOS. Taking the *Spitzer* selected AGN sample of Stern et al. (2005) as a truth sample, the Stern et al. (2012) *WISE* selection is 78 per cent complete and 95 per cent reliable. Secondly, we consider the AGN selection criteria of Assef et al. (2013):

$$W1 - W2 > \begin{cases} 0.662 \cdot e^{(0.232 \cdot (W2 - 13.97)^2)} \\ \quad \text{for } 13.97 \leq W2 \leq 17.11 \text{ mag} \\ 0.662 \text{ for } W2 < 13.97 \text{ mag} \end{cases} \quad (3.2)$$

The *W2* -threshold corresponds to $w2snr \geq 3$. The selection is established with a truth sample of UV and mid-IR photometry selected AGN from the deeper NOAO Deep Wide-Field Survey Boötes field and has a reliability of 90 per cent.

3.6.1. X-ray detection fraction

In the $18\ \text{deg}^2$ area of the XMM-XXL are 321 325 *WISE* sources and 4811 of them can be matched as counterparts to the X-ray selected AGN considering $LR_{\text{XMM},\text{WISE}} > 0.5$ with good photometry. In Fig. 3.3, we compare both infrared AGN selection criteria from Stern et al. (2012) and Assef et al. (2013), and the X-ray selection for AGN in the XMM-XXL north. The Stern et al. (2012) criterion selects 1063 infrared sources, containing 585 sources which are counterparts for the X-ray selected AGN. The Assef et al. (2013) criterion selects 2109 infrared sources, including 930 X-ray selected sources. We define the number density $N_{\text{WISE},\text{X}}$ for X-ray selected *WISE* AGN at different soft X-ray flux limits, and the number density N_{WISE} for all *WISE* selected AGN (Stern et al., 2012; Assef et al., 2013) in the XMM-XXL north. The ratio R of the cumulative number densities (hereby X-ray detection fraction) is:

$$R = \frac{N_{W2,\text{X},\text{WISE}}^{\text{cum}}(W2, F_X)}{N_{\text{WISE}}^{\text{cum}}(W2)}.$$

and depends on the infrared magnitude *W2* as well as the X-ray flux F_X , as shown in Fig. 3.3. The datasets used for the calibration of the selection criteria in COSMOS and Boötes have different depths than the XMM-XXL. Therefore, we cannot guarantee a similar reliability (by construction, typically around 90 per cent) and do not correct the AGN detection fractions.

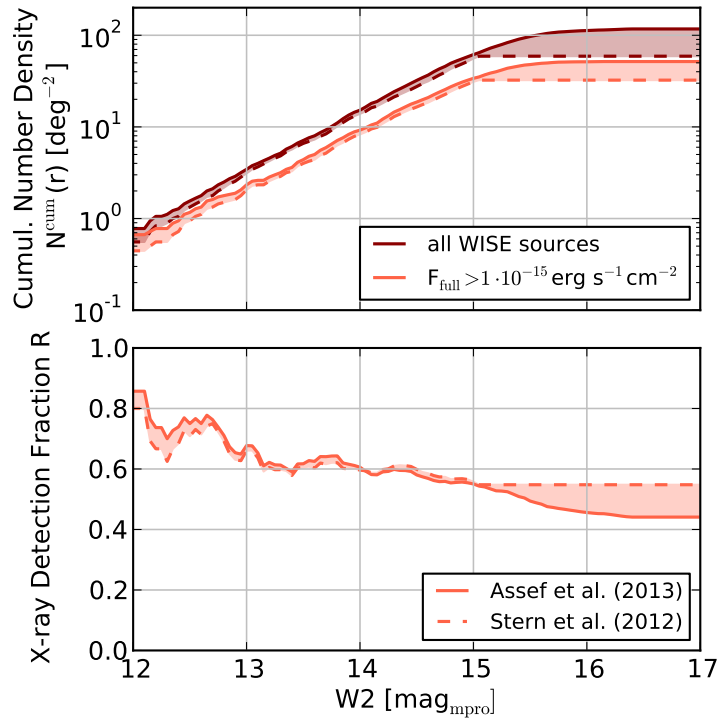


Figure 3.3.: Top Panel: Cumulative number density of infrared selected AGN and of those with X-ray counterpart in the XMM-XXL north. We apply the infrared selection threshold of Stern et al. (2012) and Assef et al. (2013). Bottom Panel: X-ray detection fraction of infrared selected AGN: We divide the number of X-ray detected *WISE* AGN by all *WISE* selected AGN in the XMM-XXL north.

In Fig. 3.3, the Stern et al. (2012) (dashed line) and the Assef et al. (2013) (solid lines) selections do not differ much in their number densities up to $W2 \leq 15$ mag. At fainter magnitude, the Assef threshold allows the selection of further AGN. Assuming a soft X-ray flux of $F_{0.5-10\text{keV}} > 1 \cdot 10^{-15} \text{ erg cm}^{-2} \text{ s}^{-1}$ and the faint $W2$ limit of the *WISE* selections, ~ 44 per cent ($W2 \leq 17$ mag) of all Assef and ~ 56 per cent ($W2 \leq 15$ mag) of all Stern selected AGN are detected in X-ray, too. For brighter magnitudes ($W2 \leq 13$ mag), the fraction increases up to ~ 67 per cent for the Assef and Stern selection.

3.6.2. Infrared and spectroscopic properties of *WISE* selected AGN

The overall population of X-ray sources with infrared counterpart comprises 4811 sources, out of which 2117 also have reliable *BOSS* classifications. In the top panels of Fig. 3.4, we plot these sources in the $W1 - W2$ colour and $W2 - W3$ colour diagram and compare the source locations with characteristic source regions from Wright et al. (2010). The classifications of our *BOSS* sources are consistent: the BLAGN1 mainly reside in the QSO and Seyfert area, the NLAGN2 extend from the spiral region in the Seyfert region. The eAGN-SFG live in the starburst region extending to the Seyfert region. The eAGN-ALG are in the spiral region, which might be caused by the contribution of the AGN emission

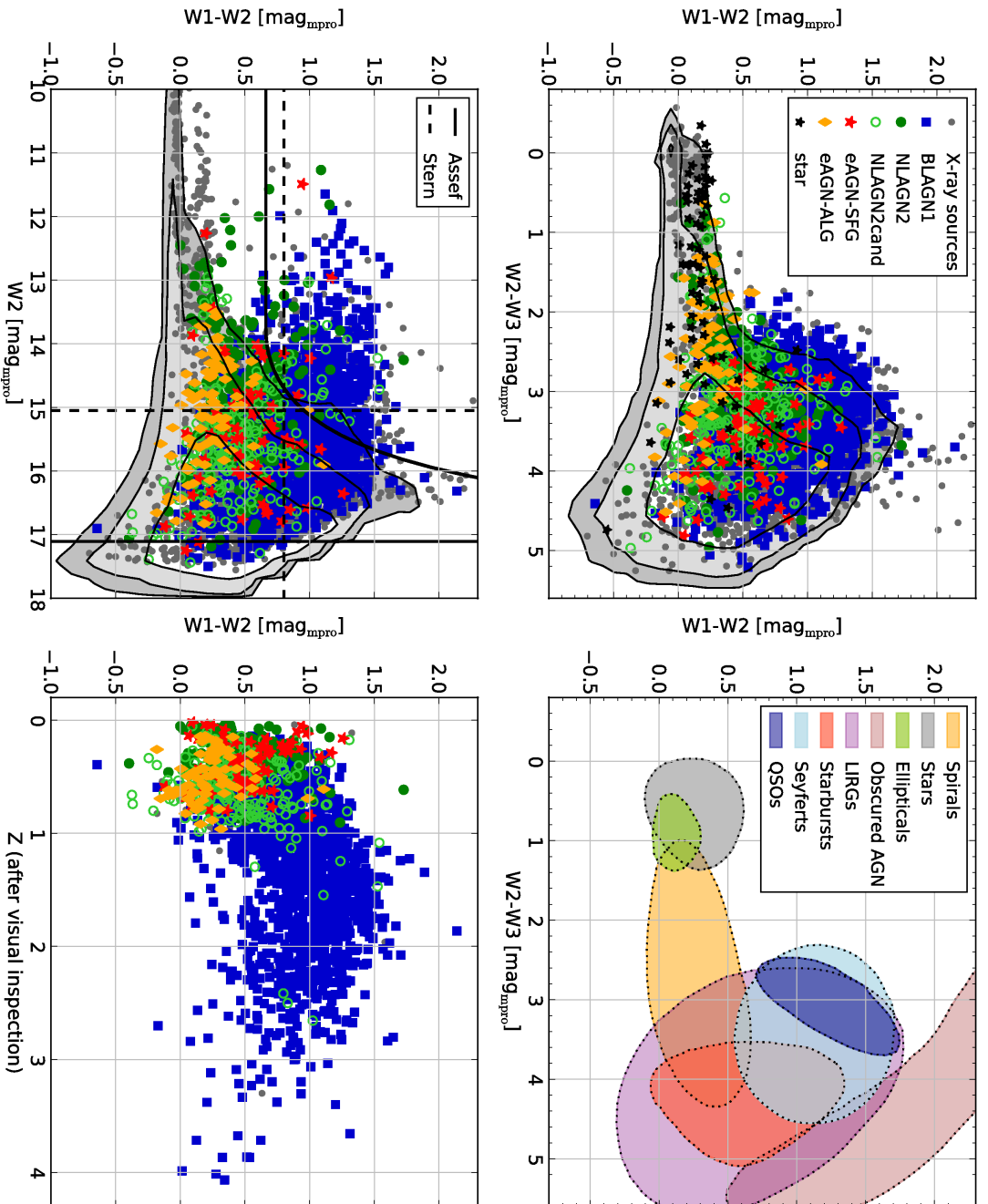


Figure 3.4.: Top Panels: *WISE* colour diagram: In the left panel, we plot the 68, 95 and 99 per cent contours of all *WISE* sources, the classified *BOSS* spectra (coloured) and the unclassified X-ray sources (black) in the XMM-XXL north. In the right panel, we plot the contours of all *WISE* sources and over plot the classified *BOSS* spectra and unclassified X-ray sources. The solid line and the dashed horizontal line mark the infrared AGN selection from Assef et al. (2013) and Stern et al. (2012), respectively. The vertical lines indicate the lower magnitude limits for this two selections. Bottom Left Panel: *WISE* colour magnitude diagram and AGN selections: We plot the contours of all *WISE* sources and over plot the classified *BOSS* spectra and unclassified X-ray sources. The solid line and the dashed lines with *WISE* counterpart.

in the *W2* and *W3* band. The stars selected via X-rays fall into the common *WISE* star region but also spread beyond.

In the bottom left panel of Fig. 3.4, we indicate the *WISE* selections from Stern et al. (2012) and Assef et al. (2013) in the *W1* – *W2* colour and *W2* magnitude diagram. The plot comprises the density contours of all *WISE* sources in the XMM-XXL north area and we overplot the X-ray sources with *WISE* counterparts and the *BOSS* observed spectra. The Stern et al. (2012) criterion selects 390 *BOSS* observed X-ray sources and the Assef et al. (2013) criterion selects 585 targets. The number statistics and classifications of the *WISE* and X-ray selected sources are listed in Table 3.2. The selected sources mainly consist of BLAGN1 (89 per cent for both selections), NLAGN2/NLAGN2cand and few eAGN. The lower right panel demonstrates the *W1* – *W2* colour and redshift dependency of X-ray selected Assef et al. (2013) AGN with spectroscopic information. Both selections are limited to a redshift range of $z < 3$ due to the overall SED shape of AGN in the infrared restframe (see Stern et al. 2012).

Table 3.2.: *WISE* properties (Stern et al., 2012; Assef et al., 2013) of X-ray selected AGN with spectroscopic information: We split the data set of X-ray selected AGN with reliable *BOSS* follow-up into different classes and indicate the number of X-ray selected AGN as well as X-ray selected *WISE* AGN for each population.

spectroscopic classification	X-ray selection	X-ray & Stern et al.	X-ray & Assef et al.
BLAGN1	1787	347	520
NLAGN2	271	17	29
NLAGN2cand	284	17	23
eAGN	171	5	6
not classified	57	4	7
total	2570	390	585

In Fig. 3.5, we show the spectral stacks of X-ray selected Assef et al. (2013) AGN at different luminosities in the redshift range $0 < z < 2$. We chose the average luminosity of $L_{0.5-2\text{keV}} = 1 \cdot 10^{44} \text{ erg s}^{-1}$ as a threshold for the high and low luminosity populations. This redshift range comprises a representative population from the BLAGN1 and both NLAGN2 and eAGN classes. The four groups of X-ray selected spectra are:

- a.) Assef selected: $L_{0.5-2\text{keV}} > 1 \cdot 10^{44} \text{ erg s}^{-1}$ ($n = 266$),
- b.) Assef selected: $L_{0.5-2\text{keV}} < 1 \cdot 10^{44} \text{ erg s}^{-1}$ ($n = 251$),
- c.) not Assef selected: $L_{0.5-2\text{keV}} > 1 \cdot 10^{44} \text{ erg s}^{-1}$ ($n = 249$),
- d.) not Assef selected: $L_{0.5-2\text{keV}} < 1 \cdot 10^{44} \text{ erg s}^{-1}$ ($n = 1010$).

The high luminosity X-ray and Assef et al. (2013) selected spectra from a.) comprise only BLAGN1 which show clear broad line features and nearly no host galaxy contribution. The stack of low luminosity sources from b.) shows emission lines which are less broad and a redder continuum indicating host galaxy contribution from NLAGN2 and host galaxy

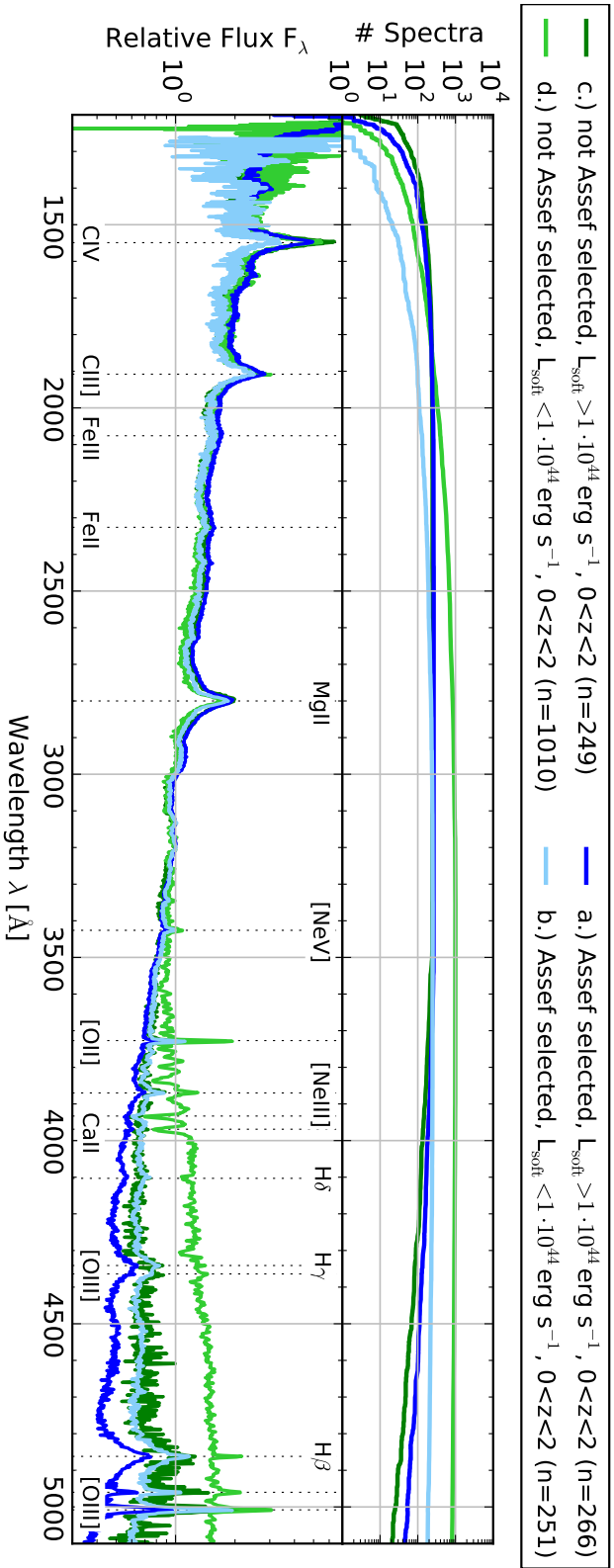


Figure 3.5.: Median spectral stack and number of contributing spectra for Assef et al. (2013) selected sources with a.) high soft X-ray luminosity and b.) low X-ray luminosity, and not Assef et al. (2013) selected AGN with c.) high soft X-ray luminosity and d.) low X-ray luminosity. The spectra have a redshift of $0.0 < z < 2.0$ and are normalized to $\lambda = 3200 \text{ Å}$.

dominated BLAGN1. The stacks from c.) and d.) are X-ray sources not selected by Assef et al. (2013). They show stronger host galaxy contribution than the Assef et al. (2013) selected sources in the same luminosity range. The stack from d.) includes the large majority of host dominated AGN.

Summarizing, 44 per cent of the Assef et al. (2013) selected AGN are also selected by X-ray and 11 per cent of all X-ray selected AGN are also infrared AGN. Our comparison of X-ray selection criteria with Assef et al. (2013) and Stern et al. (2012) is biased because the spectroscopic sample does not comprise only infrared selected AGN and is limited in the r -band. But applying the two infrared AGN selection criteria to our X-ray selected sample, they access a population of AGN with very weak host contribution and red $W1 - W2$ colours. This group includes mainly BLAGN1 and few NLAGN2 in the redshift range of $0 < z < 3$ and has a large luminosity range of $4 \cdot 10^{40} < L_{0.5-2\text{keV}} < 2 \cdot 10^{45} \text{ erg s}^{-1}$.

3.7. Summary: Uniqueness of X-ray AGN selection

Considering current and future large area surveys in different wavelength bands, the number of observable AGN populations is going to increase dramatically. Many studies underline the strong impact of selections on the characteristic features of AGN. In this work, we have access to a very large area of 18 deg², covered by multi-wavelength data, allowing for comparison of four AGN selection criteria in X-ray, optical and infrared, with high statistic reliability. We find interesting trends regarding the optical morphology, the X-ray luminosity, the redshift, and host galaxy contribution.

3.7.1. Optical emission line diagnostics

The emission line selections (Meléndez et al., 2014; Lamareille, 2010) have been fundamental to perform the classification for 98 per cent of our spectroscopic dataset in the XMM-XXL north and define the groups of BLAGN1 (70 per cent) and NLAGN2 (22 per cent). However, a minor fraction of the X-ray sample is associated to star formation galaxies (3 per cent) or absorption line galaxies (4 per cent) according to the narrow emission line properties. This group of elusive AGN does not stand out in their cross-matching properties compared to the entire population. The fraction of elusive AGN in our dataset is comparable to the COSMOS sample (Brusa et al. 2010, 4 per cent, considering $L_{0.5-2\text{keV}} > 10^{42} \text{ erg s}^{-1}$). In the AEGIS sample ($10^{40} < L_{0.5-2\text{keV}} < 10^{43} \text{ erg s}^{-1}$), Yan et al. (2011) find a larger fraction: 19 per cent of the 146 *Chandra* sources have optical star formation properties and 22 per cent are missing [OIII] or H β emissions for determinations. Elusive AGN have been referred to as optically ‘dull’ AGN or XBONGS (X-ray bright and optically normal galaxies) by Comastri et al. (2002); Maiolino et al. (2003); Caccianiga et al. (2007); Trump et al. (2009); Pons & Watson (2014). The absence of AGN signatures in their optical spectra is still a matter of debate. According to Georgantopoulos & Georgakakis (2005), it is caused by dilution effects of a strong host galaxy component. Comastri et al. (2002) argues for a strong obscuration of the nuclear source preventing optical AGN emission. Yuan & Narayan (2004) suggest that the XBONGS have a truncated disc close to the black hole causing the absence of the characteristic AGN emission lines. Extreme obscuration of the NLR by AGN-fueling dusty spirals (Kraemer et al., 2011), or AGN flickering effects (Schawinski et al., 2015) have also been suggested. Based on their soft X-ray luminosity, we can confirm that the eAGN-ALG host an AGN. The group of eAGN-SFG partly falls below the upper luminosity threshold of SFG ($L_{0.5-2\text{keV}} = 1 \cdot 10^{42} \text{ erg s}^{-1}$), but the number fraction is consistent with NLAGN2 in the same redshift and luminosity range. Liu et al. (2015, submitted) analyze the X-ray properties of the elusive AGN. 75 per cent of them have $N_H < 21.5 \text{ cm}^{-2}$ indicating the presence of a low luminosity type 1 AGN, whose optical emission is probably fully dominated by stellar emission processes (Davies et al., 2015).

Narrow Line Seyfert 1 (NLSey1) also form a part of our X-ray selected AGN sample. As shown by e.g. Osterbrock & Pogge (1985); Boller et al. (1996), this population of optically unobscured AGN typically has FWHM for H β in the range of $500 < \text{FWHM}_{\text{H}\beta} < 1500 \text{ km s}^{-1}$, very steep X-ray spectra, strong optical FeII emission, and strong variability. The NLSey1 contribute to our BLAGN1 group, but probably also affect narrow emission

line objects with $\text{FWHM}_{\text{H}\beta} < 1000 \text{ km s}^{-1}$. Castelló-Mor et al. (2012) find that NLSey1 are classified as SFG by the optical line diagnostic diagram due to their smaller H β EW. The NLAGN2 of our dataset are securely identified as AGN because of their projection in the AGN region of the optical line diagnostic diagrams, but the group of NLAGN2cand and eAGN-SFG could potentially be contaminated by NLSey1. According to Castelló-Mor et al. (2012), the NLSey1 which are projected in the SFG region have high X-ray luminosities $L_{2-10 \text{ keV}} > 10^{42} \text{ erg s}^{-1}$ and large X-ray to optical flux ratios ($\log F_{\text{X}}/F_{\text{opt}} > 0.1$). This applies to a subset of our eAGN-SFG as shown in Fig. 2.10. From the stack of the NLAGN2 and eAGN-ALG, however, we see that the majority of contributing spectra have very strong host galaxy continua (see bottom panel of Fig. 2.14). This indicates that our classification procedure for objects with $\text{FWHM}_{\text{H}\beta} < 1000 \text{ km s}^{-1}$ mainly selects optically obscured AGN and is only weakly affected by NLSey1. A dedicated study of the NLSey1 contribution in our sample would require further FeII complex and X-ray spectral analysis.

In comparison to the X-ray selection, the optical emission line selection is less affected by obscuring material around the nuclei, because the narrow emission lines arise at larger scales. However, the detection of AGN excited emission lines requires good SN ratio spectra and can be easily outshined by strong star formation. The X-ray selection accesses the population of elusive AGN, which will not have been targeted by optical line diagnostics otherwise.

3.7.2. Photometric AGN selection methods

In Fig. 3.6, we illustrate the relative sizes of the differently selected AGN samples and their reliability fractions in the XMM-XXL. The *WISE* and *SDSS* catalogues have been matched via their source positions to be within a distance of 1 arcsec. The associated X-ray sources belong to the Likelihood-Ratio match catalogue from Section 2.2.4.

Considering the limiting fluxes of *SDSS*, *WISE*, and *XMM-Newton* in the XMM-XXL north, the combination of all AGN selection criteria picks up about 600 AGN deg^{-2} . Their common subgroup includes only ~ 23 AGN deg^{-2} out of which 99 per cent are optically point-like BLAGN1 with very weak host galaxy components. Applying a less conservative limit for the positional distance between *SDSS* and *WISE* sources, the number of objects in the common subgroup with *XMM-Newton* increases from 415 (1 arcsec), to 430 (2 arcsec) and finally 434 (~ 8.5 arcsec). The total intersection of only *SDSS* and *WISE* comprises 596 sources for 1 arcsec and 623 sources for 2 arcsec.

Each of the three AGN selection methods also retrieves an exclusive population of AGN. At the full depth of $F_{0.5-10 \text{ keV}} > 1 \cdot 10^{-15} \text{ erg cm}^{-2} \text{ s}^{-1}$, ~ 380 AGN deg^{-2} are only selected in X-rays, corresponding to 80 per cent of the total X-ray selection. XDQSO and infrared selections have both access to nearly ~ 60 exclusive AGN deg^{-2} each, which corresponds to ~ 50 per cent of their full selections.

The last two selections preferentially pick up AGN which are outshining their hosts at high optical or infrared luminosities, respectively (Bahcall et al., 1997). The XDQSO selection (Bovy et al., 2011) is trained for typical optically point-like *BOSS*-QSO and is

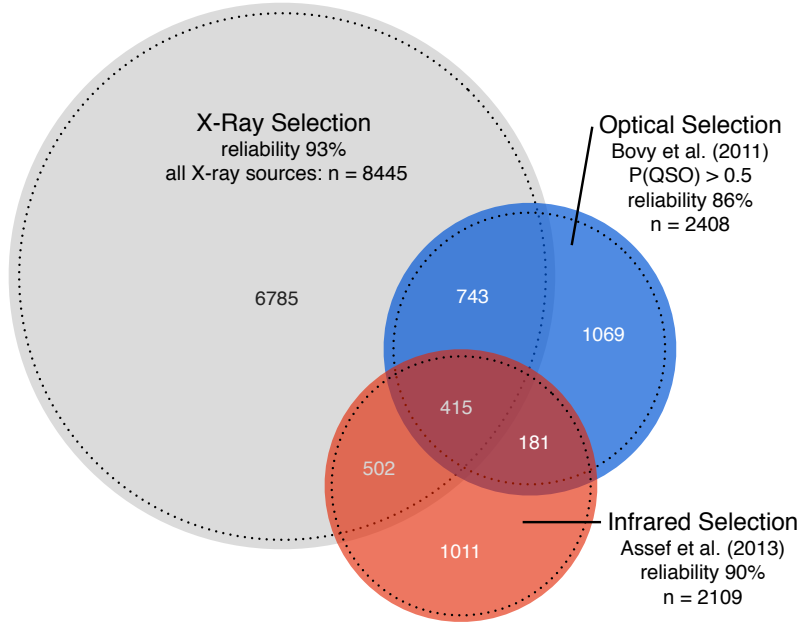


Figure 3.6.: Venn diagram of X-ray, optical (XDQSO) and infrared (Assef et al., 2013) AGN selections in the XMM-XXL north: We indicate the reliable fraction (dashed line) and number of AGN in each intersection. The numbers correspond to a positional match between *SDSS* and *WISE* of 1 arcsec.

highly sensitive within the available depth of optical *SDSS* data. This is crucial e.g. to reach a high number of QSO in the baryonic oscillations programme of *eBOSS* (Dawson et al., 2013). Our spectroscopic sample does not include *BOSS* spectra that are exclusively XDQSO selected, but these sources are most likely to be optically point-like low X-ray luminosity BLAGN1. The infrared selection from Assef et al. (2013) is limited to the redshift range of $z < 3$ and the majority of selected sources are classified as BLAGN1 having red $W1 - W2$ colours. The exclusively infrared selected AGN are expected to be low X-ray luminosity AGN (both BLAGN1 and NLAGN2) with a weak host galaxy contribution, or heavily obscured AGN (both BLAGN1 and NLAGN2).

Our study confirms that X-rays are less sensitive to dilution effects in the host galaxy, optical morphology, obscuring material, and star formation, as firstly shown by Nandra et al. (2007) and Bundy et al. (2008). In our sample, they pick up a broad variety of AGN, such as typical QSO, optically unobscured AGN with strong host galaxies, optically obscured AGN, and elusive AGN in a large luminosity and redshift range. Because of the r-band magnitude limits for the optical spectroscopy, we had access to, our sample is biased against optically faint sources, which mainly affects optically obscured NLAGN2 at higher redshift.

Based on our results, we expect that the selection method has a strong effect on statistical properties such as clustering and dark halo mass of AGN populations. As also shown by Merloni et al. (2015), at any given AGN luminosity, X-rays select systems accreting at lower Eddington rates λ . These objects reside in more massive hosts with lower

contrast of host galaxy to nuclear emission, and are missed by any other selection method. This is in line with the study of Mendez et al. (2015) focussing on the clustering properties of X-ray, radio, and infrared selected AGN from the *PRIMUS* and *DEEP2* surveys. The authors find that X-ray selected AGN cluster more than infrared galaxies and reside in more massive dark matter halos. This is not the case if the stellar mass, specific star formation rate, and redshift distributions of the selected galaxies are matched to the same control sample.

3.8. Conclusion

In this Chapter, we compared the X-ray AGN selection, which has been applied to the sources in the XMM-XXL north, to common AGN selections using optical (Bovy et al., 2011), and infrared colours (Stern et al., 2012; Assef et al., 2013). This enabled us to study the imposed selection effects on AGN and evaluate the AGN population probed by X-ray data.

The conclusions of our work are:

- (i) The bimodal FWHM-distribution of optical AGN-induced emission lines widths (e.g. $H\beta$ and $MgII$) clearly separates the population of X-ray selected AGN into broad line region emitters and narrow line region emitters. The minimum of the FWHM-distribution is at $FWHM \sim 1000$ km/s. The former emitters allow for a direct view into the central part of the accretion flow and of the broad line region, while the latter are mostly affected by the obscuration along the line of sight or dominated by the stellar emission of the host.
- (ii) The X-ray selection probes a wide variety of AGN with respect to the obscuring material along the line of sight and the contribution of the passive or active host galaxy. It allows to detect particular and peculiar classes, such as optically unobscured BLAGN1 with strong host galaxy contribution, optically obscured NLAGN2, and optically elusive AGN. Because of the r -band magnitude limits for the optical spectroscopy, we had access to, our sample is biased against optically faint sources, which mainly affects optically obscured NLAGN2 at higher redshift.
- (iii) Applied to our X-ray selected sample, we find that the optical AGN selection via the XDQSO targeting algorithm (Bovy et al., 2011) is, by construction, biased towards optically point-like sources and selects BLAGN1 with weak host features over the entire redshift range of the sample. The *WISE* colour AGN selections from Assef et al. (2013) and Stern et al. (2012) preferentially select BLAGN1 at $z < 3$ with weak hosts and red $W1 - W2$ colours. Optical emission line diagnostics are less affected by central obscuring material, but are biased against elusive AGN inside star forming galaxies or absorption line galaxies.

4. Kinematic properties of narrow line regions in X-ray selected AGN

4.1. Motivation

Feedback has been suggested to be an important process for the galaxy evolution and it is observed to take many different kinds of forms. So far, we cannot estimate which of these feedback forms are energetically important and it is necessary to investigate them all. Because AGNs are one of the most energetic sources in the host galaxy, they are very likely agents for AGN-driven outflows. These outflows can take many forms, such as radio jets, neutral, molecular, ionized outflows, X-ray warm absorbers and ultra-fast outflows. If these winds reach kiloparsec scale, the NLR should be able to trace this outflows. We need to look at the energetics of these outflows to evaluate the importance, and we have to study how the outflows interact with their environment in order to understand how the outflows affects the host. From local studies, [OIII] emission of AGN is often found in the form of ionized outflow cones and reaching velocities of a few 100 km s^{-1} . These winds might be candidates to interact with the host and are agents of feedback.

The spectroscopic X-ray selected sample in the XMM-XXL provides a sample of AGN host galaxies with redshifts up to $z = 1$, allowing to derive [OIII] emission line profiles to look for evidences of outflow. In addition, we can investigate the implication of [OIII] profiles for AGN 'unification' model and in particular for orientation-dependent unification schemes.

4.2. Introduction

In the past two decades, many observations have provided striking evidence for a link between evolutionary processes of galaxies and black holes. Magorrian et al. (1998), Gebhardt et al. (2000), Ferrarese & Merritt (2000) and Gültekin et al. (2009) find close correlations of the black hole mass and properties of the stellar bulge, such as mass, luminosity, velocity dispersion and gravitational potential. Despite the large differences in scale (8-9 dex) and mass (3 dex) between black holes and galaxies, these correlations hint to a common mechanism behind their evolutions.

4.2.1. Feedback models

The so-called ‘feedback models’ (Fabian 2012, Alexander & Hickox 2012 and references therein) provide possible explanations of the observed correlations. In such models, AGN inject a fraction of their accretion energy into the surrounding gas of the interstellar or intergalactic matter. We can estimate the ratio of the black hole’s radiative energy emitted during the accretion ($E_{\text{BH}} = 0.1 M_{\text{BH}} \cdot c^2$, assuming a 10 per cent energy efficiency conversion) over the galaxy’s binding energy ($E_{\text{galaxy}} = M_{\text{gal}} \cdot \sigma^2$, for a galaxy’s stellar velocity dispersion of $\sigma = 200 \text{ km s}^{-1}$). Under the assumption that the black hole’s mass correlates with the galaxy’s mass ($M_{\text{BH}} \approx 1.4 \cdot 10^{-3} M_{\text{gal}}$, Kormendy & Gebhardt (2001)), we obtain $E_{\text{BH}}/E_{\text{galaxy}} \approx 300$, which underlines the fact that even for a minor energy release of the black hole during the accretion process, the energy of accelerated gas may exceed the binding energy of the galaxy and can have a profound impact on the environment. This energy release can cause matter compression, gas heating, enrichment or depletion, which can either enhance star formation (positive feedback) or stop star formation (negative feedback). The latter scenario has been suggested to be the reason of the correlations between black holes and bulge properties, because the interruption of accretion fuel will terminate the AGN growth (Silk & Rees, 1998; King, 2003). Still, finding observational evidences of any causal relationship between black hole activity and star formation activity is very challenging, because feeding and feedback mechanisms do not necessarily follow a synchronized co-evolution and may happen at different times. Another reason is that it is nearly impossible to resolve the relevant scales with current observational instruments.

4.2.2. Outflows types: AGN and star formation excitation

Theoretical models of feedback processes (e.g. by Di Matteo et al. 2005, and review articles of Fabian 2012 and Alexander & Hickox 2012) suggest that outflows are common physical drivers for the coupling of the AGN’s energy to the surrounding gas. Motivated by these models, observations have been performed of, mainly, two types of outflows, as presented in 1.4.2. The first group consists of wide-angle, sub-relativistic winds driven by radiative emission of the AGN (‘radiative/quasar/wind feedback mode’). These outflows push the inner cold gas reservoir outside and preferentially occur in high-Eddington systems. The second group of outflows comprises narrow-angle relativistic jets which are directly driven by the accretion flow (‘kinetic/radio jet/maintenance feedback mode’). These outflows are traced by synchrotron emission in the radio band, and are commonly produced in lower Eddington AGN.

However, outflows observed in AGN can also originate from star formation in the host galaxy. In this case, supernovae ejecta or winds from OB stars are thermalized in shocks and create outflow bubbles. When the bubbles reach the galactic scale height, the energy is released via the minor galaxy axis and creates outflows with velocities up to 500 km s^{-1} (Rupke & Veilleux, 2013; Hill & Zakamska, 2014). These strong outflows are typically observed in galaxies which have higher star formation rates ($\gg 1 M_{\odot}/\text{yr}$) than galaxies from the ‘star formation’ main sequence (Cicone et al., 2016).

4.2.3. Observation of outflows

As mentioned before, numerous programs have been undertaken to analyze outflows in galaxies based on integrated 1D spectra. Supported by IFU e.g. *SINFONI*, *KMOS*, *MUSE*, *MaNGA* and long slit instruments e.g. X-SHOOTER, we can now also resolve detailed information for selected nearby galactic systems down to scales of hundreds pc to kpc. Recent works reveal that outflow properties depend on a variety of factors, e.g. the energy source, the accelerated material or gas, the surrounding medium, the inclination towards the host galaxy’s plane, the location and extension within the galaxy.

Focussing on radiative outflows, works by Harrison et al. (2014) and Cresci et al. (2015) show that these outflows can reach galaxy-wide scales up to tens of kpc. They impact the inhomogenous interstellar matter of the galaxy and carry gas or matter in different phases, such as ionized, neutral and molecular phases, which can be observed by absorption/emission from e.g. NaI D, CO, [OI], [OIII] $H\alpha$ and [NII] (Rupke et al., 2005; Feruglio et al., 2010; Rupke & Veilleux, 2013). Getting a full census of all these phases requires dedicated observations at different wavelengths and it is highly challenging to disentangle mass, momentum and kinetic energy of the full outflow.

In the spectra of AGN, asymmetric emission and absorption lines are characteristic tracers of outflows/inflows (Whittle, 1985). Most observed asymmetric line profiles consist of a narrow core and a broader wing component. The origin of the components is still controversially discussed. Following works by e.g. Komossa et al. (2008); Wang & Lu (2001) on NLSey1, it is suggested that the core component represents emission from the photoionized gas following the motion of the stellar bulge (ISM), which is affected by the host galaxy’s gravitational potential. The wing component, on the other hand, is a tracer for non-gravitational and radial mechanisms, e.g. outflows and inflows (Crenshaw et al., 2010; Komossa & Xu, 2007). The observed shape and offset of the emission line’s outflow component is strongly influenced by the orientation of the outflow axis, its geometry, its initial velocity and the distribution of the interstellar matter.

4.3. Outline

In this chapter, we study in detail the kinematic properties of narrow emission lines in X-ray selected AGN, in order to examine the outflow processes. Hereby, we refer to the previously presented dataset of X-ray selected AGN in the XMM-XXL, as published in Menzel et al. (2016) and introduced in Sec. 2.4.4. To perform a statistical analysis of a large AGN population, we focus on the narrow line region, which is traceable with optical spectra in both BLAGN1 and NLAGN2. This region is mainly dominated by the gravitational potential of the bulge, but is also sensitive to non-gravitational energy sources (Whittle, 1994), such as large-scale ionized outflows. Depending on the ionization level of the outflows, signatures can be observed e.g. from excited [OIII], OII, NeV atoms. We choose [OIII] as a tracer for ionized outflow, because it has two isolated and strong emission lines in the available *BOSS* spectra (4960.295 Å, 5008.24 Å). These forbidden transitions of [OIII] are caused by collisional excitation of optical/UV photons in the low density narrow line region ($\approx 10^3 \text{ cm}^{-3}$) and can be observed with the *BOSS* spectrograph for a population of AGN and galaxies in the redshift range of $0 < z < 1$.

As mentioned earlier, the origin of the observed outflows in X-ray selected AGN can be attributed to AGN activity, star formation activity or a combination of both. To disentangle these two effects, we match our X-ray selected AGN dataset to a spectroscopic sample of emission line galaxies (ELG) in the redshift range $0 < z < 1$. For the matching, we chose the [OII]-based star formation luminosity, which provides an estimate of the star formation rate for both AGN and ELG.¹ In a subsequent step, we evaluate the shape of the [OIII] profile in star forming galaxies and galaxies hosting AGN at similar star formation rates.

We then analyze the correlation of the AGN accretion power indicators, such as hard X-ray luminosity and optical/UV continuum luminosity, with the observed [OIII] outflow/inflow features. Firstly, we focus on a subsample AGN sample with significant outflows/inflows. In this sample, we perform Spearman rank correlations for the [OIII] emission line properties and AGN accretion power indicators. In a next step, we extend the analysis to the entire population of X-ray selected AGN, stacked in hard X-ray luminosity and optical/UV continuum luminosity bins. Finally, benefitting from a redshift-complete sample of AGN, we provide an estimate of the average kinetic energy and momentum rate of ionized [OIII] outflows, and their contribution to bolometric luminosity in the ‘on-phase’ of the AGN duty cycle.

¹Key parameters for the star formation properties of galaxies are e.g. specific stellar masses and star formation rate. But for these parameters our dataset requires a complicated decomposition into galaxy and AGN component in order to measure stellar mass. This demands an extensive modeling of stellar populations, starburst activity and dust attenuation which is not in the scope of this work.

4.4. Emission line fit of [OII] and [OIII]

4.4.1. Fitting Algorithm

Before the fitting process, all *BOSS* spectra were corrected for galactic extinction and shifted to rest frame wavelength. Subsequently, the emission line regions of [OII] (3727.092 Å and 3729.875 Å, unresolved by *BOSS*)² and [OIII] (4960.295 Å, 5008.24 Å) were fitted with a linear combination of gaussian components and a continuum component. The continuum of each spectrum was interpolated by a cubic polynomial function between line-free regions:

$$F_{\text{continuum}}(\lambda) = a + b \cdot \lambda + c \cdot \lambda^2 + d \cdot \lambda^3. \quad (4.1)$$

While fitting the emission lines with Gaussian components, the continuum parameters remained fixed. For the Gaussian components, we used the most common values of the parameter distribution as initial values for the fitting process. For too deviant starting conditions, the Gaussian components reconstructed additional features of the galaxy continuum missed by the polynomial function, especially in low SN spectra.

OII fit

The **OII emission** is fitted in the wavelength range $3600 < \lambda < 3850$ Å by using the continuum component and a single Gaussian component:

$$F_{\text{total}}(\lambda) = F_{\text{continuum}}(\lambda) + n \cdot e^{-\frac{(\lambda - \lambda_{\text{peak}})^2}{2 \cdot \sigma^2}} \quad (4.2)$$

with the normalization factor n , the peak wavelength λ_{peak} and the width σ . The continuum has been interpolated from $3659 < \lambda < 3709$ Å and $3749 < \lambda < 3799$ Å, and the initial conditions of the gaussian fit are $n = 1.2$, $\lambda_p = 3729$ Å and $\sigma = 2$.

[OIII] doublet fit

We are fitting the **[OIII] doublet**, in the wavelength range $4900 < \lambda < 5100$ Å with two different fitting functions. The first function requires only one gaussian component per line and the second function uses a set of two gaussians per line. The use of two gaussians accounts for the fact that gravitational as well as outflow/inflow mechanisms can contribute to the emission line feature of [OIII]. For the spectral features of the [OIII] doublet, we consider atomic physics constraints. This comprises same widths, $\sigma_a = \sigma_b$, a normalization ratio of 1:3, $n_a = n_b/3$, and a peak distance of $\lambda_{\text{peak,b}} - \lambda_{\text{peak,a}} = 47.945$ Å. The fitting function for a single gaussian component per emission line consists of:

$$F_{\text{total}}^{\text{single}}(\lambda) = F_{\text{continuum}}(\lambda) + n_a \cdot e^{-\frac{(\lambda - \lambda_{\text{peak,a}})^2}{2 \cdot \sigma_a^2}} + 3 \cdot n_a \cdot e^{-\frac{(\lambda - (47.945 \text{ Å} + \lambda_{\text{peak,a}}))^2}{2 \cdot \sigma_a^2}}. \quad (4.3)$$

The continuum has been interpolated in the wavelength range of $4900 < \lambda < 4938$ Å, $4978 < \lambda < 4987$ Å and $5027 < \lambda < 5100$ Å. The initial conditions of the single gaussian fit are $n = 1.0$, $\lambda_{\text{peak}} = 4959.4$, $\sigma = 1.7$.

²The indicated emission line wavelengths correspond to the vacuum wavelengths of the transitions and are taken from the NIST Atomic Spectra Database (2015).

The fitting function for two gaussians components per emission line is constructed as follows:

$$F_{\text{total}}^{\text{double}}(\lambda) = F_{\text{continuum}}(\lambda) + n_a \cdot e^{-\frac{(\lambda - \lambda_{\text{peak,a}})^2}{2 \cdot \sigma_a^2}} + 3 \cdot n_a \cdot e^{-\frac{(\lambda - (47.945 \text{ \AA} + \lambda_{\text{peak,a}}))^2}{2 \cdot \sigma_a^2}} \quad (4.4)$$

$$+ n_b \cdot e^{-\frac{(\lambda - \lambda_{\text{peak,b}})^2}{2 \cdot \sigma_b^2}} + 3 \cdot n_b \cdot e^{-\frac{(\lambda - (47.945 \text{ \AA} + \lambda_{\text{peak,b}}))^2}{2 \cdot \sigma_b^2}}, \quad (4.5)$$

with $n_a = 1.0$, $\lambda_{\text{peak,a}} = 4959.6$, $\sigma_a = 2.1$, $n_b = 1.3$, $\lambda_{\text{peak,b}} = 4957.4$ and $\sigma_b = 5.0$.

Evaluation of emission lines

All emission line fits are performed with a χ^2 -minimization method, using the `mpfit` routine from `idl` (Markwardt 2009). For our study, we impose a significance threshold on the results of the [OII] and [OIII] fit. The gaussian components have to fulfill the following criteria: $F/\Delta F > 2$ (with flux F and flux error ΔF), $SN_{\text{med}} > 1$, non-zero errors for widths and normalization, and a peak wavelength error of $\Delta\lambda_{\text{peak}} < 2 \text{ \AA}$. The S/N ratio is calculated as follows

$$SN_{\text{med}} = \text{Median}(F(\tilde{\lambda})/\Delta F(\tilde{\lambda})), \quad (4.6)$$

where $\tilde{\lambda}$ is restricted to the wavelength range in the vicinity of the emission lines: $3659 < \tilde{\lambda}_{\text{OII}} < 3799 \text{ \AA}$ and $4900 < \tilde{\lambda}_{\text{OIII}} < 5100 \text{ \AA}$.

The decision between single and double gaussian components for the [OIII] emission lines is based on the F-test. Following the `mpftest` routine from `idl` (Moshier 2009), we determine the differences of the chi-squares values χ , and degrees of freedom dof , from both fits. Assuming $\text{dof}_{\text{double}} < \text{dof}_{\text{single}}$, the F -value and the probability p are calculated as:

$$F = \frac{(\chi_{\text{single}} - \chi_{\text{double}})/(\text{dof}_{\text{single}} - \text{dof}_{\text{double}})}{\chi_{\text{double}}/\text{dof}_{\text{double}}} \quad (4.7)$$

$$p = p(F, \text{dof}_{\text{single}} - \text{dof}_{\text{double}}, \text{dof}_{\text{double}}) \quad (4.8)$$

Values of $p \leq 0.05$ confirm the significance of the additional gaussian component. In addition, for all spectra with double gaussian fits, we perform a visual inspection and deselect objects which are strongly influenced by sky lines or galaxy features. This applies to 27 per cent of the dataset with double gaussian fits.

Example of emission line fitting

In Fig. 4.1, we present the rest frame spectra of two AGN to demonstrate the emission line fit of the [OIII] doublet applied in this work. Both spectra are fitted with the functions $F_{\text{total}}^{\text{single}}(\lambda)$ (red line) and $F_{\text{total}}^{\text{double}}(\lambda)$ (orange line).

The fits in the first spectrum on the left hand result in chi-square values of $\chi_{\text{single}} = 159.8$ ($\text{dof}_{\text{single}} = 170$) and $\chi_{\text{double}} = 156.7$ ($\text{dof}_{\text{double}} = 167$). The F-test of both fits indicates a significance of $p = 0.34$, which means that no significant differences are found inbetween the two fits. Thus, we chose the results from $F_{\text{total}}^{\text{single}}(\lambda)$ because it has less components.

For the second spectrum on the right side, we obtain $\chi_{\text{single}} = 280.6$ ($\text{dof}_{\text{single}} = 170$) and $\chi_{\text{double}} = 195.6$ ($\text{dof}_{\text{double}} = 167$). The F-test indicates a clear difference between these spectra ($p = 4.7 \cdot 10^{-13}$) and we choose the fitting results of $F_{\text{total}}^{\text{double}}(\lambda)$ for our analysis.

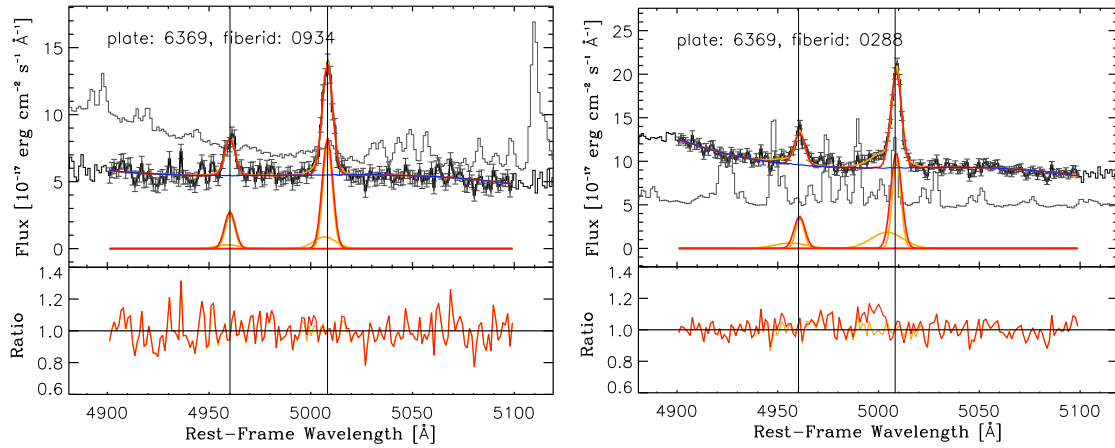


Figure 4.1.: These two AGN spectra demonstrate the [OIII] fitting process of this work. The plots show the spectral flux (black line with error bars), the sky lines (thin grey line), the fitting function $F_{\text{total}}^{\text{single}}(\lambda)$ (red line) with associated components, the fitting function $F_{\text{total}}^{\text{double}}(\lambda)$ (orange line) with associated components and the residuum for both fitting functions. The spectra on the left side is best fit with only one gaussian component per line and the right spectrum requires two gaussian components per line.

4.4.2. Characterization of asymmetric [OIII] emission line profiles

We now present the tools to describe the profiles of [OIII] lines which are successfully fitted by two significant gaussian components and are therefore candidates for outflows or inflows. We define a ‘narrow core’ component and a ‘broad wing’ component. Following:

$$|\lambda_{\text{core}} - \lambda_{\text{peak}}| < |\lambda_{\text{wing}} - \lambda_{\text{peak}}| \quad (4.9)$$

with the wavelength of the core maximum λ_{core} , the wavelength of the wing maximum λ_{wing} , and the wavelength of the entire profile maximum λ_{peak} . The core component maybe usually associated with the influence of the galaxy’s gravitational potential on the gas in the narrow line region (Greene & Ho, 2005). However, Zakamska & Greene (2014) find that this relationship might not hold for high luminosity AGN. The wing component may represent non-gravitational mechanisms, such as outflows or inflows which typically have larger widths compared to the velocity dispersion of the stellar bulge. In our dataset of X-ray selected AGN, 94 per cent of the wing components have broader line widths than the core components.

With the help of non-parametric velocity definitions, we can also describe the asymmetric emission line feature without requiring a separation into core and wing component. We calculate the cumulative flux $\Phi(v)$ under the fitted gaussian components as a function of velocity v :

$$\Phi(v) = \int_{-\infty}^v F_v^{\text{gauss}}(v') dv'. \quad (4.10)$$

The total line flux is then given by $\Phi(v = \infty)$. In a next step, we determine the flux percentiles of the line profile and calculate the corresponding velocities v_i with respect to λ_{peak} , as shown in Fig. 4.2. The individual velocities are sensitive to redshift uncertainty, but velocity differences eliminate this dependency.

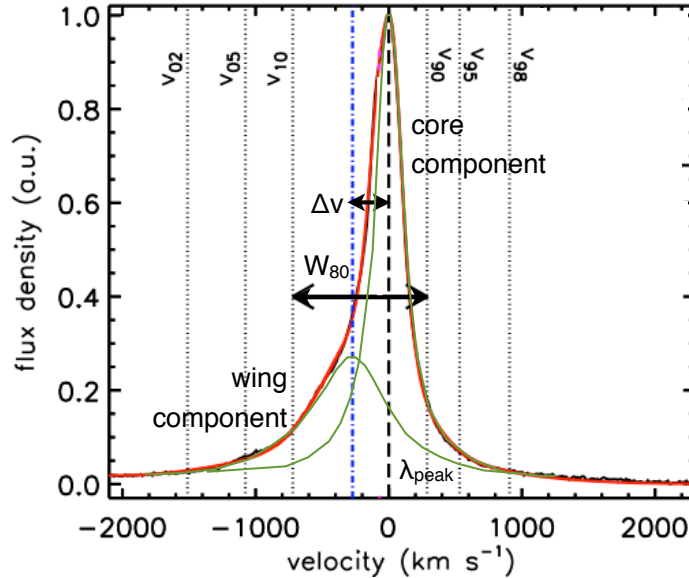


Figure 4.2.: Schematic diagram of asymmetric emission line with characteristic parameters. The graphic is adapted from Harrison et al. (2014).

The width of the emission line can be described by a large variety of parameters. In order to represent the broad wing part and be less sensitive to the low S/N ratio at high velocities, we follow the definition of Harrison et al. (2014) for the width W_{80} :

$$W_{80} = v_{90} - v_{10}. \quad (4.11)$$

For a single gaussian, W_{80} is analogous to the FWHM, and for two gaussian components, W_{80} is sensitive to the wing shift in respect to the core component.

Other authors, e.g. Rupke & Veilleux (2013), introduce the maximal projected velocity of the gas as follows

$$W_{96}^{\text{wing}} = v_{98}^{\text{wing}} - v_{02}^{\text{wing}}, \quad (4.12)$$

by only considering the wing component of the emission line. The parameter Δv describes the asymmetry of the emission line profile and can be correlated to the offset velocity of the wing:

$$\Delta v = (v_{05} + v_{95})/2. \quad (4.13)$$

For a single gaussian component Δv is equal to zero. We find, that the parameter Δv is likely to underestimate the offset velocity of the wing in comparison to $(\lambda_{\text{core}} - \lambda_{\text{wing}})$, if the core flux has a large weight at the 5th or 95th flux percentile.

In order to determine the velocity of outflows/inflows, we point out that the observed velocity of the wing component is influenced by the outflow's or inflow's inclination towards the observer. In the work of Liu et al. (2013), the authors built theoretical models for spherically symmetric or wide-angle bi-cone outflows including different obscuration effects in order to derive corrections for the observed velocities. Common nonparametric values used in outflow studies are W_{80} or W_{96} (as listed in (Harrison et al., 2014)) in order to correct for this projection and have a better estimate of the maximal velocity.

We assume that the [OIII] core and wing components are related to different physical mechanisms. Because the core component is not involved in the outflow/inflow, we determine the outflow/inflow velocity based on the wing velocity $\text{FWHM}_{\text{wing}}$. As we are not able to neither estimate the outflow's or inflow's inclination nor its geometry in fibre-fed spectra, we cannot determine the initial outflow velocity.

4.5. Presentation of AGN and ELG dataset

In order to analyze the narrow line region kinematics of AGN, we benefit from our dataset of X-ray selected AGN in the XMM-XXL north with optical spectroscopic follow-up (Menzel et al. 2016, as presented in Chapter 2). We complement this analysis with a dataset of emission line galaxies (ELG) from the *eBOSS* pilot observations (Zhu et al. 2015; Comparat et al. 2015). For our study, we require access to [OII] (3729 Å) and [OIII] (4960 Å, 5008 Å), which limits our samples to a redshift range of $0 < z < 1$ due to the wavelength threshold of the *BOSS* spectrograph ($\lambda < 10400\text{Å}$).

4.5.1. X-ray catalogue

The XMM-XXL dataset of X-ray selected AGN, as summarized in Section 2.4.4, comprises 503 BLAGN1 and 537 NLAGN2/NLAGN2cand in the redshift range of $0 < z < 1$. For simplification, we merge the X-ray selected NLAGN2 and NLAGN2cand and refer to them as ,NLAGN2'. We also introduce a subset of 32 elusive AGN (,eAGN-SFG') which have a characteristic X-ray emission of AGN ($L_{0.5-2\text{keV}} > 1 \cdot 10^{42} \text{erg s}^{-1}$) and are classified as star forming galaxies in the BPT diagram.

A complete flux limited sample

The homogeneous *BOSS* observations of AGN in the XMM-XXL field allow for the definition of a highly complete flux-limited sample of X-ray selected AGN with optical spectroscopic follow-up. Comparing to number densities in the flux-redshift plane of the complete XMM-COSMOS field (Brusa et al., 2010), we derive a subset of X-ray selected AGN with *BOSS* spectral counterparts which we estimate to be close to 90 per cent redshift complete (once fibre collisions are taken into account Blanton et al. 2003). The applied thresholds are:

$$F_{2-10\text{keV}} > 2.5 \cdot 10^{-14} \text{erg s}^{-1} \text{ and } 0 < z < 0.8. \quad (4.14)$$

The luminosity-redshift distribution is presented in Fig. 4.3 and comprises 372 AGN reaching an AGN number density of 15deg^{-2} . The complete sample includes 184 BLAGN1, 109 NLAGN2, 59 NLAGN2cand, 6 eAGN-ALG, 11 eAGN-SFG and 3 not classifiable objects.

4.5.2. ELG catalogue

The emission line galaxy sample (ELG) from Zhu et al. 2015 and Comparat et al. 2015 is taken from the early pilot observations of the extended Baryon Oscillation Spectroscopic Survey (*eBOSS*) in *SDSS-IV*. It comprises 9000 emission line galaxies with visual inspection (*BOSS* plates: 8123 - 8130, 8355, 8356) in the redshift range of $0 < z < 1.5$. The observed field covers an area of 19deg^2 and is located around $\text{RA} = 36 \text{deg}$ and $\text{Dec} = -4.5 \text{deg}$. The ELG are selected by multi-imaging surveys e.g. *SDSS*, *WISE*, *DES* and *SCUSS* to be blue galaxies likely with star formation powered emission lines. The pilot project is dedicated to provide galaxies redshifts for the study of baryonic oscillations.

For our work, we apply several selection cuts for redshift $0 < z < 1$, redshift quality $\text{ZWARNING} = 0$, reliable visual redshift ($\text{zQ} > -2$, as presented in Comparat et al. 2015), classification $\text{CLASS} = \text{GALAXY}$, and exclude AGN related sub-classification ($\text{SUBCLASS} = \text{AGN}$

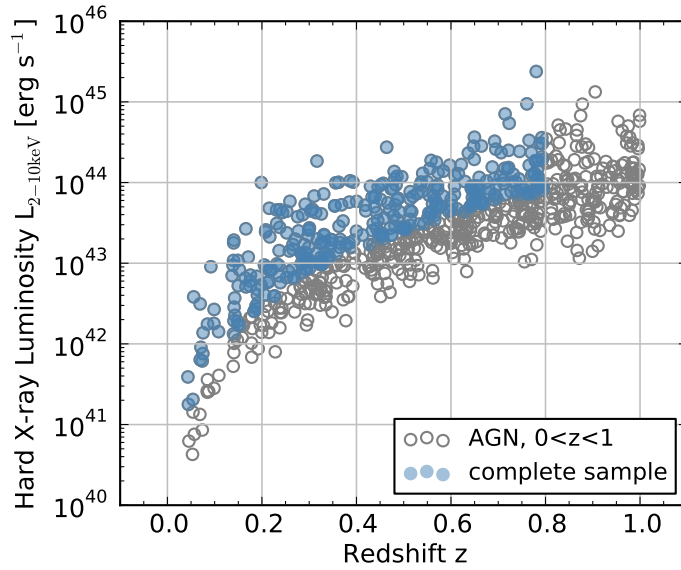


Figure 4.3.: Hard X-ray luminosity and redshift distribution of all AGN with $0 < z < 1$ (grey circles) and the complete flux-limited sample (blue).

and `SUBCLASS = BROADLINE`). However, the BOSS pipeline tends to misclassify narrow line AGN as galaxies. Thus following the Blue-OII diagnostic diagram as presented in Section 2.4.3, we deselect 257 AGN candidates based on emission line parameters provided by the BOSS pipeline product `,spZline'`. The final `,clean'` dataset contains 4117 ELG.

4.5.3. Redshift, magnitude and S/N ratio distributions

In Fig. 4.4, we present the redshift and r_{model} magnitude distribution of ELG, BLAGN1, NLAGN2, eAGN-SFG and the complete AGN sample within $0 < z < 1$. The redshift distribution of ELG reflects the selection function of the pilot program, which is dedicated to target redshift $z < 1.5$ objects and optimized for $z \geq 0.6$. As far as AGN are concerned, as shown in Section 2.5, more BLAGN1 reside at higher redshifts than the NLAGN2. This is due to the fact that NLAGN2 of same redshift have weaker optical fluxes and are too faint for the threshold of the BOSS spectrograph.

The overall ELG population is considerably fainter than the AGN. The ELG have a median magnitude of $r_{\text{model}} \approx 22$ mag, whereas AGN reach a median magnitude of $r_{\text{model}} \approx 21$ mag. This magnitude difference is also represented in their S/N ratio distributions, as shown in Fig. 4.5. The median S/N ratio distribution in the emission line regions of [OII] and [OIII] is around $SN \approx 2$ for ELG and $SN \approx 5$ for AGN.

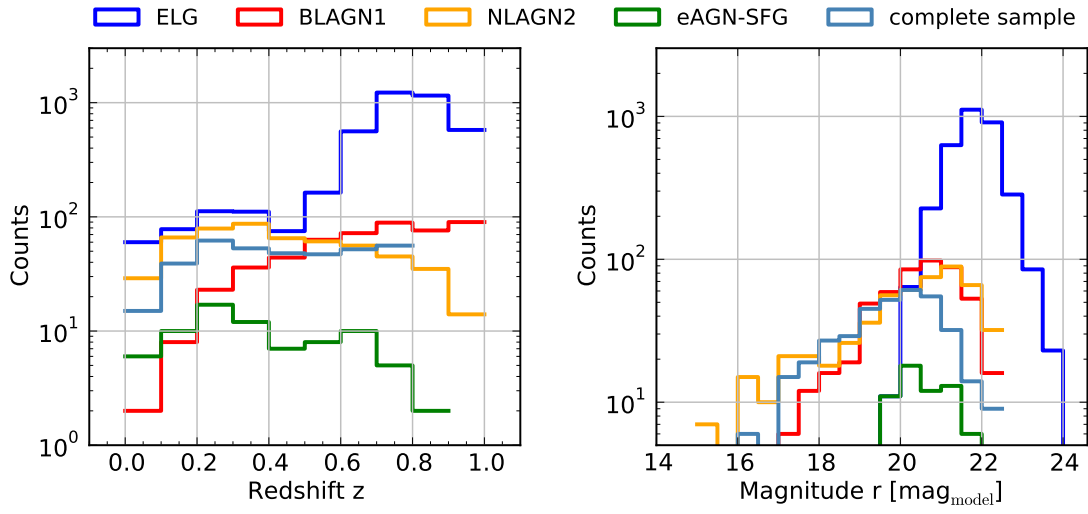


Figure 4.4.: Redshift and r_{model} magnitude distribution for ELG (blue), BLAGN1 (red), NLAGN2 (orange), eAGN-SFG (green), complete sample (light blue).

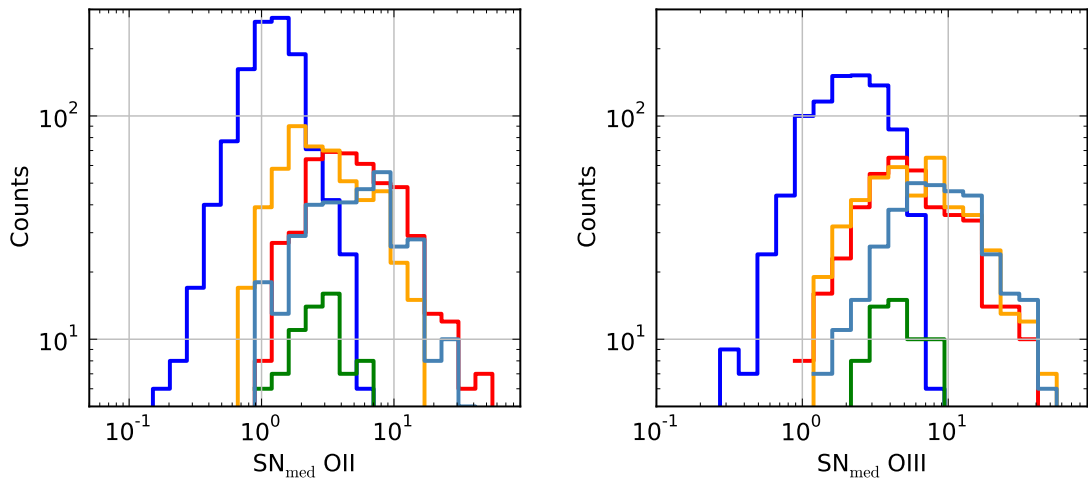


Figure 4.5.: S/N ratio-distribution in the [OII] (top panel) and [OIII] (bottom panel) emission line region for ELG (blue), BLAGN1 (red), NLAGN2 (orange).

4.6. Incidence of [OIII] outflows in star forming galaxies and AGN

In this section, we fit the [OII] and [OIII] emission lines of the BLAGN1, NLAGN2 and ELG sample using the methodology presented in Section 4.4. Subsequently, we determine the number of objects with significant emission lines and compare the incidence of ionized [OIII] outflows/inflows in the three datasets.

4.6.1. Significant [OII] and [OIII] emission lines

In Tab. 4.1, we list the number of ELG and AGN whose fitting algorithm results in the detection of significant [OII] and [OIII] emission lines. As expected, we obtain more significant line detections of [OII] in the ELG dataset and [OIII] in BLAGN1. NLAGN2 show a similar amount of significant [OII] and [OIII] emission lines, probably caused by a stronger contribution of the host galaxy emission lines in comparison to BLAGN1.

Furthermore, we also provide the number of AGN and ELG, which have a significant [OIII] wing components next to the [OIII] core component. This is an indication for ionized [OIII] outflows/inflows. In our AGN, we find 170 objects with significant [OIII] wing component, whereas there are only 13 in the ELG sample.

Table 4.1.: ELG and AGN sources with significant [OII] and [OIII] line features. Furthermore, we indicate significant [OIII] wings. In this table, we apply $SN_{\text{med}} > 1$ for the [OII] and [OIII] emission lines.

	full dataset	significant [OII] line	significant [OIII] line(s)	significant [OII] and [OIII]	significant [OIII] wing
BLAGN1	503	388	414	353	100
NLAGN2	537	449	448	391	70
sum	1040	837	862	744	170
ELG	4117	2480	1324	1077	13

4.6.2. [OIII] outflow incidence

We now analyze the incidence of ionized [OIII] outflows/inflows compared to the entire dataset and list the results in Tab. 4.2. The stated errors correspond to Poisson errors.

AGN versus Starformation

For $SN_{\text{med}} > 1$, the AGN dataset comprises 20 ± 2 per cent objects with significant incidences of outflows/inflows, whereas the ELG dataset only contains 1.0 ± 0.3 per cent. The detection of significant emission lines is very likely to be correlated with the S/N ratio of the available spectra. As we mentioned in the last section, the S/N ratio-distributions of ELG and AGN are very different. Indeed, we find for all samples a clearly increasing ratio of outflow/inflow detections for increasing median S/N ratio of the spectra.

Still, taking the S/N ratio dependence into account, it is clear that AGN (either BLAGN1 or NLAGN2) have 10 – 20 times higher incidence of significant [OIII] wings than ELG, as shown in Tab. 4.2.

Table 4.2.: Fraction of ionized [OIII] outflows/inflows in BLAGN1 and NLAGN2.

	0 < z < 1			complete sample	
	ELG [per cent]	BLAGN1 [per cent]	NLAGN2 [per cent]	BLAGN1 [per cent]	NLAGN2 [per cent]
$SN_{\text{med}} > 1$	1.0 ± 0.3	24 ± 3	16 ± 2	41 ± 6	28 ± 5
$SN_{\text{med}} > 3$	1.8 ± 0.1	30 ± 3	19 ± 3	43 ± 6	31 ± 5
$SN_{\text{med}} > 10$	-	55 ± 9	29 ± 6	60 ± 11	40 ± 10

The low outflow/inflow incidence in ELG might be explained by the fact that the majority of ELG have too low star formation rates to cause strong outflows. Lee et al. (2015) study star forming galaxies from the main sequence in the *COSMOS* field by using far-infrared photometry. The authors determine the relations between star formation rate (SFR) and stellar mass M_* as a function of redshift. Our ELG-sample has a median redshift of $z = 0.7$. For the sample of main sequence galaxies in *COSMOS*, this corresponds to a $SFR_{\text{MS}} = 1 - 5 M_* \text{ yr}^{-1}$ and $M_* = 8.5 - 9.5 M_\odot$. As we will determine in the next section, the average SFR of our ELG is $2.2 M_\odot \text{ yr}^{-1}$. Following Cicone et al. (2016), who analyse the presence of ionized outflows in star forming galaxies from *SDSS*, the presence of outflows is very unlikely for $\log(SFR/SFR_{\text{MS}}) < 2$. This reinforces our argument that the majority of ELG are no starburst galaxies with strong outflows.

Unobscured AGN (BLAGN1) versus obscured AGN (NLAGN2)

Concentrating on the AGN sample, we find a difference in the outflow/inflow incidence between optically unobscured and obscured AGN. We obtain 24 ± 3 per cent for BLAGN1 and 16 ± 2 per cent for NLAGN2 at $SN_{\text{med}} > 1$. In the following, we analyze if this difference is due to selection effects.

First, we study the incompleteness of the AGN sample caused by the optical flux threshold of the *BOSS* spectrograph. By referring to the complete sample of X-ray selected AGN in the XMM-XXL, we find that 43 ± 6 per cent of BLAGN1 and 31 ± 5 per cent of NLAGN2 show indications of outflows/inflows ($SN_{\text{med}} > 3$), which are marginally different considering the errors bars.

However, BLAGN1 and NLAGN2 have different luminosity and redshift distributions. Thus, we perform a volume limited selection by applying thresholds for S/N ratio ($SN_{\text{med}} > 3$), redshift ($z < 0.8$) and luminosity ($L_{2-10\text{keV}} > 3 \cdot 10^{43} \text{ erg s}^{-1}$). This results in the same outflow/inflow incidence in BLAGN1 and NLAGN2 (BLAGN1: 34 ± 6 per cent, NLAGN2: 27 ± 8 per cent). Summarizing, the central obscuration of AGN does not appear to have an impact on the ionized [OIII] outflow/inflow incidence.

4.7. Comparison of [OIII] emission line profiles in ELG and AGN

In the previous section, we have seen a significant difference in the incidence of [OIII] outflows/inflows in ELG and AGN. We excluded that this effect is due to the different S/N ratio. Eventually, ELG and AGN have strongly differing underlying star formation rate which has an influence on the ionized [OIII] outflows. Thus, it requires a comparison of the emission line properties of both main samples after being matched in the equivalent star formation rate. Below, we describe the methodology used to derive intrinsic star formation indicators for both ELG and AGN.

4.7.1. F_{OII} -to- F_{OIII} -ratio

We measure the flux ratio of $F_{\text{OII}}/F_{\text{OIII}}$, considering the emission lines of [OII] 3729 Å ($IP = 35.116$ eV) and [OIII] 5008 Å ($IP = 54.934$ eV), as key parameter for evaluating the characteristic released ionization energy from SF or AGN activity. This ratio allows for the evaluation of the star formation share in the line emission of our observed spectra.

We analyze the overall flux ratio distribution of BLAGN1 and ELG, in order to determine the intrinsic flux ratios for AGN, R_{AGN} , and star formation galaxies, R_{SF} . We measure the [OII] flux, \tilde{F}_{OII} , and the [OIII] flux, \tilde{F}_{OIII} in the optical spectra (without reddening correction) and calculate the flux ratio \tilde{R} for each objects, as follows:

$$\tilde{R} = \frac{\tilde{F}_{\text{OII}}}{\tilde{F}_{\text{OIII}}} = \frac{F_{\text{OII}}^{\text{SF}} + F_{\text{OII}}^{\text{AGN}}}{F_{\text{OIII}}^{\text{SF}} + F_{\text{OIII}}^{\text{AGN}}}. \quad (4.15)$$

Individual objects in our dataset are likely to have a contribution from both AGN and star formation activity in their spectra and might be influenced by SF history. Works by Silverman et al. (2009) and Kim et al. (2006) on AGN, use the medians of the F_{OII} -to- F_{OIII} -ratio to determine the AGN contribution in their star formation galaxies. Following this method, we derive the medians of the flux ratio distribution for BLAGN1 and ELG to estimate the intrinsic ratios for pure AGN and pure star formation activity:

$$R_{\text{AGN}} = \text{Median}\left(\frac{\tilde{F}_{\text{OII}}^{\text{BLAGN1}}}{\tilde{F}_{\text{OIII}}^{\text{BLAGN1}}}\right) = \frac{F_{\text{OII}}^{\text{AGN}}}{F_{\text{OIII}}^{\text{AGN}}} = 0.3 \quad (4.16)$$

$$R_{\text{SF}} = \text{Median}\left(\frac{\tilde{F}_{\text{OII}}^{\text{ELG}}}{\tilde{F}_{\text{OIII}}^{\text{ELG}}}\right) = \frac{F_{\text{OII}}^{\text{SF}}}{F_{\text{OIII}}^{\text{SF}}} = 1.8. \quad (4.17)$$

The \tilde{R} distributions are shown in Fig. 4.6. The long flux ratio tail of ELG towards lower ratios might be explained by AGN contaminants which were not deselected by the applied color and optical line diagnostic criteria (see Sec. 4.5.2). The intrinsic flux ratios R_{AGN} and R_{ELG} are likely to be broader distributions, but in the scope of this work, we make the assumption of sharp thresholds to evaluate the trends of star formation contribution.

In Tab. 4.3, we indicate the median and mode of the flux ratios \tilde{R} for BLAGN1, NLAGN2 and ELG in different redshift bins. The median \tilde{R} of BLAGN1 agrees with former works

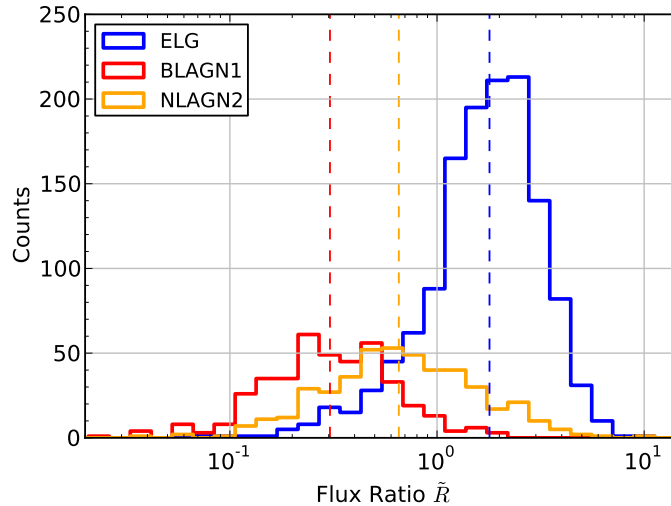


Figure 4.6.: Distributions of $F_{\text{OII}}/F_{\text{OIII}}$ Ratio for ELG (blue), BLAGN1 (red), NLAGN2 (orange). The dashed lines indicate the medians of the distributions.

by Zakamska et al. (2003) ($R_{\text{AGN}} = 0.25$ for $0.3 < z < 0.83$), Silverman et al. (2009) ($R_{\text{AGN}} = 0.21$ for $0 < z < 1$) and Kim et al. (2006) ($R_{\text{AGN}} = 0.27$ for $0.0 < z < 0.3$). This supports the hypothesis that BLAGN1 are good candidates to estimate the intrinsic flux ratio for AGN.

The median \tilde{R} for ELG coincides with the ratio of the stacked ELG spectrum of Zhu et al. (2015) ($0 < z < 1.5$, $R_{\text{SF}} = 1.67$) and does not change significantly with redshift.

We find that NLAGN2 have higher median \tilde{R} than BLAGN1, which can be attributed to an excitation of the narrow line region by both star formation and the AGN. Therefore, the flux ratio \tilde{R} ranges between the intrinsic ratio for AGN and star formation activity. We find, that the median \tilde{R} of NLAGN2 decreases for increasing redshift, which can be explained by a weaker contrast between AGN and host galaxy for higher redshifts in a flux limited sample.

Table 4.3.: Redshift dependence of the $F_{\text{OII}}/F_{\text{OIII}}$ median and mode for BLAGN1, NLAGN2 and ELG.

	Median \tilde{R}				Mode \tilde{R}
	$0 < z < 0.33$	$0.33 < z < 0.66$	$0.66 < z < 1.0$	$0 < z < 1$	$0 < z < 1$
BLAGN1	0.36 ± 0.19	0.32 ± 0.35	0.28 ± 0.28	0.30 ± 0.30	0.41
NLAGN2	0.75 ± 1.17	0.62 ± 0.71	0.53 ± 0.43	0.65 ± 0.90	0.45
ELG	1.94 ± 1.29	1.85 ± 1.20	1.77 ± 1.05	1.79 ± 1.12	2.17

4.7.2. Match of star forming galaxies and AGN in star formation rate

In the following, we will derive the star formation contribution to the [OII] line in the sample of BLAGN1, NLAGN2 and ELG. To this end, we compute the ratio of AGN and star formation contribution to the [OII] flux:

$$g_{\text{OII}} = \frac{F_{\text{OII}}^{\text{SF}}}{F_{\text{OII}}^{\text{AGN}}} = \frac{\tilde{R}/R_{\text{AGN}} - 1}{1 - \tilde{R}/R_{\text{SF}}}. \quad (4.18)$$

With (4.15), we can now derive the corrected star formation [OII] flux $F_{\text{OII}}^{\text{SF}}$ for each object based on the measured line flux ratio \tilde{R} . Obviously, this assumption only applies to objects which have significant contributions of both mechanisms ($0.3 < \tilde{R} < 1.8$). All objects which are clearly dominated by star formation activity ($\tilde{R} > 1.8$) contribute with the full measured [OII] flux to $F_{\text{OII}}^{\text{SF}}$; thus the star formation corrected [OII] flux of the full sample is derived as follows:

$$F_{\text{OII}}^{\text{SF}} = \begin{cases} g_{\text{OII}}/(g_{\text{OII}} + 1) \cdot \tilde{F}_{\text{OII}}, & \text{for } 0.3 < \tilde{R} < 1.8 \text{ and } F_{\text{OII}}^{\text{SF}} > \Delta\tilde{F}_{\text{OII}} \\ \tilde{F}_{\text{OII}}, & \text{for } \tilde{R} \geq 1.8 \end{cases} \quad (4.19)$$

For objects which are dominated by AGN activity ($\tilde{R} < 0.3$) or whose errors of the [OII] flux are larger than $F_{\text{OII}}^{\text{SF}}$, we can only derive upper limits for $F_{\text{OII}}^{\text{SF}}$ by referring to the measured [OII] flux error:

$$F_{\text{OII}}^{\text{SF, upper limit}} = \Delta\tilde{F}_{\text{OII}}, \quad \text{for } \tilde{R} \leq 0.3 \text{ or } F_{\text{OII}}^{\text{SF}} < \Delta\tilde{F}_{\text{OII}}. \quad (4.20)$$

We now calculate the corresponding luminosities $L_{\text{OII}}^{\text{SF}}$ for the three datasets. The star formation luminosity $L_{\text{OII}}^{\text{SF}}$ can be transformed into star formation rate (SFR), by applying the conversion as presented by Kennicutt (1998):

$$\text{SFR}_{\text{OII}} = (1.4 \pm 0.5) \cdot 10^{-41} L_{\text{OII}}^{\text{SF}} \text{ M}_{\odot} \text{ yr}^{-1}. \quad (4.21)$$

In Fig. 4.7, we show all objects with significant star formation luminosity and corresponding SFR; in Fig. 4.8, we present all ELG and AGN where we can only determine upper limits for $L_{\text{OII}}^{\text{SF}}$. We find that the bulk of ELG has a median SFR of $2.2 \text{ M}_{\odot} \text{ yr}^{-1}$, which is higher than the median SFR of AGN ($0.5 \text{ M}_{\odot} \text{ yr}^{-1}$). This SFR For comparison studies of star formation properties in the following sections, the sample is going to be split in a high and low SFR sample, with a threshold of $L_{\text{OII}}^{\text{SF}} = 6 \cdot 10^{40} \text{ erg s}^{-1}$ corresponding to $\text{SFR} \simeq 1 \text{ M}_{\odot} \text{ yr}^{-1}$.

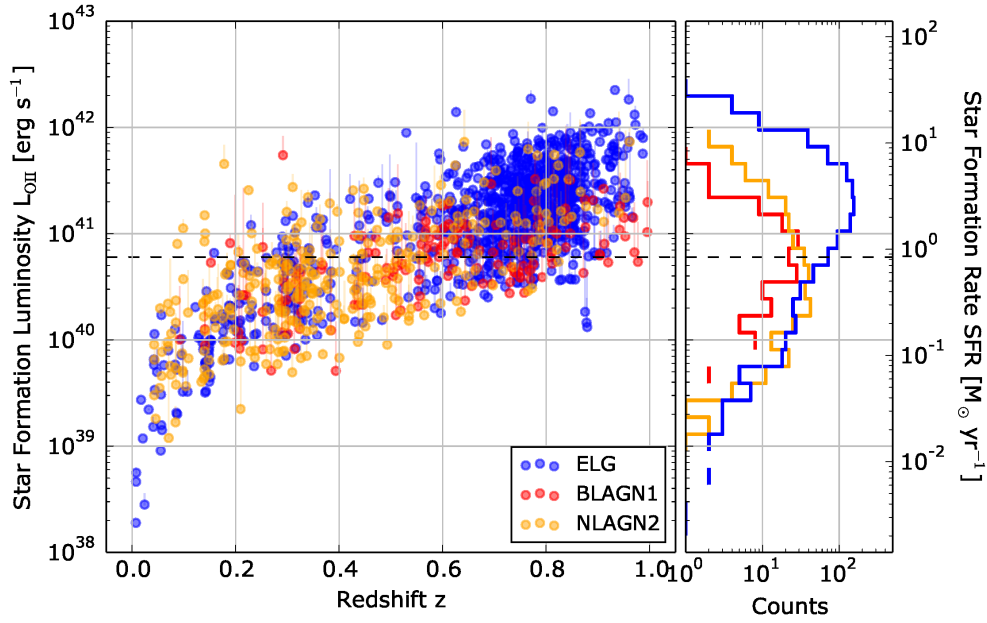


Figure 4.7.: Distribution and histogram of [OII] star formation luminosity or star formation rate as function of redshift for ELG (blue), BLAGN1 (red) and NLAGN2 (orange). The vertical lines refer to the measured [OII] luminosity of each objects. The dashed horizontal line indicates the threshold for the separation into the high-and-low-SFR sample.

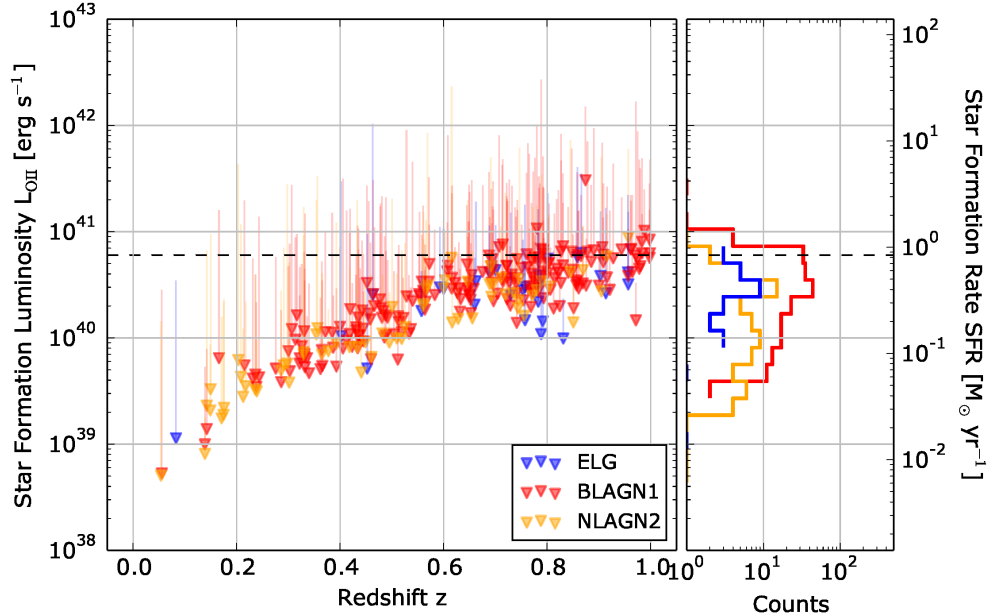


Figure 4.8.: Distribution and histogram for upper limits of [OII] star formation luminosity and star formation rate as function of redshift for ELG (blue), BLAGN1 (red) and NLAGN2 (orange). The vertical lines refer to the measured [OII] luminosity of each objects. For comparison with Fig. 4.7, the dashed horizontal line indicates the threshold for the separation into the high-and-low-SFR sample.

4.7.3. Average [OIII] profiles in host galaxies of high and low star formation rate

After the determination of SFR for the BLAGN1, NLAGN2 and ELG sample, we now perform spectral stacks in comparable SFR bins. This allows to analyze the [OIII] emission line features in star forming galaxies and AGN host galaxies, matched in the same star formation property.

Stacking procedure and error determination

For the median spectral stack, each spectrum is redshifted, corrected for galactic extinction, the previously fitted polynomial continuum is subtracted and the flux is converted into luminosity.

The main error source is the polynomial fit which does not model the true galaxy features and reveals the systematics of the initial fitting model. The estimation of the total error of the stack is based on a bootstrapping method. We create 100 new samples by randomly choosing spectra from the primary set. Hereby, we allow for multiple drawings. In a next step, we recompute the spectral stack for the 100 samples and derive their emission line properties. The standard deviation for these emission line parameters provide error estimates for the primary spectral stack. The detailed spectral fits as well as the residuals are attached in Appendix B.

Spectral stacks of [OII] and [OIII] emission

In Fig. 4.9, we show the stacked spectra of BLAGN1, NLAGN2 and ELG in the [OII] and [OIII] wavelength region as a function of SFR. The top row shows the spectral stacks for the low SFR sample ($\text{SFR} < 1 \text{ M}_{\odot} \text{ yr}^{-1}$) and the bottom row for the high SFR sample ($\text{SFR} > 1 \text{ M}_{\odot} \text{ yr}^{-1}$). In Tab. 4.4, we provide the number of contributing spectra as well as line features for the stacks in the [OII] and [OIII] range.

For both the low and high SFR samples, the [OIII] emission of BLAGN1 and NLAGN2 can be modeled by two significant gaussian components, whereas the ELG stack requires only one gaussian component.

The measured flux ratios $F_{\text{OII}}/F_{\text{OIII}}$, for BLAGN1 and NLAGN2 are in agreement with the median values from Sec. 4.7.1, whereas the flux ratio for ELG is larger than the previously estimated R_{SF} ($R_{\text{SF,stack}} \approx 2.3$ versus $R_{\text{SF}} = 1.8$). This is probably due to AGN contaminants, which contribute in the lower flux ratio tail.

[OIII] outflow features in star forming galaxies and AGN host galaxies

As previously mentioned, the [OIII] emission line in the spectral stack of the AGN is fitted with two gaussians, whereas in the ELG stack only one gaussian is required. In order to allow for a better visual comparison of the profile features of [OIII], we show the (maximum) normalized spectral stacks in Fig. 4.10. In the following, we compare the emission line features at different SFR.

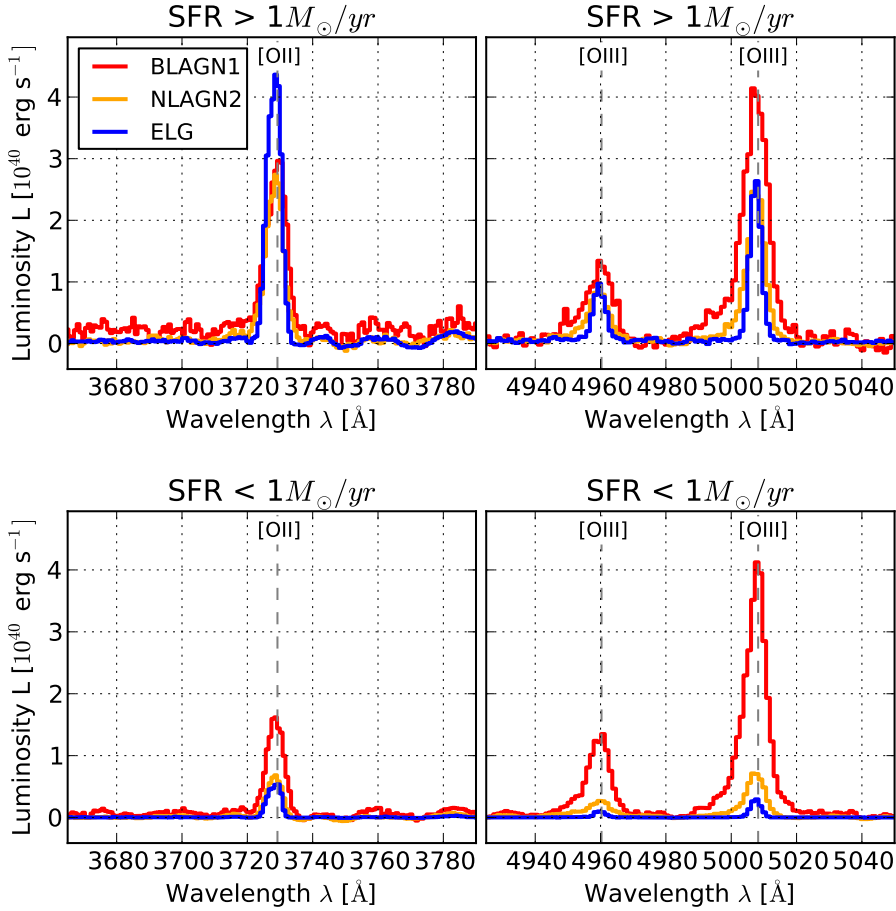


Figure 4.9.: Spectral stacks of ELG (blue), BLAGN1 (red) and NLAGN2 (orange) in the wavelength region of [OII] and [OIII]. Top panel: high SFR sample ($> 1 M_{\odot} \text{yr}^{-1}$). Bottom panel: low SFR sample ($< 1 M_{\odot} \text{yr}^{-1}$). We note that the line luminosities of the presented stacked spectra strongly depend on the distribution within the L_{OII}^{SF} bin and limit intergroup comparisons.

Independently of the SFR, we find that the average [OIII] core components of BLAGN1 and NLAGN2 have larger velocity dispersions³ than ELG ($\sigma_{\text{core}}^{\text{AGN}} = 156 \pm 43 \text{ km s}^{-1}$, $\sigma^{\text{ELG}} = 98 \pm 8 \text{ km s}^{-1}$). This difference in the velocity dispersion might be due to several reasons. The location of the narrow line regions which are excited by star formation or the AGN is not intrinsically the same. Thus, gas clouds in the centre of the galaxies around AGN have higher measured velocity dispersions than more distant and diffuse clouds excited by star formation. But, if one assumes that the narrow line region is located at the same distance to the black hole, independently of its excitation mechanism, it implies that the host galaxy mass in ELG is smaller than in AGN. Another reason for the difference in velocity dispersion might be caused by the pipeline design of the *BOSS* spectrograph, and results in a higher redshift uncertainty for the AGN. However, Hewett

³The velocity dispersions correspond to $\text{FWHM}/2.3548$. Here, the resolution of the *BOSS* spectrograph ($\sigma_{\text{BOSS}} = 55 \text{ km s}^{-1}$) has been subtracted in quadrature.

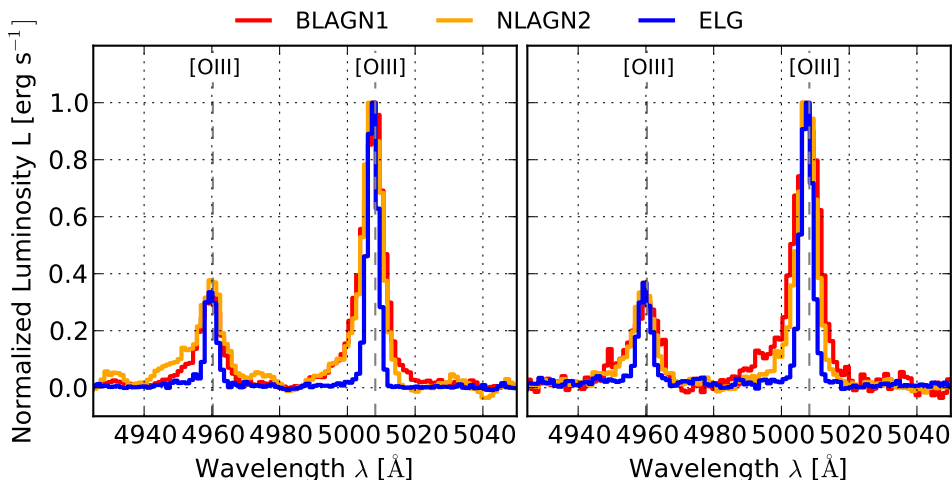


Figure 4.10.: For a better comparison of the [OIII] profile, we present the normalized spectral stacks of ELG (blue), BLAGN1 (red) and NLAGN2 (orange) in the wavelength region of [OIII]. Left panel: low SFR sample ($< 1 M_{\odot} \text{ yr}^{-1}$). Right panel: high SFR sample ($> 1 M_{\odot} \text{ yr}^{-1}$). The y-axis is normalized to the maximum luminosity of each spectral stack.

& Wild (2010) show that the correlation between multiple emission line cores, which are observable in the *BOSS* wavelength range, guarantees that the systematic redshift error $\Delta z/(1+z)$ does not exceed 30 km s^{-1} . Therefore, this effect can be considered as minor.

As described in Sec. 4.2.3, wing components in the [OIII] emission lines indicate an additional mechanism causing outflows or inflows. In the spectral stack of both AGN samples, we find asymmetric [OIII] emission lines which are clear incidences for the presence outflows/inflows, in contrast to ELG, where no asymmetry is observed. The FWHM of the significant [OIII] wings in AGN are in the range of $\text{FWHM}_{\text{wing}} = 840 - 1120 \text{ km s}^{-1}$ and have an offset velocity of $\Delta v = -100 - -230 \text{ km s}^{-1}$. Comparing the non-parametric width equivalent W_{80} , both BLAGN1 and NLAGN2 have $W_{80} = 580 - 840 \text{ km s}^{-1}$ which largely exceed the widths of ELG with $W_{80} \approx 260 \text{ km s}^{-1}$. In Fig. 4.11, we indicate W_{80} for the three mentioned samples, according to the spectral stacks of the high SFR sample and a low SFR sample. For W_{96} , BLAGN1 are within a range of $648 - 2454 \text{ km s}^{-1}$ and NLAGN2 within $551 - 2133 \text{ km s}^{-1}$.

Summarizing, the difference in the line profiles of AGN and ELG is an indication that, at comparable star formation strength, the presence of blueshifted wings in the [OIII] profile of AGN is caused by an additional non-gravitational motion next to star formation activity. This is very likely to be a mechanism triggered by AGN activity, as we will analyze in the following section.

Finally, we show in Fig. 4.12, the normalized spectral stacks of BLAGN1, NLAGN2 and ELG where only upper limits can be derived for SFR or $L_{\text{OII}}^{\text{SF}}$, respectively. The [OIII]

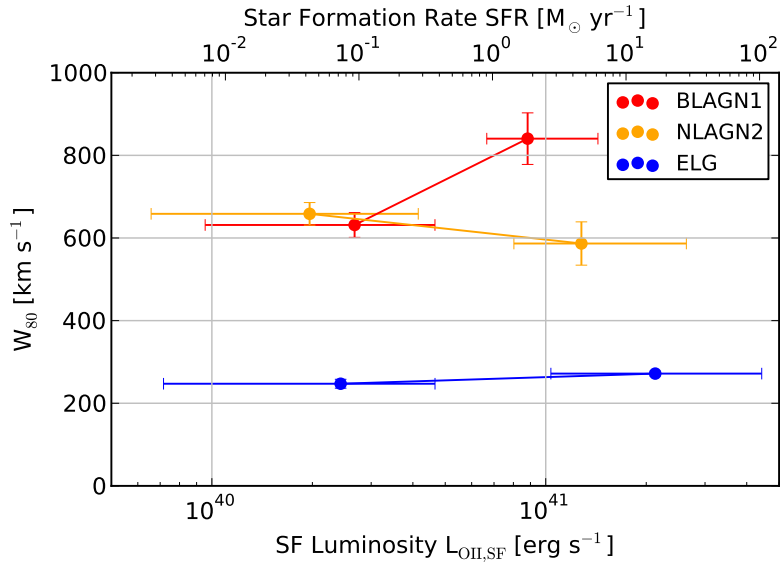


Figure 4.11.: Diagram of the non-parametric width measurement of asymmetric emission lines W_{80} for spectral stacks of ELG (blue), BLAGN1 (red), NLAGN2 (orange). The stacks are performed for different SFR or $L_{\text{OII}}^{\text{SF}}$, respectively, and clearly show a significant difference in the [OIII] line width of AGN and ELG, which excludes star formation to be the main origin of outflows/inflows in AGN.

profile of the ELG spectral stack has a very similar width (W_{80}) compared to BLAGN1 and NLAGN2. This supports the hypothesis that the ELG sample is contaminated by AGN at the low flux ratio tail of the R distribution. The visual inspection of this ELG sample with upper star formation rate limits, only flagged one [OIII] outflow candidate, because the majority of the spectra has strong sky lines in the [OIII] regions.

This reinforces the knowledge that the line ratio $F_{\text{OII}}/F_{\text{OIII}} < 0.3$ is a good indication of AGN ionizing radiation.

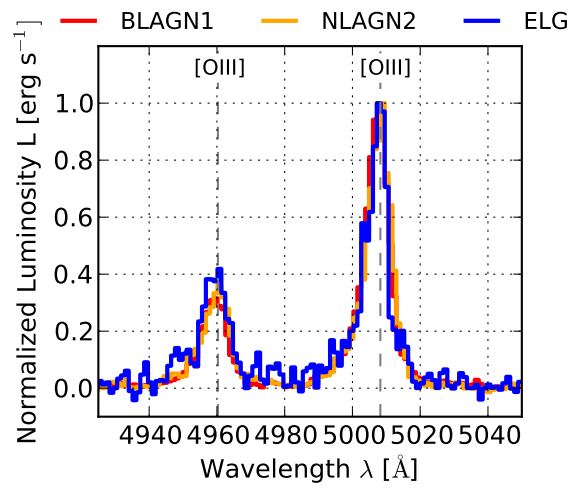


Figure 4.12.: Normalized spectral stacks of ELG (blue), BLAGN1 (red), NLAGN2 (orange) with upper limits for SFR or $L_{\text{OII}}^{\text{SF}}$, respectively.

Table 4.4.: Emission line parameters of [OII] (3729 Å) and [OIII] (5008 Å) for spectral stacks of BLAGN1, NLAGN2 and ELG in different star forming luminosity bins. The errors of $L_{\text{OII}}^{\text{SF}}$ indicate the 15.87th and 84.12th percentile, and the errors of [OIII] line components are derived with bootstrapping methods.

AGN type	#	$L_{\text{OII}}^{\text{SF}}$ [erg s ⁻¹]	SFR [M _⊙ yr ⁻¹]	L_{OII} [erg s ⁻¹]	$L_{\text{OIII}}^{\text{core}}$ [erg s ⁻¹]	FWHM _{core} ^{OIII} [km s ⁻¹]	$L_{\text{OIII}}^{\text{wing}}$ [erg s ⁻¹]	FWHM _{wing} ^{OIII} [km s ⁻¹]	W_{80}^{OIII} [km s ⁻¹]	Δv [km s ⁻¹]
Selection: $L_{\text{OII}}^{\text{SF}} > 6 \cdot 10^{40}$ erg s ⁻¹ , SFR > 1 M _⊙ yr ⁻¹										
BLAGN1	97	$8.8_{-2.2}^{+5.5} \cdot 10^{40}$	$1.2_{-0.5}^{+0.9}$	$(2.0 \pm 0.2) \cdot 10^{41}$	$(2.9 \pm 0.8) \cdot 10^{41}$	475 ± 56	$(1.3 \pm 0.6) \cdot 10^{41}$	1122 ± 253	840 ± 62	-230 ± 41
NLAGN2	109	$1.3_{-0.5}^{+1.4} \cdot 10^{41}$	$1.8_{-0.9}^{+2.0}$	$(1.8 \pm 0.2) \cdot 10^{41}$	$(1.3 \pm 0.4) \cdot 10^{41}$	339 ± 57	$(6.8 \pm 2.9) \cdot 10^{40}$	845 ± 231	587 ± 52	-128 ± 43
ELG	829	$2.1_{-1.1}^{+2.3} \cdot 10^{41}$	$3.0_{-1.9}^{+3.4}$	$(2.4 \pm 0.1) \cdot 10^{41}$	$(1.2 \pm 0.4) \cdot 10^{41}$	249 ± 5			272 ± 6	
Selection: $L_{\text{OII}}^{\text{SF}} < 6 \cdot 10^{40}$ erg s ⁻¹ , SFR < 1 M _⊙ yr ⁻¹										
BLAGN1	256	$2.7_{-1.7}^{+2.0} \cdot 10^{40}$	$0.4_{-0.3}^{+0.3}$	$(1.0 \pm 0.1) \cdot 10^{41}$	$(1.3 \pm 0.4) \cdot 10^{41}$	304 ± 45	$(2.1 \pm 0.4) \cdot 10^{41}$	710 ± 86	631 ± 30	-104 ± 15
NLAGN2	282	$2.0_{-1.3}^{+2.2} \cdot 10^{40}$	$0.3_{-0.2}^{+0.3}$	$(3.9 \pm 0.2) \cdot 10^{40}$	$(4.2 \pm 0.4) \cdot 10^{40}$	366 ± 16	$(1.6 \pm 0.4) \cdot 10^{40}$	857 ± 67	658 ± 27	-198 ± 14
ELG	248	$2.4_{-1.7}^{+2.2} \cdot 10^{40}$	$0.3_{-0.3}^{+0.3}$	$(2.8 \pm 0.3) \cdot 10^{40}$	$(1.2 \pm 0.1) \cdot 10^{40}$	227 ± 10			247 ± 11	
Selection: Upper limits for $L_{\text{OII}}^{\text{SF}}$ and SFR										
BLAGN1	204	$2.8_{-1.9}^{+2.7} \cdot 10^{40}$	$0.4_{-0.3}^{+0.4}$	$(1.3 \pm 0.1) \cdot 10^{41}$	$(3.5 \pm 0.5) \cdot 10^{41}$	414 ± 23	$(2.6 \pm 0.5) \cdot 10^{41}$	945 ± 78	712 ± 28	-117 ± 19
NLAGN2	68	$1.3_{-0.9}^{+2.0} \cdot 10^{40}$	$0.2_{-0.1}^{+0.3}$	$(9.2 \pm 1.5) \cdot 10^{40}$	$(1.9 \pm 0.5) \cdot 10^{41}$	419 ± 49	$(1.3 \pm 0.5) \cdot 10^{41}$	897 ± 111	734 ± 57	-159 ± 26
ELG	27	$2.8_{-1.7}^{+1.3} \cdot 10^{40}$	$0.4_{-0.3}^{+0.3}$	$(1.4 \pm 0.2) \cdot 10^{41}$	$(9.3 \pm 7.4) \cdot 10^{40}$	230 ± 96	$(2.3 \pm 0.6) \cdot 10^{41}$	719 ± 485	669 ± 214	-124 ± 111

4.8. Correlation of [OIII] outflows with AGN accretion properties

After finding that star formation is not the main origin of the [OIII] outflows observed in AGN, we are led to the simple hypothesis that AGN activity causes the asymmetry in the [OIII] profile. In order to test this hypothesis further, we analyze [OIII] outflow features and their dependency on characteristic AGN accretion indicators, such as optical/UV continuum and hard X-ray luminosity. In the first part of this Section, we concentrate on a subset of 170 X-ray selected AGN which show asymmetric [OIII] line profiles with significant core and wing components in their optical spectra. With this subsample, we perform a Spearman rank correlation of the line features and the AGN accretion indicators. In a second part of this Section, we extend our analysis to study average ionized [OIII] outflow features of the entire dataset of X-ray selected AGN. As part of this work, we perform spectral stacks in dedicated hard X-ray and optical/UV luminosity bins.

4.8.1. AGN subsample with significant ionized [OIII] outflows/inflows

Our dataset of X-ray selected AGN contains a subsample of 170 AGN whose asymmetric [OIII] emission lines which are fitted by significant core and wing components. This subsample comprises 100 BLAGN1 and 70 NLAGN2 in the redshift range $0 < z < 1$.

In the following, we analyze the [OIII] emission line in these AGN spectra, present a selection of AGN with extreme outflows properties and finally, perform a Spearman rank correlation to study the [OIII] profile and its dependency on optical/UV and hard X-ray luminosity.

Asymmetric [OIII] line features

As mentioned in Sec. 4.2.3, the asymmetric [OIII] line features can be decomposed into a narrow core component and a broad wing component. The flux/luminosity of the components can give insights into the ‘excitation mechanism’ and the width of the components is related to the velocity field of the NLR. We present the distribution of all [OIII] line parameters in Fig. 4.13.

We firstly study the flux/luminosity of the [OIII] components. The BLAGN1 have larger overall luminosities than NLAGN2 which is probably due to faint optical limit of the *BOSS* spectrograph and/or obscuration of emission by gas or matter. We obtain median luminosities of $L_{\text{core}} = 2.3 \cdot 10^{41} \text{ erg s}^{-1}$ and $L_{\text{wing}} = 2.9 \cdot 10^{41} \text{ erg s}^{-1}$ in BLAGN1; and $L_{\text{core}} = 1.1 \cdot 10^{41} \text{ erg s}^{-1}$ and $L_{\text{wing}} = 1.0 \cdot 10^{41} \text{ erg s}^{-1}$ in NLAGN2. Comparing both [OIII] components, we find that the (median) wing component contributes 56 per cent to the total luminosity of the asymmetric profile in BLAGN1, and 47 per cent in NLAGN2. Similar results have been presented in previous works of optically selected AGN by Zhang et al. (2011) and Peng et al. (2014) finding that the wing component comprises 46 per cent of the total emission in a sample of nearby Type 1 AGN (*SDSS* DR4) and 48 per cent in a sample of BPT selected nearby Type 2 AGN (from DR7). Mullaney et al. (2013) obtains a wing contribution of 45 per cent to the total line flux in a large Type 2 sample (from DR7).

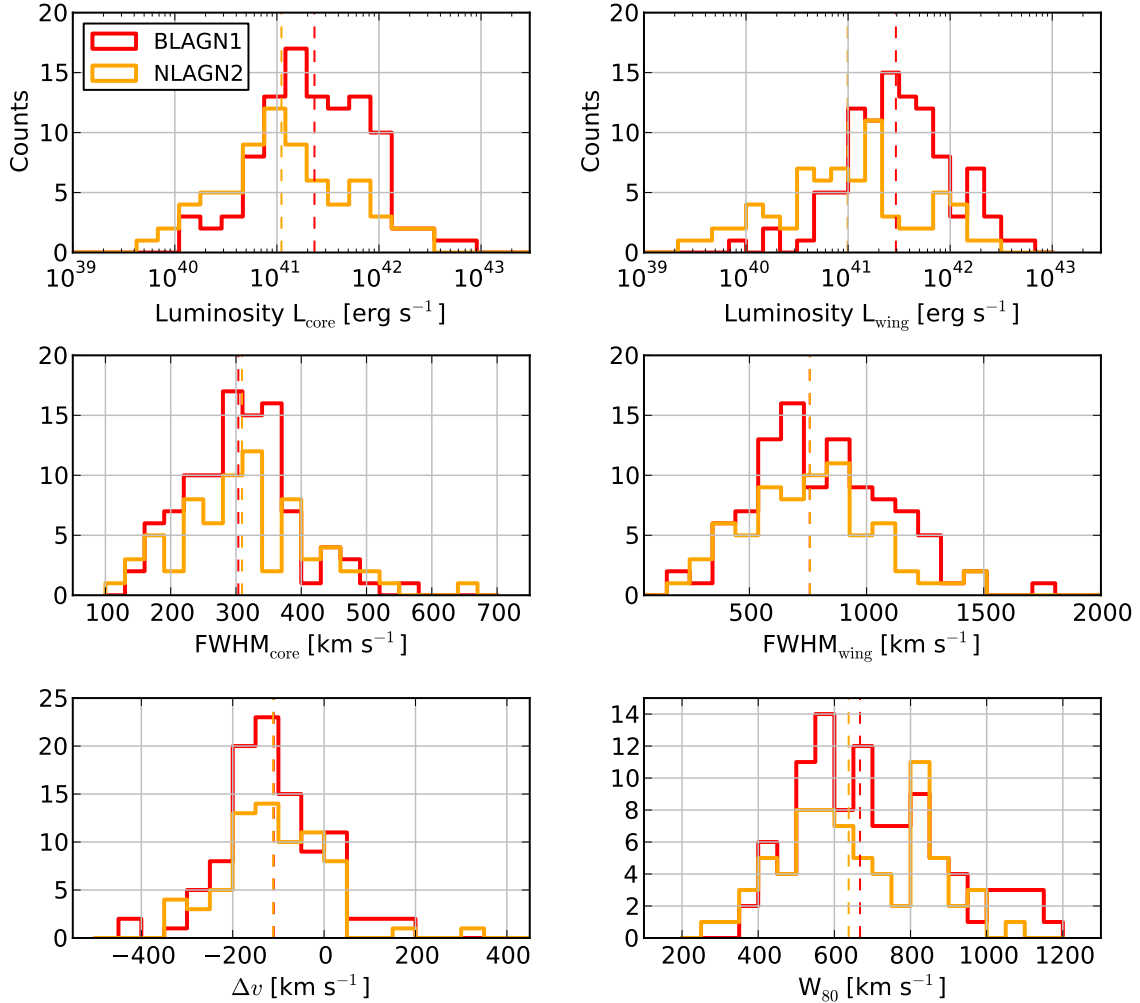


Figure 4.13.: Distribution of [OIII] emission line parameters of BLAGN1 (red) and NLAGN2 (orange). The dashed lines indicated the median for each distribution.

This result can be confirmed by a Spearman Rank correlation of core and wing luminosity for our subsample. BLAGN1 have a correlation coefficient of $r_{\text{Spearman}} = 0.66$ ($p < 10^{-13}$), NLAGN2 have $r_{\text{Spearman}} = 0.73$ ($p < 10^{-12}$) and the group including both AGN types has $r_{\text{Spearman}} = 0.74$ ($p < 10^{-30}$). Peng et al. (2014) find similar results for Type 1 ($r_s = 0.663$) and Type 2 AGN ($r_s = 0.701$). This correlation might be due to the fact that the gas from the core and wing component are illuminated by the same source.

Concentrating on the velocity dispersions of the two components, we find that the narrow core component (corrected for the resolution of the *BOSS* spectrograph: $\sigma_{\text{core}} = \sqrt{(\text{FWHM}_{\text{wing}}/2.3584)^2 - 55^2}$ km s⁻¹) has a median width of 171 km s⁻¹ and 174 km s⁻¹, and maximal values of $\sigma_{\text{core}} = 230$ km s⁻¹ and $\sigma_{\text{core}} = 373$ km s⁻¹ for BLAGN1 and NLAGN2, respectively. The core widths agree with typical velocity dispersion of stellar bulges (Whittle, 1994).

The FWHM of the wing component has a range of $\text{FWHM}_{\text{wing}} = 194 - 1748$ km s⁻¹ for BLAGN1 (and $\text{FWHM}_{\text{wing}} = 242 - 1445$ km s⁻¹ for NLAGN2). The median $\text{FWHM}_{\text{wing}}$

of 1055 km s^{-1} is similar for both BLAGN1 and NLAGN2. Clearly, the broad [OIII] wing components in AGN, which are correlated to outflows, exceed velocities which can be reached during extreme star formation processes.

The parameter W_{80} provides a measure of the width of the entire asymmetric [OIII] profile. We find, that its range (BLAGN1: $W_{80} = 374 - 1169 \text{ km s}^{-1}$, NLAGN2: $W_{80} = 297 - 1067 \text{ km s}^{-1}$) and median are comparable for both AGN types (BLAGN1: $W_{80} = 667 \text{ km s}^{-1}$, NLAGN2: $W_{80} = 637 \text{ km s}^{-1}$).

The parameter Δv represents the velocity offset of the [OIII] wing component in our X-ray selected AGN subsample. We find that the majority of our sources have blueshifted line wings ($\Delta v < 0$) and only 16 per cent are redshifted ($\Delta v > 0$).

The comparison of the Δv with $\text{FWHM}_{\text{wing}}/2.3584$ reveals an interesting insight into the velocity profile of the ionized [OIII] outflow. As displayed in Fig. 4.14, we find that broader [OIII] wing components have higher blueshifts than narrower wing components, which is supported by a weak correlation in the Spearman rank analysis ($r_{\text{Spearman}} = -0.153$, $p < 0.046$). If we assume that broader wings are located in the more inner NLR, it implies that the [OIII] outflows in AGN are decelerated by the ISM of the host galaxy. This result has also been shown in works of Jin et al. (2012) (nearby Type 1 AGN sample from *2XMMi* and *SDSS* DR7) and Komossa et al. (2008). The missing redshifted AGN can be explained by obscuration of the redshifted outflow cones due to the galactic plane (Crenshaw et al., 2010; Bae & Woo, 2016)).

Thus, given the prevalence of blueshifts, we can conclude that we mainly face winds coming towards the observers' line of sight in our X-ray selected AGN. The observed projected velocity is supposed to be affected by the orientation of the outflow cone and the presence of decelerating material in the ISM.

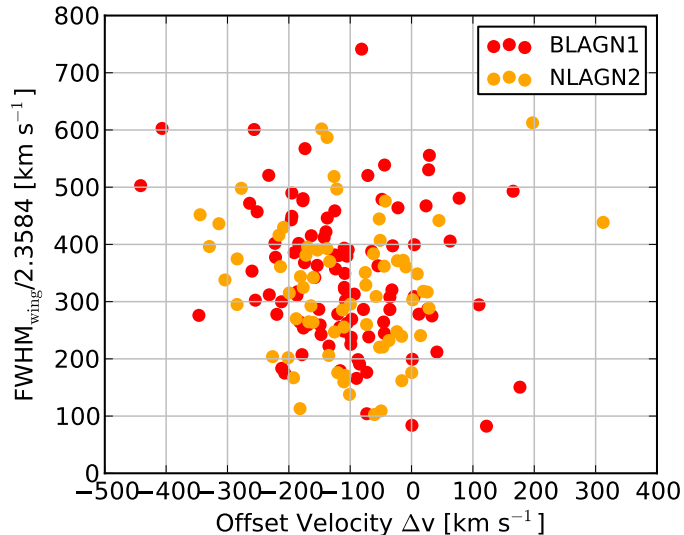


Figure 4.14.: Distribution of the offset velocity and velocity dispersion of BLAGN1 (red) and NLAGN2 (orange)

Most extreme outflows

As illustration, we present a selection of most extreme outflows from our AGN sample. The highest velocity outflow has a $\text{FWHM}_{\text{wing}} = 1748 \text{ km s}^{-1}$ and the most luminous outflow has $L_{\text{wing}} = 6.8 \cdot 10^{42} \text{ erg s}^{-1}$. These are both observed in BLAGN1 and presented in Fig. 4.15 (top left panel: $L_{2-10 \text{ keV}} = 7.3 \cdot 10^{43} \text{ erg s}^{-1}$, $z = 0.763$ and top right panel: $L_{2-10 \text{ keV}} = 2.4 \cdot 10^{45} \text{ erg s}^{-1}$, $z = 0.78$).

The object with the most blueshifted wing is an BLAGN1 with $\Delta v = -407 \text{ km s}^{-1}$ (see Fig. 4.15 bottom left panel, $L_{2-10 \text{ keV}} = 2.1 \cdot 10^{43} \text{ erg s}^{-1}$, $z = 0.707$) and the most redshifted wing is found in a NLAGN2 with $\Delta v = 312 \text{ km s}^{-1}$ (bottom right panel, $L_{2-10 \text{ keV}} = 1.6 \cdot 10^{44} \text{ erg s}^{-1}$, $z = 0.843$).

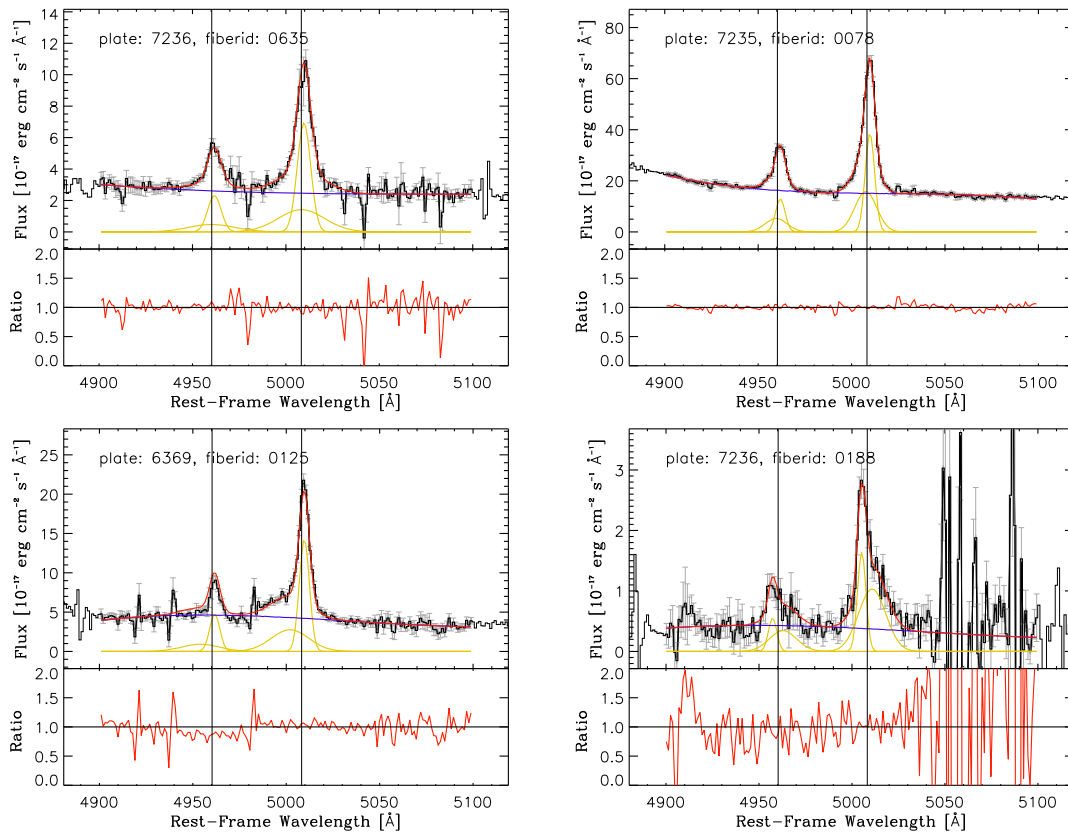


Figure 4.15.: Selected *BOSS* spectra with extreme outflow/inflow characteristics: broadest wing (top left panel), most luminous wing (top right panel), most blueshifted wing (bottom left panel), most redshifted wing (bottom right panel). The plots show the spectral flux (black line), the individual fitted components (yellow line) and the total fit (red line). Furthermore, we present the residual for the fit of each individual spectrum in the attached lower panels.

Study of [OIII] features and their dependency on AGN accretion properties

For the presented subsample of X-ray selected AGN, we want to study the asymmetric [OIII] profile and its dependency on AGN accretion properties. Thus, we choose the hard X-ray flux $F_{2-10\text{keV}}$ (and luminosity $L_{2-10\text{keV}}$), as well as the optical/UV continuum flux $F_{5100\text{\AA}}$ (and luminosity $L_{5100\text{\AA}}$) as AGN accretion sensitive parameters. Out of the 170 AGN from the subsample, 92 BLAGN1 and 57 NLAGN2 have non-zero hard X-ray fluxes, and all 100 BLAGN1 have non-zero optical/UV continuum flux.

The optical/UV continuum luminosity $L_{5100\text{\AA}}$ (at $\lambda = 5100\text{\AA}$) is representative for the ‘blue bump’-UV-emission which is released by the accretion disk of the AGN. This emission causes collisional excitations of [OIII] in the low-density NLR which is followed by de-excitation through forbidden line transitions. Thus, the temperature of the disk strongly impacts the excitation probability of the [OIII] 5008\AA . In our sample, the AGN continuum at $\lambda = 5100\text{\AA}$ can be well defined for spectra of BLAGN1, but for NLAGN2 this emission region suffers heavy extinction and superposition by host galaxy features.

The hard X-ray luminosity $L_{2-10\text{keV}}$ represents the disk emission which is inverse-Compton scattered on the electrons in the corona. This emission can reach up to few hundreds of keV and can be measured in both BLAGN1 and NLAGN2. Furthermore, it is less sensitive to obscuration effects in contrast to the soft X-ray luminosity.

The common primary source of the both introduced luminosities makes a tight correlation very likely. We study the correlation between $L_{5100\text{\AA}}$ and $L_{2-10\text{keV}}$ with the help of the BLAGN1 sample and obtain a strong correlation ($r_{\text{Spearman}} = 0.75$, $p < 10^{-16}$). The slope of the bisector regression is $\log(L_{5100\text{\AA}}/L_{2-10\text{keV}}) \propto 0.86$, as shown in Fig. 4.16. Jin et al. (2012) make a similar comparison for a sample of Type 1 AGN (from *SDSS* DR7 and *2XMMi*). They obtain $r_{\text{Spearman}} = 0.88$ ($< 10^{-17}$) and the linear bisector regression results in $\log(L_{5100\text{\AA}}/L_{2-10\text{keV}}) \propto 0.92 \pm 0.05$.

We now perform Spearman Rank correlations between the flux or luminosity of the [OIII] line components (F_{core} , F_{wing} , L_{core} , L_{wing}) and the recently presented AGN accretion related fluxes and luminosities ($F_{5100\text{\AA}}$, $F_{2-10\text{keV}}$, $L_{5100\text{\AA}}$, $L_{2-10\text{keV}}$). This allows to study if the central AGN is the excitation mechanism of the asymmetric [OIII] line. We expect the luminosities to correlate better because of the factor $4\pi d_L^2$.

For BLAGN1, we find that [OIII] fluxes and luminosities correlate with hard X-ray and the optical/UV continuum (see Fig. 4.17 and Tab. 4.5). This is an indication, that the excitation of the static as well as outflowing/inflowing [OIII] NLR is very likely to be induced by the radiation of the AGN. Applying the Fisher transformation (R. A. Fisher, 1915) on the correlation coefficients of the flux-flux and luminosity-luminosity correlations, we can evaluate if the two correlations are significantly different or not. We only find a significant difference ($p_{\text{Fisher}} < 0.5$) between the $F_{c+w}-F_{5100\text{\AA}}$ ($r_{\text{Spearman}} = 0.736$) and $F_{c+w}-F_{2-10\text{keV}}$ ($r_{\text{Spearman}} = 0.559$) correlation. The larger correlation coefficient of $F_{c+w}-F_{5100\text{\AA}}$ follows the assumption about the the optical/UV nature of the line exciting mechanism.

Assuming that AGN were accreting at a constant rate and constantly ionize the NLR, we expect a tight correlation between X-ray emission and optical emission line luminosities.

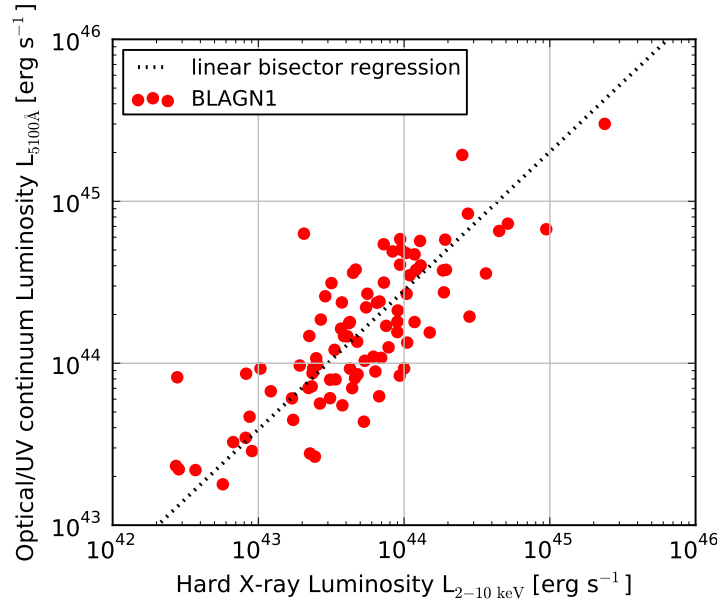


Figure 4.16.: Correlation of hard X-ray luminosity and optical/UV continuum luminosity for a subset of 92 BLAGN1 with significant [OIII] core and wing components. The dashed line indicates the bisector of the log linear regressions.

For L_{c+w} as a function of $L_{2-10\text{keV}}$, we obtain a correlation coefficient of $r_{\text{Spearman}} = 0.762$ and a slope of 0.85 ± 0.07 . This is in agreement with studies of Berney et al. (2015) in a sample of *Swift*/*BAT* selected AGN ($r_{\text{Pearson}} = 0.63$ and a slope of 0.85 ± 0.05) as well as in works of Ueda et al. (2015) and Winter et al. (2009). The scatter of the correlations indicate, that the [OIII] flux is modulated by additional factors which could be related to the physical properties of the narrow line regions and/or the long travel time of the AGN emission to the distant NLR.

For the NLAGN2, we obtain in general very low coefficients for the correlations which is probably due to stronger star formation contribution from the host to the emission line features in the optical spectra.

We now focus on the shape of the [OIII] lines by studying velocities, such as $\text{FWHM}_{\text{core}}$, $\text{FWHM}_{\text{wing}}$, W_{80} and velocity offsets Δv in the AGN subsample and their correlation with with the AGN accretion related luminosities ($L_{5100\text{\AA}}$, $L_{2-10\text{keV}}$). For the BLAGN1, we find that the Spearman rank coefficients of the FWHM and W_{80} indicate a correlation with $L_{5100\text{\AA}}$ and $L_{2-10\text{keV}}$ (see Fig. 4.18), but are generally weaker than for F_{core} , F_{wing} , L_{core} or L_{wing} in the previous paragraph. According to the Fisher transformation, there is no difference between all four correlations. Thus, the assumed different origin of the velocity dispersion from the narrow core and the velocity of the broad wing component is not reflected in the correlations with the AGN accretion indicators.

The parameter Δv has a weak anti-correlation with the $L_{5100\text{\AA}}$, meaning that [OIII] wings are more blueshifted for higher luminosities.

For the NLAGN2, we observe no correlations of the FWHM , W_{80} or Δv with hard X-ray luminosity or optical/UV continuum luminosity.

Table 4.5.: Spearman rank correlation of [OIII] emission line parameters with hard X-ray flux and optical/UV continuum flux. The p-values in brackets indicate the probability that no correlation is present. For the bottom table, we indicate the median of [OIII] FWHM, W_{80} and Δv .

Line parameter	AGN type	correlation with $F_{5100\text{\AA}}$	correlation with $F_{2-10\text{keV}}$
F_{core}	BL	0.672 ($< 10^{-13}$)	0.508 ($< 10^{-6}$)
	NL		0.250 (0.06)
F_{wing}	BL	0.664 ($< 10^{-13}$)	0.520 ($< 10^{-6}$)
	NL		0.208 (0.12)
$F_{\text{c+w}}$	BL	0.736 ($< 10^{-17}$)	0.559 ($< 10^{-8}$)
	NL		0.325 (0.014)

Line parameter	AGN type	correlation with $L_{2-10\text{keV}}$	correlation with $L_{5100\text{\AA}}$
L_{core}	BL	0.608 ($< 10^{-9}$)	0.663 ($< 10^{-13}$)
	NL	0.599 ($< 10^{-6}$)	
L_{wing}	BL	0.686 ($< 10^{-13}$)	0.737 ($< 10^{-17}$)
	NL	0.677 ($< 10^{-8}$)	
$L_{\text{c+w}}$	BL	0.689 ($< 10^{-13}$)	0.762 ($< 10^{-19}$)
	NL	0.724 ($< 10^{-9}$)	

Line parameter	AGN type	median of distribution	correlation with $L_{5100\text{\AA}}$	correlation with $L_{2-10\text{keV}}$
FWHM _{core}	BL	$(423^{+98}_{-111}) \text{ km s}^{-1}$	0.435 ($< 10^{-6}$)	0.383 ($< 10^{-3}$)
	NL	$(431^{+154}_{-121}) \text{ km s}^{-1}$		-0.013 (0.921)
FWHM _{wing}	BL	$(1055^{+500}_{-286}) \text{ km s}^{-1}$	0.284 (0.004)	0.369 (0.001)
	NL	$(1056^{+378}_{-387}) \text{ km s}^{-1}$		0.097 (0.475)
W_{80}	BL	$(667^{+206}_{-153}) \text{ km s}^{-1}$	0.49 ($< 10^{-3}$)	0.385 ($< 10^{-3}$)
	NL	$(637^{+206}_{-186}) \text{ km s}^{-1}$		0.189 (0.16)
Δv	BL	$(-110^{+110}_{-89}) \text{ km s}^{-1}$	-0.248 (0.013)	0.039 (0.712)
	NL	$(-111^{+98}_{-90}) \text{ km s}^{-1}$		0.132 (0.329)

Summarizing the results of this Section, we find a strong correlation between the [OIII] core/wing fluxes and the AGN accretion indicators, $L_{5100\text{\AA}}$ and $L_{2-10\text{keV}}$, which supports the hypothesis, that AGN are the excitation mechanism of the observed forbidden [OIII] transition in the our X-ray selected AGN spectra. The better correlation with the optical/UV flux is in agreement with the general picture about the photo ionizing UV radiation coming from the accretion disk. Furthermore, the core and wing widths correlate with both accretion related luminosities. Comparing BLAGN1 and NLAGN2, we find no differences for the [OIII] component velocities and velocity offsets. This indicates an independency of

the outflowing [OIII] features from central optical obscuration.

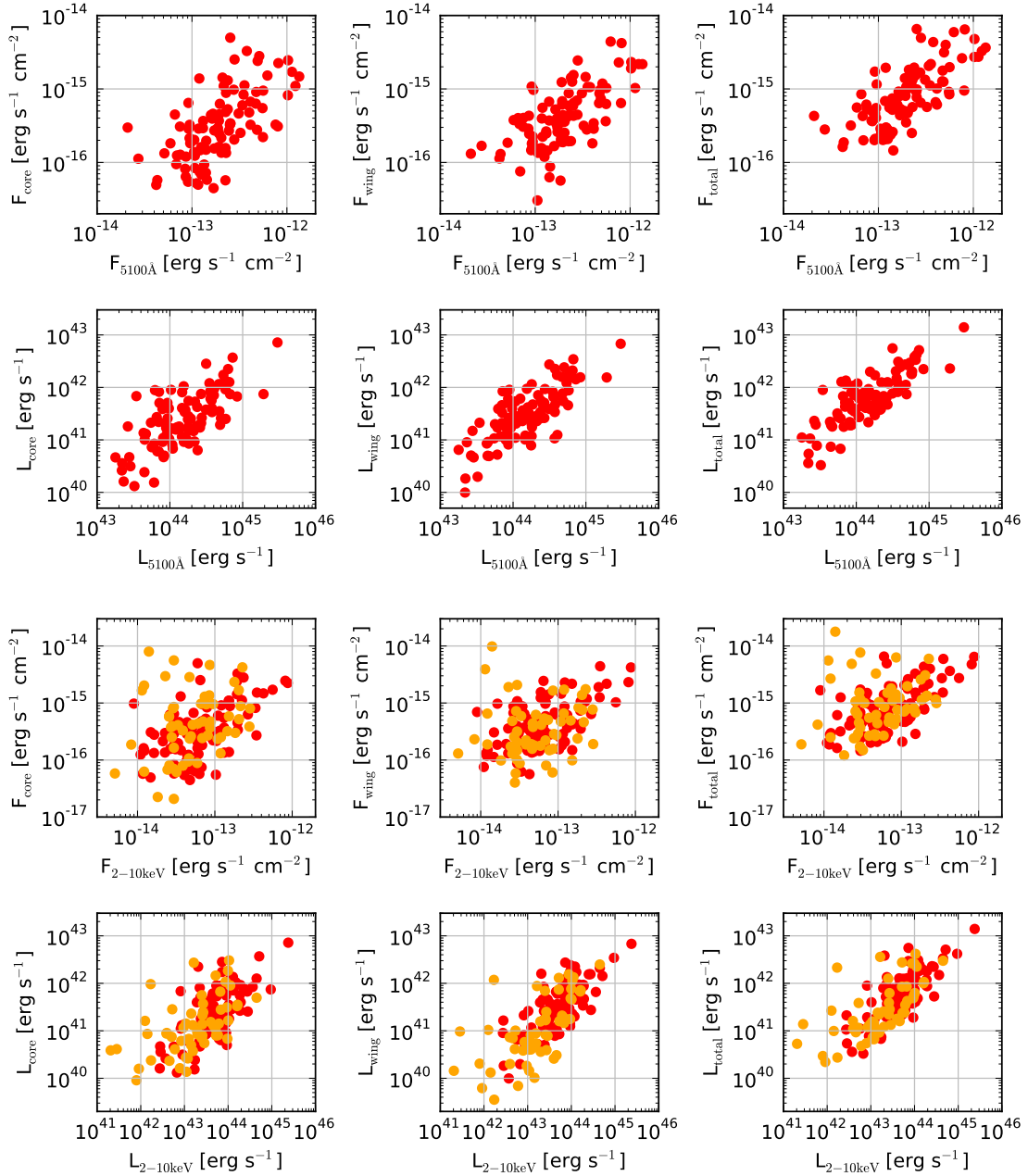


Figure 4.17.: Spearman Rank correlation of flux and luminosities of [OIII] components in BLAGN1 (red), NLAGN2 (orange) with optical/UV continuum flux or luminosity (two top rows) and hard X-ray flux or luminosity (two bottom rows).

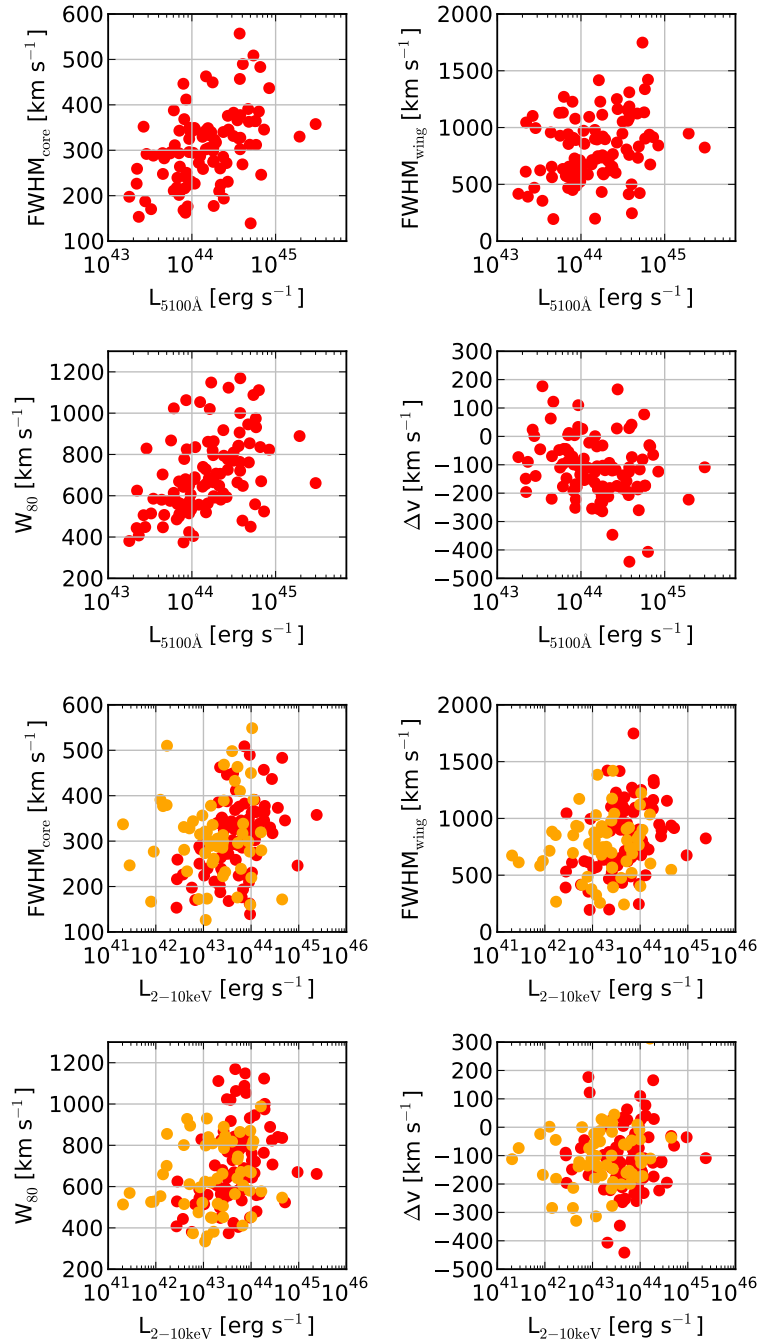


Figure 4.18.: Spearman Rank correlation of velocity-related parameters of [OIII] components in BLAGN1 (red), NLAGN2 (orange) with optical/UV continuum luminosity (two top rows) and hard X-ray luminosity (two bottom rows).

4.8.2. [OIII] outflows in the entire AGN population

In the subsample of AGN with significant asymmetric line components, we found strong correlations between [OIII] features and AGN accretion indicators. We now study the [OIII] outflows properties for the entire sample of X-ray selected AGN. Thus, we perform spectral stacks in dedicated luminosity bins and analyze the [OIII] line profile dependency on the hard X-ray luminosity and the optical/UV continuum luminosity.

AGN samples for spectral stacking

Firstly, we select all objects which have a hard X-ray band detection and create subsamples for BLAGN1 ($n = 417$), NLAGN2 ($n = 383$), BLAGN1 and NLAGN2 ($n = 800$), elusive AGN with star formation features ($n = 32$) and the redshift-complete subsample of X-ray selected AGN ($n = 376$). Secondly, we create a subsample of BLAGN1 which have non-zero optical/UV continuum luminosity ($n = 502$). The number of AGN with hard X-ray detections is limited to the sensitivity in the hard X-ray band, whereas for all BLAGN1, we can derive the optical/UV continuum luminosity from the *BOSS* spectra. We present the luminosity distributions of the introduced subsets in Fig. 4.19.

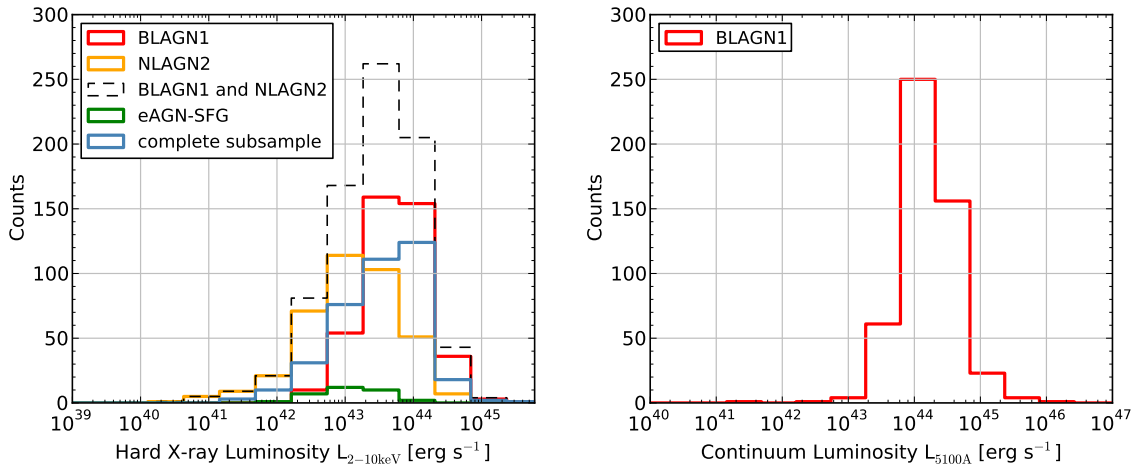


Figure 4.19.: Histogram of hard X-ray luminosity (left panel) and optical/UV continuum luminosity (right panel) for BLAGN1 (red), NLAGN1 (orange), elusive AGN in star forming galaxies (green) and the complete subsample of X-ray selected AGN (blue).

We now group the AGN populations (excluding eAGN-SFG objects) in three equal size luminosity bins and derive the spectral stacks in each luminosity bin. Following the methods presented in Sec. 4.7.3, we de-redden the individual spectra, subtract the continuum and convert them to luminosity. The median stacks are normalized to their maximum luminosity in order to compare the lines profiles. The spectral fits of the spectra and associated residuals are shown in Appendix C. In Tab. 4.6, we present the emission line parameters of [OIII] (5008 \AA). The indicated errors of the emission line features are derived by bootstrapping methods.

Excitation mechanism of [OIII] outflows

In order to study the excitation mechanism of [OIII] outflows, we stack BLAGN1 in AGN accretion-related luminosity bins ($L_{5100\text{\AA}}$ and $L_{2-10\text{keV}}$), as shown in Fig. 4.20, and determine the detailed [OIII] line properties. This allows to study which luminosity correlates better with the [OIII] profile in AGN.

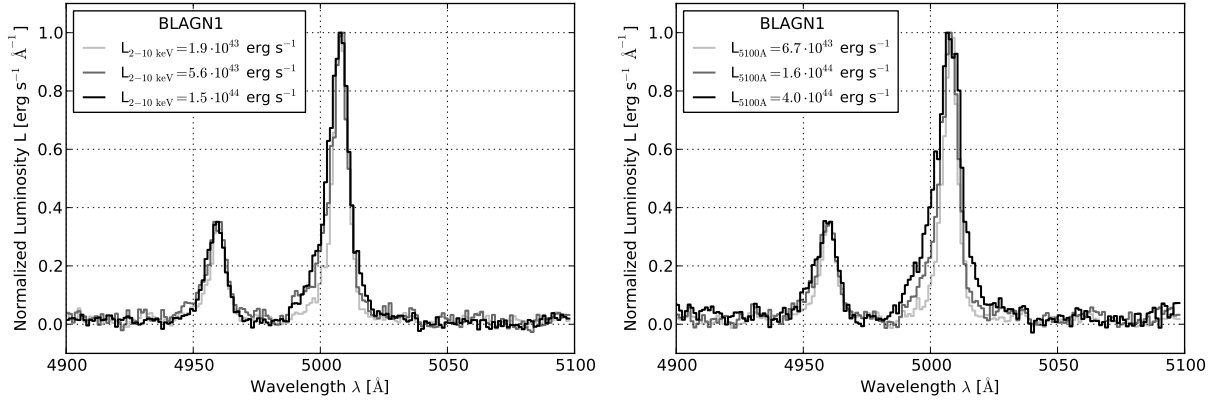


Figure 4.20.: Spectral stack of BLAGN1 in bins of hard X-ray luminosity and optical/UV continuum luminosity. The y-axis is normalized to the maximum luminosity of each spectral stack.

As presented in Fig. 4.21 (and Tab. 4.6), we find that the core and wing luminosity of BLAGN1 are correlated with both $L_{5100\text{\AA}}$ and $L_{2-10\text{keV}}$, which agrees with the Spearman rank correlation analysis from Sec. 4.8.1. The slopes of the core and wing luminosities as a function of $L_{5100\text{\AA}}$ and $L_{2-10\text{keV}}$ are comparable (for the core: $\alpha \approx 0.6$, for the wing: $\alpha \approx 1.1$). The velocities of the [OIII] component and W_{80} are more strongly correlated to L_{5100} than to $L_{2-10\text{keV}}$. Furthermore, the velocity of the wing component has a steeper slope ($\alpha = 483 \pm 68$ for L_{5100}) than the core component ($\alpha = 164 \pm 48$ for L_{5100}). For Δv , we cannot find a correlation in the binned spectral stacks.

In agreement with the previous section, we can conclude that average ionized [OIII] outflows are excited by the optical/UV continuum of the AGN. Additionally, we find that the $\text{FWHM}_{\text{core}}$ is less correlated to the AGN-related luminosity than $\text{FWHM}_{\text{wing}}$. Thus, we assume that the velocity dispersion of the narrow core component is dominated by the gravitational potential of the stellar bulge, and the wing component is largely tracing the velocity of the outflow launched by the AGN.

Impact of optical obscuration on [OIII] outflows

We are interested to test whether the optical obscuration of the central AGN has an impact on the [OIII] properties, and focus now on the spectral stacks of BLAGN1 and NLAGN2 performed in hard X-ray luminosity bins as presented in Fig. 4.22. For low luminosity bins, the stack of NLAGN2 shows a strong contribution of the host galaxy which clearly contaminates the AGN features. Our continuum model is not optimized to fit dedicated galaxy features and therefore, we cannot derive reliable wing features for low luminosity

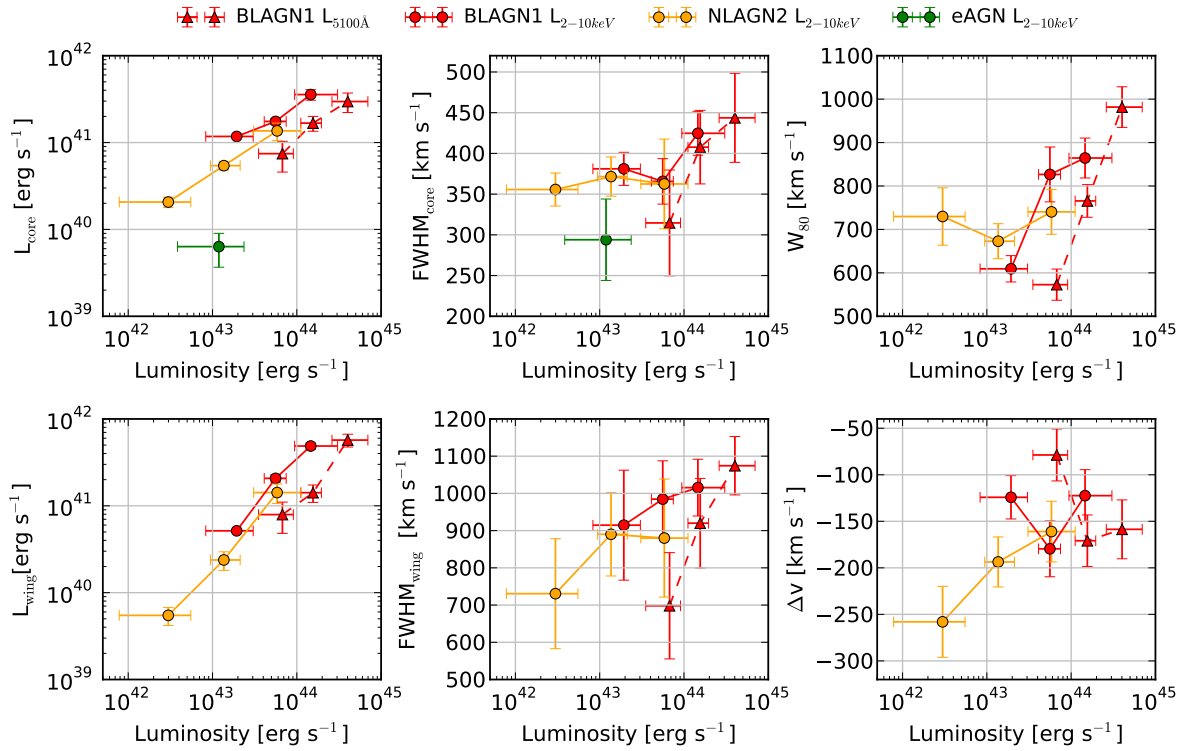


Figure 4.21.: Correlation of [OIII] parameters with optical/UV continuum luminosity and hard X-ray from stacked AGN. The markers indicated BLAGN1 stacked in L_{5100} (blue), BLAGN1 stacked in $L_{2-10\text{keV}}$ (red), and NLAGN2 stacked in $L_{2-10\text{keV}}$ (green).

bins in NLAGN2 and derive trends. Galactic line features strongly influences the wing fit of the [OIII] (4960 Å) emission line in particular.

We now compare the stacks of the BLAGN1 and NLAGN2 for two similar X-ray luminosity bins, which allows to study representative [OIII] line features for AGN of equivalent accretion properties, see Fig. 4.23. We find that the emission line features of both AGN are almost identical (see also Fig. 4.21 and Tab. 4.6). This leads to the conclusion, that the central obscuration has none or only a minor impact on the outflow properties.

In addition, we compare these results with the stacked spectra of eAGN-SFG. For this small subsample of 32 objects, we fit the [OIII] line with only one significant gaussian component, see Fig. 4.23. Apparently, eAGN-SFG do not have any [OIII] outflow features even if their X-ray luminosities indicate the presence of an AGN (see Menzel et al. (2016), Sec. 2.5.3). We know from the BPT diagram, that the gravitational NLR (core) component is dominantly excited by the star formation. Apparently, the central AGN is not able to excite and release [OIII] outflows in parts of the NLR. This might be due to very strong obscuration or galaxy dilution (for high SFR).

Concluding the analysis in this Section, the average ionized [OIII] outflows in our X-ray

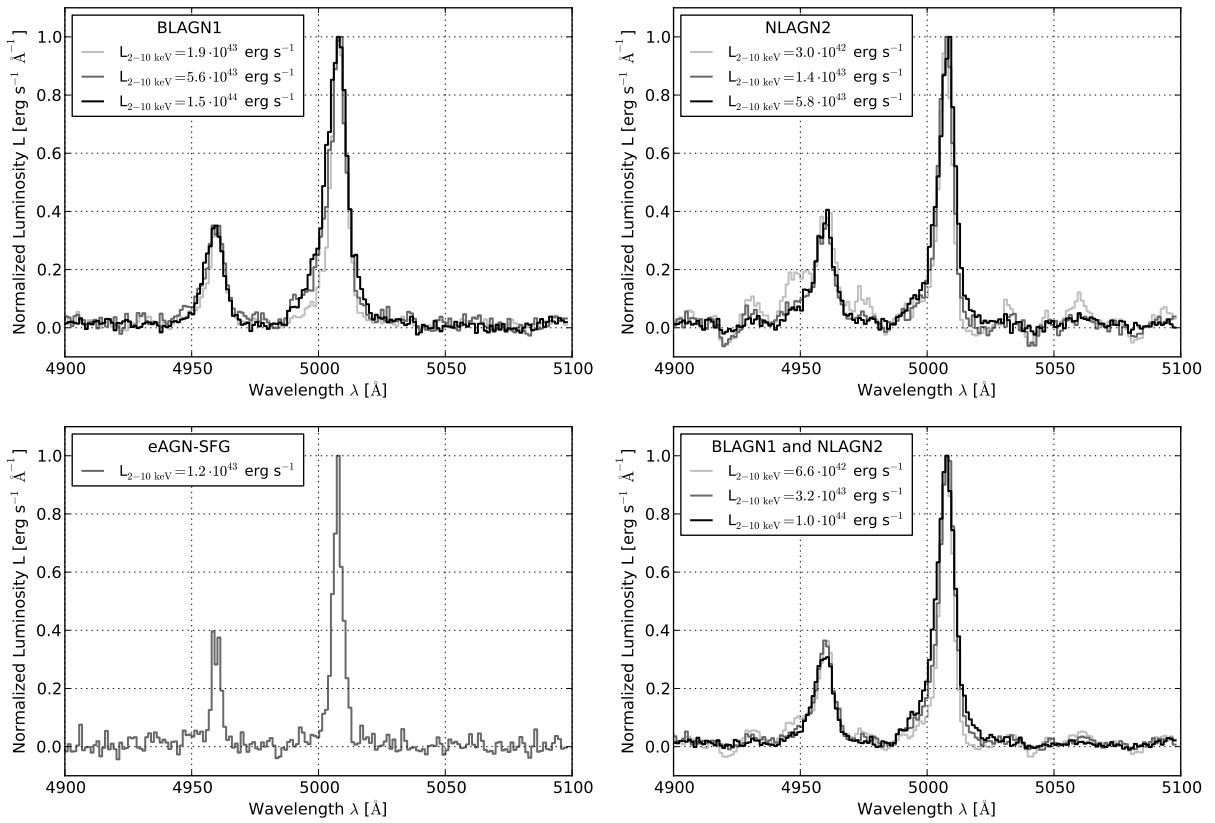


Figure 4.22.: Spectral stack of BLAGN1, NLAGN2 and all AGN in bins of hard X-ray luminosity. The y-axis is normalized to the maximum luminosity of each spectral stack.

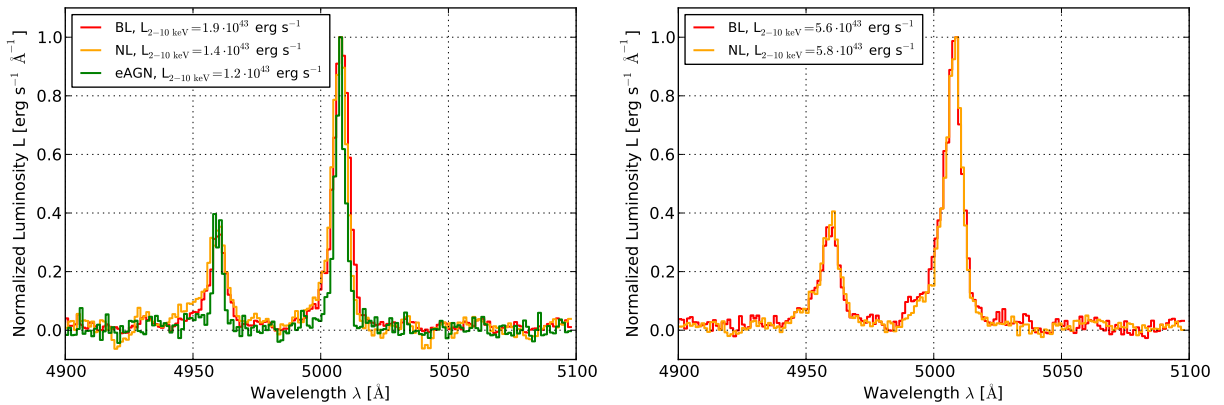


Figure 4.23.: Spectral stack of BLAGN1 (red), NLAGN2 (orange) and eAGN-SFG (green) in hard X-ray luminosity bins of $\approx 1.5 \cdot 10^{43} \text{ erg s}^{-1}$ and $\approx 5.7 \cdot 10^{43} \text{ erg s}^{-1}$. The y-axis is normalized to the maximum luminosity of each spectral stack.

selected AGN correlates with hard X-ray luminosity. The sample of BLAGN1 proves that the correlation is even better with the optical/UV continuum luminosity, but the latter

has the disadvantage not to be accessible for the entire population of AGN. We find that the [OIII] wing component is tracing an additional velocity field which can be attributed to the radial outflow beyond to the velocity of the stellar bulge. The profile of BLAGN1 and NLAGN2 for comparable AGN accretion properties have similar accretion properties indicating that the outflow characteristics are independent of the central obscuration.

Based on the obtained [OIII] profile parameters from the spectral stacks, we can now estimate the kinetic power and momentum boost which is 'transported' by average ionized [OIII] outflow properties in AGN. This is a highly valuable information for the impact of [OIII] feedback processes on the galaxy evolution.

Table 4.6.: [OIII] emission line parameter for BLAGN1, NLAGN2, eAGN-SFG and complete AGN sample in bins of hard X-ray luminosity and optical/UV continuum luminosity.

AGN type	$L_{5100\text{\AA}}$ [erg s ⁻¹]	L_{core} [erg s ⁻¹]	FWHM _{core} [km s ⁻¹]	L_{wing} [erg s ⁻¹]	FWHM _{wing} [km s ⁻¹]	W_{80} [km s ⁻¹]	Δv [km s ⁻¹]	z_{med}	R_{max} [kpc]
BLAGN1 (n=167)	$(6.8_{-3.2}^{+2.4}) \cdot 10^{43}$ $(1.6_{-0.4}^{+0.4}) \cdot 10^{44}$ $(4.0_{-1.4}^{+3.0}) \cdot 10^{44}$	$(7.5 \pm 2.9) \cdot 10^{40}$ $(1.7 \pm 0.3) \cdot 10^{41}$ $(3.0 \pm 0.8) \cdot 10^{41}$	315 ± 65 408 ± 45 444 ± 55	$(7.9 \pm 3.1) \cdot 10^{40}$ $(1.4 \pm 0.3) \cdot 10^{41}$ $(5.7 \pm 1.0) \cdot 10^{41}$	698 ± 143 920 ± 120 1074 ± 78	573 ± 36 766 ± 38 982 ± 47	-78 ± 28 -171 ± 28 -159 ± 32	0.45 0.65 0.84	5.82 7.02 7.84
AGN type	$L_{2-10\text{keV}}$ [erg s ⁻¹]	L_{core} [erg s ⁻¹]	FWHM _{core} [km s ⁻¹]	L_{wing} [erg s ⁻¹]	FWHM _{wing} [km s ⁻¹]	W_{80} [km s ⁻¹]	Δv [km s ⁻¹]	z_{med}	R_{max} [kpc]
BLAGN1 (n=139)	$(1.9_{-1.1}^{+1.1}) \cdot 10^{43}$ $(5.6_{-1.5}^{+1.9}) \cdot 10^{43}$ $(1.5_{-0.5}^{+1.6}) \cdot 10^{44}$	$(1.2 \pm 0.1) \cdot 10^{41}$ $(1.8 \pm 0.1) \cdot 10^{41}$ $(3.6 \pm 0.5) \cdot 10^{41}$	381 ± 20 366 ± 28 425 ± 27	$(5.2 \pm 0.1) \cdot 10^{40}$ $(2.1 \pm 0.2) \cdot 10^{41}$ $(4.9 \pm 0.4) \cdot 10^{41}$	914 ± 148 985 ± 103 1015 ± 76	609 ± 30 826 ± 63 864 ± 46	-124 ± 23 -180 ± 30 -122 ± 28	0.46 0.70 0.80	5.88 7.25 7.62
NLAGN2 ^a (n=128)	$(3.0_{-2.2}^{+2.6}) \cdot 10^{42}$ $(1.4_{-0.4}^{+0.8}) \cdot 10^{43}$ $(5.8_{-2.8}^{+5.3}) \cdot 10^{43}$	$(2.1 \pm 0.3) \cdot 10^{40}$ $(5.4 \pm 0.6) \cdot 10^{40}$ $(1.4 \pm 0.3) \cdot 10^{41}$	356 ± 20 372 ± 24 362 ± 55	$(5.5 \pm 1.3) \cdot 10^{39}$ $(2.4 \pm 0.6) \cdot 10^{40}$ $(1.4 \pm 0.4) \cdot 10^{41}$	731 ± 148 890 ± 112 880 ± 159	729 ± 66 673 ± 40 740 ± 52	-258 ± 38 -194 ± 27 -161 ± 33	0.21 0.39 0.66	3.49 5.30 7.05
BLAGN1	$(6.6_{-4.8}^{+6.3}) \cdot 10^{42}$	$(4.1 \pm 0.3) \cdot 10^{40}$	352 ± 20	$(1.2 \pm 0.1) \cdot 10^{40}$	836 ± 148	602 ± 66	-193 ± 38	0.29	4.41
NLAGN2 (n=267)	$(3.2_{-1.1}^{+1.6}) \cdot 10^{43}$ $(1.1_{-3.4}^{+1.3}) \cdot 10^{44}$	$(1.3 \pm 0.1) \cdot 10^{41}$ $(3.2 \pm 0.5) \cdot 10^{41}$	364 ± 28 416 ± 27	$(9.0 \pm 2.0) \cdot 10^{41}$ $(3.0 \pm 0.4) \cdot 10^{41}$	937 ± 103 1039 ± 76	705 ± 42 811 ± 33	-165 ± 32 -131 ± 23	0.56 0.78	6.57 7.53
eAGN-SFG (n=33)	$(1.2_{-0.8}^{+1.2}) \cdot 10^{43}$	$(6.34 \pm 2.67) \cdot 10^{39}$	294 ± 50					0.49	6.11
complete sample (n=124)	$(8.4_{-6.0}^{+6.3}) \cdot 10^{42}$ $(4.3_{-1.8}^{+1.8}) \cdot 10^{43}$ $(1.1_{-0.2}^{+1.0}) \cdot 10^{44}$	$(4.0 \pm 0.6) \cdot 10^{40}$ $(1.3 \pm 0.3) \cdot 10^{41}$ $(3.3 \pm 0.5) \cdot 10^{41}$	369 ± 19 350 ± 42 436 ± 28	$(1.0 \pm 0.3) \cdot 10^{40}$ $(1.2 \pm 0.3) \cdot 10^{41}$ $(2.3 \pm 0.5) \cdot 10^{41}$	762 ± 97 855 ± 149 1155 ± 110	640 ± 35 682 ± 46 793 ± 45	-203 ± 19 -128 ± 35 -118 ± 34	0.23 0.47 0.66	3.66 5.98 7.08

^ainfluenced by strong host galaxy features

4.8.3. The average outflow momentum rate and kinetic power of AGN outflows

Outflows are suggested to play an important role during feedback processes in galaxies. We know from IFU and multi-wavelength studies that they carry different phases, such as molecular, ionized or neutral material. We are interested in understanding, how the ionized [OIII] phase contributes to this process. We therefore determine the kinetic power and momentum boost of the average ionized [OIII] outflow in our sample and put them in the relation to the bolometric luminosity of the galaxy and the total momentum boost required to obtain the $M_{\text{BH}} - \sigma$ relation King et al. (2011); Zubovas & King (2012).

Introduction of required parameters

The analysis of the stacked [OIII] profile from the previous Section 4.8.2 allows for a determination of the average kinetic properties of the ionized [OIII] gas phase. As introduced by Cano-Díaz et al. (2012), the outflow rate $\dot{M}_{\text{out}}^{\text{ion}}$ and the kinetic power $P_{\text{kin}}^{\text{ion}}$ can be calculated as follows:

$$\dot{M}_{\text{out}}^{\text{ion}} = 164 \cdot \frac{C L_{44}^{\text{OIII,wing}} v_3}{\langle n_{e3} \rangle 10^{[\text{O}/\text{H}]} R_{\text{out,kpc}}} M_{\odot} \text{ yr}^{-1} \quad (4.22)$$

$$P_{\text{kin}}^{\text{ion}} = 5.17 \cdot 10^{43} \cdot \frac{C L_{44}^{\text{OIII,wing}} v_3^3}{\langle n_{e3} \rangle 10^{[\text{O}/\text{H}]} R_{\text{out,kpc}}} \text{ erg s}^{-1}. \quad (4.23)$$

Involved parameters are the wing luminosity, $L_{44}^{\text{OIII,wing}}$ of [OIII] in $10^{44} \text{ erg s}^{-1}$ (see Tab. 4.6), the wing velocity, v_3 in 1000 km s^{-1} , the electron density, n_{e3} in 1000 cm^{-3} , the radius of outflow $R_{\text{out,kpc}}$ in kpc, the ‘condensation’ factor, C , and the metallicity in solar units $10^{[\text{O}/\text{H}]}$.

The wing velocity, v , is the strongest uncertainty contributor to the kinetic energy. As discussed in Sec. 4.4.2, we chose the FWHM of the [OIII] wing component (see Tab. 4.6) as a parameter for the line of sight outflow velocity. Without further information about the outflow geometry and direction, we are not able to correct for any projection effects. The electron density, n_e , can be determined by different emission line tracers in the system. In case of missing emission line detection, previous studies assume typical value for n_e are in the range of $n_e = 100 - 1000 \text{ cm}^{-3}$. Works based on IFU observations by Cresci et al. (2015), Liu et al. (2013), assume a value of $n_e = 100 \text{ cm}^{-3}$. Harrison et al. (2014) use $n_e = 500 \text{ cm}^{-3}$ and Cano-Díaz et al. (2012) choose $n_e = 1000 \text{ cm}^{-3}$. A recently measured electron density for a $z \approx 1.5$ AGN (XID5395) from Brusa et al. (2016) ranges at $n_e = 780 \pm 300$. For the determination of the outflow’s electron density from available spectra, one requires the temperature-sensitive line wing ratios e.g. from SII and OII. Our stacks of X-ray selected AGN in the emission line regions of SII and [OII] do not allow for a decomposition into core and wing components. Therefore, we apply an electron density in the range of $n_e = 100 - 1000 \text{ cm}^{-3}$.

The determination of the outflow radius R_{out} would require access to high-resolution IFU observations of the individual objects. For our dataset comprising spectra from the same follow-up fibre-fed instrument, we can make a simple assumption based on the fibre radius of the *BOSS* spectrograph, as the maximal extension of the region within the aperture of

the fibre corresponds to 1 arcsec. We can then derive the maximal radius R_{\max} of the outflows based on the median redshift distribution of the stacked group, as shown in Tab. 4.6. The largest radius we obtain is 7.8 kpc, which is in agreement with most extreme observed outflows reaching up to 16 kpc (Harrison et al., 2014). For the estimation of the kinetic power, we assume that outflow radius can span a range of $R_{\text{out}} = 1 \text{ kpc} - R_{\max}(z_{\text{med}})$. The ‘condensation’ factor, $C = \langle n_e \rangle^2 / \langle \int n_e^2 f dV / \int f dV \rangle$, correlates with the electron density distribution in the ionized gas clouds. Assuming that all ionized clouds have the same density, the mass of the outflowing gas is independent of the filling factor f of the emitting clouds and one can apply $C = 1$. Finally, the metallicity in the ionized outflows is assumed to be solar: $10^{[O/H]} = 1$ (Asplund et al 2009).

Kinetic power of [OIII] outflows

We calculate the average AGN kinetic power of the ionized outflow derived from the fit to the [OIII] line in stacked spectra of different luminosity bins of $L_{2-10 \text{ keV}}$ and L_{5100} , and present the results in Fig. 4.24. The different markers indicate the kinetic power assuming the maximal and minimal ranges of n_e and R . We find that the kinetic power correlates with hard X-ray and optical/UV continuum luminosity, and ranges in the order of $P_{\text{kin}}^{\text{ion}} = 10^{40} - 10^{41} \text{ erg s}^{-1}$ for $R = R_{\max}(z_{\text{med}})$ and $n_e = 100 \text{ cm}^2$.

To compare the kinetic power of the outflow with the entire radiative power of the AGN, we derive the fraction of the ionized outflow kinetic luminosity over the bolometric luminosity. The bolometric luminosity is calculated with the median bolometric correction factor for this dataset from Liu et al. (2016) as follows:

$$L_{\text{bol,x}} = 18 \cdot L_{2-10 \text{ keV}}. \quad (4.24)$$

In the bottom panel of Fig. 4.24, we show that the kinetic outflow power contribution is a constant of ≈ 0.01 per cent and maximally reaches 0.2 per cent of the total bolometric luminosity.

The dataset of X-ray selected AGN in the XMM-XXL comprises a highly redshift complete sample of 372 AGN with spectroscopic follow-up. The entire analysis is equally performed on this subsample. Also for this sample, we obtain a kinetic power of $P_{\text{kin}}^{\text{ion}} = 3 \cdot 10^{40} - 3 \cdot 10^{41} \text{ erg s}^{-1}$ and a contribution to the bolometric luminosity of < 0.2 per cent

Momentum boost of [OIII] outflows

We now determine the average momentum rate $\dot{M}_{\text{kin}}^{\text{ion}} v$ of the ionized outflow within the maximal and minimal ranges of n_e and R . Additionally, we determine the ‘momentum boost’ by comparing this outflow momentum rate to the radiative momentum output of the entire AGN ($= L_{\text{bol}}/c$ k). In Fig. 4.25, we show that the momentum boost is stable for different AGN momentum rates and ranges from 10^{-3} to 1. For the complete subsample, we obtain an AGN momentum rate of $6 \cdot 10^{31} - 4 \cdot 10^{34} \text{ g cm s}^{-2}$ and an associated momentum boost of $10^{-3} - 0.6$.

Theoretical models [references] have shown that outflows with momentum boost in the order of 20 have a major impact on the $M_{\text{BH}}-\sigma$ scaling relation. Our data show, that [OIII] outflows cannot be responsible for establishing this relationship. Works by e.g. Ciccone et

al. (2014) with molecular outflows find that these outflows are more massive and provide higher momentum boost. Unfortunately, we are lacking the measurement of associated molecular outflows require study of multi-phases to estimate the full feedback process in our AGN.

As a consequence of the analysis in this Section, we find that the kinetic power and momentum rate of ionized [OIII] outflow phases are not sufficient to explain feedback processes in AGN.

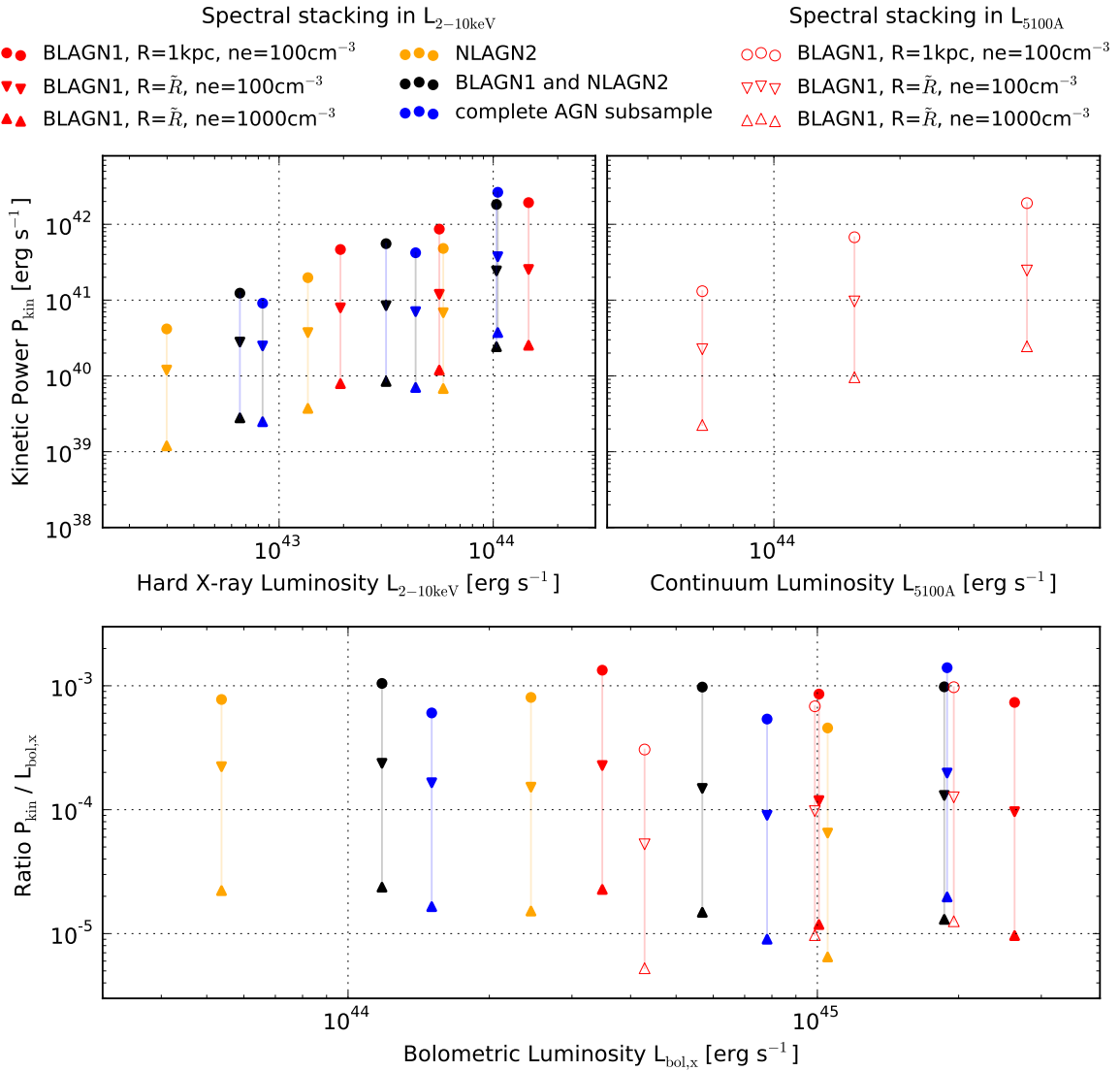


Figure 4.24.: Top panels: Average kinetic power of the AGN ionized outflows. Bottom panel: Contribution to the bolometric luminosity in hard X-ray and continuum luminosity bins.

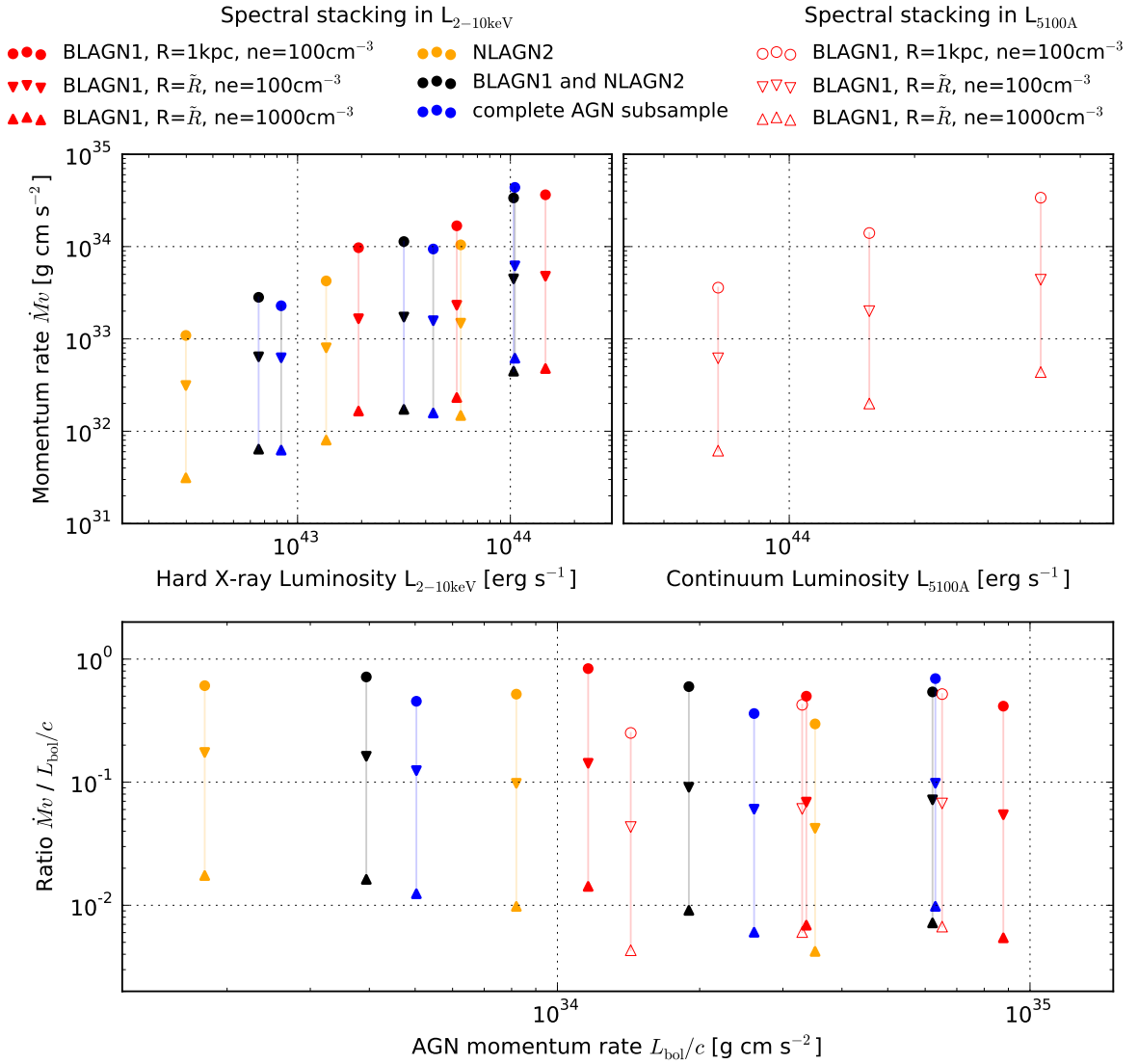


Figure 4.25.: Top panels: Average outflow momentum rate. Bottom panel: Ratio (,momentum boost') with AGN momentum rate in hard X-ray and continuum luminosity bins.

4.9. Discussion

In this Chapter, we focussed on ionized outflows and inflows in the narrow lines regions of a large X-ray selected AGN sample, and studied their incidence, excitation mechanism and impact on feedback. Herby, we concentrated on the [OIII] (5008 Å) emission line, which is sensitive to ionizing radiation reaching galaxy-wide extent. We developed a dedicated emission line fitting algorithm, which provides detailed information about the [OIII] emission line profile. This algorithm includes up to two gaussian components per emission line, and allows for the study of NLR parts which are affected by the gravitational potential of the stellar bulge and NLR parts, which are affected by outflows or inflows. The comparison with [OIII] emission line profiles in star forming galaxies and the correlation of [OIII] line parameters with AGN accretion indicators give insights in the excitation mechanism of these outflows.

Comparable studies of [OIII] outflows in X-ray selected AGN surveys have been performed by Harrison (2016) with a sample of 89 AGN at the redshift range $1.1 < z < 1.7$ from *Chandra* and *XMM-Newton* catalogues with *KMOS* follow-up, analyzing the emission line luminosities as a function of X-ray luminosity and the impact of obscuration. Ueda et al. (2015) studies 103 *Swift/BAT* observed sources with optical spectroscopic follow-ups from the *South African Astronomical Observatory*. They focus on the relationships between X-ray and optical (low and high ionization) emissions lines. In contrast to these works our sample exceeds the size of the previous surveys (837 AGN), and additionally probes a highly redshift complete AGN population which can give predictions about representative [OIII] outflows in AGN.

Optically selected large AGN surveys from *SDSS* have been studied in the e.g. works by Zhang et al. (2011); Jin et al. (2012); Mullaney et al. (2013); Peng et al. (2014) and Woo et al. (2016). These works address correlation of [OIII] line parameters with AGN properties and spectral features, impact of radio emission and the ability of the [OIII] core component to trace stellar velocity dispersions.

How often do [OIII] outflows occur in AGN?

For the study of [OIII] outflow incidence, we refer to a subsample in our X-ray selected dataset. Among this sample, we find that 35 per cent of the objects have indications for [OIII] outflows or inflows. This should be considered as a lower limit, because S/N ratio and obscuration by the host galaxy strongly effect the detection of significant [OIII] outflows.

The [OIII] outflow/inflow incidence is difficult to compare with recent literature values, because of biases due to selection criteria and S/N ratio of the spectra. Mullaney et al. (2013) finds 17 per cent of outflows for optically selected Type 1 and Type 2 AGN (*SDSS* DR7), whereas Harrison et al. (2014) find ≥ 70 per cent in a representative sample of X-ray selected Type 2 with $L_{OIII} > 7 \cdot 10^{40} \text{ erg s}^{-1}$ and $z < 0.2$.

The large majority (84 per cent) of our [OIII] profiles shows blueshifted [OIII] wing features which is consistent with the widely used model of biconical outflows. Works related to this model (e.g. Crenshaw et al. 2010) assume that outflow cone which is pointing away from the observer suffers extinction from the stellar disk. The explanation of origin of redshifted [OIII] wings requires a detailed modeling taking into account narrow line kinematics (Bae

& Woo, 2016), which is not in the scope of this work.

Does star formation cause [OIII] outflows?

In order to analyze the impact of star formation activity on the observed [OIII] outflows, we compare our dataset with a sample of 4117 emission line galaxy (ELG) (Zhu et al., 2015) from *eBOSS* which are part of the study of baryonic oscillations in galaxies at redshift $0 < z < 1.5$.

The median velocity dispersions (corrected for the resolution of the spectrograph) of the [OIII] emission lines in ELG ($\sigma \approx 110 \text{ km s}^{-1}$) and the [OIII] core component in AGN ($\sigma_{\text{core}} = 150 \text{ km s}^{-1}$) correspond to the normal narrow line region velocity dispersions of local Seyfert galaxies ($\sigma < 250 \text{ km s}^{-1}$). However, we find that the sample of ELG tends to have less broad cores than AGN. This velocity dispersion difference can be caused by a variety of factors: The distance of the excited NLR to the central nuclei might be different in case of star formation; or ELG might have smaller stellar masses than AGN which results in a less strong gravitational potential for the NLR. Another factor can be the impact of selection effect as presented by Bongiorno et al. (2012), who studied a sample of X-ray selected AGN in the *COSMOS* field and discuss that the likelihood to find an AGN - of a certain Eddington ratio in a galaxy of a certain mass - is smaller for less massive galaxies in flux limited samples. This effect has also been discussed by Merloni & Heinz (2008) and observationally confirmed by Aird et al. (2012).

In the ELG sample, we find that that only 1-2 per cent of the galaxies show indications of outflows or inflows which are affecting the [OIII] emission line. The large difference of this incidence in AGN and ELG is independent of S/N ratio and represents a clear evidence for an additional component shaping the [OIII] line profiles in AGN. We identify this with an outflow associated with or driven by the central accreting SMBH.

To further prove that star formation is not the major driver of [OIII] outflows, we matched BLAGN1, NLAGN2 and ELG in star formation rate and performed spectral stacking. We find that stacked ELG spectra show nearly no indications for [OIII] outflows, which agrees well with the works of Zhu et al. (2015), who analyzed star formation driven wind features in the same dataset of ELG. Ciccone et al. (2016) discuss the correlation of outflow incidence with the star formation rate and conclude that typical main sequence star formation galaxies do not have enough SFR to produce these strong outflows as observed in starburst galaxies. Our ELG sample can be associated to this main sequence and thus the effect of star formation is unlikely to cause wings in the [OIII] profiles.

In contrast to the ELG, we can fit significant [OIII] wing components to the spectral stacks of BLAGN1 and NLAGN2, and obtain median velocities of $\text{FWHM}_{\text{wing}} = 1000 \text{ km s}^{-1}$ and maximal velocities of $\text{FWHM}_{\text{wing}} = 1800 \text{ km s}^{-1}$. These velocities largely exceed extreme observed outflows of starburst galaxies with median velocities of 500 km s^{-1} and maximal 1000 km s^{-1} (e.g. Rupke & Veilleux 2013, Hill & Zakamska 2014).

Summarizing, we find a significant outflowing/inflowing component in the [OIII] profile

of the X-ray selected AGN. For comparable SFR, this is opposed to ELG, where no ionized [OIII] outflows/inflow features can be observed. Complemented by the striking difference of outflow incidence in AGN and ELG, we can assume that the presence of ionized [OIII] outflows/inflows in our AGN is not caused by star formation and requires an excitation mechanism, most likely originating in the AGN itself.

Does AGN activity cause [OIII] outflows?

In this Chapter, we performed correlations with characteristic AGN accretion indicators such as optical/UV continuum luminosity and hard X-ray luminosity. The firstly mentioned luminosity is directly released from the accretion disk, but can be diluted by strong host features (especially in NLAGN2). The hard X-ray luminosity represents the inverse Compton scattered emission from the disk, but shows a scatter compared to the optical/UV continuum. However, X-rays can be considered as largely unaffected by gas obscuration and are a good surrogate of the AGN continuum luminosity in both BLAGN1 and NLAGN2.

We demonstrated that the observed [OIII] wing component in the optical spectra of our X-ray selected AGN might be largely due to AGN activity. Our results are confirmed by works of Concas et al. (2016, in prep.) who studied *SDSS* galaxies at different stellar masses and star formation rates, and found that the wing component in the [OIII] profile is due to AGN contribution.

Going into detail, the luminosities of the [OIII] component in the sample of BLAGN1 correlate more strongly with the optical/UV continuum than with the hard X-ray luminosity. This is reasonable, because the optical/UV continuum of the accretion disk is directly responsible for the [OIII] excitation, whereas the hard X-ray luminosity represents reprocessed emission from the disk. The scatter between [OIII] luminosity and hard X-ray emission is caused by a variety of effects. This are e.g. the properties of the NLR, such as the covering factor, the density of the gas and contamination by star formation. Further luminosity-dependent parameters are e.g. the spectral slope between UV and X-ray, the opening angle of the NLR cone and the NLR density (see references in Ueda et al. 2015). The travel time between the turning-on of the AGN, which is immediately visible in UV and X-ray, and the narrow line region is another complexity factor of the scatter. We cannot resolve the location of the outflow, but estimate the radius from the fibre size of the *BOSS* spectrograph, which leads to a travel time of $3 \cdot 10^4 - 2 \cdot 10^5$ yr, consistent with estimates of AGN flickering timescales by Schawinski et al. (2015).

The long travel time between the central AGN and the distant NLR would imply, that we observe AGN-excited outflows in galaxies whose AGN just turned-off. Unfortunately, the ELG sample is not selected for this science case and does not include a complete sample of galaxies to evaluate this effect.

The study of FWHM of the [OIII] components as a function of AGN accretion-related luminosity supports the idea, that the broad core component traces an additional velocity field beyond the gravitational potential of the stellar bulge, which is mainly shaping the narrow component.

The study of [OIII] outflows in NLAGN2 is challenging, because host galaxy features are more dominant in the optical spectra. Only for luminous NLAGN2 the host contribution decreases and AGN emission line profiles can be estimated. For future studies, we require dedicated host-AGN decomposition algorithms in order to obtain ‘clean’ AGN features.

What is the [OIII] outflow geometry in AGN?

According to the ‘obscuration by orientation’ picture of AGN (e.g. Antonucci 1993), BLAGN1 and NLAGN2 are intrinsically the same. In a simple AGN model, the black hole is surrounded by an obscuring toroidal structure and the NLR is located at large distance from the black hole being observable for both AGN types. The central obscuring ‘torus’ should channel the AGN emission in a biconical shape and thus, one should observe faster and more blueshifted [OIII] wings in BLAGN1 than in NLAGN2.

In our dataset, the narrow [OIII] core component, which is affected by the gravitational potential of the stellar bulge, shows no significant differences between BLAGN1 and NLAGN2, which agrees with the initial hypothesis. Anyhow, we observe that for BLAGN1 and NLAGN2, at comparable AGN accretion power, the [OIII] wing velocity and blueshift as well as the incidence of [OIII] outflows are similar. This is a clear disagreement with the orientation-dependent unification scheme and a bi-conical outflow structure.

Previous studies about the effect of the central obscuration on [OIII] outflow features e.g. by Mullaney et al. (2013) find that Type 2 AGN have smaller outflow widths; and Peng et al. (2014) observes a large blueshift for Type 1 AGN. We have to note that, in contrast to our sample, both samples have been optically selected and no additional AGN accretion-related threshold has been applied. The observed difference in BLAGN1 and NLAGN2 might be caused by selection effects.

Given our well-controlled selection, we conclude that the simple AGN unification model with an homogenous torus causing a biconical outflow model is not sufficient to explain our observations. We suggest, that the outflow gets dispersed after leaving the torus, as illustrated in Fig. 4.26. This allows for the observation of equally fast and blueshifted [OIII] emission line profiles in both BLAGN1 and NLAGN2.

The velocity offset of the [OIII] wing component is only weakly correlated to $L_{5100\text{\AA}}$ ($r_{\text{Spearman}} = -0.248$). Similar studies have been performed by Zhang et al. (2011) and Peng et al. (2014). In addition, we find that the outflow decelerates while passing the ISM, as been shown in the correlation between Δv and $\text{FWHM}_{\text{wing}}$ and agreeing with works of Woo et al. (2016).

We conclude, that the geometry of [OIII] ionized outflows is strongly influenced by the intergalactic medium which is decelerating the outflowing gas. Opposed to traditional outflow models, we suggest that a kinematic dispersion occurs after the outflow leaves the torus. This results in outflow features which are independent (or weakly influenced) from the nuclear obscuration properties of AGN.

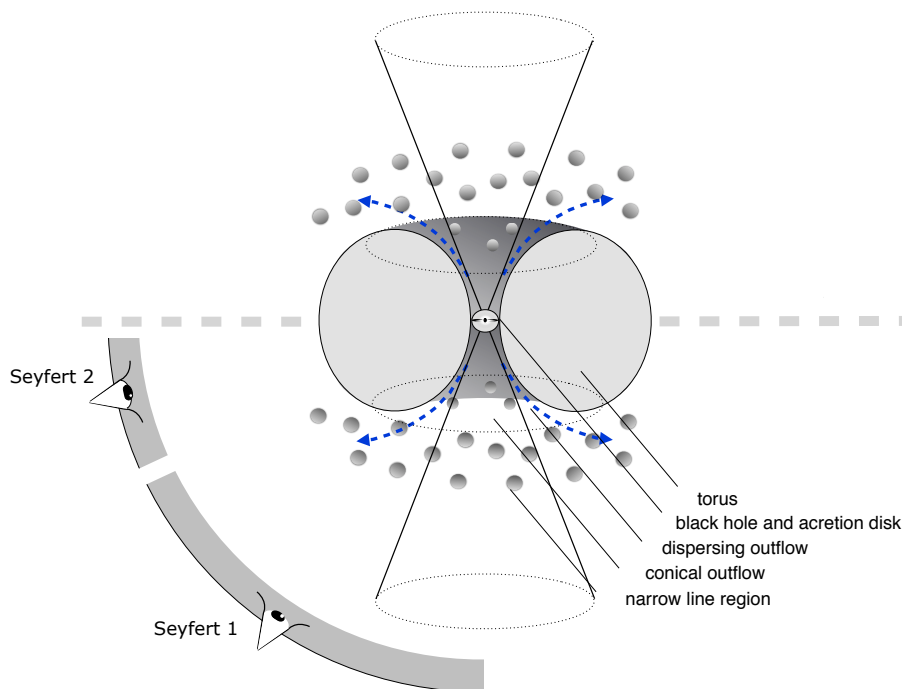


Figure 4.26.: Model of a bipolar conical and a dispersing outflow shaped by the torus.

Do [OIII] outflows contribute to the feedback process in AGN?

In order to evaluate the impact of [OIII] outflows in feedback processes, we firstly estimated the released kinetic energy of an average ionized [OIII] outflow at around $P_{\text{kin}}^{\text{ion}} = 3 \cdot 10^{40} - 3 \cdot 10^{41} \text{ erg s}^{-1}$. This kinetic power contributes < 0.2 per cent to the bolometric luminosity output. Our results for the kinetic power of the ionized outflow should be considered as estimate, because we cannot determine the outflow radius, projection corrected [OIII] wing FWHM and the electron density for each source and refer to commonly used values. Anyhow, studies on X-ray selected AGN e.g. from Brusa et al. (2015) determine kinetic powers in the same order of magnitude. Most extreme ionized [OIII] outflows have been observed by Harrison et al. (2012) in high redshift luminous QSOs and reach kinetic powers up to $P_{\text{kin}}^{\text{ion}} \approx 10^{45} \text{ erg s}^{-1}$.

Starting from the average kinetic energy of the [OIII] outflows, we extrapolate the total energy released during the ‘on-phase’ of the AGN. Assuming a typical AGN lifetime (‘on-phase’) of $3 \cdot 10^7 \text{ yr}$ (Hopkins et al., 2005), results in a total energy of $E^{\text{ion}} \approx 10^{55} - 10^{57} \text{ erg}$ released by ionized [OIII] outflows in the sources in our sample. For an average black hole mass of $M_{\text{BH}} = 10^8 M_{\odot}$ with a 10 per cent radiative efficiency from the accretion process ($E_{\text{BH}} \approx 10^{61} \text{ erg}$), only $0.01 - 10^{-4}$ per cent of the emitted energy is driving the ionized [OIII] outflows. Extending the view to the entire galaxy with a velocity dispersion of $\sigma = 200 \text{ km s}^{-1}$, the total released energy by ionized [OIII] outflows does not exceed the binding energy ($E_{\text{gal}} \approx 10^{59} \text{ erg}$) and is lower by a factor of a 1 – 100.

Next to the kinetic energy, also the average momentum rate of the outflow contributes

strongly to the feedback process. Works by King et al. (2011); Zubovas & King (2012) predict that AGN accreting close to the Eddington limit have outflow momentum fluxes of $\sim 20 L_{\text{bol}}/c$, which supports the idea of AGN-driven feedback creating shock waves to propagate into the surrounding ISM. For our sample we obtain rates of $10^{31} - 10^{34} \text{ g cm s}^{-1}$, which have - compared to the total momentum rate of the AGN - a momentum boost in the order of 10^{-3} to 1. In contrast to that, studies about molecular outflows (e.g. Cicone et al. 2014) obtain larger momentum boost in the order of $\sim 20 L_{\text{bol}}/c$.

Concluding, the properties of the ionized [OIII] outflows are not sufficient to be solely responsible for feedback mechanisms in AGN. One has to be aware that outflows carry different phases of gas and matter which are not included in this work's scope. Thus, we suggest that ionized [OIII] phases accompany further outflow phases such as molecular and neutral phases (Feruglio et al., 2015; Rupke & Veilleux, 2011; Cicone et al., 2014) which have a major share in the feedback process.

4.10. Summary: Relevance of ionized outflows for AGN feedback

We studied the narrow emission line kinematics in X-ray selected AGN. Concentrating on the [OIII] emission line allows for a detection of ionized gas clouds being affected the gravitational potential of the galaxies or by outflows or inflows. We developed a dedicated line fitting algorithm to decompose the [OIII] emission into these two components, for AGN at a redshift $0 < z < 1$. In order to derive the excitation mechanism and characteristic properties of the observed outflows, we compared the OIII emission line profile with a sample of star forming emission line galaxies and performed correlation studies with AGN properties. The redshift complete sample of AGN allows for an estimate of the average kinematic power released by an average ionized [OIII] outflow in the overall population of X-ray selected AGN, which can be used to evaluate the impact on feedback processes.

In the following, we conclude with the main scientific outcomes of this Chapter:

- (i) We find incidences of ionized OIII outflow/inflow features in > 35 per cent of a highly redshift complete AGN sample ($F_{2-10\text{keV}} > 2.5 \cdot 10^{-14} \text{ erg s}^{-1}$, $0 < z < 0.8$). 75 per cent of the OIII wing components are blueshifted and can be interpreted as outflows. The blueshift-velocity dispersion indicates that the outflows are decelerated by the ISM.
- (ii) The ionized OIII outflow features in our X-ray selected AGN sample cannot be caused solely by star formation. We find strong correlations of line luminosity with AGN properties, such as hard X-ray luminosity and optical/UV continuum luminosity, which indicates that the AGN is the excitation mechanism of [OIII] outflows. The outflow velocity of the [OIII] line is affected by the radial velocity of the AGN wind and the velocity dispersion of the narrow core component caused by the gravitational component of the stellar bulge.
- (iii) We observe that ionized OIII outflow/inflow features are similar in BLAGN1 and NLAGN2, and have the same [OIII] wing profiles at comparable hard X-ray luminosity. This disagrees with the model of a biconical outflow structure in the AGN unification scheme. We suggest that a dispersion of the outflow might cause the orientation independence.
- (iv) The elusive AGN-SFG show no characteristic AGN [OIII] outflow features next to the star formation excited NLR, which supports the hypothesis, that the central AGN is completely obscured or, less likely, outshone by the galaxy.
- (v) The kinetic power of average ionized [OIII] outflows contributes ≈ 0.01 per cent to the bolometric luminosity of the AGN and their momentum boost is in the order of ≈ 0.1 . This is not sufficient for the feedback process causing the $M_{\text{BH}} - \sigma$ -relation for AGN and their host galaxies.

5. Forecast for *eROSITA* AGN population, summary and prospects for the future

5.1. Forecast for the AGN population of *eROSITA*

In the upcoming all sky X-ray survey by *eROSITA* (Merloni et al., 2012; Predehl et al., 2014), a large X-ray AGN population which will be discovered. Our dataset in the XMM-XXL enables us to predict the number densities and characteristics of this population. The following section presents the *eROSITA* instrument and its follow-up programmes. Furthermore, we predict the spectroscopic completeness of X-ray selected AGN and the X-ray detection fraction of optical and infrared selected AGN in the *eROSITA* survey.

5.1.1. *eROSITA* instrument

The name *eROSITA* stands for *extended Roentgen Survey with an Imaging Telescope Array*. Together with the Russian hard X-ray telescope (*ART-XC*), this instrument constitutes the scientific payload onboard the German-Russian *Spektrum-Roentgen-Gamma* (SRG) mission, which is due to be launched in late 2017.

The *eROSITA* telescope follows a long tradition of X-rays instruments developed at MPE. The X-ray mission *ROSAT* was launched in 1990 and made great progress in resolving the all-sky cosmic X-ray background into individual sources. The subsequent pencil-beam mission, *XMM-Newton*, launched in 1999, had access to the hard X-ray bands and contributed to study, among many other subjects, the obscured SED shape of AGN. *eROSITA* is designed to pursue the study of the X-ray sky and fulfill multiple scientific goals, such as

- (i) the study of galaxy clusters in order to analyze large scale structure and test cosmological models,
- (ii) the study of AGN in order to analyze different obscurations, evolutionary states and activity episodes,
- (iii) the discovery and study of rare objects,
- (iv) the study of solar and galactic neighborhood.

The instrumental design of *eROSITA* is motivated by its science goals, which require an all-sky survey, high precision, high sensitivity for both point like and extended sources, and the availability of both soft and hard X-ray bands.

The telescope structure, as presented in Fig. 5.1, has a diameter of $d = 1.9$ m and a length of $l = 3.1$ m, and has a weight of ~ 800 kg. The mirror system consists of seven

identical and co-aligned mirror modules with 54 shells ($l = 30$ cm, $r = 36$ cm). Each shell is coated by nickel and supported by a spider wheel. The multi-module structure enables a shortening of the focal length to 1.6 m (in comparison to *XMM-Newton*) and the co-alignment ensures their identical field of view. The X-ray photons are detected by a pn-CCD camera with an image area of 28.8×28.8 mm² (384 x 384 pixels with $75 \mu\text{m}$ pixel size) and a field of view of $d = 1.03$ deg. The on-axis spatial resolution (HEW at 1.5 keV is 15 arcsec) and effective area at low energies (1365 cm² at 1 keV) are comparable with the instrument *XMM-Newton*. *eROSITA* will reach the highest sensitivity in the 0.5–8 keV band ($\sim 10^{-14} - 10^{-15}$ erg s⁻¹ cm⁻²), compared to its predecessors all-sky X-ray instruments, such as *HEAO-1* ($\sim 10^{-11}$ erg s⁻¹ cm⁻², Piccinotti et al. 1982) and *ROSAT* ($\sim 10^{-13}$ erg s⁻¹ cm⁻², 2RXS Boller et al. 2016).

To ensure the CCD working temperature of -90°C , the thermal control is realized by two radiators and cryogenic heat pipes. The *eROSITA* instrument suffers a flux of 30–40 high energetic particles per second which have a strong impact on the electronics. The instrument is protected by a copper shield against particles and an additional Aluminum/Boron/Beryllium shield for their fluorescence. Merloni et al. (2012) predicts that the soft band of the instrument will be dominated by the cosmic X-ray background ($2.14 \cdot 10^{-3}$ cts s⁻¹ arcmin⁻²), and the hard band ($E > 5$ keV) will be dominated by the high-energy particle background ($0.92 \cdot 10^{-3}$ cts s⁻¹ arcmin⁻²).

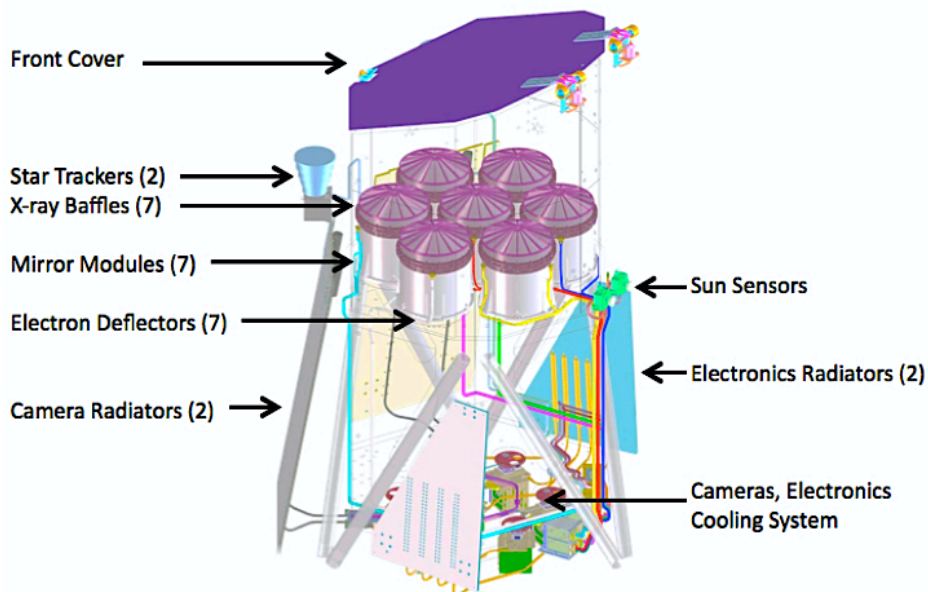


Figure 5.1.: Schematic diagram of *eROSITA* telescope structure. Graphic taken from Merloni et al. (2012).

After launch, *eROSITA* will reach its position in the Lagrangian point L2 at a distance of circa one million kilometers from Earth. In L2, *eROSITA* suffers from higher cosmic radiation than inside the Earth's magnetic field, but it is less exposed to strong heat differences e.g. in low earth orbit. The observation axis of the instrument is always perpendicular to the sun, which results in shallowest exposure at the ecliptic equator and deepest exposure

at the ecliptic poles area. *eROSITA* performs one full circle every four hours and shifts one degree per day. As a consequence, the full sky will be covered after 180 days.

For an angular resolution averaged across the field of view of about 26" (half energy width, Burwitz et al. 2014), the predicted flux limits of *eROSITA* in an equatorial field are presented in Tab. 5.1. There, eRASS:*n* corresponds to the depth reaches after the *n*th all-sky survey.

Table 5.1.: *eROSITA* flux limits during 4 years survey time.

	eRASS:1	eRASS:2	eRASS:4	eRASS:8
Survey time [yr]	0.5	1	2	4
$F_{0.5-2\text{keV}}$ [erg s ⁻¹ cm ⁻²]	$4.0 \cdot 10^{-14}$	$2.5 \cdot 10^{-14}$	$1.5 \cdot 10^{-14}$	$9.8 \cdot 10^{-15}$

Comparing to the *ROSAT* all-sky survey (Voges et al., 1999), the X-ray selected AGN density of *eROSITA* over the whole sky is going to increase from $\sim 3 \text{ deg}^{-1}$ to $\sim 90 \text{ deg}^{-1}$. The *XMM-Newton* survey in the XMM-XXL (Menzel et al., 2016) reaches a depth comparable to the deepest planned *eROSITA* exposure near the ecliptic poles ($F_{0.5-2\text{keV}} \sim 4.0 \cdot 10^{-15} \text{ erg s}^{-1} \text{ cm}^{-2}$) covering a solid angle of $\approx 500 \text{ deg}^2$.

5.1.2. Follow-up programmes of *eROSITA* sources

For the understanding of the *eROSITA* AGN population, it is of high interest to perform spectroscopic follow-up in order to retrieve information about redshift as well as obscuration, accretion, host galaxy and outflows/inflows properties. For the spectroscopic follow-up of X-ray AGN, it is first necessary to perform correct optical or infrared counterpart associations.

As shown in Fig. 5.2, the *eROSITA* survey will benefit from large photometric surveys in different wavelength bands. During the first exposure phase of *eROSITA* (eRASS:1), primary multi-band imaging surveys for counterpart associations are *SDSS*, *WISE*, *VHS*, *GALEX* and soon to be released *PanSTARRS*. Deeper imaging data for final *eROSITA* full-sky scans (eRASS:8) can be provided by *DES*, *Euclid* and *LSST*.

Spectroscopic follow-up will be obtained among others, with *eBOSS* (Dawson et al., 2016) in the northern hemisphere and in the future with *4MOST* (www.4most.eu) in the southern hemisphere.

5. Forecast for *eROSITA* AGN population, summary and prospects for the future

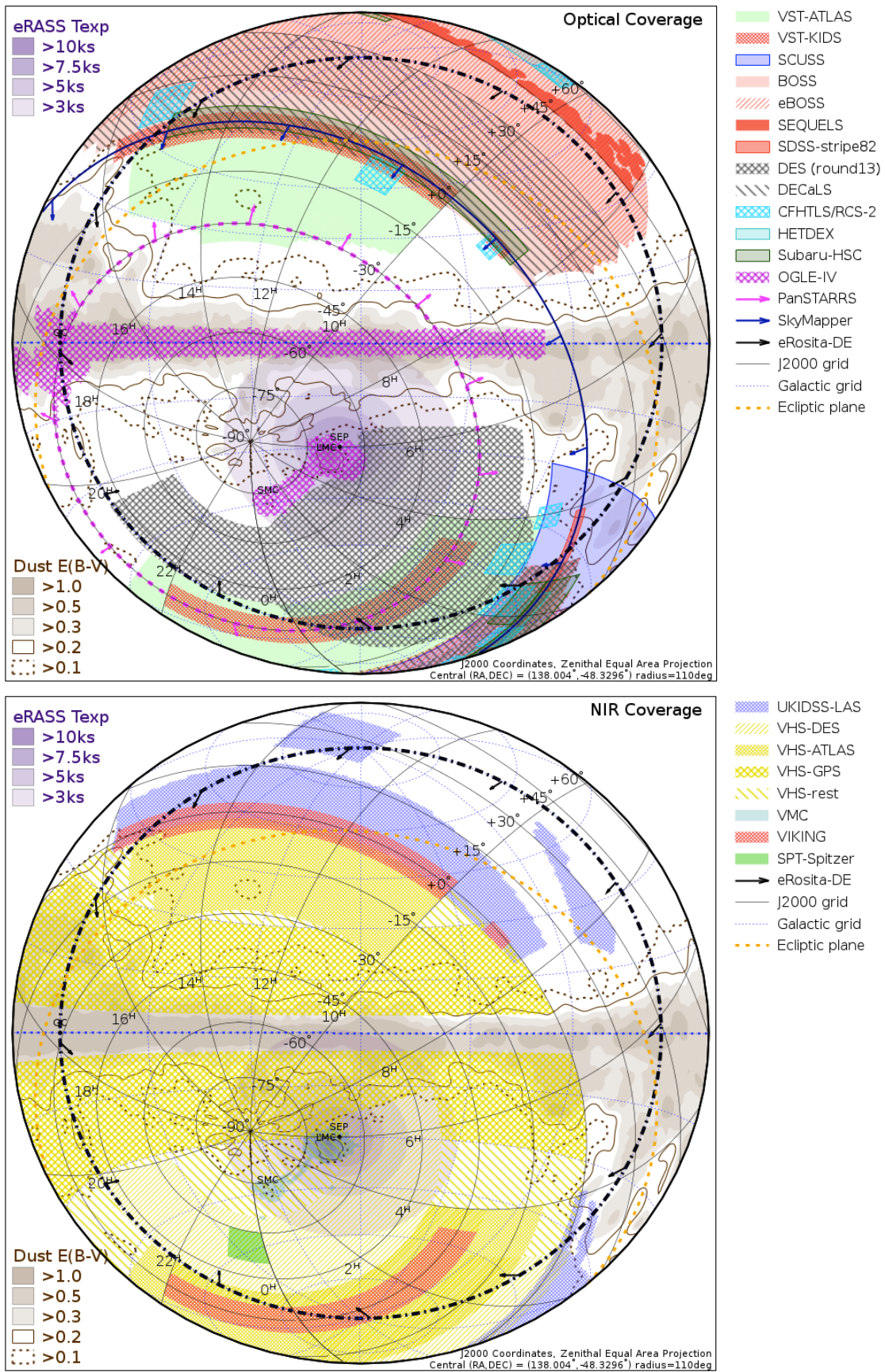


Figure 5.2.: *eROSITA* sky coverage of selected optical and NIR wide area surveys on the West Galactic Hemisphere. Graphic courtesy: Tom Dwelly (MPE).

5.1.3. *SPIDERS* - Spectroscopic follow-up of *eROSITA* sources

The extended Baryon Oscillation Spectroscopic Survey (*eBOSS*) (Dawson et al., 2016) comprises two main optical spectroscopic follow-up programs for quasars and luminous red galaxies. Within these programs, an average of 50 fibres per plate are allocated to the follow-up of sources associated with X-ray emission, primarily AGN and cluster galaxies, belonging to *SPIDERS* (Spectroscopic follow-up of *eROSITA* sources).

The goals of *SPIDERS* are, firstly, to obtain a large sample of X-ray emitting accreting black holes to better understand quasar physics; secondly, to obtain redshifts and velocity dispersions for a large sample of X-ray clusters. The samples for the follow-up will be defined using the *ROSAT* All-Sky Survey (*RASS*; Voges et al. 1999; Boller et al. 2016), the XMM Slew Survey (*XMMSL*; Warwick et al. 2012), and *eROSITA*. In total, it will determine redshifts of 20000 X-ray emitting AGN (25% of them are in common with the *eBOSS* cosmological program), and about 60000 galaxies in ~ 5000 galaxy clusters.

eROSITA's first data are expected to become available in summer 2018. During the four consecutive years the following eight successively deeper *eROSITA* All Sky X-ray Survey catalogs (*eRASS*:1 through *eRASS*:8) will be provided. Given this timeline, the targeting strategy for *SPIDERS* is divided into several tiers depending on the available data at the time of observation. In *Tier 0*, which is prior to the availability of *eRASS* data, *SPIDERS* will target *RASS* and *XMMSL* targets. In *Tier 1*, *eRASS*:1 data (provided mid 2018) will be targeted by *SPIDERS* in Fall 2018. *eRASS*:3 is planned to be available mid 2019 and will be targeted as part of *Tier 2* with *SPIDERS* in Fall 2019. *SDSS-IV* will observe *eRASS* sources in the Western half of the sky ($180^\circ < l < 360^\circ$, Galactic Coordinates) which is accessible to the *eROSITA*-DE consortium.

For Tier 0 point sources/AGN, on average, *RASS* identifies 3 sources deg^{-2} and *XMMSL* (covering about 50% of the *eBOSS* area) provides an additional 0.2 deg^{-2} . The match to the optical counterpart is performed in two steps: first the *WISE* counterparts are found using a bayesian method developed based on that of Budavári & Szalay (2008), taking into account priors in color-magnitude space, then counterparts in the *SDSS* DR9 imaging data are determined with a simple positional match. Eventually, only a fraction of the *RASS* sources (0.8 deg^{-2}) not already observed spectroscopically and with $r > 17$ are targeted by *SPIDERS*, leading to a total of ~ 6000 *RASS* AGN spectra.

For Tier 0 extended sources/clusters (Clerc et al. 2016, MNRAS, in press), Planck-detected clusters, XCLASS clusters (Clerc et al. 2012; Sadibekova et al. 2014) as well as galaxy clusters derived from photon overdensities in *RASS* by the Constrain Dark Energy with X-ray Clusters (CODEX) team that have been matched to likely cluster members in *SDSS* DR9 by using the red-sequence Matched-filter Probabilistic Percolation method (redMaPPer; Rykoff et al. 2014). Because the galaxy targets are concentrated in dense clusters, they are subject to fibre collisions and only 7-8 deg^{-2} have assigned fibres. When including previous *SDSS* legacy spectroscopic observations, we reach a median of approximately 10 galaxies per cluster with spectroscopic redshifts.

For Tier 1 and 2 point sources/AGN, eRASS:1 and eRASS:3 will be matched to *SDSS* DR9 imaging and we will target AGN with $17 < r < 22$. The large majority of brighter sources is already part of previous *BOSS* observations. In the *eROSITA*-DE sky area, this will yield about 4000 targets in eRASS:1 and 7000 in eRASS:3 that are not already targeted by *eBOSS*. Including both *eBOSS* and *SPIDERS*, there will be ~ 15000 *eROSITA*-detected AGN with optical spectra from *SDSS*-IV.

For Tiers 1 and 2 extended sources/clusters, member galaxies will be identified using the same methods as for CODEX and XCLASS, but the improved spatial resolution and depth will allow the targeting of intrinsically less massive and/or more distant clusters. The number of galaxies assigned fibres per cluster will range from 10 to 1 depending on how close and rich the cluster is. Based on estimate cluster counts in *eROSITA* simulations, we expect target densities of 7 deg^{-2} in eRASS:1 and 10 deg^{-2} in eRASS:3.

5.1.4. Spectroscopic completeness for *SPIDERS*

In order to predict the spectroscopic completeness of *SPIDERS* (and other future *eROSITA* follow-up programmes), we first calculate, for the XMM-XXL survey, the number densities N of:

- (i) all X-ray sources, and of those with
- (ii) matched *SDSS* counterparts ($LR_{\text{XMM,SDSS}} > 1.5$),
- (iii) r -band within $15 < r < 22.5 \text{ mag}^1$,
- (iv) *BOSS* follow-up, or
- (v) reliable redshift ($Z_{\text{CONF}} = 3$ and $Z_{\text{CONF}} = 30$).

In addition, we define the fibre collision correction:

$$\mu = \frac{N(LR_{\text{XMM,SDSS}} > 1.5, 15 < r < 22.5 \text{ mag})}{N(\text{BOSS spectra})} \quad (5.1)$$

which has an influence on the number densities of *BOSS* followed-up AGN. The number densities as well as the fibre collision correction at different soft X-ray fluxes is listed in Table 5.2.

In Fig. 5.3, we show the spectroscopic completeness of our dataset as a function of X-ray flux. The fractions correspond to the number of sources with reliable redshifts over the total number of X-ray sources (yellow line), sources with matched *SDSS* counterparts (green line) and sources within the r -band limits (blue line). We indicate the fractions at different X-ray fluxes and highlight the *eROSITA* survey depths. After the correction for fibre collision (dashed lines), the spectroscopic completeness for all *BOSS* targets ($15 < r < 22.5 \text{ mag}$) ranges from 85 per cent at XMM-XXL depth to 96 per cent for eRASS:1 depth. Note that the spectroscopic completeness for all X-ray sources with optical counterparts ($LR_{\text{XMM,SDSS}} > 1.5$)² drops at $F_{0.5-2 \text{ keV}} \geq 4 \cdot 10^{-14} \text{ erg s}^{-1}$; this is due to the counterpart distribution, which shifts towards brighter optical magnitudes with shallow X-ray fluxes (see Fig. 2.2) and reduces the number of *BOSS* targets within the

¹Note that this magnitude cut also includes bright sources, which are part of the previous *BOSS* observations.

²The positional accuracy of *eROSITA* is smaller than in *XMM-Newton*, which has an effect on the matching Likelihood of X-ray sources and their optical counterparts.

Table 5.2.: Top Panel: List of X-ray sources with *SDSS* counterparts and unique *BOSS* spectra in the XMM-XXL north adapted to different soft X-ray depths. The fibre collision correction is calculated by the number of *BOSS* followed-up spectra over *BOSS* targets within the r -band limit. Bottom Panel: List of X-ray sources with reliable redshifts ($Z_CONF = 3$ or $Z_CONF = 30$) and spectroscopic classification in the XMM-XXL north.

<i>eROSITA</i> scan (Scanning time)	$F_{0.5-2\text{keV}}$ [$\text{erg s}^{-1} \text{cm}^{-2}$]	X-ray sources [deg^{-2}]	<i>SDSS</i> counterparts $\text{LR}_{\text{XMM,SDSS}} > 1.5$ [deg^{-2}]	<i>SDSS</i> counterparts $15 < r < 22.5$ mag [deg^{-2}]	<i>BOSS</i> follow-up spectra [deg^{-2}]	fibre collision correction μ
	$3.0 \cdot 10^{-13}$	0.56	0.56	0.33	0.28	1.20
	$1.0 \cdot 10^{-13}$	3.61	3.56	2.61	2.06	1.27
eRASS:1 (0.5 yr)	$4.0 \cdot 10^{-14}$	13.2	12.7	10.8	8.56	1.27
eRASS:2 (1 yr)	$2.5 \cdot 10^{-14}$	27.5	25.2	24.5	17.1	1.30
eRASS:4 (2 yr)	$1.5 \cdot 10^{-14}$	61.3	52.7	49.1	38.0	1.29
eRASS:8 (4 yr)	$9.8 \cdot 10^{-15}$	110	87.3	82.6	64.5	1.28
	$6.0 \cdot 10^{-15}$	187	132	126	98.4	1.28
	$3.0 \cdot 10^{-15}$	331	190	182	141	1.29
	$1.0 \cdot 10^{-15}$	438	219	208	163	1.28

<i>eROSITA</i> scan (Scanning time)	$F_{0.5-2\text{keV}}$ [$\text{erg s}^{-1} \text{cm}^{-2}$]	reliable redshift [deg^{-2}]	BLAGN1 [deg^{-2}]	NLAGN2 [deg^{-2}]	NLAGN2cand [deg^{-2}]	eAGN-ALG [deg^{-2}]	eAGN-SFG [deg^{-2}]
	$3.0 \cdot 10^{-13}$	0.28	0.17	0.06	0.00	0.00	0.06
	$1.0 \cdot 10^{-13}$	1.94	1.72	0.06	0.00	0.11	0.06
eRASS:1 (0.5 yr)	$4.0 \cdot 10^{-14}$	8.39	6.89	0.78	0.33	0.22	0.11
eRASS:2 (1 yr)	$2.5 \cdot 10^{-14}$	16.6	13.3	1.94	0.83	0.22	0.17
eRASS:4 (2 yr)	$1.5 \cdot 10^{-14}$	35.8	28.7	3.33	2.00	0.67	0.72
eRASS:8 (4 yr)	$9.8 \cdot 10^{-15}$	59.6	47.3	5.28	4.22	0.94	1.17
	$6.0 \cdot 10^{-15}$	87.9	67.8	7.28	7.50	1.94	1.72
	$3.0 \cdot 10^{-15}$	122	91.1	10.4	11.3	3.61	2.94
	$1.0 \cdot 10^{-15}$	138	98.8	13.2	14.3	4.78	3.94

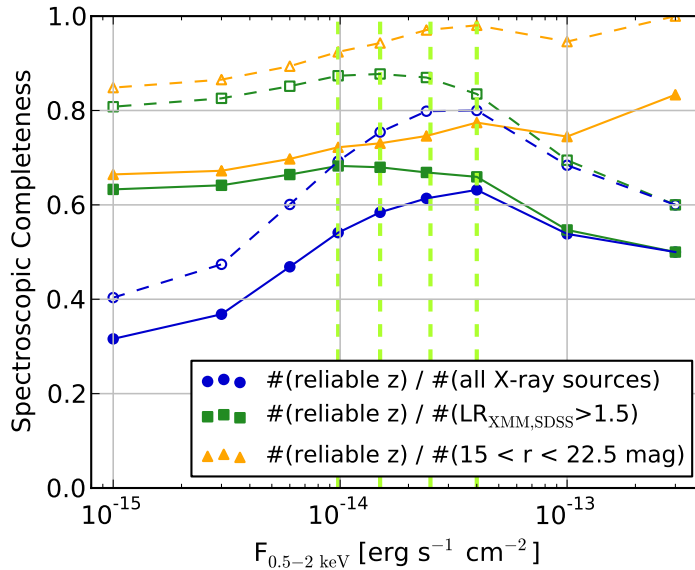


Figure 5.3.: Spectroscopic completeness in the XMM-XXL north: We show the fractions of X-ray sources with reliable redshift ($Z_{\text{CONF}} = 3$ and $Z_{\text{CONF}} = 30$) over the number of all X-ray sources (blue), matched *SDSS* counterparts ($LR_{\text{XMM,SDSS}} > 1.5$) (green), and r -band within $15 < r < 22.5$ mag (yellow). In addition, we apply the fibre collision correction to the fraction of sources with reliable redshift (dashed lines with empty markers) to obtain the intrinsic spectroscopic completeness. The vertical green dashed lines indicate the flux depths of *eROSITA* (from left: eRASS:8, eRASS:4, eRASS:2, eRASS:1).

r -band threshold ($r \leq 15 - 17$ mag). The overall spectroscopic completeness for all X-ray sources at deep X-ray flux limits reflects both the sensitivity limits of *SDSS* for the optical counterparts and the faint r -band threshold of the *BOSS* spectrograph.

The optical classification of the AGN also correlates with the X-ray flux. For the XMM-XXL depth, our AGN sample comprises 73 per cent BLAGN1, 20 per cent NLAGN2/NLAGN2cand and 6 per cent elusive AGN (eAGN). For the *eRASS:8*, these ratios change to 80 per cent BLAGN1, 16 per cent NLAGN2/NLAGN2cand and 4 per cent eAGN.

In Fig. 5.4, we show the distribution of *SPIDERS* sources in the soft X-ray luminosity and redshift plane, in comparison to other X-ray selected surveys. The central panel shows the combined simulated³ Tier 1 and 2 of the *SPIDERS* survey for point-like objects compared to a sample including all X-ray sources in the 3XMM catalog matched to a spectroscopic object in wide area surveys (from VIPERS, VVDS-WIDE, DEEP2, AGES, GAMA, SDSS-I-II-III, MCG, 6dF, 2MRS, 2dFGRS), and a sample of spectroscopic X-ray sources detected in four deep fields COSMOS, Lockman Hole, CDFS and CDFN.

The top panel groups all known X-ray sources from 3XMM and the deep fields, and adds a sample of *SPIDERS* low redshift QSO which are optically selected by the XDQSO algo-

³The simulation is based on the AGN luminosity function of Hasinger et al. (2005) and the F_X/F_O ratio distribution in the *XMM-COSMOS* of Brusa et al. (2010).

rithm in eBOSS (see Sec. 3.5).

Overall, the SPIDERS spectroscopic X-ray selected sample will be 2 – 3 times larger than the total number of X-ray AGN with spectroscopic redshift currently known, and about a factor 10 larger than the number of X-ray AGN with known redshift in any coherent, contiguous, well defined, X-ray survey.

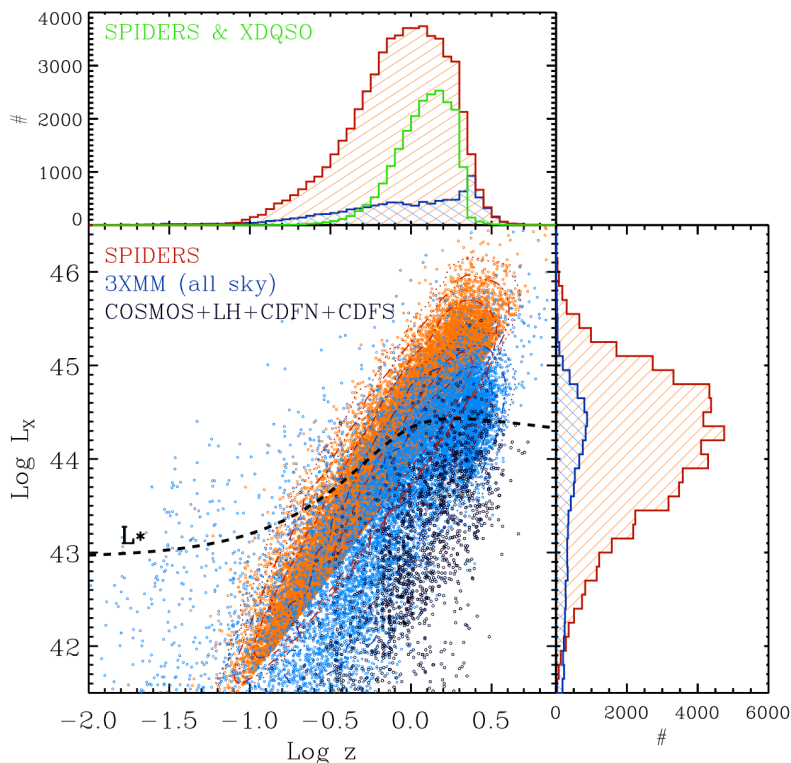


Figure 5.4.: Central Panel: Soft X-ray luminosity and redshift plane of Tier 1 and Tier 2 point like *SPIDERS* targets (orange), the 3XMM catalogue with spectroscopic counterparts (blue) and X-ray sources with spectroscopic information from the deep fields COSMOS, Lockman Hole, CDFS and CDFN (black). The thick dashed line is the approximate location of the break luminosity L_* in the AGN X-ray luminosity function (based on Hasinger et al. 2005 and the F_X/F_O ratio distribution in the XMM-COSMOS of Brusa et al. 2010.). Upper Panel: The histogram includes a sample of *SPIDERS* sources also targeted by the optical XDQSO selection.

5.1.5. Comparison of AGN selections for *eROSITA* depths

As presented in Sec. 3.7, we calculated the fractions of X-ray, infrared and optical selected AGN at different *eROSITA* depths. Even at eRASS:8 X-ray fluxes, there is a unique AGN population which would not have been selected by any of the other two methods. The X-ray detection fraction at different *eROSITA* depths for the subgroup of *XDQSO* and *WISE* selected AGN is presented in Fig. 5.5, and follows the explained procedures from Section 3.5 and Section 3.6. In Fig. 5.6, we show the Venn diagram of sources which are selected by optical, infrared and X-ray AGN selection criteria.

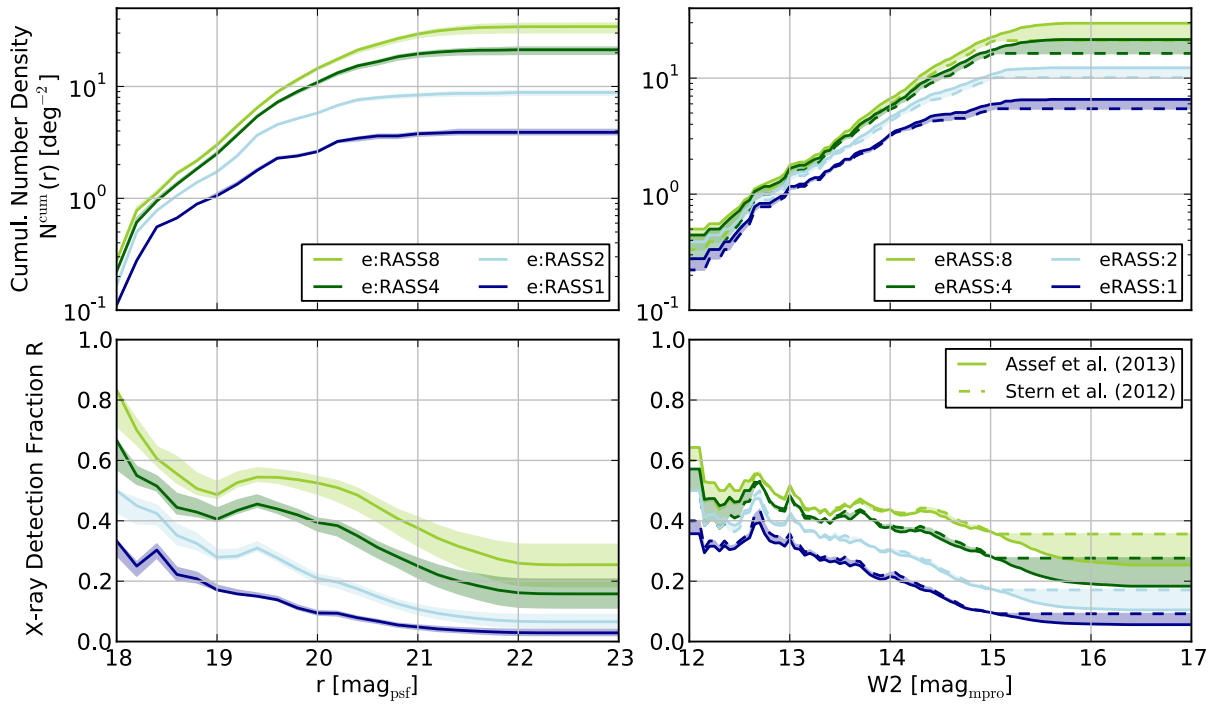


Figure 5.5.: Left Panel: XDQSO selected AGN with X-ray counterparts for the *eROSITA* X-ray depths ($P_{\text{sum}}(\text{QSO}) > 0.5$ (central line) and $P_{\text{sum}}(\text{QSO}) > 0.8$ (lower border) as well as > 0.2 (upper border)); top left: Cumulative number density; bottom left: X-ray detection fraction. Right Panel: infrared selected AGN with X-ray counterpart for the *eROSITA* X-ray depths (threshold of Stern et al. (2012) and Assef et al. (2013)); top right: Cumulative number density; bottom right: X-ray detection fraction.

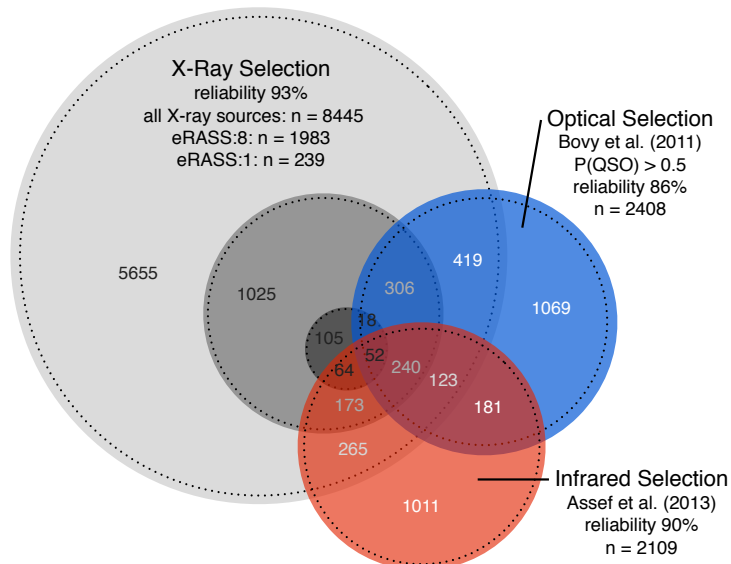


Figure 5.6.: Venn diagram of X-ray, optical (XDQSO) and infrared (Assef et al., 2013) AGN selections in the XMM-XXL north: We indicate the flux depths for eRASS:8 and eRASS:1 of *eROSITA*, the reliable fraction (dashed line) and number of AGN in each intersection.

5.2. Summary of the Thesis

In this thesis, we have investigated the properties of a X-ray selected AGN sample in the XMM-XXL field with optical spectroscopic follow-up, including the selection methods, host galaxy contamination, demographics (optically obscured and obscured AGN), and emission line properties. Furthermore, we performed a detailed study of [OIII] emission line profiles to assess evidences for outflows, their geometry and their possible impact on AGN feedback. The sample in the XMM-XXL field is highly suitable for our analysis, because the X-ray selection accesses AGN populations which are hidden for other selection criteria e.g. optical or infrared. In addition, the spectroscopic follow-up gives insights into the redshift distribution, optical obscuration, host galaxy properties and outflow/inflow signatures of AGN.

As part of our work, we presented and publicly released one of the largest contiguous catalogues of X-ray selected and spectroscopically observed AGN to date (Menzel et al., 2016). It provides a unique data set to study the optical properties of X-ray selected AGN and also serves as a pilot study for the *eROSITA* follow-up programme *SPIDERS* in SDSS-IV.

The survey contains 8445 point-like X-ray sources covering an area of $\sim 18 \text{ deg}^2$ in the XMM-XXL north area reaching down to a flux of $F_{0.5-10 \text{ keV}} > 1.0 \cdot 10^{-15} \text{ erg cm}^{-2} \text{ s}^{-1}$. They have been cross-matched to their optical (*SDSS*) and infrared (*WISE*) counterparts via the Maximum-Likelihood-Ratio method. The *BOSS* spectrograph followed up 3042 sources within $15 < r_{\text{psf}/\text{model}} < 22.5 \text{ mag}$ and after visual inspection, we obtained 2578 sources with reliable redshifts. The sample covers a redshift range of $0 < z < 5$ and a luminosity range of $2 \cdot 10^{39} < L_{0.5-2 \text{ keV}} < 4 \cdot 10^{45} \text{ erg s}^{-1}$.

For the study of the AGN properties of our X-ray selected sample, we introduced a spectral classification method which is based on optical emission line properties provided by the *BOSS* pipeline. We analyzed properties, such as the line widths of AGN-induced and star-formation-induced emission lines and finally derived the following classes for a subset of 2570 spectra: 1787 BLAGN1, 271 NLAGN2, 284 NLAGN2cand, 78 eAGN-SFG, 93 eAGN-ALG, 85 stars and 2 BL Lac. 57 sources cannot be classified, because of missing emission line information.

We compared the X-ray AGN selection to common AGN selections using optical emission line diagnostics (Baldwin et al., 1981; Kauffmann et al., 2003; Kewley et al., 2006; Meléndez et al., 2014; Lamareille et al., 2004; Lamareille, 2010), optical (Bovy et al., 2011), and infrared colours (Stern et al., 2012; Assef et al., 2013). This enabled us to study the imposed selection effects on AGN and evaluate the AGN population probed by X-ray data. Finally, we studied the narrow emission line kinematics in X-ray selected AGN. Concentrating on the [OIII] emission line allows for a detection of ionized gas clouds affected by the gravitational potential of the stellar bulge or by outflows/inflows. We developed a dedicated line fitting algorithm to decompose the [OIII] emission into these two components, for AGN at a redshift $0 < z < 1$. In order to derive the excitation mechanism of the observed outflows, we compared the [OIII] emission line profile with a sample of star-forming emission line galaxies and performed correlation studies with AGN properties. The

redshift complete sample of AGN allows for an estimate of the average kinematic power and momentum rate released by an average ionized [OIII] outflow in the overall population of X-ray selected AGN, and their contribution to feedback processes.

In the following, we conclude with the main scientific outcomes of this analysis:

- (i) The bimodal FWHM-distribution of optical AGN-induced emission lines widths (e.g. H β and MgII) clearly separates the population of X-ray selected AGN into broad line region emitters and narrow line region emitters. The minimum of the FWHM-distribution is at FWHM \sim 1000 km/s. The former emitters allow for a direct view into the central part of the accretion flow and of the broad line region, while the latter are mostly affected by the obscuration along the line of sight or dominated by the stellar emission of the host.
- (ii) The X-ray selection probes a wide variety of AGN with respect to the obscuring material along the line of sight and the contribution of the passive or active host galaxy. It allows to detect particular and peculiar classes, such as optically unobscured BLAGN1 with strong host galaxy contribution, optically obscured NLAGN2, and optically elusive AGN. Because of the *r*-band magnitude limits for the optical spectroscopy, we had access to, our sample is biased against optically faint sources, which mainly affects optically obscured NLAGN2 at higher redshift.
- (iii) Applied to our X-ray selected sample, we find that the optical AGN selection via the XDQSO targeting algorithm (Bovy et al., 2011) is, by construction, biased towards optically point-like sources and selects BLAGN1 with weak host features over the entire redshift range of the sample. The *WISE* colour AGN selections from Assef et al. (2013) and Stern et al. (2012) preferentially select BLAGN1 at $z < 3$ with weak hosts and red $W1 - W2$ colours. Optical emission line diagnostics are less affected by central obscuring material, but are biased against elusive AGN inside star forming galaxies or absorption line galaxies.
- (iv) We find incidences of ionized OIII outflow/inflow features in > 35 per cent of a highly redshift complete AGN sample ($F_{2-10\text{keV}} > 2.5 \cdot 10^{-14} \text{ erg s}^{-1}$, $0 < z < 0.8$). 75 per cent of the OIII wing components are blueshifted and can be interpreted as outflows. The blueshift-velocity dispersion indicates that the outflows are decelerated by the ISM.
- (v) The ionized OIII outflow features in our X-ray selected AGN sample cannot be caused solely by star formation. We find strong correlations of line luminosity with AGN properties, such as hard X-ray luminosity and optical/UV continuum luminosity, which indicates that the AGN is the excitation mechanism of [OIII] outflows. The outflow velocity of the [OIII] line is affected by the radial velocity of the AGN wind and the velocity dispersion of the narrow core component caused by the gravitational component of the stellar bulge.
- (vi) We observe that ionized OIII outflow/inflow features are similar in BLAGN1 and NLAGN2, and have the same [OIII] wing profiles at comparable hard X-ray luminosity. This disagrees with the model of a biconical outflow structure in the AGN unification scheme. We suggest that a dispersion of the outflow might cause the orientation independence.
- (vii) The elusive AGN-SFG show no characteristic AGN [OIII] outflow features next to the star formation excited NLR, which supports the hypothesis, that the central AGN is

completely obscured or, less likely, outshone by the galaxy.

- (viii) The kinetic power of average ionized [OIII] outflows contributes ≈ 0.01 per cent to the bolometric luminosity of the AGN and their momentum boost is in the order of ≈ 0.1 . This is not sufficient for the feedback process causing the $M_{\text{BH}} - \sigma$ -relation for AGN and their host galaxies.

5.3. Future prospects

We currently face an exciting time in which ongoing and soon to be started instruments allow for exploration of wider and deeper regions of the extragalactic sky, covering nearly all wavelength ranges. These technical advances will have a big impact on the completeness of AGN selection criteria as well as on our understanding of physical processes in AGN and especially the interaction with the ambient host galaxies.

In the coming years, multi-object optical spectrographs with characteristics similar to *BOSS* or with higher performance (e.g. *4MOST*, de Jong et al. 2014; *DESI*) will be able to provide highly complete, and very efficient follow-up programmes for the upcoming *eROSITA* all-sky X-ray surveys, bringing the study of AGN populations to an unprecedented level of statistical accuracy. The *SPIDERS* programme as a part of *eBOSS* represents one of the first follow-up surveys and already started to provide successful spectroscopic data of X-ray selected sources.

5.3.1. X-ray selected AGN populations

We show that individual AGN selection criteria can miss substantial parts of the entire population due to the wide range of varying AGN SED features. These features are influenced by e.g. accretion, obscuration, host galaxy emission and can correlate with different orientations or evolutionary states. The combination of multiple selections can correct for missing populations and strongly improves the completeness of selected AGN.

In our work, we put a strong emphasis on the X-ray AGN selection tracing high-energetic processes in the central nuclear region and benefiting from the relative insensitivity to gas obscuration and star formation contamination. This allows for a selection of AGN populations covering a wide range of accretion, obscuration and host properties. The X-ray instrument *eROSITA* will soon contribute to the observation of the entire extragalactic X-ray sky and provide so far the highest sensitivity data over such a large area. As presented in this thesis, the pilot study of the *SPIDERS* programme accesses an interesting optical spectroscopic dataset of AGN with different host galaxy contributions and properties. Partnering up with selection from additional existing multi-wavelength bands, e.g. in infrared (*WISE*, full-sky) and optical (*SDSS*, northern hemisphere), will immediately allow for the selection of a highly complete full-sky AGN population including e.g. AGN dominated, star formation dominated, obscured or Compton-thick populations.

In future, the AGN population from *SPIDERS* will be subject to wide range of analyses. An interesting study is the composition of stellar populations, length and presence of star formation episodes, and strength of dust attenuation. This will give exciting insights into the characteristics of galaxies hosting AGN and allows for correlations with AGN properties, such as luminosity or accretion behavior. Furthermore, the X-ray selected AGN population contains rare subgroups, such as elusive AGN. Their origin is still matter of debate. Despite clear AGN-like X-ray luminosities, the AGN features are missing in the optical spectra. This might either be due to strong obscuration or to the time delay between the turning-on of the central AGN and the excitation of the narrow line regions.

Further studies of this population will provide for either cases interesting new insights into obscurations or flickering processes of AGN. The *SPIDERS* follow-up programme benefits from the combination of both X-ray data and optical data for AGN, which enable comparison studies of disk and corona related properties, e.g. variability and correlation between dust/gas obscurations. An additional topic of research will be clustering and the study of dark matter haloes.

5.3.2. Impact of outflows on AGN feedback

In this work, we focussed on the presence of ionized outflows in AGN. Our sample benefits for the study of ionized [OIII] outflows from the high redshift-completeness and the optical spectroscopy. We find that [OIII] outflows are likely to be excited by AGN emission, but contribute only little to the feedback between AGN and host galaxy. For this reason, it is very important to conduct further studies to understand the nature of feedback caused by outflows in AGN.

Based on our data, we could estimate the average kinetic power and momentum rate ionized [OIII] outflows during the AGN phase. For better estimates of this power, we require more precise information on the size and location of the outflow, as well as the electron density in the narrow line region. The former can be achieved by integral field spectroscopy, which does not only allow for the determination of outflow location and orientation, but can also trace regions of star formation activity, and enable to study the impact of negative/positive feedback. The electron density instead can only be derived in high S/N ratio spectra. Future 30-m-telescope generations (*TMT*) instruments will provide the necessary data to improve the determination of the narrow line micro-physics.

Knowing that outflows carry many phases of ionized, neutral and molecular matter/gas, we will have to access multi-wavelength data for their detection. High resolution X-ray spectra map ionized iron (e.g. *Chandra*, *Nustar*, *Athena+*), jet mode excitations can be measured by radio instruments (e.g. *JVLA LOFAR*, *SKA*), molecular outflows e.g. CO are likely to be traced by e.g. with *ALMA* and outflows ionizing e.g. forbidden lines in the narrow line region can be assed by optical instruments. Optimally, one should observe outflows with integral field spectroscopy units in different wavelength-bands and observe in similar time ranges. But up until now, this can only be conducted with coordination as well as cost intense campaigns for typically small sample sizes.

The understanding of feedback characteristics for the entire AGN population is highly challenging. As discussed in this work, AGN activity and star formation happen non-periodically and span different times scales. Many additional factors, such as light travel time and orientation can have further impacts on the observation of these processes in individual objects. In the future, studies about the complete feedback picture, will likely require large samples of AGN populations with integral fields spectroscopy in multi-wavelength bands. The work presented here is a first systematic attempt to shed light on such a complex phenomenology in a large and highly complete sample.

A. AGN Catalogue in the XMM-XXL

We publish the catalogue of X-ray, optical, infrared, and spectroscopic properties of the 8445 X-ray selected sources in the northern XMM-XXL field, which is accessible in this website: <http://www.mpe.mpg.de/XraySurveys> under [Surveys] > [XMM-XXL].

In Table A.1, we list the catalogue parameters with information on:

- (i) the X-ray imaging with *XMM-Newton*;
- (ii) the optical imaging with *SDSS* and XDQSO selection probabilities ;
- (iii) the infrared imaging with *WISE*;
- (iv) the *BOSS* pipeline information;
- (v) the redshift information of the visual inspection and the classification.

The full X-ray catalogue of the X-ray selected sources in the XMM-XXL with complete information about their X-ray properties will be provided in the paper of (Liu et al., 2016).

Table A.1.: Information about catalogue columns of X-ray selected AGN in the northern XMM-XXL field.

Column	Name	Description
1	UXID	UXID from (Liu et al., 2016)
2	RA_XMM	RA-position from (Liu et al., 2016) in deg
3	DEC_XMM	Dec-position from (Liu et al., 2016) in deg
4	RADECERR_XMM	Error RA- and Dec-position from (Liu et al., 2016) in deg
5	FLUX_FULL	Full X-ray flux $F_{0.5-10\text{ keV}}$ from (Liu et al., 2016) in $\text{erg s}^{-1}\text{cm}^{-2}$
6	FLUX_SOFT	Soft X-ray flux $F_{0.5-2\text{ keV}}$ from (Liu et al., 2016) in $\text{erg s}^{-1}\text{cm}^{-2}$
7	FLUX_HARD	Hard X-ray flux $F_{2-10\text{ keV}}$ from (Liu et al., 2016) in $\text{erg s}^{-1}\text{cm}^{-2}$
8	LUM_FULL	Full X-ray luminosity $F_{0.5-10\text{ keV}}$ from (Liu et al., 2016) in erg s^{-1}
9	LUM_SOFT	Soft X-ray luminosity $F_{0.5-2\text{ keV}}$ from (Liu et al., 2016) in erg s^{-1}
10	LUM_HARD	Hard X-ray luminosity $F_{2-10\text{ keV}}$ from (Liu et al., 2016) in erg s^{-1}
11	OBJID	<i>SDSS</i> -ID from <i>SDSS</i> DR-8 (Aihara et al., 2011)
12	RA_SDSS	RA-position from <i>SDSS</i> DR8 in deg
13	DEC_SDSS	Dec-position from <i>SDSS</i> DR8 in deg
14	RAERR_SDSS	Error for RA-position from <i>SDSS</i> DR8 in deg
15	DECERR_SDSS	Error Dec-position from <i>SDSS</i> DR8 in deg
16	LR_XMMSDSS	Likelihood-Ratio of the matching with <i>SDSS</i> counterpart
17-21	PSF_MAG	Psf-magnitudes for u, g, r, i, z in AB-mag from <i>SDSS</i> DR8
22-26	PSFERR_MAG	Error for psf-magnitudes for u, g, r, i, z in AB-mag from <i>SDSS</i> DR8
27-31	MODEL_MAG	Model-magnitudes for u, g, r, i, z in AB-mag from <i>SDSS</i> DR8
32-36	MODELERR_MAG	Error for model-magnitudes for u, g, r, i, z in AB-mag from <i>SDSS</i> DR8
37	TYPE	Optical morphology: 3 - galaxy like, 6 - star like (Aihara et al., 2011)
38	PQSOSUM	Summed XDQSO QSO probability (Bovy et al., 2011)
39	GOOD	<i>BOSS</i> good flag (Bovy et al., 2011)
40	WISE_DESIGN	Designation from all <i>WISE</i>
41	RA_WISE	RA-position from all <i>WISE</i> in deg
42	DEC_WISE	Dec-position from all <i>WISE</i> in deg
43	RASIG_WISE	One-sigma uncertainty for RA-position from all <i>WISE</i> in deg
44	DECSIG_WISE	One-sigma uncertainty for Dec-position from all <i>WISE</i> in deg
45	LR_XMMWISE	Likelihood-Ratio of the matching with <i>WISE</i> counterpart (Georgakakis et al)
46-49	MPRO_MAG	Mpro-magnitudes of $W1, W2, W3$ and $W4$ in Vega-mag from all <i>WISE</i>
50-53	MPROSIG_MAG	Profile-fit photometric measurement uncertainty for $W1, W2, W3$ and $W4$ in Vega-mag from all <i>WISE</i>
54	CLEAN	Exclusion of diffraction spikes, halos, optical ghosts and blended sources (ccflag = 0 for $W1$ and $W2$, NB ≤ 2): 1 - photometric conditions are fulfilled, 0 - photometric conditions are not fulfilled
55	PLATE	<i>BOSS</i> plate number
56	FIBERID	<i>BOSS</i> fibre-ID number
57	MJD	<i>BOSS</i> MJD
58	Z_BOSS	Redshift from the automatic <i>BOSS</i> pipeline
59	ZERR_BOSS	Error for Z_BOSS
60	ZWARNING	Redshift warning flag from the automatic <i>BOSS</i> pipeline
61	SN_MEDIAN_ALL	Average S/N ratio of all five <i>SDSS</i> bands from the automatic <i>BOSS</i> pipeline
62	Z	Redshift after visual inspection and refit of spectrum with <code>spreduce1d.pro</code>
63	ZERR	Error for Z
64	Z_CONF	Redshift confidence flag from visual inspection: 3 - reliable redshift, 2 - not robust redshift, 1 - bad spectrum, 30 - reliable visual redshift and pipeline failure, 20 - not robust visual redshift and pipeline failure
65	CLASS	Classification for Z_CONF = 3 spectra: BLAGN1, NLAGN2, NLAGN2cand, eAGN-ALG, eAGN-SFG, NOC (not classified)
66	STAR/BLLAC	Star: star, BL LAC: bllac

B. Spectral stacks of star formation calibrated AGN and ELG

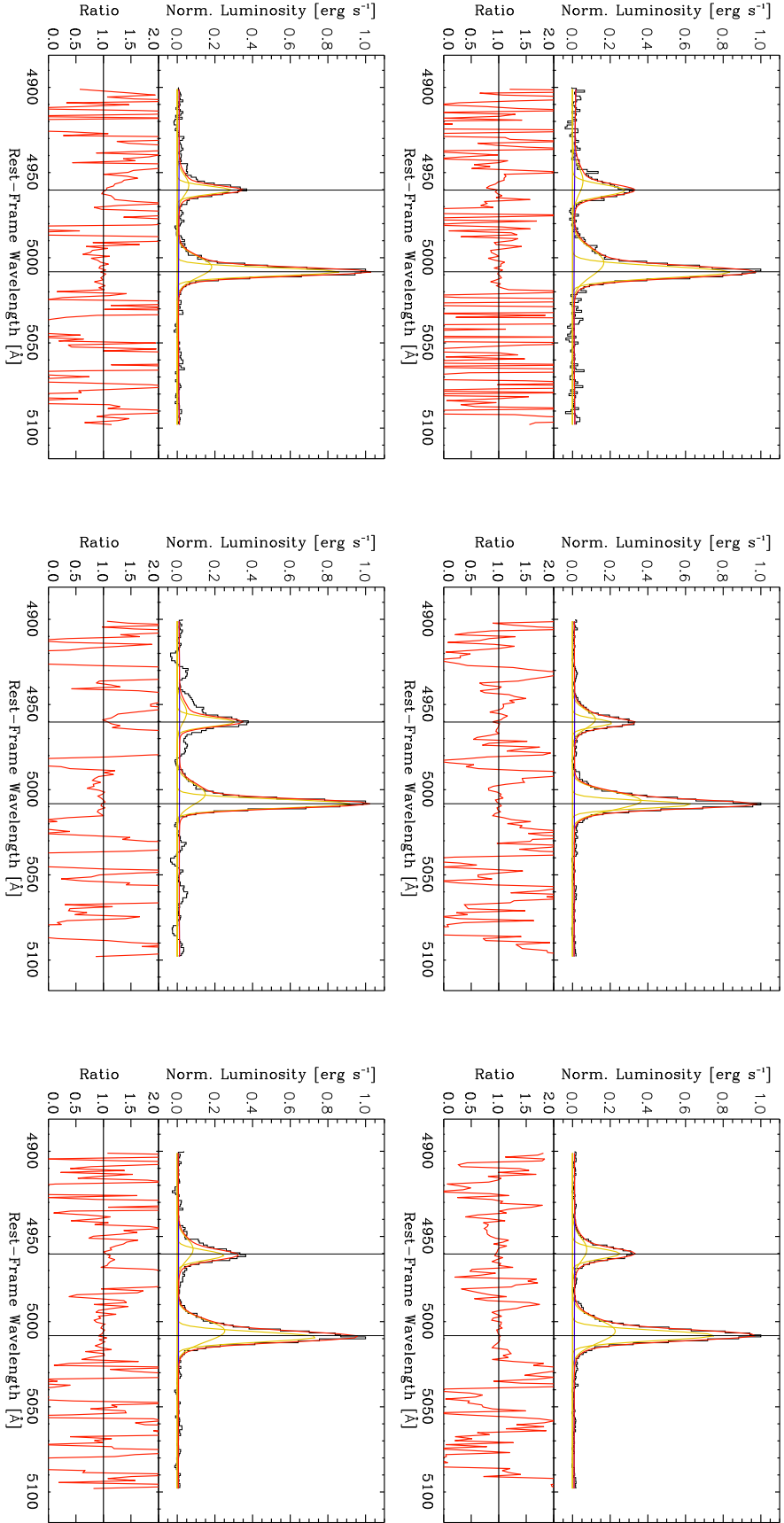


Figure B.1.: Spectral stacks of OIII region with maximum normalized luminosity from Sec. 4.7.3. Top panels: BLAGN1. Bottom Panels: NLAGN3. From left to right: $L_{OIII}^{SF} > 6 \cdot 10^{41} \text{ erg s}^{-1}$, $L_{OIII}^{SF} < 6 \cdot 10^{41} \text{ erg s}^{-1}$, upper limit L_{OIII}^{SF} .

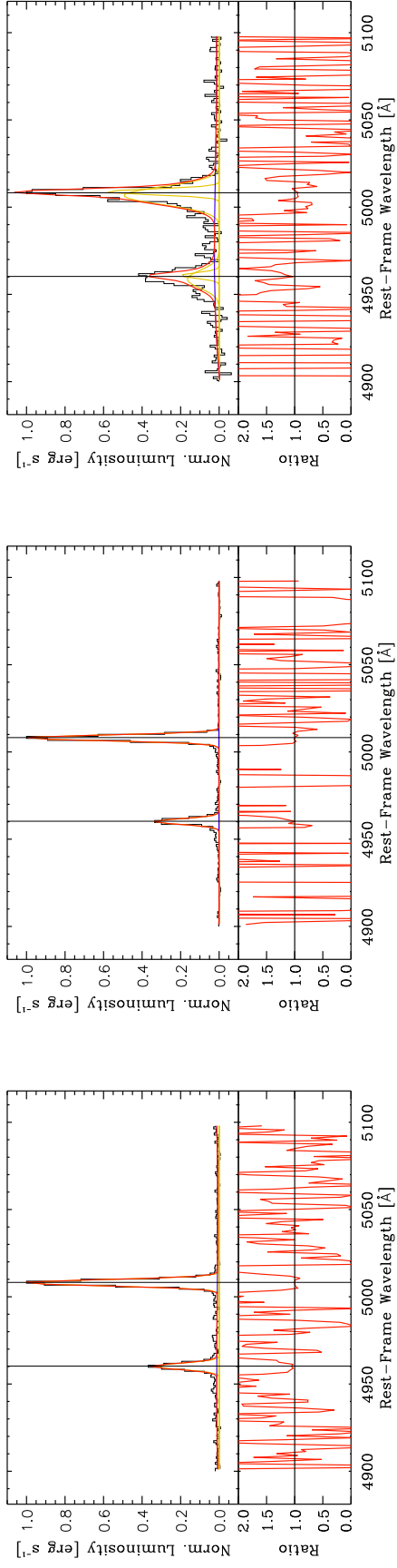


Figure B.2.: Spectral stacks of OIII region with maximum normalized luminosity from Sec. 4.7.3 for ELG. From left to right: $L_{OIII}^{SF} > 6 \cdot 10^{41} \text{ erg s}^{-1}$, $L_{OIII}^{SF} < 6 \cdot 10^{41} \text{ erg s}^{-1}$, upper limit L_{OIII}^{SF} .

C. Spectral stacks of hard X-ray and optical/UV continuum luminosity binned AGN sample

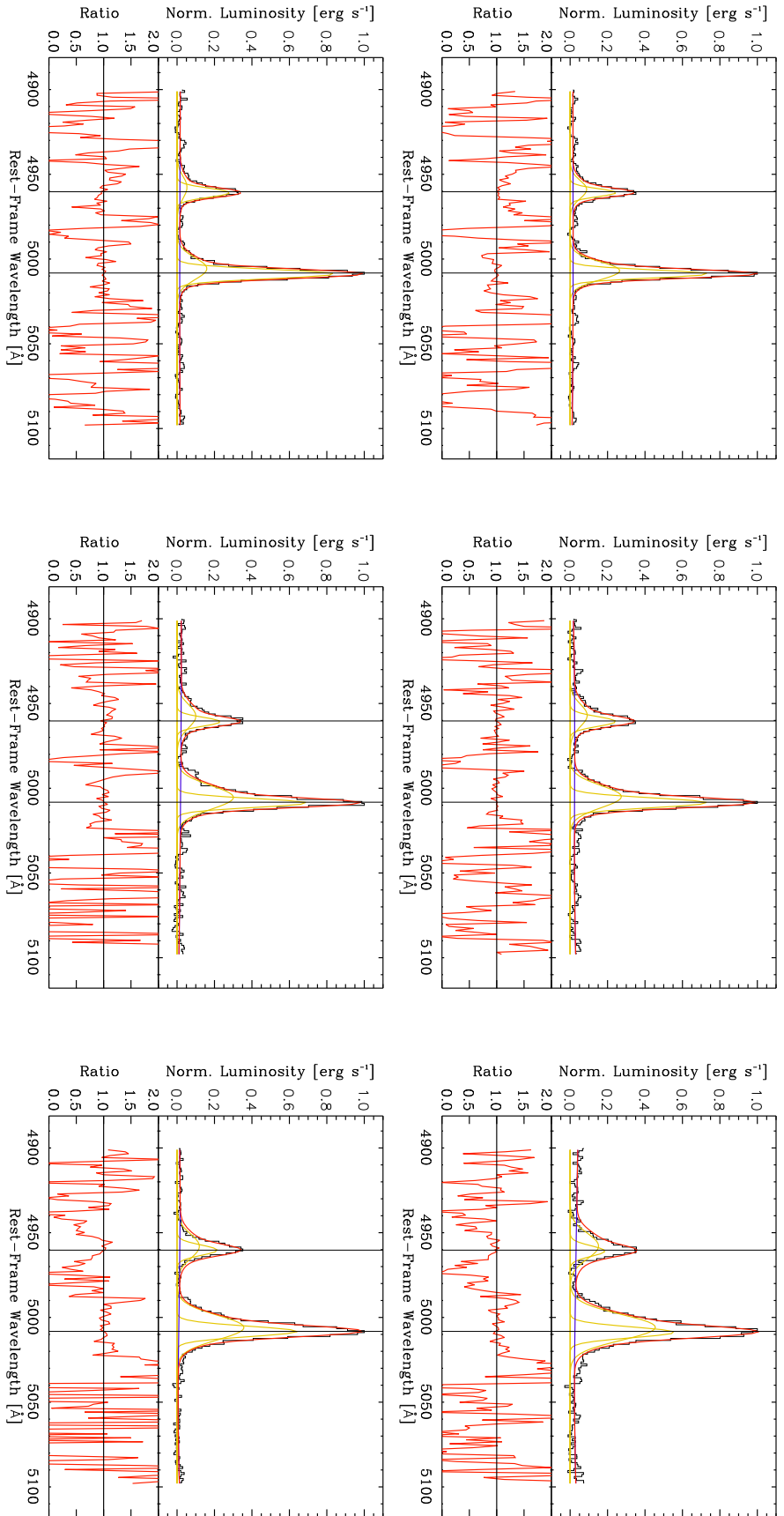


Figure C.1: Spectral stacks of OIII region for BLAGN1 from Sec. 4.8.2 binned in hard X-ray and optical/UV continuum luminosity. Top panel: $L_{5100 \text{ \AA}} = 6.8 \cdot 10^{43} \text{ erg s}^{-1}$, $L_{5100 \text{ \AA}} = 1.6 \cdot 10^{44} \text{ erg s}^{-1}$, $L_{5100 \text{ \AA}} = 4.0 \cdot 10^{44} \text{ erg s}^{-1}$ (from left to right). Bottom panel: $L_{2-10 \text{ keV}} = 1.9 \cdot 10^{43} \text{ erg s}^{-1}$, $L_{2-10 \text{ keV}} = 5.6 \cdot 10^{43} \text{ erg s}^{-1}$, $L_{2-10 \text{ keV}} = 1.5 \cdot 10^{44} \text{ erg s}^{-1}$ (from left to right).

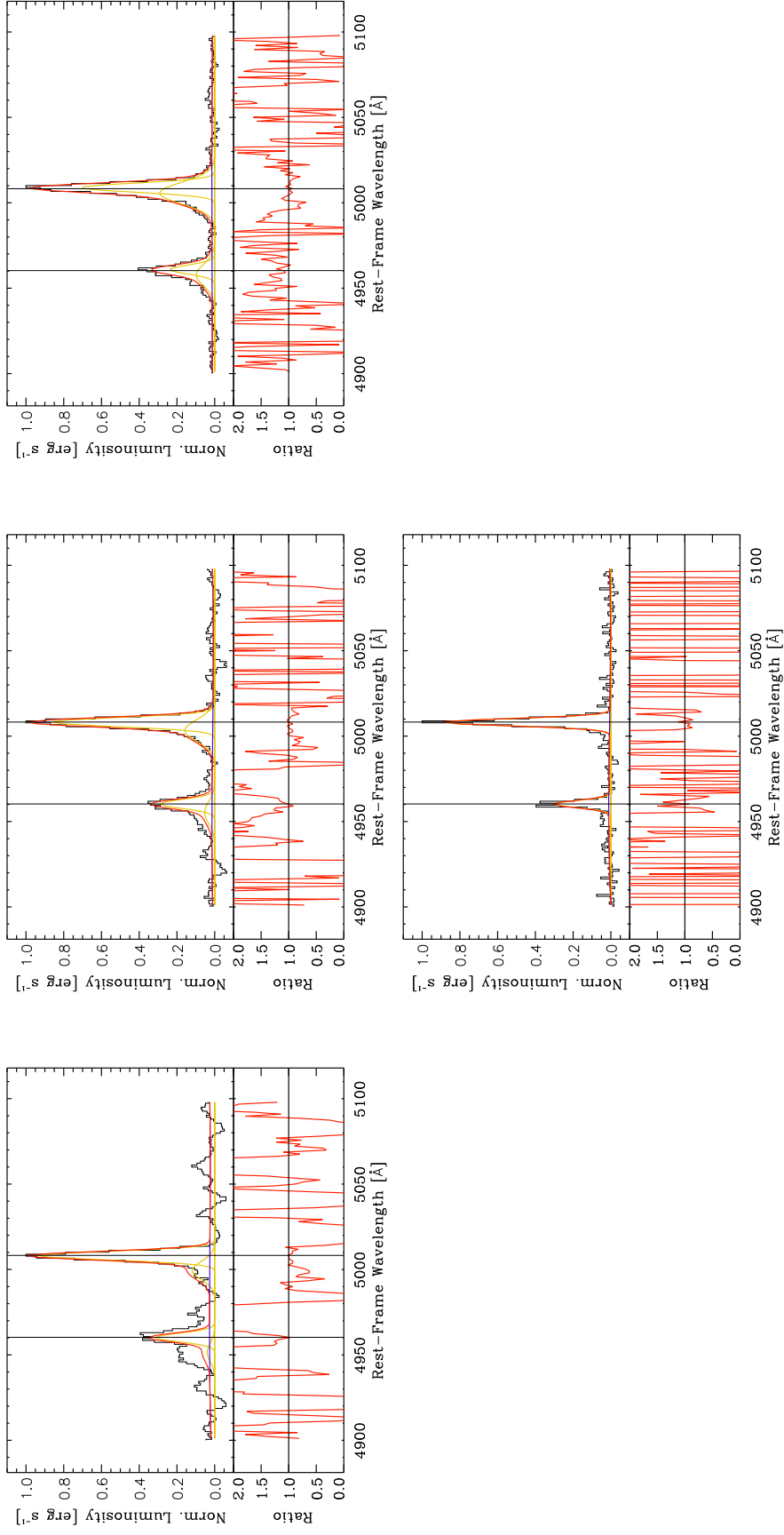


Figure C.2.: Spectral stacks of OIII region for NLAGN2 and eAGN-SFG from Sec. 4.8.2 binned in hard X-ray luminosity. Top panel: NLAGN2, $L_{2-10\text{keV}} = 3.0 \cdot 10^{42} \text{ erg s}^{-1}$, $L_{2-10\text{keV}} = 1.4 \cdot 10^{43} \text{ erg s}^{-1}$, $L_{2-10\text{keV}} = 5.8 \cdot 10^{44} \text{ erg s}^{-1}$ (from left to right). Bottom panel: eAGN-SFG, $L_{2-10\text{keV}} = 1.2 \cdot 10^{43} \text{ erg s}^{-1}$.

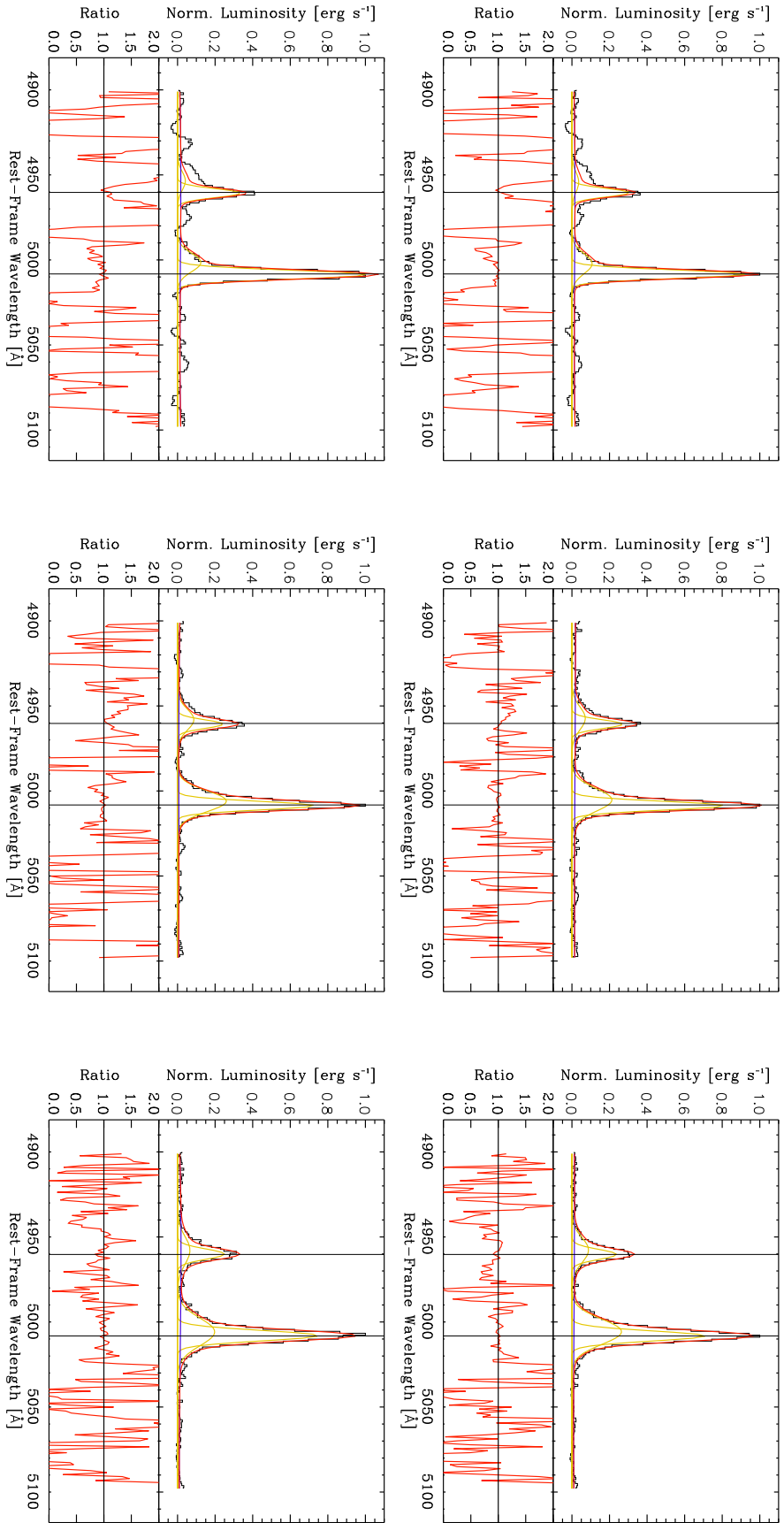


Figure C.3.: Spectral stacks of OIII region for BLAGN1&NLAGN2 and complete sample from Sec. 4.8.2 binned in hard X-ray luminosity. Top panel: BLAGN1&NLAGN2, $L_{2-10\text{keV}} = 6.6 \cdot 10^{42} \text{ erg s}^{-1}$, $L_{2-10\text{keV}} = 3.2 \cdot 10^{43} \text{ erg s}^{-1}$, $L_{2-10\text{keV}} = 1.0 \cdot 10^{44} \text{ erg s}^{-1}$ (from left to right). Bottom panel: eAGN-SFG, $L_{2-10\text{keV}} = 8.4 \cdot 10^{42} \text{ erg s}^{-1}$, $L_{2-10\text{keV}} = 4.3 \cdot 10^{43} \text{ erg s}^{-1}$, $L_{2-10\text{keV}} = 1.1 \cdot 10^{44} \text{ erg s}^{-1}$ (from left to right).

Bibliography

- Antonucci, R. 1993, *ARA&A*, 31, 473
- Ahn, C. P., Alexandroff, R., Allende Prieto, C., et al. 2012, *ApJS*, 203, 21
- Aihara, H., Allende Prieto, C., An, D., et al. 2011, *ApJS*, 193, 29
- Aird, J., Nandra, K., Laird, E. S., et al. 2010, *MNRAS*, 401, 2531
- Aird, J., Coil, A. L., Moustakas, J., et al. 2012, *ApJ*, 746, 90
- Alam, S., Albareti, F. D., Allende Prieto, C., et al. 2015, arXiv:1501.00963
- Alexander, D. M., Bauer, F. E., Brandt, W. N., et al. 2003, *AJ*, 126, 539
- Alexander, D. M., & Hickox, R. C. 2012, *NewAR*, 56, 93
- Allen, J. T., Hewett, P. C., Maddox, N., Richards, G. T., & Belokurov, V. 2011, *VizieR Online Data Catalog*, 741,
- Assef, R. J., Stern, D., Kochanek, C. S., et al. 2013, *ApJ*, 772, 26
- Aversa, R., Lapi, A., de Zotti, G., Shankar, F., & Danese, L. 2015, *ApJ*, 810, 74
- Bae, H.-J., & Woo, J.-H. 2016, arXiv:1606.05348
- Baganoff, F. K., Maeda, Y., Morris, M., et al. 2003, *ApJ*, 591, 891
- Bahcall, J. N., Kirhakos, S., Saxe, D. H., & Schneider, D. P. 1997, *ApJ*, 479, 642
- Balbus, S. A., & Hawley, J. F. 1998, *Reviews of Modern Physics*, 70, 1
- Baldwin, J. A., Phillips, M. M., & Terlevich, R. 1981, *PASP*, 93, 5
- Beckmann, V., & Shrader, C. R. 2012, *Active Galactic Nuclei*, ISBN-13: 978-3527410781. 350 pages. Wiley-VCH Verlag GmbH, 2012,
- Bentz, M. C., Walsh, J. L., Barth, A. J., et al. 2009, *ApJ*, 705, 199
- Vanden Berk, D. E., Richards, G. T., Bauer, A., et al. 2001, *AJ*, 122, 549
- Berney, S., Koss, M., Trakhtenbrot, B., et al. 2015, *MNRAS*, 454, 3622
- Best, P. N., Kauffmann, G., Heckman, T. M., et al. 2005, *MNRAS*, 362, 25
- Birzan, L., McNamara, B. R., Nulsen, P. E. J., Carilli, C. L., & Wise, M. W. 2008, *ApJ*, 686, 859-880

- Blaes, O., Hubeny, I., Agol, E., & Krolik, J. H. 2001, *ApJ*, 563, 560
- Blanton, M. R., Lin, H., Lupton, R. H., et al. 2003, *AJ*, 125, 2276
- Boehringer, H., Voges, W., Fabian, A. C., Edge, A. C., & Neumann, D. M. 1993, *MNRAS*, 264, L25
- Boller, T., Brandt, W. N., & Fink, H. 1996, *A&A*, 305, 53
- Boller, T., Freyberg, M. J., Trümper, J., et al. 2016, *A&A*, 588, A103
- Bolton, A. S., Schlegel, D. J., Aubourg, É., et al. 2012, *AJ*, 144, 144
- Bongiorno, A., Merloni, A., Brusa, M., et al. 2012, *MNRAS*, 427, 3103
- Bondi, H., & Hoyle, F. 1944, *MNRAS*, 104, 273
- Bovy, J., Hennawi, J. F., Hogg, D. W., et al. 2011, *ApJ*, 729, 141
- Boyle, B. J., Shanks, T., Croom, S. M., et al. 2000, *MNRAS*, 317, 1014
- Brandt, W. N., & Hasinger, G. 2005, *ARA&A*, 43, 827
- Brandt, W. N., & Alexander, D. M. 2015, arXiv:1501.01982
- Brusa, M., Comastri, A., Mignoli, M., et al. 2003, *A&A*, 409, 65
- Brusa, M., Civano, F., Comastri, A., et al. 2010, *ApJ*, 716, 348
- Brusa, M., Bongiorno, A., Cresci, G., et al. 2015, *MNRAS*, 446, 2394
- Brusa, M., Perna, M., Cresci, G., et al. 2016, *A&A*, 588, A58
- Bruzual, G., & Charlot, S. 2003, *MNRAS*, 344, 1000
- Buchner, J., Georgakakis, A., Nandra, K., et al. 2015, *ApJ*, 802, 89
- Budavári, T., & Szalay, A. S. 2008, *ApJ*, 679, 301-309
- Bundy, K., Georgakakis, A., Nandra, K., et al. 2008, *ApJ*, 681, 931
- Burwitz, V., Predehl, P., Friedrich, P., et al. 2014, *Proc. SPIE*, 9144, 91441X
- Caccianiga, A., Severgnini, P., Della Ceca, R., et al. 2007, *A&A*, 470, 557
- Cano-Díaz, M., Maiolino, R., Marconi, A., et al. 2012, *A&A*, 537, L8
- Castelló-Mor, N., Barcons, X., Ballo, L., et al. 2012, *A&A*, 544, AA48
- Cavagnolo, K. W., McNamara, B. R., Nulsen, P. E. J., et al. 2010, *ApJ*, 720, 1066
- Chiappetti, L., Clerc, N., Pacaud, F., et al. 2013, *MNRAS*, 429, 1652
- Churazov, E., Forman, W., Jones, C., Boumlhringer, H. 2000, *A&A*, 356, 788
- Churazov, E., Sazonov, S., Sunyaev, R., et al. 2005, *MNRAS*, 363, L91

- Cicone, C., Maiolino, R., Sturm, E., et al. 2014, *A&A*, 562, A21
- Cicone, C., Maiolino, R., & Marconi, A. 2016, *A&A*, 588, A41
- Civano, F., Elvis, M., Brusa, M., et al. 2012, *ApJS*, 201, 30
- Clavel, J., Nandra, K., Makino, F., et al. 1992, *ApJ*, 393, 113
- Clerc, N., Pierre, M., Pacaud, F., & Sadibekova, T. 2012, *MNRAS*, 423, 3545
- Clerc, N., Adami, C., Lieu, M., et al. 2014, *MNRAS*, 444, 2723
- Coleman, G. D., Wu, C.-C., & Weedman, D. W. 1980, *ApJS*, 43, 393
- Comastri A. et al., 2002, *ApJ*, 571, 771
- Comparat, J., Delubac, T., Jouvel, S., et al. 2015, arXiv:1509.05045
- Cowie, L. L., Songaila, A., Hu, E. M., & Cohen, J. G. 1996, *AJ*, 112, 839
- Crenshaw, D. M., Schmitt, H. R., Kraemer, S. B., Mushotzky, R. F., & Dunn, J. P. 2010, *ApJ*, 708, 419
- Cresci, G., Mainieri, V., Brusa, M., et al. 2015, *ApJ*, 799, 82
- Croston, J. H., Kraft, R. P., Hardcastle, M. J., et al. 2009, *MNRAS*, 395, 1999
- Cuadra, J., Nayakshin, S., Springel, V., & Di Matteo, T. 2006, *MNRAS*, 366, 358
- de Jong, R. S., Barden, S., Bellido-Tirado, O., et al. 2014, *Proc. SPIE*, 9147, 91470M
- Davies, R., Burtscher, L., Rosario, D., et al. 2015, arXiv:1505.00536
- Davis, S. W., Woo, J.-H., & Blaes, O. M. 2007, *ApJ*, 668, 682
- Dawson, K. S., Schlegel, D. J., Ahn, C. P., et al. 2013, *AJ*, 145, 10
- Dawson, K. S., Kneib, J.-P., Percival, W. J., et al. 2016, *AJ*, 151, 44
- Del Moro, A., Alexander, D. M., Mullaney, J. R., et al. 2013, *A&A*, 549, A59
- Delvecchio, I., Gruppioni, C., Pozzi, F., et al. 2014, *MNRAS*, 439, 2736
- Devriendt, J. E. G., Guiderdoni, B., & Sadat, R. 1999, *A&A*, 350, 381
- Done, C., Gierliński, M., Sobolewska, M., & Schurch, N. 2007, *The Central Engine of Active Galactic Nuclei*, 373, 121
- Donley, J. L., Rieke, G. H., Rigby, J. R., & Pérez-González, P. G. 2005, *ApJ*, 634, 169
- Donley, J. L., Koekemoer, A. M., Brusa, M., et al. 2012, *ApJ*, 748, 142
- Eisenstein, D. J., Weinberg, D. H., Agol, E., et al. 2011, *AJ*, 142, 72
- Elitzur, M., & Shlosman, I. 2006, *ApJL*, 648, L101

- Elvis, M., Wilkes, B. J., McDowell, J. C., et al. 1994, *ApJS*, 95, 1
- Fanaroff, B. L., & Riley, J. M. 1974, *MNRAS*, 167, 31P
- Fabian, A. C., Rees, M. J., Stella, L., & White, N. E. 1989, *MNRAS*, 238, 729
- Fabian, A. C., & Ross, R. R. 2010, *Space Sci.Rev.*, 157, 167
- Fabian, A. C. 2012, *ARA&A*, 50, 455
- Fabian, A. C., Lohfink, A., Kara, E., et al. 2015, *MNRAS*, 451, 4375
- Feltre, A., Hatziminaoglou, E., Fritz, J., & Franceschini, A. 2012, *MNRAS*, 426, 120
- Ferrarese, L., & Merritt, D. 2000, *ApJL*, 539, L9
- Feruglio, C., Maiolino, R., Piconcelli, E., et al. 2010, *A&A*, 518, L155
- Feruglio, C., Fiore, F., Carniani, S., et al. 2015, *A&A*, 583, A99
- Fioc, M., & Rocca-Volmerange, B. 1997, *A&A*, 326, 950
- Fiore, F., Brusa, M., Cocchia, F., et al. 2003, *A&A*, 409, 79
- Fischer, T. C., Crenshaw, D. M., Kraemer, S. B., et al. 2011, *ApJ*, 727, 71
- R. A. Fisher, 1915, *Biometrika*, 4, 507-521
- Forman, W., Jones, C., Churazov, E., et al. 2007, *ApJ*, 665, 1057
- Ford, H. C., Harms, R. J., Tsvetanov, Z. I., et al. 1994, *ApJL*, 435, L27
- Fukugita, M., Ichikawa, T., Gunn, J. E., et al. 1996, *AJ*, 111, 1748
- Gallagher, S. C., Brandt, W. N., Chartas, G., et al. 2006, *ApJ*, 644, 709
- Gaskell, C. M. 2009, *NewAR*, 53, 140
- Garcet, O., Gandhi, P., Gosset, E., et al. 2007, *A&A*, 474, 473
- Gavignaud, I., Bongiorno, A., Paltani, S., et al. 2006, *A&A*, 457, 79
- Gebhardt, K., Bender, R., Bower, G., et al. 2000, *ApJL*, 539, L13
- Georgakakis, A., & Nandra, K. 2011, *MNRAS*, 414, 992
- Georgantopoulos, I., & Georgakakis, A. 2005, *MNRAS*, 358, 131
- Ghez, A. M., Duchene, G., Morris, M., et al. 2002, *Bulletin of the American Astronomical Society*, 34, 68.04
- Gibson, R. R., Jiang, L., Brandt, W. N., et al. 2009, *ApJ*, 692, 758
- Gilfanov, M. 2004, *Progress of Theoretical Physics Supplement*, 155, 49
- Gilfanov, M., & Merloni, A. 2014, *Space Sci.Rev.*, 183, 121

- Gofford, J., Reeves, J. N., Turner, T. J., et al. 2011, *MNRAS*, 414, 3307
- Goulding, A. D., Alexander, D. M., Lehmer, B. D., & Mullaney, J. R. 2010, *MNRAS*, 406, 597
- Granato, G. L., & Danese, L. 1994, *MNRAS*, 268, 235
- , J. E., & Ho, L. C. 2005, *ApJ*, 627, 721
- Grimm, H.-J., Gilfanov, M., & Sunyaev, R. 2003, *MNRAS*, 339, 793
- Gültekin, K., Richstone, D. O., Gebhardt, K., et al. 2009, *ApJ*, 698, 198
- Gunn, J. E., & Peterson, B. A. 1965, *ApJ*, 142, 1633
- Gunn, J. E., Siegmund, W. A., Mannery, E. J., et al. 2006, *AJ*, 131, 2332
- Haardt, F., & Maraschi, L. 1991, *ApJL*, 380, L51
- Hao, L., Strauss, M. A., Tremonti, C. A., et al. 2005, *AJ*, 129, 1783
- Harrison, C. M., Alexander, D. M., Swinbank, A. M., et al. 2012, *MNRAS*, 426, 1073
- Harrison, C. M., Alexander, D. M., Mullaney, J. R., & Swinbank, A. M. 2014, *MNRAS*, 441, 3306
- Harrison, C. M., 2016, *Springer Theses: Observational Constraints on the Influence of Active Galactic Nuclei on the Evolution of Galaxies*, Springer International Publishing Switzerland
- Hasinger, G., Miyaji, T., & Schmidt, M. 2005, *A&A*, 441, 417
- Hasinger, G. 2008, *A&A*, 490, 905
- Heckman, T. M., Kauffmann, G., Brinchmann, J., et al. 2004, *ApJ*, 613, 109
- Hewett, P. C., & Wild, V. 2010, *MNRAS*, 405, 2302
- Hickox, R. C., Jones, C., Forman, W. R., et al. 2009, *ApJ*, 696, 891
- Hickox, R. C., Mullaney, J. R., Alexander, D. M., et al. 2014, *ApJ*, 782, 9
- Hill, M. J., & Zakamska, N. L. 2014, *MNRAS*, 439, 2701
- Ho, L. C., Filippenko, A. V., & Sargent, W. L. W. 1997, *ApJ*, 487, 568
- Hopkins, P. F., Hernquist, L., Martini, P., et al. 2005, *ApJL*, 625, L71
- Hopkins, A. M., & Beacom, J. F. 2006, *ApJ*, 651, 142
- Hopkins, P. F., Richards, G. T., & Hernquist, L. 2007, *ApJ*, 654, 731
- Hopkins, P. F., Murray, N., & Thompson, T. A. 2009, *MNRAS*, 398, 303
- Hopkins, P. F., Hayward, C. C., Narayanan, D., & Hernquist, L. 2012, *MNRAS*, 420, 320

- Hoyle, F., & Lyttleton, R. A. 1941, *MNRAS*, 101, 227
- Jin, C., Ward, M., & Done, C. 2012, *MNRAS*, 422, 3268
- Kauffmann, G., Heckman, T. M., Tremonti, C., et al. 2003, *MNRAS*, 346, 1055
- Kauffmann, G., & Heckman, T. M. 2009, *MNRAS*, 397, 135
- Kaspi, S., Smith, P. S., Netzer, H., et al. 2000, *ApJ*, 533, 631
- Kennicutt, R. C., Jr. 1998, *ApJ*, 498, 541
- Kewley, L. J., Groves, B., Kauffmann, G., & Heckman, T. 2006, *MNRAS*, 372, 961
- King, A. 2003, *ApJL*, 596, L27
- King, A. R., Zubovas, K., & Power, C. 2011, *MNRAS*, 415, L6
- Kim, M., Ho, L. C., & Im, M. 2006, *ApJ*, 642, 702
- Kishimoto, M., Hönig, S. F., Antonucci, R., et al. 2011, *A&A*, 527, A121
- Komossa, S., & Xu, D. 2007, *ApJL*, 667, L33
- Komossa, S., Xu, D., Zhou, H., Storchi-Bergmann, T., & Binette, L. 2008, *ApJ*, 680, 926-938
- Kormendy, J., & Gebhardt, K. 2001, 20th Texas Symposium on relativistic astrophysics, 586, 363
- Kormendy, J., & Ho, L. C. 2013, *ARA&A*, 51, 511
- Krolik, J. H., & Begelman, M. C. 1986, *Bulletin of the American Astronomical Society*, 18, 903
- Krolik, J. H. 2001, *ApJ*, 551, 72
- Kraemer, S. B., Schmitt, H. R., Crenshaw, D. M., et al. 2011, *ApJ*, 727, 130
- Lacy, M., Petric, A. O., Sajina, A., et al. 2007, *AJ*, 133, 186
- Lamareille, F., Mouhcine, M., Contini, T., Lewis, I., & Maddox, S. 2004, *MNRAS*, 350, 396
- Lamareille, F. 2010, *A&A*, 509, AA53
- Laor, A., & Draine, B. T. 1993, *ApJ*, 402, 441
- Lawrence, A., Rowan-Robinson, M., Efstathiou, A., et al. 1991, *MNRAS*, 248, 91
- Lee, N., Sanders, D. B., Casey, C. M., et al. 2015, *ApJ*, 801, 80
- Liu, G., Zakamska, N. L., Greene, J. E., Nesvadba, N. P. H., & Liu, X. 2013, *MNRAS*, 436, 2576

- Liu, Z., Merloni, A., Georgakakis, A., et al. 2016, MNRAS, 459, 1602
- Luo, B., Brandt, W. N., Xue, Y. Q., et al. 2010, ApJS, 187, 560
- Lusso, E., & Ciotti, L. 2011, A&A, 525, AA115
- Lynden-Bell, D., & Rees, M. J. 1971, MNRAS, 152, 461
- Lynds, C. R. 1967, ApJ, 147, 396
- Lynds, R. 1971, ApJL, 164, L73
- Nandra, K., Georgakakis, A., Willmer, C. N. A., et al. 2007, ApJL, 660, L11
- Magorrian, J., Tremaine, S., Richstone, D., et al. 1998, AJ, 115, 2285
- Madau, P., & Dickinson, M. 2014, ARA&A, 52, 415
- Mainzer, A., Bauer, J., Grav, T., et al. 2011, ApJ, 731, 53
- Maiolino R. et al., 2007, MNRAS, 334, L59
- Mason, R. E. 2015, Planetary and Space Science, 116, 97
- Maraston, C., Pforr, J., Henriques, B. M., et al. 2013, MNRAS, 435, 2764
- Marconi, A., Risaliti, G., Gilli, R., et al. 2004, MNRAS, 351, 169
- Markowitz, A. G., Krumpe, M., & Nikutta, R. 2014, MNRAS, 439, 1403
- Martínez-Sansigre, A., Rawlings, S., Lacy, M., et al. 2005, *Nature*, 436, 666
- Mateos, S., Barcons, X., Carrera, F. J., et al. 2005, A&A, 444, 79
- Di Matteo, T., Springel, V., & Hernquist, L. 2005, *Nature*, 433, 604
- Meléndez, M., Heckman, T. M., Martínez-Paredes, M., Kraemer, S. B., & Mendoza, C. 2014, MNRAS, 443, 1358
- Mendez, A. J., Coil, A. L., Aird, J., et al. 2013, ApJ, 770, 40
- Mendez, A. J., Coil, A. L., Aird, J., et al. 2015, arXiv:1504.06284
- Menzel, M.-L., Merloni, A., Georgakakis, A., et al. 2016, MNRAS, 457, 110
- Merloni, A., & Heinz, S. 2008, MNRAS, 388, 1011
- Merloni, A., Predehl, P., Becker, W., et al., 2012, *eROSITA Science Book: Mapping the Structure of the Energetic Universe*, astro-ph, arXiv:1209.3114
- Merloni, A., & Heinz, S. 2013, Planets, Stars and Stellar Systems. Volume 6: Extragalactic Astronomy and Cosmology, 6, 503
- Merloni, A., & Bongiorno, A. 2013, MmSAI, 84, 675
- Merloni, A., Bongiorno, A., Brusa, M., et al. 2014, MNRAS, 437, 3550

- Merloni A., 2015, Chapter in "Astrophysical Black Holes", Haardt F., Gorini V., Moschella U., Treves A., Colpi M. (Eds.), Lecture Notes in Physics, Volume 905, 2016, p. 101-143, Springer International Publishing Switzerland
- Messias, H., Afonso, J. M., Salvato, M., Mobasher, B., & Hopkins, A. M. 2014, *A&A*, 562, AA144
- Morganson, E., Green, P. J., Anderson, S. F., Ruan, J. J., & TDSS Team, S. C., PS1 Consortium 2015, American Astronomical Society Meeting Abstracts, 225, #113.02
- Mullaney, J. R., Alexander, D. M., Fine, S., et al. 2013, *MNRAS*, 433, 622
- Myers, A. D., Palanque-Delabrouille, N., Prakash, A., et al. 2015, *ApJS*, 221, 27
- Nandra, K., & Pounds, K. A. 1994, *MNRAS*, 268, 405
- Nandra, K., George, I. M., Mushotzky, R. F., Turner, T. J., & Yaqoob, T. 1997, *ApJ*, 477, 602
- Nandra, K., Clavel, J., Edelson, R. A., et al. 1998, *ApJ*, 505, 594
- Nandra, K., Mushotzky, R. F., Arnaud, K., et al. 2002, *ApJ*, 576, 625
- Nenkova, M., Sirocky, M. M., Nikutta, R., Ivezić, Ž., & Elitzur, M. 2008, *ApJ*, 685, 160-180
- Netzer, H. 1990, *Active Galactic Nuclei*, 57
- Netzer, H. 2013, *The Physics and Evolution of Active Galactic Nuclei*, by Hagai Netzer, Cambridge, UK: Cambridge University Press, 2013,
- NIST_ASD, A. Kramida and Yu. Ralchenko and J. Reader and and NIST ASD Team, NIST Atomic Spectra Database (ver. 5.3), [Online]. Available: <http://physics.nist.gov/asd> [2016, May 28]. National Institute of Standards and Technology, Gaithersburg, MD., year = 2015
- Osterbrock, D. E., & Pogge, R. W. 1985, *ApJ*, 297, 166
- Osterbrock, D. E., & Ferland, G. J. 2006, *Astrophysics of gaseous nebulae and active galactic nuclei*, 2nd. ed. by D.E. Osterbrock and G.J. Ferland. Sausalito, CA: University Science Books, 2006,
- Pâris, I., Petitjean, P., Aubourg, É., et al. 2012, *A&A*, 548, AA66
- Pâris, I., Petitjean, P., Aubourg, É., et al. 2014, *A&A*, 563, A54
- Peng, Z.-X., Chen, Y.-M., Gu, Q.-S., & Zhang, K. 2014, *Research in Astronomy and Astrophysics*, 14, 913-922
- Pereyra, N. A., Vanden Berk, D. E., Turnshek, D. A., et al. 2006, *ApJ*, 642, 87
- Peterson, B. M. 1997, *An introduction to active galactic nuclei*, Publisher: Cambridge, New York Cambridge University Press, 1997 Physical description xvi, 238 p. ISBN 0521473489,

-
- Peterson, B. M., Ferrarese, L., Gilbert, K. M., et al. 2004, ApJ, 613, 682
- Piccinotti, G., Mushotzky, R. F., Boldt, E. A., et al. 1982, ApJ, 253, 485
- Piconcelli, E., Jimenez-Bailón, E., Guainazzi, M., et al. 2005, A&A, 432, 15
- Pier, E. A., & Krolik, J. H. 1992, ApJ, 401, 99
- Pier, E. A., & Krolik, J. H. 1993, ApJ, 418, 673
- Pierre, M., Valtchanov, I., Altieri, B., et al. 2004, JCAP, 9, 011
- Polletta, M., Tajer, M., Maraschi, L., et al. 2007, ApJ, 663, 81
- Pons, E., & Watson, M. G. 2014, A&A, 568, AA108
- Pounds, K. A., Reeves, J. N., King, A. R., et al. 2003, MNRAS, 345, 705
- Pradhan, A.K. &Nahar, S.N. 2011, Atomic Astrophysics and Spectroscopy, Cambridge University Press
- Predehl, P., Andritschke, R., Becker, W., et al. 2014, Proc. SPIE, 9144, 91441T
- Quataert, E., Narayan, R., & Reid, M. J. 1999, ApJL, 517, L101
- Radomski, J. T., Piña, R. K., Packham, C., et al. 2003, ApJ, 587, 117
- Rafferty, D. A., McNamara, B. R., & Nulsen, P. E. J. 2008, ApJ, 687, 899-918
- Ranalli, P., Comastri, A., & Setti, G. 2003, A&A, 399, 39
- Rees, M. J., Silk, J. I., Werner, M. W., & Wickramasinghe, N. C. 1969, *Nature*, 223, 788
- Rees, M. J. 1984, ARA&A, 22, 471
- Reeves, J. N., & Turner, M. J. L. 2000, MNRAS, 316, 234
- Reeves, J. N., O'Brien, P. T., & Ward, M. J. 2003, ApJL, 593, L65
- Reynolds, C. S., & Begelman, M. C. 1997, ApJ, 488, 109
- Reynolds, C. S., Young, A. J., Begelman, M. C., & Fabian, A. C. 1999, ApJ, 514, 164
- Richards, G. T., Myers, A. D., Gray, A. G., et al. 2009, ApJS, 180, 67
- Richards, G. T., Kruczek, N. E., Gallagher, S. C., et al. 2011, AJ, 141, 167
- Risaliti, G., & Elvis, M. 2004, Supermassive Black Holes in the Distant Universe, 308, 187
- Ross, N. P., Myers, A. D., Sheldon, E. S., et al. 2012, ApJS, 199, 3
- Rupke, D. S., Veilleux, S., & Sanders, D. B. 2005, ApJS, 160, 115
- Rupke, D. S. N., & Veilleux, S. 2011, ApJL, 729, L27
- Rupke, D. S. N., & Veilleux, S. 2013, ApJ, 768, 75

- Rykoff, E. S., Rozo, E., Busha, M. T., et al. 2014, *ApJ*, 785, 104
- Sadibekova, T., Pierre, M., Clerc, N., et al. 2014, *A&A*, 571, A87
- Salpeter, E. E. 1964, *ApJ*, 140, 796
- Sanders, D. B., Soifer, B. T., Elias, J. H., et al. 1988, *ApJ*, 325, 74
- Sanders, D. B., Phinney, E. S., Neugebauer, G., Soifer, B. T., & Matthews, K. 1989, *ApJ*, 347, 29
- Schartmann, M., Meisenheimer, K., Camenzind, M., Wolf, S., & Henning, T. 2005, *A&A*, 437, 861
- Schartmann, M., Meisenheimer, K., Klahr, H., et al. 2009, *MNRAS*, 393, 759
- Schawinski, K., Koss, M., Berney, S., & Sartori, L. F. 2015, *MNRAS*, 451, 2517
- Schnittman, J. D., Krolik, J. H., & Noble, S. C. 2013, *ApJ*, 769, 156
- Schnorr Müller, A., Storchi-Bergmann, T., Riffel, R. A., et al. 2011, *MNRAS*, 413, 149
- Schödel, R., Ott, T., Genzel, R., et al. 2002, *Nature*, 419, 694
- Schweitzer, M., Lutz, D., Sturm, E., et al. 2006, *ApJ*, 649,
- Scoville, N., & Norman, C. 1995, *ApJ*, 451, 510 79
- Shakura, N. I., & Sunyaev, R. A. 1973, *A&A*, 24, 337
- Shankar, F., Weinberg, D. H., & Miralda-Escudé, J. 2009, *ApJ*, 690, 20
- Shemmer, O., Romano, P., Bertram, R., et al. 2001, *ApJ*, 561, 162
- Shi, Y., Ogle, P., Rieke, G. H., et al. 2007, *ApJ*, 669, 841
- Shen, Y., Greene, J. E., Ho, L. C., et al. 2015, *ApJ*, 805, 96
- Silverman, J. D., Lamareille, F., Maier, C., et al. 2009, *ApJ*, 696, 396
- Silk, J., & Rees, M. J. 1998, *A&A*, 331, L1
- Silva, L., Granato, G. L., Bressan, A., & Danese, L. 1998, *ApJ*, 509, 103
- Smee, S. A., Gunn, J. E., Uomoto, A., et al. 2013, *AJ*, 146, 32
- Soltan, A. 1982, *MNRAS*, 200, 115
- Stalin, C. S., Petitjean, P., Srianand, R., et al. 2010, *MNRAS*, 401, 294
- Stern, D., Eisenhardt, P., Gorjian, V., et al. 2005, *ApJ*, 631, 163
- Stern, D., Assef, R. J., Benford, D. J., et al. 2012, *ApJ*, 753, 30
- Storchi-Bergmann, T., Lopes, R. D. S., McGregor, P. J., et al. 2010, *MNRAS*, 402, 819

- Stoughton, C., Lupton, R. H., Bernardi, M., et al. 2002, *AJ*, 123, 485
- Sutherland, W., & Saunders, W. 1992, *MNRAS*, 259, 413
- Tanaka, Y., Nandra, K., Fabian, A. C., et al. 1995, *Nature*, 375, 659
- Tajer, M., Polletta, M., Chiappetti, L., et al. 2007, *A&A*, 467, 73
- Telfer, R. C., Zheng, W., Kriss, G. A., & Davidsen, A. F. 2002, *ApJ*, 565, 773
- Tristram, K. R. W., Burtscher, L., Jaffe, W., et al. 2014, *A&A*, 563, A82
- Trump, J. R., Impey, C. D., Taniguchi, Y., et al. 2009, *ApJ*, 706, 797
- Ueda, Y., Akiyama, M., Ohta, K., & Miyaji, T. 2003, *ApJ*, 598, 886
- Ueda, Y., Akiyama, M., Hasinger, G., Miyaji, T., & Watson, M. G. 2014, *ApJ*, 786, 104
- Ueda, Y., Hashimoto, Y., Ichikawa, K., et al. 2015, *ApJ*, 815, 1
- Ueda, Y., Watson, M. G., Stewart, I. M., et al. 2008, *ApJS*, 179, 124
- Ulrich, M.-H., Maraschi, L., & Urry, C. M. 1997, *ARA&A*, 35, 445
- Urry, C. M., & Padovani, P. 1995, *PASP*, 107, 803
- Uttley, P., McHardy, I. M., Papadakis, I. E., Cagnoni, I., & Fruscione, A. 2000, *MNRAS*, 312, 880
- Vanden Berk, D. E., Richards, G. T., Bauer, A., et al. 2001, *AJ*, 122, 549
- Voges, W., Aschenbach, B., Boller, T., et al. 1999, *A&A*, 349, 389
- Volonteri, M. 2010, *A&A Rev.*, 18, 279
- Wang, T., & Lu, Y. 2001, *A&A*, 377, 52
- Warwick, R. S., Saxton, R. D., & Read, A. M. 2012, *A&A*, 548, A99
- Whittle, M. 1985, *MNRAS*, 213, 1
- Whittle, M. 1994, *Mass-Transfer Induced Activity in Galaxies*, 63
- Winter, L. M., Mushotzky, R. F., Reynolds, C. S., & Tueller, J. 2009, *ApJ*, 690, 1322
- Woo, J.-H., Kim, J. H., Imanishi, M., & Park, D. 2012, *AJ*, 143, 49
- Woo, S. C., Turnshek, D. A., Badenes, C., & Bickerton, S. 2013, *MNRAS*, 434, 1411
- Woo, J.-H., Bae, H.-J., Son, D., & Karouzos, M. 2016, *ApJ*, 817, 108
- White, S. D. M., & Rees, M. J. 1978, *MNRAS*, 183, 341
- Wright, E. L., Eisenhardt, P. R. M., Mainzer, A. K., et al. 2010, *AJ*, 140, 1868
- Xie, X., Shao, Z., Shen, S., Liu, H., & Li, L. 2016, *ApJ*, 824, 38

- Yan, R., Ho, L. C., Newman, J. A., et al. 2011, ApJ, 728, 38
- Yan, R., & Blanton, M. R. 2012, ApJ, 747, 61
- Yip, C. W., Connolly, A. J., Szalay, A. S., et al. 2004, AJ, 128, 585
- Young, S., Axon, D. J., Robinson, A., Hough, J. H., & Smith, J. E. 2007, *Nature*, 450, 74
- Yuan, F., & Narayan, R. 2004, ApJ, 612, 724
- Zakamska, N. L., Strauss, M. A., Krolik, J. H., et al. 2003, AJ, 126, 2125
- Zakamska, N. L., & Greene, J. E. 2014, MNRAS, 442, 784
- Zdziarski, A. A., Fabian, A. C., Nandra, K., et al. 1994, MNRAS, 269, L55
- Zel'dovich, Y. B., & Novikov, I. D. 1964, Soviet Physics Doklady, 9, 246
- Zhang, K., Dong, X.-B., Wang, T.-G., & Gaskell, C. M. 2011, ApJ, 737, 71
- Zhu, G. B., Comparat, J., Kneib, J.-P., et al. 2015, ApJ, 815, 48
- Zubovas, K., & King, A. 2012, ApJL, 745, L34